Efficiently Maximising Power Generation from Thermoelectric Generators

Andrea Montecucco

BSc, MSc

Submitted in fulfilment of the requirements for the

Degree of Philosophy Doctorate

Supervisor: *Prof. Andrew R. Knox*

Academic Year 2013-2014

Abstract

Thermoelectric generators (TEGs) convert the thermal energy flowing through them into DC electrical energy in a quantity dependant on the temperature difference across them and the electrical load applied, with a conversion efficiency of typically 5 %. Nonetheless, they can be successfully employed to recover energy from waste heat and their use has increased rapidly in recent years, with applications ranging from microwatts to kilowatts, due to energy policy legislations and increasing energy cost determined by climate change, environmental issues and availability of energy sources.

The performance of TEGs, subject to thermal and electrical effects, can vary considerably depending on the operating conditions, therefore it is necessary to measure and characterise their performance, and to understand their dynamic behaviour and interaction with the other parts of the system. Based on this knowledge it is then desired to develop an effective electronic system able to control these devices so as to maximise the power generated and increase the overall efficiency of the system.
Several TEGs can be electrically connected in series and/or parallel (forming an array) to provide the required voltage and/or current. However, TEGs are usually employed in environments with time-varying temperatures, thermal powers and electrical loads. As a consequence in most TEG systems the individual thermoelectric devices can be subject to temperature mismatch due to operating conditions. Therefore it is of relevant importance to accurately simulate the evolution of thermoelectric systems during thermal and electrical transients. At the same time accurate experimental performance data are necessary to permit precise simulations. Unfortunately, there is still no standardised method to test the electrical and thermal performance of TEGs.
This thesis tackles these key challenges and contributes to the pool of existing knowledge about TEGs dealing with four main topics: testing of thermoelectric generators, simulation of thermoelectric generating systems, design and production of power electronic converters for thermoelectric generators, and physical applications of thermoelectric generators.

After an introduction to the physical phenomena underlying the operation of TEGs, this thesis describes the innovative test system built at the University of Glasgow to assess the performance of TEG devices in the "real-world". The fixture allows a single TEG device to be tested with thermal

input power up to $1\,kW$ and hot temperature up to 800°C with minimal thermal losses and thermal shock; the mechanical clamping force can be adjusted up to $5\,kN$, and the temperatures are sensed by thermocouples placed directly on the TEGs surfaces. A computer program controls all the instruments in order to minimise errors and to aid accurate measurement and test repeatability. The test rig can measure four TEGs simultaneously, each one individually controlled and heated. This allows testing the performance of TEG arrays under mismatched conditions, *e.g.*, dimensions, clamping force, temperature, etc. Under these circumstances experimental results and a mathematical analysis show that when in operation each TEG in the array will have a different electrical operating point at which maximum energy can be extracted and problems of decreased power output arise.

This thesis provides the transient solution to the one-dimensional heat conduction equation with internal heat generation that describes the transfer and generation of heat throughout a thermoelectric device with dynamic exchange of heat through the hot and cold sides. This solution is then included in a model in which the Peltier effect, the thermal masses and the electrical behaviour of the system are also considered. The resulting model is created in Simulink and the comparison with experimental results from a TEG system confirms the accuracy of the simulation tool to predict the evolution of the thermoelectric system both in steady-state and during thermal or electrical transients.

This thesis presents an investigation of the optimum electrical operating load to maximise the power produced by a TEG. Both fixed temperature difference and fixed thermal input power conditions are considered. Power electronic converters controlled by a Maximum Power Point Tracking (MPPT) algorithm are used to maximise the power transfer from the TEG to the load. The MPPT method based on the open-circuit voltage is arguably the most suitable for the almost linear electrical characteristic of TEGs. An innovative way to perform the open-circuit voltage measurement during the pseudo-normal operation of the power converter is presented. This MPPT technique is supported by theoretical analysis and used to control an efficient synchronous Buck-Boost converter capable of interfacing TEGs over a wide range of temperatures. The prototype MPPT converter is controlled by an inexpensive microcontroller, and a lead-acid battery is used to accumulate the harvested energy. Experimental results using commercial TEG devices demonstrate the ability of the MPPT converter to accurately track the maximum power point during steady-state and thermal transients.

This thesis also presents two practical applications of TEGs. The first application exploits the thermal energy generated by a stove to concurrently produce electrical energy and heat water, while the second application recovers the heat energy rejected to ambient by a car's exhaust gas system to generate electrical energy for battery charging.

To Napo

Contents

List of Tables

List of Figures

Acknowledgments

First I would like to thank my supervisor Prof. Andrew Knox, who supervised me as boss, mentor and friend.
Thanks to Jonathan Siviter for three incredible University years together, sharing offices and labs, travels and nights out, problems and achievements.
Thanks to Paul Mullen for the last six months working and joking around together.
Thanks to Peter Miller, invaluable technician and consultant.
Thanks to James R. Buckle for his precious advices at the beginning of my postgraduate studies.
Thanks to Joseph Melone for sharing the office with me, and for the banter.
Thanks to my other colleagues and friends for all the time spent together: Laura Meriggi, Lourdes Ferre Llin, Matthias Willig, Jeremiah Matthey and Vincenzo Pusino.
Thanks to all the people at European Thermodynamics Ltd with whom I worked and especially to Kevin Simpson, States Chiwanga, Ismini Dimitriadou, Mark Robbins and Ashley Fullham. The industrial experience that they've added contributed so much to make this doctorate a precious life experience.
Thanks to my great friends Maurizio Alvarez, Craig Clanachan, Antonio Samarelli, Grace Zhou Hang and a special hug to my colleague, flatmate, and best friend Marcos Compadre Torrecilla.

Finally and above all, my greatest thanks are reserved for my family, who have always been there for me, no matter where I was going; and here I am, thanks to Ignazia, Cesare and Chiara.

" I declare that, except where explicit reference is made to the contribution of others, this dissertation is the result of my own work and has not been submitted for any other degree at the University of Glasgow or any other institution.

Signature _____

Printed name _____ "

List of Acronyms

ADC Analogue-to-Digital Conversion

AUV Autonomous underwater vehicle

CAD Computer-Aided Design

CAN Controller Area Network

CCM Continuous Conduction Mode

CHP Combined Heat and Power

CMPPT Central Maximum Power Point Tracking

DC Direct Current

DCM Discontinuous Conduction Mode

DMPPT Distributed Maximum Power Point Tracking

ESC Extremum Seeking

FEA Finite Element Analysis

HCD Hybrid Centralised-Distributed

HE Heat Equation

IC Integrated Circuit

I^2C Inter Integrated Circuit

INC Incremental Conductance

LCO Limit Cycle Oscillation

LIN Local Interconnected Network

MPP Maximum Power Point

MPPT Maximum Power Point Tracking

NEDC New European Driving Cycle

PC Personal Computer

PCB Printed Circuit Board

PI Proportional Integral

PID Proportional Integral Derivative

PWM Pulse Width Modulation

P&O Perturb & Observe

PSU Power Supply Unit

RMS Root Mean Square

RMSE Root Mean Square Error

PV Photovoltaic

RF Radio-frequency

SMPS Switch-Mode Power Supply

TEG Thermoelectric Generator

TPV Thermophotovoltaic

TVS Transient Voltage Suppression

USB Universal Serial Bus

WSN Wireless Sensor Network

Chapter 1

Introduction

Thermoelectric devices are physically and electrically robust semiconductor devices that can directly convert thermal energy into electrical energy and *vice-versa*. They are composed of n- and p-doped semiconductor pellets electrically connected in series (to achieve and/or sustain higher voltages) and thermally in parallel. A ceramic layer serves as electrical isolation and mechanical substrate. The resulting device, described in Chapter 3, can work in heat pumping (cooling or heating) or electrical power generating mode. This thesis focuses on the latter function.
In power generation mode the TEG produces a voltage differential when a temperature gradient is established at its sides, due to the Seebeck effect. When a load is connected to the TEG's terminals current flows through the device producing heat by Joule heating and pumping additional heat from the hot to the cold side because of the Peltier effect, which is considered a parasitic effect in power generation; in fact the Peltier effect effectively increases the overall thermal conductivity of the device.
TEGs are commercially produced in a wide range of sizes from a few millimetres to several centimetres on a side. The cross-sectional area of the pellets greatly influences the internal resistance and the current-voltage rating of the device. A module with wide pellets can fit a small number of pellets, therefore it will have relatively small output voltage and internal resistance, but high output current. Multiple modules can be electrically connected in series or parallel in order to achieve higher output voltages and currents and provide the required power level.
TEGs can use almost any source of thermal energy and they have a number of advantages over other energy conversion methods: they are robust, light in weight, reliable and have no mechanical moving parts, hence they have no vibration or maintenance requirements and are silent in operation. Nowadays TEGs find most use in the recovery of heat wasted by other processes, with applications from sensors, to vehicles, to industrial plants, as presented in Chapter 2.

The TEG can be electrically modelled in steady-state as a voltage source in series with an internal resistance. For a given temperature difference the electrical power delivered by the TEG varies

depending on the current drawn by the electrical load connected to its terminals. To maximise the power transferred from the TEG at any fixed temperature difference the load's impedance should equal the TEG's internal resistance, as stated by the *'maximum power transfer theorem'*.
In order to properly design a thermoelectric power generating system it is important to have data available about the performance of off-the-shelf TEGs. However, to date there is no standardised way of testing thermoelectric devices, whose performance reported in the manufacturer's datasheet is sometimes different from practical use. In an attempt to provide a solution to this problem, an innovative test system to assess device performance in the 'real world' has been developed at the University of Glasgow. The test rig can be employed both as a performance evaluator and as a quality control unit, due to its ability to provide repeatable testing of four TEGs concurrently. It can also be used to rapidly characterise devices of different dimensions at the same time.
These features allow investigation of the effects of series and parallel connection of TEGs under mismatched conditions, *e.g.*, temperature difference, dimensions and mechanical clamping pressure. The study presented in Chapter 4 quantifies the performance of interconnected TEG arrays when the elements are not all equally heated. Also, the effect that non-optimal electrical operating points have on the thermal balance of each TEG is analysed. A theoretical analysis provides a way to predict the thermal and electrical behaviour of the system when several TEG devices are electrically connected in series or parallel, under balanced or unbalanced thermal conditions. Experimental results taken from an operating thermoelectric generating system using multiple thermally unbalanced TEGs confirm the theoretical analysis and provide a quantification of the power lost due to temperature mismatch. The results presented are discussed and a comparison between series and parallel connection of TEG arrays is provided. These results can then be used to assist in deciding the number of TEGs and type of interconnection of TEG arrays.

Thermoelectric systems usually include thermal masses, TEG devices and power and control electronics, and they are influenced by several thermal and electronic phenomena whose interaction is complex. Moreover TEGs are often employed in thermally dynamic environments which frequently undergo transients. Actual Computer-Aided Design (CAD) tools do not yet include the ability to model thermoelectric effects therefore they cannot be successfully used to accurately simulate the electro-thermal coupled effects which take place during changes in the system operating conditions, *e.g.*, temperature, power or load changes. These problems are not yet fully assessed in literature and industry. To carefully design the whole system in cases of frequent changes of operating conditions and during start-up and shut-down, it becomes necessary to model these thermal transients and dynamic characteristics.
Chapter 5 first introduces a mathematical solution of the heat conduction equation for thermoelectric devices with internal Joule heat generation and dynamic exchanges of heat through the hot and cold sides, and then couples it with the other thermal and electrical phenomena occurring in real thermoelectric systems. The resulting physical model takes into account the dynamic relationships between the several thermal masses and the dominant thermoelectric phenomena occurring in a generalised thermoelectric system. The physical model is then used as the basic structure to develop

a computer tool capable of accurate simulations of the thermal and electrical dynamics of a physical thermoelectric power generating system. This model is created in *Simulink* and *Matlab* and a comparison between experimental and simulated results is presented to demonstrate the effectiveness and accuracy of the proposed simulation model.

In practical applications the temperature difference across the TEG device varies in time, therefore specialised power electronic converters are used to interface TEGs to the attached load while tracking the optimum electrical operating point for the TEG. These so-called Maximum Power Point Tracking (MPPT) converters are typically employed to maximise the power extracted at any thermal operating point.
Ideally each TEG should be independently electronically controlled but this would greatly increase the number and complexity of the MPPT power electronic converters needed and adversely affect the cost of implementing the system. As a consequence TEGs are often interconnected to form arrays with each array connected to a separate MPPT converter. This leads to the formation of what is called a Distributed Maximum Power Point Tracking (DMPPT) subsystem in which each TEG array's electrical operating point is controlled independently.
Among the several MPPT algorithms existing in literature, the *fractional open-circuit* method is arguably the most suited for TEGs due to their linear electrical characteristic. Chapter 6 presents an innovative technique to measure the open-circuit voltage of the TEGs during the normal switching of the converter with minimal reduction in collection efficiency. This MPPT technique is used to control a synchronous Buck-Boost converter, which accepts a wide input voltage range and is consequently able to harvest power from the TEGs over a wide range of operating temperatures. The MPPT converter described in Chapter 6 has been designed minimising cost, dimensions and weight. The prototype converter is tested with real TEGs, both in steady-state and under thermal transients, and the experimental results show exceptional performance in terms of electrical and energy collection efficiencies.

The knowledge generated and the technology designed during the research activity associated with this Ph.D. work has then been used to apply the thermoelectric power generating technology to stove applications and automotive applications, described in Chapter 7.

1.1 Thesis structure

Following is a brief description of each chapter forming this thesis:

- Chapter 2 examines recent applications of TEGs for waste heat recovery and presents a review of updated literature relative to the topics investigated in this thesis.
- Chapter 3 describes the physical phenomena, related to thermoelectricity, that constitute the

basis for understanding the contents of this thesis. The mechanical structure of a common commercial TEG device is presented and its electrical characteristic is analysed in general terms to highlight the link between geometrical parameters and the thermal and electrical performance. The steady-state power balance is also analysed and the figure of merit and efficiency are defined.

- Chapter 4 presents the test system developed to measure the electrical and thermal performance of TEG devices. The test rig allows testing of up to four devices concurrently, each with independent control over temperature difference, mechanical and electrical loading. The effect of temperature mismatch on power production is studied when a number of TEGs are electrically connected in series and parallel to form a TEG array. This chapter also investigates the maximum power production with constant thermal power input.

- Chapter 5 proposes the steady-state and transient solution to the one-dimensional heat conduction equation for thermoelectric devices with internal Joule heat generation and dynamic exchange of heat on both sides. This analytical solution is then incorporated into a computer model developed in *Matlab* and *Simulink* to accurately simulate the electro-thermal dynamics occurring in a thermoelectric generating system. Simulation results are compared to experimental results to validate the model as a reliable tool to predict the performance and aid in the design of thermoelectric systems.

- Chapter 6 starts by examining the need for electronic converters able to maximise power production in thermoelectric power generating systems and describes the most commonly used MPPT algorithms. An innovative technique to measure the open-circuit voltage of TEGs connected to a buck or buck-boost derived DC-DC converter without interrupting its operation is then presented. A theoretical analysis validating the description of the measurement event and the losses introduced by the required additional components is also provided. This technique is used to develop an efficient version of the fractional voltage MPPT method, which controls a synchronous Buck-Boost converter equipped with an original snubber circuit to suppress overvoltage transients. The resulting MPPT converter is shown to demonstrate excellent tracking performance in steady-state and during thermal or load transients when experimentally tested with a TEG array.

- Chapter 7 examines practical applications of TEGs to recover waste heat from other necessary processes and their use to convert thermal energy into usable electrical power. Firstly, TEGs are applied to a solid fuel stove in a symbiotic system that simultaneously produces electricity and heats cold water from the heat produced in the stove. Secondly, the MPPT electronics intended to be used in an automotive TEG system that recovers waste heat from the exhaust gas is presented.

- Chapter 8 reviews the thesis' contents and reflects on the conclusions evinced from the research activity undertaken for this study.

1.2 Original contribution

Following is a list of the innovative contributions originated from the research work undertaken that are included in this thesis and published in peer-refereed journals, patents and conferences proceedings as listed in the next section:

- Test rig to measure the performance of thermoelectric generators and mathematical formulation to predict their behaviour at any thermal state (Chapter 4).
- Study of maximum power production with constant thermal power input (Chapter 4).
- Theoretical analysis and experimental results on the power lost due to temperature mismatch of TEGs connected in series and parallel (Chapter 4).
- Transient solution to the 1-D heat conduction equation with internal Joule heat generation and dynamic exchange of heat on the sides (Chapter 5).
- Computer model to accurately simulate dynamic thermoelectric systems (Chapter 5).
- Technique to measure the open-circuit voltage of a thermoelectric generator connected to a DC-DC converter, during its pseudo-normal operation (Chapter 6).
- Theoretical analysis of the losses introduced by such MPPT technique (Chapter 6).
- Snubber circuit to damp overshoot voltage spikes occurring during the open-circuit transient event (Chapter 6).
- Maximum power point tracking synchronous buck-boost converter for thermoelectric generators (Chapter 6).
- Technique to efficiently detect discontinuous conduction mode in converters interfacing energy sources to batteries to prevent reverse current flow (Chapter 6).
- Mechanical fixture for combined electricity generation and water heating from a stove (Chapter 7).
- Technique to protect a Bi_2Te_3 TEG from excessive hot temperature (Chapter 7).
- Simulation model for automotive TEG heat recovery systems (Chapter 7).
- Electronic system to maximise power generation from automotive TEG heat recovery systems (Chapter 7).

1.3 List of publications

The work presented in this thesis has in part been published in the references listed below.

1.3.1 Patents

[P1] A.R. Knox, A. Montecucco, K. Simpson, "Thermoelectric Generators," *UK Patent No. GB1301335.4; International Patent No. PCT/GB2014/050199*

1.3.2 Journal papers

[J1] A. Montecucco, A.R. Knox, "Maximum Power Point Tracking Converter Based on the Open-Circuit Voltage Method for Thermoelectric Generators," *IEEE Transactions on Power Electronics*, in print, Mar. 2014
doi:10.1109/TPEL.2014.2313294

[J2] A. Montecucco, J. Siviter, A.R. Knox, "The Effect of Temperature Mismatch on Thermoelectric Generators Electrically Connected in Series and Parallel," *Applied Energy*, vol. 123, pp. 47–54, Jun. 2014
doi:10.1016/j.apenergy.2014.02.030

[J3] O. Maganga, N. Phillip, A. Montecucco, J. Siviter, K.J. Burnham, A.R. Knox, K. Simpson, "Hardware Implementation of Maximum Power Point Tracking for Thermoelectric Generators," *Journal of Electronic Materials*, vol. 43, no. 6, pp. 2293–2300, Jun. 2014
doi:10.1007/s11664-014-3046-0

[J4] A. Montecucco, and A.R. Knox, "Accurate Simulation of Thermoelectric Power Generating Systems," *Applied Energy*, vol. 118, pp. 166–172, Apr. 2014
doi:10.1016/j.apenergy.2013.12.028

[J5] A. Montecucco, J. Buckle, J. Siviter, A.R. Knox, "A New Test Rig for Accurate Nonparametric Measurement and Characterization of Thermoelectric Generators," *Journal of Electronic Materials*, vol. 42, no. 7, pp. 1966–1973, Jul. 2013
doi:10.1007/s11664-013-2484-4

[J6] A. Montecucco, J. Buckle, A.R. Knox, "Solution to the 1-D unsteady heat conduction equation with internal Joule heat generation for thermoelectric devices," *Applied Thermal Engineering*, vol. 35, pp. 177–184, Mar. 2012
doi:10.1016/j.applthermaleng.2011.10.026

1.3.3 Conference papers

[C1] A. Montecucco, J. Siviter, A.R. Knox, "The Importance of Designing for the Overall Optimum Performance of the Thermoelectric System," in Proc. *Italian Conference on Thermoelectrics* (GiTe), CNR, Padova (IT), Feb. 2014

[C2] A. Montecucco, J. Siviter, A.R. Knox, "The Effect of Temperature Mismatch on Interconnected TEG Arrays," in Proc. *European Conference on Thermoelectrics* (ECT), ESTEC, Noordwijk (NL), Nov. 2013

[C3] A. Montecucco, J. Siviter, A.R. Knox, "Thermoelectric Power Conditioning with Embedded MPPT Control," in Proc. *European Conference on Thermoelectrics* (ECT), ESTEC, Noordwijk (NL), Nov. 2013

[C4] A. Montecucco, M. Compadre Torrecilla, A.R. Knox, "Thermoelectric Energy Harvester for Sensor Applications," in Proc. *European Conference on Thermoelectrics* (ECT), ESTEC, Noordwijk (NL), Nov. 2013

[C5] A. Montecucco, O. Magangam N. Phillip, J. Siviter, K.J. Burnham, A.R. Knox, K. Simpson, "Hardware Implementation of Maximum Power Point Tracking for Thermoelectric Generators," in Proc. *International Conference on Thermoelectrics* (ICT), Kobe (JP), Jul. 2013

[C6] S. Chiwanga, K. Simpson, R. Gilchrist, A. Montecucco, "Characterisation of Commercial ThermoElectric Module using Experimental and Numerical Techniques to Compile Performance Data," at *3rd Conference on Thermoelectrics*, Berlin (D), Nov. 2012

[C7] A. Montecucco, J. Siviter, A.R. Knox, "Simple, Fast and Accurate Maximum Power Point Tracking Converter for Thermoelectric Generators," in Proc. *IEEE Energy Conversion Congress and Exposition* (ECCE), Raleigh NC (USA), Sep. 2012
doi:10.1109/ECCE.2012.6342530

[C8] A. Montecucco, J. Buckle, J. Siviter, A.R. Knox, "A new test rig for accurate non-parametric measurement and characterisation of thermoelectric generators," in Proc. *International Conference on Thermoelectrics* (ICT), Aalborg (DK), Jul. 2012

Chapter 2

Literature Review

2.1 Background of thermoelectric devices

A thermoelectric device can be used in two different operating modes: heat pumping and power generating. The former mode of operation occurs when electrical current is applied to its terminals and the device pumps heat from one side to the other depending on the direction of current flow; heat pumping operation is exploited in either heating or cooling applications. The power generation mode of operation relates to the conversion of part of the heat flowing through the device into Direct Current (DC) electrical current when a temperature difference is maintained across it.
The basic thermodynamics and thermoelectric phenomena necessary for understanding the system-level behaviour of thermoelectric devices can be found in '*Direct Energy Conversion: fundamentals of electric power production*' by Decher [1], while '*Thermoelectrics Handbook: Macro to Nano*' edited by Rowe [2] represents the reference handbook in which the physics, chemistry and microelectronics of the thermoelectric science are covered in depth.

Thermoelectric devices have long been used in cooling applications for electronic devices, as reviewed by Simons and Chu [3], and more recently as refrigerators in the applications evaluated by Min and Rowe [4] and by Astrain [5], or to improve the efficiency of water heaters, as tried by Luo [6]. Very recently Siviter, Knox *et al.* [7, 8] suggested the large-scale application of thermoelectric heat pumps to improve the efficiency of power plants based on the Rankine cycle.
When used in electrical power generating mode thermoelectric devices are usually referred to as TEGs. This is the mode of operation investigated in this thesis.
In the past the use of TEGs has been restricted to specialized medical, military, remote and space applications, due to their relatively high cost and low efficiency (around 5%), but high reliability. Rowe [9] provides an overview of such earlier applications and assesses the potential of thermoelectric power generation as an alternative source of electrical power. NASA's Voyager 1 spacecraft, launched

in 1977 and powered by three Radioisotope Thermoelectric Generators (RTGs), has entered interstellar space in 2013 and has travelled farther than anyone, or anything, in history. The radioactive Plutonium isotopes used as power source are enough to provide electrical power to the spacecraft through at least 2020, which would mark 43 years of continual operation. The current power level is $315\,W$ (down from $470\,W$ at launch) [1].

In recent years increasing environmental issues and energy cost have motivated research into alternative commercial methods of generating electrical power. Thermoelectrics is one of several that has emerged as a viable source of electricity especially in applications of *waste* heat recovery. Rowe [10] reviews recent advances in the development of high performance thermoelectric materials, novel devices and applications, also investigating the economics of waste heat recovery. In this situation the thermal input power is essentially free, *i.e.* heat is rejected to ambient as the product of some other necessary process. The next sections of this chapter presents a review of updated literature related to applications of TEGs for electrical power generation from waste heat.

2.2 Applications of thermoelectric devices

The recovery of waste heat from the exhaust gas is one of the applications of TEGs with the highest potential and it is recently receiving great interest and funding. In TEG automotive applications the exhaust gas temperatures ranges from 300°C to 600°C for diesel and from 500°C to 1000°C for petrol, depending on where in the system the temperature is measured.

In 2001 Haidar and Ghojel [11] investigated the applicability of TEGs to the recovery of medium-temperature waste heat from a low-power stationary diesel engine, but did not present a complete system. Anatychuck *et al.* [12] presented a TEG system mounted on a stationary diesel plant comprising six cylinders and as many separate exhaust gas outlet channels; however, despite claiming a maximum power produced of $1350\,W$ not many experimental results were disclosed. BMW was the first car manufacturer to develop a TEG system and an on-vehicle test produced $600\,W$ of electrical power (the latest results were presented by Crane *et al.* in 2011 [13]). However, whilst the system shows relatively high power output and preferred thermal performance, the very low output voltage around one Volt negatively impacts the overall system efficiency due to difficulties in dealing with low voltage and high current. Risse and Zellbeck [14] published an interesting thermal simulation of a prototype TEG heat exchanger, predicted a maximum of $358\,W$ of electrical power generated at $160\,km/h$ and calculated a reduction in fuel consumption of $0.7\,\%$ per $100\,W$ generated by TEGs, but their analysis focused mainly on the thermodynamics of the heat exchanger and they did not use real TEGs.

The most commonly used material for commercial TEG devices is Bismuth Telluride (Bi_2Te_3), however they can work up to a maximum of 300°C and the future price and availability of *Tellurium* is uncertain. As a consequence of these two main factors, the exploitation of the energy rejected

[1] http://voyager.jpl.nasa.gov/

to ambient through the car's exhaust gas calls for advancements in the thermoelectric performance of materials suited for high-temperature. Promising performance could in the future be offered by materials like *Silicides* and *Skutterudites* as suggested by Brignone and Ziggiotti [15], and *Oxides* as reviewed by Fergus [16]. These materials have a variety of issues (*e.g.*, they are difficult to form electrical connections to, are chemically reactive at high temperatures in the presence of *Oxygen* and expensive to manufacture) which still have to be overcome before their large-scale commercial deployment is viable.

Bass and Killander [17] presented in 1996 a prototype thermoelectric generator for wood-fired stoves, producing up to $10\,W$ from a $75x75\,mm^2$ TEG. The heat transfer to the TEG system was poor because the TEG system was simply placed on the top of the stove, which was not very flat, and cooling was provided by a $2\,W$ fan blowing air over the heat sink. In 2004 Nuwayhid [18] proposed a similar system cooled by air convection and capable of producing up to $4.2\,W$ from a single $56x56\,mm^2$ TEG. In 2010 Rinalde *et al.* [19] developed a prototype TEG system for firewood stoves, producing $12.3\,W$ from a temperature difference of 200°C with two TEGs. The authors reported problems of non-uniform contact pressure and results inferior to those predicted by the manufacturer. In 2011 Champier [20] presented a TEG system for stoves that was tested in the lab with a gas heater, and it produced a maximum of $9.5\,W$ from a $56x56\,mm^2$ device. The authors highlighted the influence made on heat transfer by mechanical pressure and thermal contact resistances. Very recently O'Shaughnessy, Kinsella *et al.* [21, 22] proposed a TEG system for portable biomass cookstoves that uses commercially-available parts to produce up to $5.9\,W$ from a $40x40\,mm^2$ TEG and an average of $3\,Wh$ of energy stored in a $3.3\,V$ *lithiumiron phosphate* battery during a typical 1 hour long burn.
The main aim of all the aforementioned systems applying TEGs to stoves is to produce electrical power and they rely on inefficient natural or forced air convection for the cooling of the TEGs' cold side. Min and Rowe [23] provided an alternative solution to overcome the low efficiency drawback: combining generation of heat and power into a "symbiotic" system, in which the heat released to the cold side is used to pre-heat water, thus effectively creating a Combined Heat and Power (CHP) system. The authors show that the overall efficiency of the symbiotic system is equal to that of a conventional heating system, but with the advantage that both electricity and heat are produced. A similar symbiotic system was developed also by Vieira and Mota [24]. Chen *et al.* [25] examined the feasible deployment of TEGs in various CHP plants, analysing efficiency improvements, technical drawbacks and economic benefits.

In 1998 Furue *et al.* [26] calculated that up to $184\,kW$ of electrical power could be recovered from the heat of the exhaust gas of a $10\,MW$ internal combustion engine driving a conventional generator. In 2003 Kyono *et al.* [27] estimated that similar figures (around $150\,kW$) could be obtained by applying TEGs to the vapour condenser of a steam power plant. In 2009 Kaibe *et al.* [28] installed a TEG system in the $25\,kW$ carbon furnace at the Awazu plant of Komatsu Ltd. The system, comprising of 16 $50x50\,mm^2$ TEGs, generates up to $214\,W$ of electrical energy when the temperature

difference across each TEGs is around 200°C. Suter *et al.* [29] presented a theoretical study of the use of a $1\,kW$ TEGs system to harvest geothermal energy from a temperature difference around 200°C.
Using an idealised model believed to over-estimate results by around 10 %, Sark [30] predicted that an increase in overall efficiency of $8 - 23\,\%$ could be achieved by incorporating TEGs into Photovoltaic (PV) modules. Yang and Yin [31] compared a system composed of PV and water heating to another one that included TEGs between the PV and the water; the experimental results show that the use of TEGs actually slightly reduces the overall power produced because of the reduced efficiency of the PV cells due to reduced cooling efficiency. However, the authors suggest that the use of higher efficiency TEGs could potentially improve the overall efficiency by as much as 14 %. Xiao *et al.* [32] used Finite Element Analysis (FEA) to predict that a three-stage solar thermoelectric module could achieve around 10 % efficiency with a solar concentration ratio of approximately 100. Qiu and Haiden [33] combined thermoelectrics to Thermophotovoltaic (TPV), i.e conversion of infra-red radiation into electricity. The residual heat stream is taken from the TPV and supplied to the TEG, which produced $306\,W$ contributing to a total system efficiency of 5.2 %.

Another common application of TEGs is to harvest small quantities of energy to power sensors and low-power electronics. Ferrari *et al.* [34] demonstrated that a $30x30\,mm^2$ TEG subject to a temperature difference of 30°C could power a passive sensor with Radio-frequency (RF) transmitter requiring $31.8\,mW$. Yu *et al.* [35] presented a solar cell mechanically connected to a thermoelectric device with a heat sink on the opposite side of solar incidence to improve the cell's efficiency by 5.2 %. Ramadass and Chandrakasan [36], and Kim [37] propose electronic systems for TEGs to harvest heat at a low temperature difference of a few °C. Wang *et al.* [38] designed a power management system with 25 % end-to-end efficiency intended for Wireless Sensor Networks (WSNs). Elefsiniotis *et al.* [39] invented a thermoelectric energy harvesting device that uses phase change materials as thermal masses and exploits the temperature differences during aircraft's take-off and landing. Elefsiniotis *et al.* [40] also propose a power management board for energy-autonomous wireless sensor nodes.
Buckle *et al.* [41] proposed a novel application of TEGs to power Autonomous underwater vehicles (AUVs) based on buoyancy gliding, exploiting the depth-related variation in oceanic temperature by transporting a neutral buoyancy thermal mass in the system.

Patyk calculated that the use of TEGs can lead to specific energy cost savings in cars, CHP and stove applications [42], but that TEGs would contribute to lower improvements to a generic engine-driven generator, *e.g.*, cars and CHP production, if compared to steam expanders [43]. Nevertheless, TEGs offer a number of advantages over steam expanders, whose use is not widespread, *e.g.*, reliability and modularity. Ismail and Ahmed [44] reviewed recent patents filed about thermoelectric power generation.
All the aforementioned literature indicate that TEGs can now be successfully applied to recover waste heat from vehicles, stoves and geothermal energy and used in symbiotic systems (water heating and solar-based). They have clear potential to harvest power to supply sensors (mW) as much as low-

medium ($1 - 1000\,W$) power electrical loads. It must be highlighted that in applications of waste heat harvesting the low conversion efficiency is not a serious drawback *per se*, but it is important to maximise the power obtained from the TEGs in order to minimise the cost per Watt produced and make thermoelectric technology economically competitive. This is examined in more detail in Section 2.5. Moreover, recent advances in thermoelectric materials reported by Zebarjadi *et al.* [45], Biswas *et al.* [46] and Metha *et al.* [47], as well as 'mass-production' volumes will continue to lead to a further improvement of TEGs' efficiency and reduction of their cost, respectively.

Some innovative work related to stoves and automotive applications was undertaken for this Ph.D. and is presented in Chapter 7.

2.3 Testing of thermoelectric generators

When designing a thermoelectric generating system, the thermal/electrical engineer often relies on data provided by the manufacturer, therefore it is important to have precise knowledge of the performance of off-the-shelf TEGs. However, it is not easy to precisely determine the performance of thermoelectric devices; results often depend on how the tests are performed, and they are difficult to replicate on different measurement systems. Traditionally, heat power is more difficult to quantify than electrical power because of various losses and ways of transferring heat energy from one body to another.

Several measurement systems have been developed in the past. Rauscher *et al.* (Komatsu Ltd) [48] suggest that employing a reference material in form of a reference block to measure the heat flow is not an effective solution because the accuracy is limited by the uncertainty of the reference material's heat conductivity (up to 5 %) and that the relatively large blocks which are needed dissipate power by radiation or convection. They therefore used a thermally guarded resistive heater with thermal isolation and radiation screen. Takazawa *et al.* [49] developed an efficiency measurement system for temperature differences up to $550\,K$. They used load transducers to measure mechanical pressure, radiation shielding and a reference material block on the cold side to measure the heat flux without losses to ambient. Sandoz-Rosado and Stevens [50] created a test rig that can test thermoelectric devices at up to 500°C; heat losses from the heating block were accounted for with an accuracy of 5 %. Their repeatability study reported a deviation of measured parameters of less than 9 %. They also claim that the TEG's ceramic layer can decrease the maximum power output of a TEG by as much as 18 %. Han *et al.* [51] developed a test system whose heater can provide a maximum of only $40\,W$, so that test results are provided for temperature differences up to $40\,K$ on a $40x40\,mm^2$ device. Finally, Anatychuk and Havrylyuk [52] employ heat meters for direct measurement of the heat flux. It is interesting to note that in all these systems the heating block is positioned on the top.

However, despite the test systems described above, to date there is no standardised way of testing

thermoelectric devices [2]. As a result, the performance obtained by the user is often better (or worse) than that described in the datasheets; neither case is suitable for the user because the electrical load might not be able to cope with either higher or lower power produced by the TEG. Kinsella *et al.* [22] found a considerable difference between the TEG's internal resistance measured in their test rig and that provided by the manufacturer, for several values of temperature difference, when using a rig based on the design developed by Sandoz-Rosado [50].
The problem of discrepancies between measured and datasheet performance is particularly acute when dealing with large-scale applications, in which it is more difficult to predict how the whole system will behave, and for which the higher number of devices increases the magnitude of deviation from predicted error. The designer of such large thermoelectric systems needs to select the modules most suitable to the application; hence having accurate performance data for the products the designer wishes to use is desirable.

In an attempt to provide a solution to this problem, an innovative test system to assess device performance in the 'real world' was developed at the University of Glasgow. The maximum temperature that can be reached on the hot-side of the fixture is determined by the thermal conductivity of the device under test and it can be as high as 800°C with minimal thermal losses and thermal shock; the clamping force can be adjusted up to $5\,kN$, and the temperatures are sensed by thermocouples placed directly on the TEG's surfaces. A computer program controls all the instruments in order to minimise errors and to aid accurate measurement and test repeatability. The developed system minimises heat losses during measurements and takes residual losses into consideration for the calculation of the test device's thermal conductivity and thermal efficiency.
The electrical characterisation of a TEG, obtained maintaining a constant temperature difference across the device, highlights its essentially linear behaviour in steady-state, so that it can effectively be modelled by a DC voltage source in series with an internal resistance; this is well explained by Rowe and Min [53] and by Lineykin [54]. Therefore for the 'maximum power transfer theorem' [55] if the load impedance matches the internal resistance then maximum power is transferred, as also explained by Laird *et al.* [56]. The electrical operating point at which the TEG delivers the maximum possible power to the external load for a given temperature difference is labelled the Maximum Power Point (MPP) and is equal to half the open-circuit voltage or equivalently half of the short-circuit current.

As the use of TEGs extends into progressively lower cost applications [43] the overall system economics dictate that a compromise must be found between the number of MPPT converters and the number of TEG modules connected to each converter. In the design of thermoelectric systems it is a key requirement to ensure that minimal temperature mismatch is applied to TEG devices in the same system. Reported literature about large TEG systems do not enquire about the temperature

[2]The National Physical Laboratory (NPL) in the UK are leading an international effort to produce a standardised test method but this is not expected for some time yet, principally due to the need to resolve the measurement discrepancies between other countries' National Laboratories for standard test samples.

difference present across individual TEG devices however, asymmetry in the position of the TEGs in relation to the thermal input power leads to variable temperature distributions across the TEGs. Some prototype systems show total performance to be lower than expected and sometimes thermoelectric system designers are not even aware of the effects of thermal imbalance on power output. No thorough analytical study has been found that attempts to quantify the magnitude of this problem. Liang *et al.* [57] presented some experimental results for two TEGs electrically connected in parallel under different temperatures but the authors focused only on showing how their theoretical model compared to real results. They did not quantify the power lost due to mismatched conditions relative to the maximum power that the two TEGs would be producing if electrically loaded independently.

Chapter 4 presents a test rig, developed during this Ph.D., able to characterise four TEGs simultaneously, each one individually controlled. This allows testing of the effects of series and parallel connection of TEGs under mismatched conditions, *e.g.*, temperature difference, dimensions and clamping force.

2.4 Simulation of thermoelectric systems

It is of fundamental importance to carefully simulate thermoelectric systems in the design phase, especially for large-scale systems in which materials cost is of great relevance. However, thermoelectric systems are usually composed of thermal masses, TEGs and power and control electronics, and they are influenced by several thermal and electronic phenomena whose interaction is complex. Moreover, TEGs are often used in dynamic environments with varying temperatures. Actual CAD tools do not yet include the ability to model thermoelectric effects therefore they cannot be successfully used to accurately simulate the electro-thermal coupled effects which take place during changes in the system operating conditions, *e.g.*, temperature, power or load changes.

Books about thermoelectrics [1, 2] consider thermoelectric systems under steady-state and when in equilibrium. Few papers [58, 59, 54, 60, 61] consider the simulation of thermal transients found in practical thermoelectric systems, or effects due to variation in the electrical system parameters. In practice most thermoelectric applications are subject to electro-thermal transients. In cooling applications for electronic devices [3] heat is generated by Integrated Circuits (ICs) depending on use, therefore a controller is usually employed to vary the cooling capacity in order to maintain the desired temperature regardless of thermal transients. In thermoelectric power generation operating temperatures are often changeable, especially in applications to the automotive field or to stoves, where start-up and shut-down considerations represent a significat thermal transient condition. Thermoelectric transients are yet not fully assessed in literature and industry, as explained next.
Chen L. *et al.* [60] investigate the electrical response of thermoelectric devices to load transients and

show that a common type of thermoelectric module has a very fast electrical dynamic response, in the order of nano-seconds. This means that the direct energy conversion taking place in the practical thermoelectric systems can be considered instantaneous. Hence it does not influence the thermal dynamics, which are controlled only by the thermal elements, *i.e.* the thermal heat capacities of the system.
Chen M. *et al.* [61] and Lineykin and Ben-Yaakov [54] include the transient term in the model as a parallel electrical capacitor; in this way they deal with the additional time-related term, due to the change in stored heat energy, converting the thermal model into an equivalent electrical circuit. The module is divided into a grid of small elements, each one taking into account the heat conduction, Joule heating, Peltier heating/cooling and the thermal mass; hence an accurate equivalent circuit is composed of a series of RC cells. Additionally, other parts of the thermoelectric system such as the ceramic plates and the heat sinks need to be included as thermal impedances. The accuracy of their simulation is related to the number of cells used which is tuned depending on the capacity of the thermal masses of these external elements relative to the thermoelectric module. These kinds of models available for circuit simulators like SPICE and ANSYS do not offer a theoretical solution to the problem and are sometimes difficult to use, due principally to the division of the module in multiple elements whose parameters are difficult to obtain from the datasheets of the manufacturers. Most importantly, the models do not offer a theoretical solution to the problem because their governing equations are based on steady-state.
A more appropriate and reliable approach would be to study these devices through the physical equations which describe their behaviour; among these, the most important is the heat equation. Alata, Naji and Al-Nimr *et al.* [58, 59] have already explored this possibility but they used fixed temperatures as boundary conditions at the two sides of the thermoelectric device assuming that those temperatures are not varying, *i.e.* supposing thermal isolation.
Chapter 5 introduces a mathematical solution of the heat conduction equation for thermoelectric devices, with internal Joule heat generation and dynamic exchanges of heat through the hot and cold sides.

The thermal time constants of thermoelectric systems are orders of magnitude higher compared to the electrical response time. This means that during thermal transients there are "spikes" in power generation and efficiency before the thermal time constants bring the system to steady-state operation. During changes in the operating conditions the effects of thermal transients are so profound that both the heat sources and the electronics are affected. Therefore the impact of transients on the entire system, besides the steady-state behaviour, is relevant. Depending on the thermal power input to the system, the number of TEG modules and the power output from the cold side these thermal transients can last for relatively long periods of time, in the range of tens or hundreds of seconds. To carefully design the whole system in case of frequent changes of operation conditions and during start-up and shut-down, it becomes necessary to model these thermal transients and dynamic characteristics.
Very recently two interesting works by Cheng and Huang [62] and Meng *et al.* [63] proposed two

models for thermoelectric coolers. The former slightly overestimates the temperature difference in steady-state, while the second has a maximum error of 4.5 K over a temperature difference of around 37 K (with a current input of 1 A). Jang *et al.* [64] simulate a TEG system applied to a chimney used for venting a boiler or stove, but only the steady state is considered and simulation results differ by 9 % from experimental data.
Chapter 5 couples the solution of the heat equation with the other thermal and electrical phenomena occurring in real thermoelectric systems. The resulting model of the physical system, developed in *Simulink* and *Matlab*, is able to accurately simulate the thermal and electrical dynamics of a physical thermoelectric power generating system.

The simulation of automotive TEG systems attracts great interest from both industry (BWM [13], FIAT's project *HeatReCar*[3] [65], the Technology Strategy Board (TSB) project "VIPER", and the European Union "PowerDriver" described in Chapter 7) and academics; Wang *et al.* [66] propose a mathematical model to simulate a TEG that uses the vehicles' exhaust gas as the heat source, but simulate only in steady state.
Chapter 7 presents an adaptation of the simulation model to a generic TEG system for vehicles. This model copes with the rapidly varying thermal operating conditions commonly found in standard driving cycles.

2.5 Maximising power generation from TEGs

TEGs are often employed in dynamic environments with time-varying temperature differences, *e.g.* cars' exhaust gas systems, therefore it is of great importance to quickly and precisely set the best electrical operating point in order to always maximise the harvested power. This function can be performed by DC-DC power electronic converters whose input voltage (corresponding to the TEG's voltage at-load) is set by an appropriate MPPT algorithm that matches the virtual load seen by the TEG to its actual internal resistance by controlling the duty cycle of the converter. These so-called MPPT converters are typically employed to maximise the power extracted at any thermal operating point. Their ability to maintain the TEG at the MPP is usually referred to as MPPT efficiency.
In common large TEG systems, several TEG devices are electrically interconnected in arrays, each one controlled by a dedicated MPPT electronic converter. This leads to the formation of what is called a DMPPT subsystem in which each TEG array's electrical operating point is controlled independently in a similar way as for PV systems, as well described by Pilawa-Podgurski and Perreault [67]. Wu *et al.* [68, 69] proposed an interesting solution, called Hybrid Centralised-Distributed (HCD) in which individual TEGs (or TEG arrays) are connected in series to a centralised converter; each TEG is also connected to its own distributed converter. Since the current in the series is the same, the distributed converters are used to impose different currents in each TEG, but most of the power

[3] http://www.heatrecar.com/

is processed by the centralised converter.
Poshtkouhi *et al.* [70] use a 3D CAD tool to model a PV installation site to evaluate the cost/performance trade-off for panel-level DMPPT and found that the energy yield benefit usually outweighs the power electronics' cost. Although there is no work in literature focusing on the economics of DMPPT for TEGs, it is reasonable to assume similar results as for PV systems; especially when non-uniform temperature distributions are expected across the TEG devices the use of DMPPT technology could reduce the power lost to temperature mismatch. This is however a design choice which is influenced not only by the power harvesting benefits but also by the cost, size and weight penalties linked to the higher number of converters used.
Sometimes an additional inverter with Central Maximum Power Point Tracking (CMPPT) can be used to interface to the grid, as explained by Vitelli [71]. Molina *et al.* [72] proposed a grid-connected TEG system.

The choice of converter typology depends on the output and input voltages; as an example, for connection to DC micro-grids a high step-up gain converter is required, as in the applications described by Laird and Lu [73] and by Sun *et al.* [74], while for connection to a $12\,V$ car battery the Boost or Buck-Boost types are the most common typologies.
Both Vieira and Mota [24] and Kinsella *et al.* [22] use a SEPIC converter. Yu and Chau [75] use a Ćuk converter.
For low input voltages, Damaschke [76] in 1997 designed a self-starting Boost converter able to work down to $300\,mV$. Carlson *et al.* [77] proposed a Boost converter that operates with input voltages ranging from $20\,mV$ to $250\,mV$ while supplying a regulated $1\,V$ output. Ramadass and Chandrakasan [36] designed a converter for input voltages as low as $35\,mV$ tested with output power up to $300\,\mu W$.
The work presented in this thesis uses a synchronous Buck-Boost to operate over a wide input voltage range and consequently harvest power from the TEGs over a wide range of temperature differences. Orellana *et al.* [78] and Hester *et al.* [79] used the synchronous Buck-Boost for PV MPPT.

The most commonly known MPPT algorithms are described in detail in Chapter 6, however, next are reported the most important works found in the literature about the use of such MPPT algorithms to maximise power generation from TEGs.
In literature, the most used MPPT algorithm for TEGs is the Perturb & Observe (P&O). Nagayoshi and Kajikawa [80, 81] presented a prototype Buck-Boost with P&O but do not provide the MPPT efficiency of their system. Chen *et al.* [60] report improvements up to 100 % when interfacing the load with a Boost converter instead of directly connecting the resistive load, but they do not investigate the MPPT efficiency of their converter. Kim and Lai [82] design the voltage and current loops for a boost-cascaded-with-buck converter in the frequency domain utilising the P&O method. They tested the system using a Power Supply Unit (PSU) in series with a power resistor but did not estimate the MPPT efficiency. Vieira and Mota [24] claim that their P&O algorithm increases the harvest

of energy by 34 % compared to direct connection of the TEG system to the battery. Champier *et al.* [83] use a Boost converter with P&O and claim a MPPT efficiency around 99 %, obtained by calculations.
The Incremental Conductance (INC) algorithm is also used. The design of the INC MPPT control proposed by Kim *et al.* [84] is based on the frequency response of the Boost converter and shows a 95 % tracking efficiency.
Another MPPT technique that is starting to be applied to TEG systems is the Extremum Seeking (ESC). Phillip, Maganga *et al.* [85, 86] simulated and compared the experimental performance of P&O and ESC; the latter showed good tracking potential but its implementation proved complicated.

The aforementioned MPPT algorithms have originally been developed for PV systems, in which the relationship between voltage and current is logarithmic. On the contrary in a TEG even if the open-circuit voltage varies with the temperature difference and the internal resistance varies with the average device temperature, for each thermal operating point the electrical characteristic is linear and the TEG can be modelled as a voltage source in series with a resistance; therefore at any given temperature difference the MPP is found at half of the open-circuit voltage or half of the short-circuit current. MPPT algorithms that use this relationship either measure the open-circuit voltage or the short-circuit current and they are termed "fractional open-circuit"; they provide a number of advantages over the other MPPT algorithms. The disadvantage of the fractional open-circuit method is that no energy flows from the TEG to the converter during the sampling time because the converter must be disconnected from the TEG to allow for the measurement of open-circuit voltage or short-circuit current and hence during this time the TEG is not delivering energy to the external circuit.

Cho and Kim *et al.* [87, 88] presented an interesting MPPT converter composed of a boost converter using the fractional open-circuit technique followed by a Buck for output voltage regulation. The simulated MPPT power transfer efficiency is higher than 98 %. Schwartz [89] uses a 69 % SEPIC converter with fractional open-circuit. Laird and Lu [73] found that the fractional short-circuit method tracked the MPP better than the P&O and produced a steadier input voltage. Kim [37] does not estimate the tracking efficiency.

Chapter 6 introduces an innovative open-circuit voltage measurement technique that can be undertaken during the normal switching operation of the synchronous Buck-Boost converter used, with minimal reduction in collection efficiency. Unlike the reviewed literature, the tracking performance of this MPPT converter is evaluated with great accuracy using a real TEG system and comparing the experimental results to the experimentally-obtained electrical characterisation of the TEGs used.

2.6 Conclusions

The literature review presented in this chapter confirms the growing interest from both academia and industry in the research and use of TEGs especially for the recovery of waste heat from other necessary processes. Nevertheless, more research and development must be undertaken in order to develop more efficient devices, more accurate simulation tools, and functional but cost-effective MPPT electronics.

The contribution of this thesis to the pool of existing knowledge is threefold:

1. Testing of thermoelectric devices: an original testing apparatus for automated testing of the performance of thermoelectric generators was built. The test rig exploits some features already presented in literature, but allows the use of several TEGs concurrently, each with independent settings for the temperature difference and mechanical force applied to each device. The results produced are accurate and repeatable.

2. Simulation of thermoelectric systems: the physical phenomena of thermoelectricity are analytically characterised in both the steady-state and transient domain, enabling the development of a novel computer-aided simulation tool able to predict the dynamic evolution of thermoelectric systems during varying thermal and electrical conditions.

3. Development of MPPT electronics: an original technique is proposed to improve the performance of the fractional open-circuit MPPT technique and efficient converters are developed for TEG applications to vehicles or stoves. These MPPT converters are tested with real TEGs to determine actual performance with precision.

Chapter 3

Theory of Thermoelectric Devices

Thermoelectric refers to direct conversion of thermal energy into electricity and *vice versa* [1]. This chapter presents the thermoelectric effects and the structure of thermoelectric devices. The thermoelectric phenomena, known for over a hundred years, can be employed for heat pumping, temperature sensing and power generation. The latter is the operational mode of interest in this thesis, therefore the main purpose of this chapter is to outline the principles of thermoelectric generators. Understanding the thermoelectric effects is of fundamental importance for the engineering design of any thermoelectric system.

This chapter aims at describing the most important effects related to thermoelectrics and the thermoeletric device from a systems point of view. Extensive further reading about the physics, chemistry and microelectronics involved is given in *Thermoelectrics Handbook: Macro to Nano* [2].

This chapter first covers the definition of the thermoelectric effects; then, the key parameters and design challenges relative to thermoelectric devices are discussed; finally, the steady-state behaviour of thermoelectric devices is analysed.

3.1 Physical phenomena of thermoelectricity

Four physical phenomena are relevant to the study of thermoelectric devices: the *Seebeck* effect, the *Peltier* effect, the *Thomson* effect and the *Joule* heating effect. The *Kelvin* relationships describe an important link between the first three of these effects.

3.1.1 The Seebeck effect

In semiconductors, electrons and holes are considered to be charge carriers when they do not participate in covalent bonds. They can easily be set in motion and the resulting electrical current is measured in terms of the number of electrons moving past a given point in a given time; in the case of the S.I. system, in one second [90]. The measure unity is termed *ampere* [A] and it equals the movement of $6.25 \cdot 10^{18}$ electrons per second. Charge carriers can be set in motion by the flow of heat. Whenever an electrical conductor is placed between two different temperatures, the conductor transfers thermal energy from the warmer side to the colder one, and charge carriers are moved in the same direction. To take advantage of this flux of charge carriers, it is necessary to close the circuit. If a second identical conductor is used, there will be an equal movement of charge carriers in both conductors, which results in no net current flow. By using two dissimilar materials the current in one conductor will not equal that generated in the other, thus resulting in a net continuous current flow; such current is equivalent to the difference of the two thermally-generated currents in the two conductors. The existence of this net current flow indicates that a voltage is created due to the movement of heat, and a direct measurement of this voltage can be taken across the open circuit terminals of the pair. This voltage is referred to as the Seebeck voltage, after the discovery of thermoelectromotive forces by T.J. Seebeck in 1821; however, this thermoelectric phenomenon was initially discovered in 1794 by the Italian physicist Alessandro Volta [91].
According to this effect, a voltage is produced in a circuit of two dissimilar materials when the two junctions are maintained at different temperatures. The open-circuit thermoelectric potential V_{OC} is obtained from the following equation:

$$V_{OC} = \alpha \Delta T \tag{3.1}$$

where $\Delta T\,[K]$ is the temperature difference across the two junctions, and $\alpha\,[V/K]$ is the Seebeck coefficient, which gives the rate of change of $V_{OC}\,[V]$ with ΔT:

$$\alpha = \frac{\Delta V_{OC}}{\Delta T} \tag{3.2}$$

α is a 'combined' coefficient associated with the properties of the materials used and is defined for $\Delta T \to 0$. The Seebeck coefficient of the junction between two materials is the difference between the two absolute coefficients and experimental data show that metals' Seebeck coefficients are very small. On the contrary, however, values in the hundreds of $\mu V/K$, negative or positive, are typical for good thermoelectric semiconducting materials.

3.1.2 The Peltier effect

As with the Seebeck effect, another interesting physical effect can be observed due to electrical current flow at the junction of dissimilar materials when the electrons flow across a discontinuity in the energy levels of the conduction bands in the coupled materials.
The Peltier effect was discovered in 1844 by the French physicist J.C.A. Peltier. The Peltier effect states that if a direct current is passed through a circuit of dissimilar materials, one junction will be heated and the other will be cooled. This is the reversed Seebeck effect and it is also polarised in that, if the direction of current flow is reversed, heat absorption and dissipation locations are also reversed. Peltier heating (or cooling) can be interpreted as being due to the change in the average kinetic energy of a charge carrier when it crosses a junction.
The Peltier coefficient, measured for $\Delta T \to 0$, is labelled $\pi\,[V]$ and defined as

$$\pi = \frac{P_P}{I} \tag{3.3}$$

where P_P is the heat-transfer rate from the junction and I is the direct current flowing in the circuit. The Peltier coefficient has the dimensions of voltage and gives the magnitude of the heating or cooling that occurs at a junction of two dissimilar materials.

3.1.3 The Thomson effect

The Thomson effect was discovered in 1854 by the British physicist William Thomson (Lord Kelvin). This effect states that there is reversible absorption or liberation of heat (in excess of the Joule dissipation I^2R) in a homogeneous material simultaneously exposed to a thermal gradient under the passage of an electric current. The heat absorbed by the conductor when the current flows toward the higher temperature is

$$P_T = \tau I \Delta T \tag{3.4}$$

where $\tau\,[V/K]$ is the Thomson coefficient. Both the Seebeck and Peltier coefficients are defined for junctions between two conductors, while the Thomson coefficient is a property of a single conductor. Thus the Peltier and Seebeck coefficients can only be determined for pairs of materials whereas the Thomson coefficient is directly measurable for individual materials. The Thomson effect is frequently excluded from the analysis of thermoelectric devices because usually much smaller than the Joule heating [92, 93]. However, its contribution can be significant for large temperature differences [94, 95].

3.1.4 The Kelvin relationships

The Peltier coefficient is related to the Seebeck coefficient by the following relationship:

$$\pi = \alpha T_j \tag{3.5}$$

where T_j is the temperature at the junction. This result is widely substantiated through experimental evidence and hence the assumption of reversibility appears valid. Eq. 3.5 constitutes a simple way to determine π and allows Eq. 3.3 to be re-written as

$$P_P = \alpha I T_j \tag{3.6}$$

The Thomson coefficient is related to the Seebeck coefficient by the following relationship:

$$\tau = T_{AVG} \frac{d\alpha}{dT} \tag{3.7}$$

where T_{AVG} is the average temperature of the material.

3.2 The thermoelectric power generation device

TEGs are devices that convert thermal energy directly into electrical energy. The DC voltage produced by the device is directly related to the temperature difference between the surfaces of the device.

3.2.1 Mechanical structure

Doped semiconductors have been shown to be materials with excellent thermoelectric properties. Multiple pellets of p- and n-doped semiconductors are connected electrically in series and thermally in parallel, as shown in Fig. 3.1. The voltage from each pellet is added such that a device comprising many such pellets produces and/or sustains higher voltages. Each p- and n-pair is referred to as thermocouple. The magnitude of the voltage also depends on the materials in use, and different materials may be optimised for different temperature regions [15, 96]. The most commonly used material is Bismuth Telluride (Bi_2Te_3), however other materials like *Silicides, Skutterudites, Oxysulphides, Ti-S, Ni-Cr-S* and *Cobalt* oxides are being developed for automotive and industrial applications over a range of temperatures [97, 16].
A typical Bismuth Telluride (Bi_2Te_3) thermocouple has a Seebeck coefficient of around $350\,\mu V/K$.

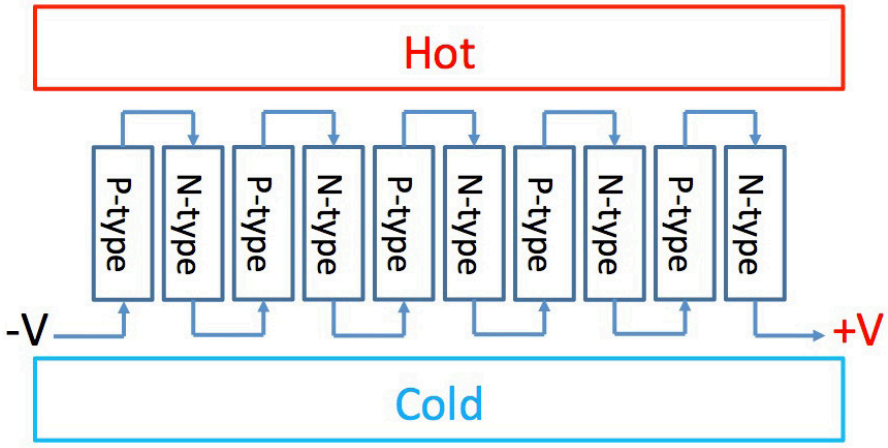

Figure 3.1: Schematic diagram of thermoelectric couples in a thermoelectric device used as thermoelectric generator (TEG).

In a large thermoelectric device there are typically 127, 254 or 449 pairs of couples and the device can achieve open circuit voltages of over $30\,V$ at high ΔT.

Fig. 3.2 shows a 3D cut-away isometric drawing of a TEG module in which thermal energy is applied on the bottom ('hot') surface. The pellets are electrically series-connected by soldering to copper tabs and, due to electron current flowing in a direction opposite to that of the holes, the potentials from the pellets are series-adding. An Aluminium-based ceramic (often AlN) layer serves as electrical isolation between couples and as a mechanical substrate for the device assembly. The resulting module is quite robust and reliable, and operates without any vibration or noise since there are no moving parts. In operation, the TEG will be subject to a range of thermal and mechanical stresses and these stresses limit the physical size of commercial TEG modules to typically less than $100x100\,mm^2$. The stresses induced in the module are in part a consequence of the variation in the physical size of the top and bottom layers enclosing the pellets of the thermoelectric material, and the variation in size is a consequence of the mismatch in the thermal expansion or contraction of the materials used to construct the TEG. Current flow in the semiconductor material directly changes its thermal conductivity which in turn affects the slope of the thermal gradient and adds to the mechanical stresses experienced during operation of the device.

Externally applied thermal energy is conducted through the module while additional heat is generated (Joule heating) inside the module and pumped (Peltier effect) through the hot and cold sides as described by the coloured arrows.

Thermoelectric devices can be operated in Peltier mode for heat pumping, and in Seebeck mode for power generation. In both operating modes all the thermoelectric phenomena described in Section 3.1 occur concurrently; however, the Peltier and Seebeck effects are the dominant effects for heat pumping and power generation, respectively.

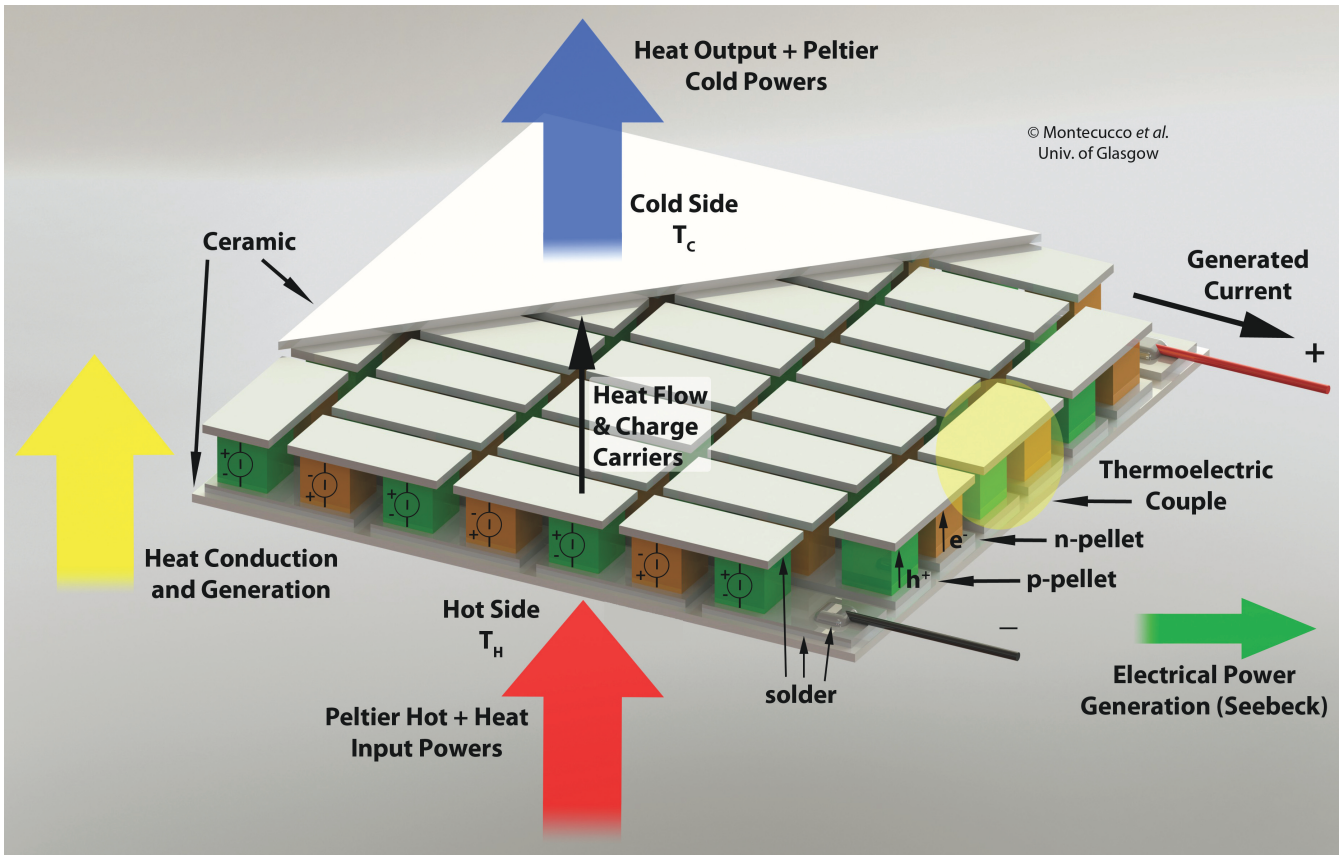

Figure 3.2: 3D model of a thermoelectric generator showing the main physical effects.

3.2.2 Thermal and electrical conductivities

The thermal (κ) and electrical (σ) conductivities are important parameters because they control the flow of heat and current. The former should be low to retain heat across the junctions and to maintain a large temperature gradient. The latter should be high because it influences the self-heating (Joule effect) of the material, *i.e.* low internal resistance to minimise self-heating. The thermal conduction paths for the p- and n-pellets are in parallel, so that the total open-circuit thermal conductance for N thermocouples is

$$\kappa_{OC} = N\left(\kappa_p \frac{A}{L} + \kappa_n \frac{A}{L}\right) \tag{3.8}$$

where $L\,[m]$ is the lenght of the semiconductor pellets, $A\,[m^2]$ is the cross-sectional area of the pellets, and $\kappa\,[W/mK]$ is the thermal conductivity of the semiconductor materials.
In power generation the Peltier effect is parasitic and unwanted because it effectively pumps heat from the hot to the cold side of the device. As a consequence, the effective thermal resistance of the TEG depends to a certain extent on the magnitude of the current flowing in the external circuit. When the TEG is open-circuited the thermal conductance is defined by Eq. 3.8, but as soon as current is drawn by an external circuit the effective thermal conductance of the TEG is modified.

Product Code	Pellet Area (mm^2)	Pellet Number	Electrical V_{OC} (V)	Electrical I_{SC} (A)	Electrical R_{int} (Ω)
GM250-449-10-12	1	898	17	1	16.5
TEHP1-12656-0.2	6.25	252	2.7	7.5	0.35

Table 3.1: Comparison of some geometrical and electrical parameters between two TEG devices offered by European Thermodynamics Ltd. Both TEGs have a surface area of $3136\,mm^2$. The electrical parameters are measured at $\Delta T = 100°C$.

Low electrical current will lead to a reduced thermal conductance increase (high thermal resistance; low heat pumping), and high electrical current will lead to a greatly increased thermal conductance (low thermal resistance; high heat pumping). If the TEG is electrically short-circuited, the TEG will have the highest possible thermal conductance. This condition is normally avoided because it leads to a very inefficient thermal circuit with a large amount of heat energy being transferred from the 'hot' to the 'cold' side with no benefit in electrical power generation. Succinctly put, in power generation mode the Peltier effect reduces the temperature difference across the device and consequently the voltage and power produced by it.
The variation of the effective thermal resistance can be exploited to create a variable thermal resistor based on the Peltier effect, as suggested by Min [98].

The electrical resistance is more relevant than its inverse (conductance), because the N thermocouples are in series. Thus the internal resistance of the device is

$$R_{int} = N\left(\rho_p \frac{L_p}{A_p} + \rho_n \frac{L_n}{A_n}\right) \tag{3.9}$$

where $\rho\,[\Omega m]$ is the bulk electrical resistivity of the materials. It is normally assumed that the metallic connections between the semiconductor pellets have negligible resistance, *cf.* the bulk material. However, this assumption clearly does not hold true if the electrical resistance built up in the solder connections and connectors to the load ($R_{contact}$) is comparable with the internal resistance of the TEG device. This typically occurs if the pellets have relatively wide cross-sectional area or in small modules, or if the module uses long electrical connection leads. In such cases $R_{contact}$ should be taken into account and the total resistance seen by the load updated to $R_{teg} = R_{int} + R_{contact}$.
The number of thermocouples is chosen depending on the ratings of current and voltage desired. Considering a TEG module of certain fixed dimensions, in order to produce higher voltage it is necessary to have a higher number of pellets (assuming constant temperature). This implies that the cross-sectional area of the pellets shrinks, hence R_{int} increases, thus reducing the current rating. Conversely, a smaller number of wider thermocouples will produce smaller voltage and higher current [99]. By way of example, Table 3.1 shows how the size and number of pellets influences the current-voltage ratings in two TEGs offered by European Thermodynamics Ltd.

The thickness of the pellets usually influences the balance between power production and thermal efficiency. Taller pellets generally have higher thermal and electrical resistances, decreasing the thermal flux through the device thus increasing thermal efficiency and decreasing the amount of power production due to higher electrical resistance. This topology also tends to favour a greater ΔT across the thermoelectric material with relatively small temperature gradients across the alumina layers forming the outer surfaces of the TEG. An upper limit on the length of the pellets is determined by the mechanical stability of the device due to column buckling when compressed between the hot and cold heat exchangers.

3.2.3 Precautions on the use of TEGs

The principal advantages of TEGs are simplicity and reliability due to lack of moving parts. However, there are still some precautions on their use that should be observed. Factors that could negatively impact on the reliability of TEGs are manufacturing issues and thermal expansion.
It is not advisable to connect thermoelectric modules either in series or in parallel if their output characteristics are different; otherwise some modules might absorb electric power, leading to Peltier effect cooling and unexpected system thermal behaviour.
It is highly recommended to prevent the hot-side temperature of the thermoelectric device from exceeding the melting temperature of the solder employed to secure the semiconductor pellets to the copper tabs hot-pressed onto the ceramic outer plates. The minimum temperature for the TEG can be less than $0°C$, provided any water that may be present in the TEG's structure (*e.g.*, between adjacent pellets) does not freeze, causing (usually permanent) physical damage to the device. In uncommon cases very rapid changes in temperature can cause damage to the module due to thermally induced stresses caused by differential rates of thermal expansion and contraction.
It is extremely important to ensure that even distribution of heat is achieved on both sides of the device, using heat spreaders to prevent hot spots. When designing the thermoelectric system it is necessary to pay attention to removing heat from the cold side as well as providing it to the hot side, in order to maintain the desired temperature difference. In practical situations it is frequently the cold side of the TEG that has the greatest impact on system performance.

3.3 TEGs in steady-state

This section describes the steady-state behaviour of a generic TEG and its power balance when constant temperatures are maintained at its faces.

3.3.1 Equivalent electrical model of a TEG

It was explained in Section 3.2.1 that the Seebeck voltages produced by each pellet are in series, hence from an electrical circuit point of view they can be simplified to a single DC voltage source. Section 3.2.2 described the internal resistance of a TEG module, which is distributed within each pellet and the associated solder connections. As a consequence a TEG can effectively be electrically modelled as a voltage source in series with an internal resistance [53, 54], as shown in Fig. 3.3. The values of both the voltage produced and the internal resistance vary with temperature. However, for a constant temperature difference across the TEG device both the open-circuit voltage and the internal resistance are constant therefore the electrical characteristic under steady-state conditions is linear.

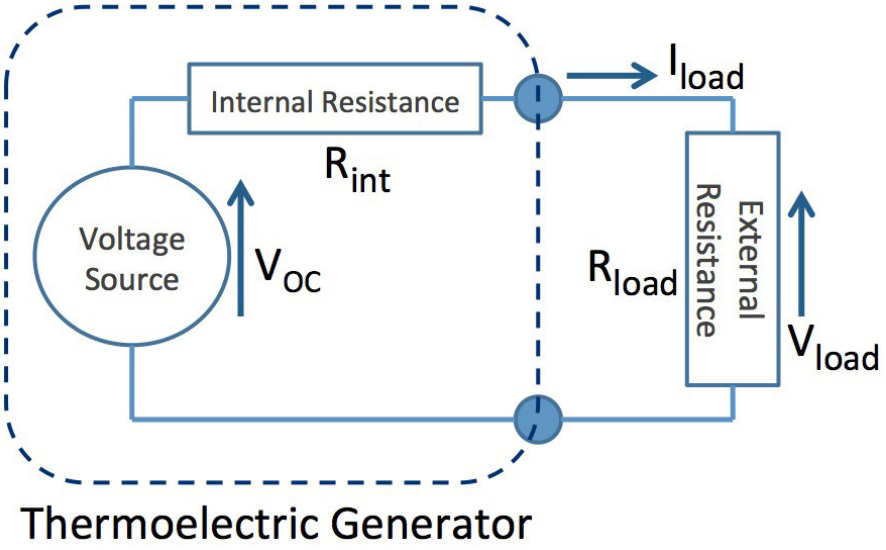

Figure 3.3: Electrical model of a thermoelectric generator.

The *maximum power transfer* concept is very important for TEGs because they do not behave in the same way as regulated power supplies. At any given ΔT, as the load resistance decreases, so does the output voltage, while when the load resistance approximates to infinity, the output voltage tends to the open-circuit voltage. The load voltage V_{load} can be written as

$$V_{load} = V_{OC} - R_{int} I_{load} \tag{3.10}$$

Multiplying and differentiating both sides of Eq. 3.10 by I_{load} results in

$$\frac{dP_{load}}{dI_{load}} = V_{OC} - 2R_{int} I_{load} \tag{3.11}$$

In order to find the load current for maximum power generation, I_{MP}, equating Eq. 3.11 to zero

solves for

$$I_{MP} = \frac{V_{OC}}{2R_{int}} \tag{3.12}$$

which occurs when $R_{load} = R_{int}$, as stated by the maximum power transfer theorem. When this condition is satisfied the load voltage is equal to half of the open-circuit voltage:

$$V_{MP} = \frac{V_{OC}}{2} \tag{3.13}$$

and the maximum available power that can be extracted from the TEG is

$$P_{max} = \frac{V_{OC}^2}{4R_{int}} \tag{3.14}$$

It is important to highlight that the aim of the previous analysis was not finding the best load for a fixed thermal input, as it will be done in Section 4.4. Here we are studying the linearity of the electrical characteristic for a constant temperature difference. Obtaining the electrical characteristic at constant temperature difference requires a tight control over the thermal input power to the hot side of the TEG, which will need to be varied considerably going from open-circuit to short-circuit, for which the lowest and highest thermal input powers are required, respectively.

For the analysis of small dimension devices the thermal and electrical contact effects should be taken into account, as described by Gao Min in [100]; however, such analysis goes beyond the scope of this thesis and will not be further discussed here.

3.3.2 Electrical characterisation

Electrical characterisation of a device usually refers to measurement of its voltage-vs-current and power-vs-current curves, to describe its steady-state performance and electrical behaviour under different loading conditions. Chapter 4 describes a procedure that can be used to achieve the electrical characterisation of TEGs and has been used extensively at the University of Glasgow and at European Thermodynamics Ltd.

Fig. 3.4 shows the performance curve for a thermoelectric module (product code: *GM250-449-10-12* by *European Thermodynamics Ltd.*) formed of 449 couples with a physical size of $55x55\,mm^2$ when operated at a temperature difference ΔT of $220°C$. The blue straight line represents the voltage versus current (V-I) characteristic, while the red curved line is the power curve (P-I) for the device. The open-circuit voltage V_{OC} is the voltage when no current is drawn by the load, while the short-circuit current I_{SC} is the current when the TEG's terminals are shorted together. The maximum power point lies at the point when $I_{load} = I_{SC}/2$ or $V_{load} = V_{OC}/2$ and is established when the equivalent electrical load resistance in the external circuit connected to the TEG exactly equals the

internal electrical resistance R_{int} of the TEG, as stated by the theorem of maximum power transfer [55]. R_{int} is the inverse slope of the V-I line and its absolute value is dependent on the temperature at which the TEG is operating and hence does not have an absolute value. When the TEG is operated to the left of the maximum power point as shown in Fig. 3.4, reduced current flows through the TEG and the effective thermal conductivity of the TEG (which depends also on the current flow, due to the parasitic Peltier effect) decreases. Under this condition the thermal energy conducted via the TEG is less than that at the maximum power point and hence a lower thermal load is imposed on the overall system. This is advantageous in most circumstances since it leads to increased thermal efficiency of the system. When the TEG is operated to the right of the maximum power point then the thermal conductivity increases and the thermal energy conducted via the TEG is greater than that which flows at the maximum power point. Operation in the region to the right on Fig. 3.4 leads to a reduced thermal efficiency of the system. For the module data shown in Fig. 3.4, the maximum power is approximately $13.2\,W$ with a corresponding output voltage of $16.5\,V$ (being half of the open-circuit voltage of $33\,V$).

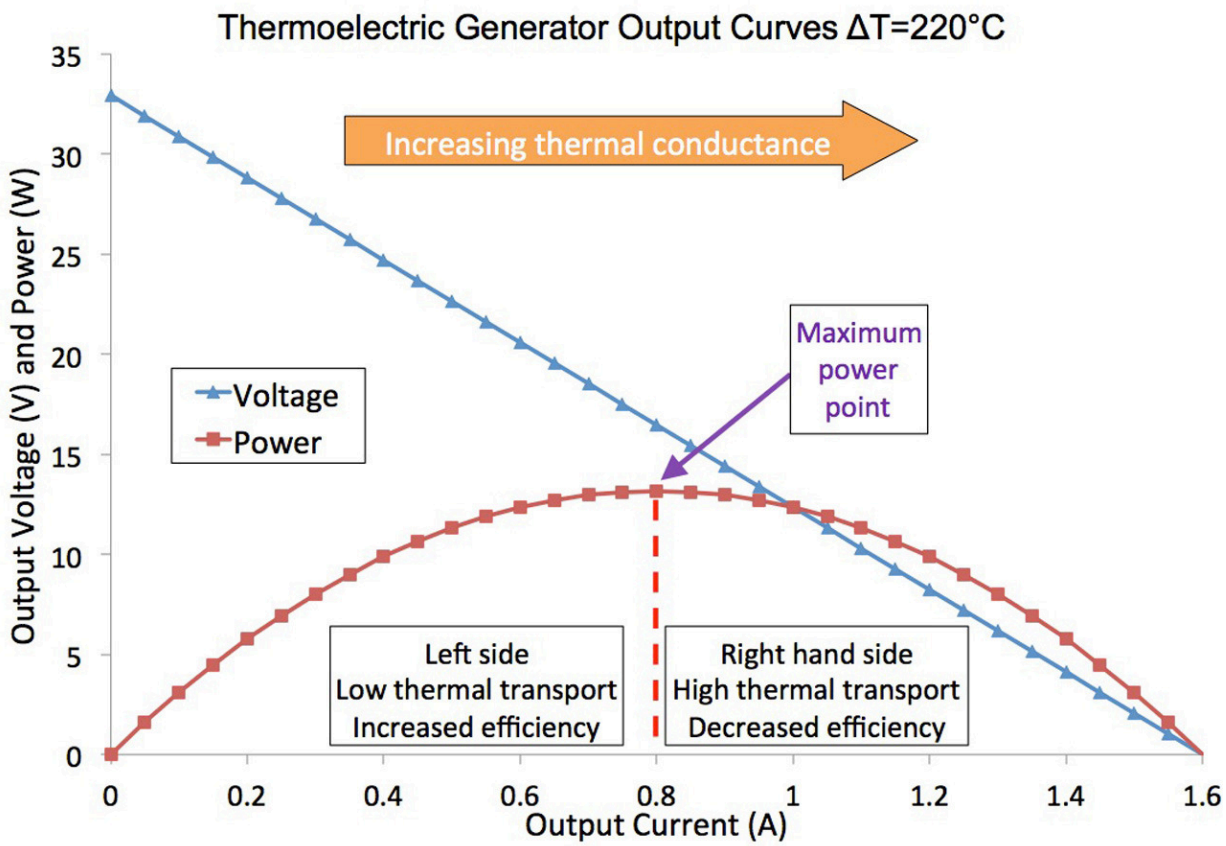

Figure 3.4: Electrical characterisation (V-I and P-I curves) of the thermoelectric device *GM250-449-10-12* by *European Thermodynamics Ltd.*

3.3.3 Balance of powers

It is instructive, in the analysis and design of thermoelectric systems, to understand the flow of thermal and electrical energies. It is relevant to the work of this thesis to study thermoelectric devices from a system point-of-view therefore the TEG is considered in its entirety and is analysed for its behaviour in the system.
The thermal power input to the hot junction is given by

$$Q_H = \frac{kA\Delta T}{L} + \alpha T_H I - \frac{1}{2} R_{int} I^2 \tag{3.15}$$

where k is the overall conduction coefficient, A is the area and L the thickness of the TEG, ΔT is the temperature gradient, α is the Seebeck coefficient, T_H is the temperature at the hot side, I is the current produced and R_{int} is the overall internal resistance of the device.
As explained in a paper by Ben-Yaakov and Lineykin [54], Eq. 3.15 is derived from the steady-state solution of the one-dimensional heat conduction equation for solids with internal energy generation, which is written as:

$$\frac{\partial^2 T}{\partial x^2} + \frac{\dot{g}}{k} = 0 \tag{3.16}$$

where $\dot{g}$ is the rate of heat internally generated per unit volume $[W/m^3]$.
Assuming constant temperatures at the hot and cold side as boundary conditions $[T(t,0) = T_H; T(t,L) = T_C]$, Eq. (3.16) can be solved as:

$$T(x) = T_H - \frac{\dot{g}}{2k} x^2 + \frac{T_C - T_H + \frac{\dot{g}}{2k} L^2}{L} x \tag{3.17}$$

Combining this result to the equation of heat transfer $q = -kA\frac{\partial T}{\partial x}$, the expression for the heat flow through the hot side becomes

$$Q_H = \frac{kA\Delta T}{L} - \frac{1}{2} R_{int} I^2 \tag{3.18}$$

Taking into account the Peltier heating or cooling effect at the junctions this equation becomes Eq. 3.15. Note that the Peltier effect causes the absorption of additional heat.
The solution for the cold side is similar; the two results show that the Joule heating in the bulk material is equally divided between the hot and cold sides. All these results are shown by the coloured arrows in Fig. 3.2.

The thermodynamic efficiency is defined as the ratio of the electrical power output P_{out} to the thermal power input Q_H to the hot junction:

$$\eta = \frac{\textit{electrical power to the load}}{\textit{heat power absorbed at the hot junction}} = \frac{P_{out}}{Q_H} \tag{3.19}$$

3.3.4 Figure of merit and maximum thermal efficiency

The figure of merit of thermoelectric devices is an important parameter of the materials employed [30, 66]. It is defined as

$$Z = \frac{\alpha^2}{\rho\kappa}[K^{-1}] \tag{3.20}$$

Even a small increase in the figure of merit can lead to significant improvements in the performance of the TEG. The figure of merit varies with temperature therefore the goal is to find materials with large figures of merit in the range of temperature of interest. This problem involves the simultaneous control of three parameters: the Seebeck coefficient α, the electrical resistivity ρ and the thermal conductivity κ. Each of these three quantities is a function of the density of charge carriers. As the charge carriers concentration increases, the Seebeck coefficient and the electrical resistivity decrease, while the thermal conductivity increases. However, the role of the thermal conductivity is minor because the increasing contribution of electronic thermal transport is relatively small if compared to that associated with phonon (lattice wave) motion, which is independent of electron density [101]. Highly doped semiconductors with carriers concentrations around $10^{19}\,cm^{-3}$ have good Seebeck coefficients, low electrical resistivities and fairly low thermal conductivities.
It is more convenient to consider the *dimensionless figure of merit* [66]

$$ZT = \frac{L}{R_{int}A}\frac{\alpha^2}{k}\frac{T_H + T_C}{2} \tag{3.21}$$

where the electrical conductivity was written as $\sigma = L/(R_{int}A)$ and the average temperature of the device as $T_{AVG} = (T_H + T_C)/2$. ZT is a convenient figure for comparing the potential efficiency of thermoelectric devices using different materials, even when the preferred operating range of temperature is different. Greater values of ZT indicate greater thermodynamic efficiency.
Recent works claim substantial improvements to the figure of merit at material level [45, 46, 47], however, there are on-going discussions in the scientific literature about the experimental methods used to obtain the ZT value by different research groups, which leads to results that an independent observer finds difficult to compare to one other objectively. Well-performing materials used in commercial modules all have ZT values around unity; values of at least 3 or 4 are considered to be essential for thermoelectrics to compete with mechanical generation and refrigeration in thermodynamic efficiency where large power levels (kWs upwards) are concerned. The work undertaken for this thesis did not involve research into materials and techniques to improve the performance of the TEG device and most of the results presented are obtained with commercial devices measured at the device level where much of the uncertainty has been removed: it is the devices' performance, rather than the materials determining this performance, that is of interest.

The maximum thermodynamic efficiency η_{max} for converting thermal energy into electrical energy

is defined as [2]

$$\eta_{max} = \frac{T_H - T_C}{T_H} \frac{\sqrt{1+ZT}-1}{\sqrt{1+ZT}+\frac{T_C}{T_H}} \tag{3.22}$$

The first term on the right hand side of Eq. 3.22, $(T_H - T_C)/T_H$, represents the Carnot efficiency and it is reduced by the second term which depends on the figure of merit.

Chapter 4

Testing of Thermoelectric Generators

The thermoelectric manufacturing industry has not yet agreed a standardised method to test both the thermal parameters and the electrical performance of TEGs. Major challenges include the open-circuit thermal conductivity, device efficiency, and ensuring repeatable accurate measurement. This chapter presents the test system developed during the course of the work presented here that is intended to provide data about device performance in a 'real world' situation as is likely to be encountered by prospective end-users of such devices. Performance data are provided for some of the TEG devices used in the following chapters of this thesis, used individually or electrically connected in series and parallel, for conditions of constant temperature difference or fixed input thermal power. This chapter also quantifies the performance of interconnected TEG arrays when the elements are not all equally thermally heated. A theoretical analysis is used to predict the thermal and electrical behaviour of the system when several TEG devices are electrically connected in series or parallel, under balanced or unbalanced thermal conditions. Experimental results confirm the theoretical analysis and provide a figure relative to the magnitude of power lost due to temperature mismatch.

The following section summaries the major issues encountered during the development of this measurement system and the iterations made in the design to address the shortcomings identified. The final version of the test rig is then presented and used to determine experimental results for the performance of some commercial TEG devices. Next, the maximum power that can be produced in conditions of fixed thermal input power is studied. The final section presents experimental results showing the effect of temperature mismatch on the power produced by arrays of TEGs electrically connected in series or parallel.

4.1 Issues in developing the test rig

Efforts to solve the problem of reliably testing TEG devices at the University of Glasgow were started by Dr. James Buckle in 2008. The work has been continued throughout this Ph.D. by the author and, after several iterations and considerable time spent in developing the methodology and process control software, the current version of the measurement test rig provides excellent accuracy and repeatibility. The following sections describe the major steps in the development work leading to the present apparatus. A version very similar to that currently in use has also been supplied to European Thermodynamics Ltd who are using the equipment for the characterisation of a range of their products.

4.1.1 First test rig

On the cold side the first test rig used a water cooled aluminum block with a labyrinth path for the water; for the hot side three high-power resistors were bolted to an aluminum heat spreader block. The TEG was positioned in between the hot and cold sides and the whole fixture then fastened together using threaded metal rods with nuts and spring washers (for mechanical compliance). Fig. 4.1 shows a CAD model of this mechanical fixture. The measurement system included a PSU to power the resistors (thus varying the thermal power to the hot side), an electronic load connected to the TEG, a datalogger to record the hot and cold side blocks' temperatures, and a chiller to cool down the water on the cold side. All the electronic instruments were controlled by a test program written in *Agilent* VEE Pro, which is a graphical programming tool for automated control of laboratory equipment.

This measurement system could obtain a satisfactory electrical characterisation, however it had the following issues.

1. Hot side on the top: heated air naturally rises therefore convection losses were an issue.
2. Maximum temperature of the power resistors around 150°C. Most TEGs can easily be operated far in excess of this temperature.
3. Labyrinth on the cold side might lead to unbalanced temperature distribution on the face of the thermoelectric device.
4. Chiller had an accuracy and hysterisis of ±2°C.
5. No mechanical pressure reading.
6. No measurement of the temperatures directly in contact with the TEG's sides.
7. Thermal "short-circuit" through the rods clamping the system together.

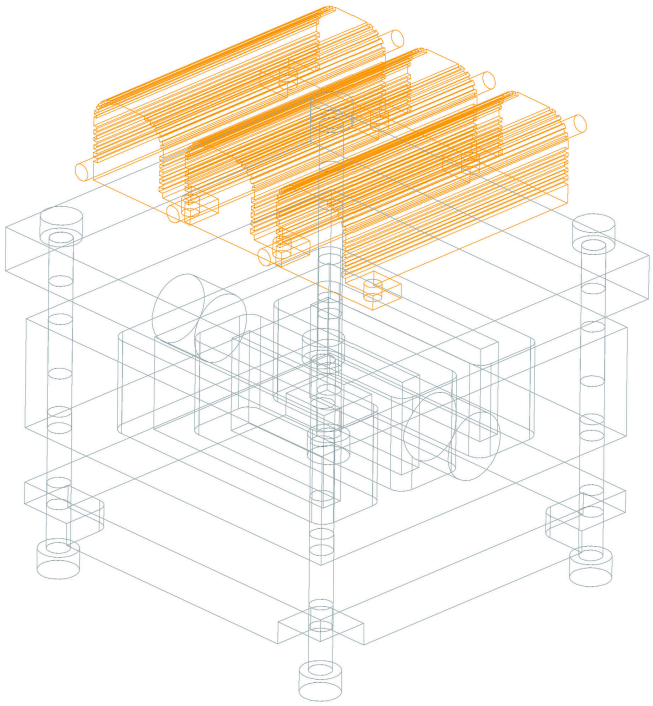

Figure 4.1: CAD model of the first measurement system used at the University of Glasgow for the testing the electrical performance of TEGs. Used with permission from Dr. J. Buckle.

4.1.2 Second test rig

Fig. 4.2 shows the second version of the test rig, which partially solved the issues with the first iteration.

A flat plate mica heater capable of 220 W and a maximum temperature of 280°C was clamped between two L-shaped aluminum brackets, and positioned on the bottom of the mechanical assembly. This solved issues 1 and 2. Slots were milled in the orange heat spreader plate and the water block face in contact with the TEG so that the thermocouples could sit close to the TEG's sides to solve issue 6. This iteration gave improved performance but was still far from satisfactory in terms of being able to produce reliable, accurate and consistent results.

4.1.3 Third test rig

The availability of *Crystal-Technica*'s hot surface igniters led to the design of the third test rig. These devices are normally used as the ignition source in oil and kerosene heating applicances. The heaters are easier to thermally couple to other surfaces and they can withstand higher input power (500 W) and temperatures (1200°C). A new hot block was made in copper, accomodating two such heaters.

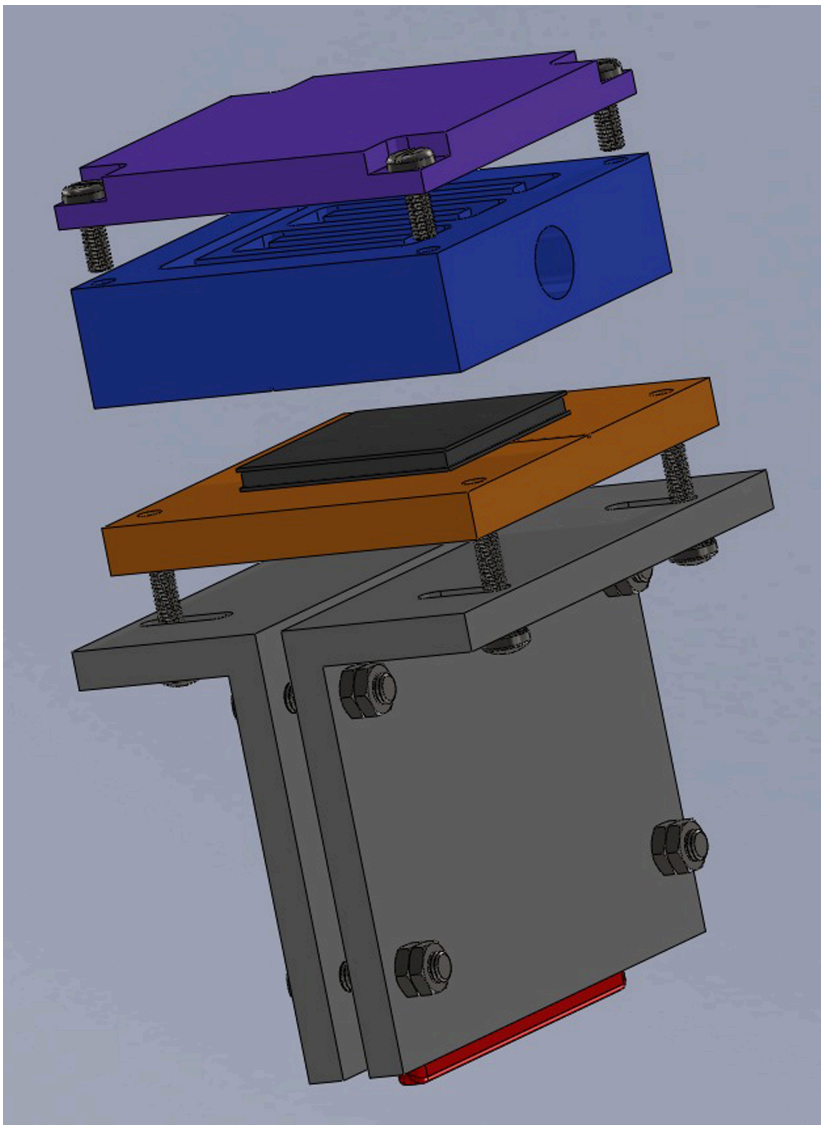

Figure 4.2: CAD model of the second measurement system used at the University of Glasgow for the testing the electrical performance of TEGs.

A new cold block was also designed with four pipes running straight through, to improve on issue 3. The resulting hot and cold blocks are shown in Fig. 4.3. Also, a 20 litre water tank was added on the output of the chiller to average the temperature of the water entering the cold side. This averaging function greatly reduced the time required for a test by virtue of an effectively constant temperature being present on the cold side.

This test rig was tested up to 600°C using two heaters. Fig. 4.4 shows the effective temperature distribution on the cap of the heater unit (the opposite side to the face in contact with the TEG) by the colour variation of the copper due to oxidation, also influenced by the different thermal contact resistances due to clamping pressure imbalances. The small copper shims are used as packers to accommodate the variation in thickness in each of the heater elements.

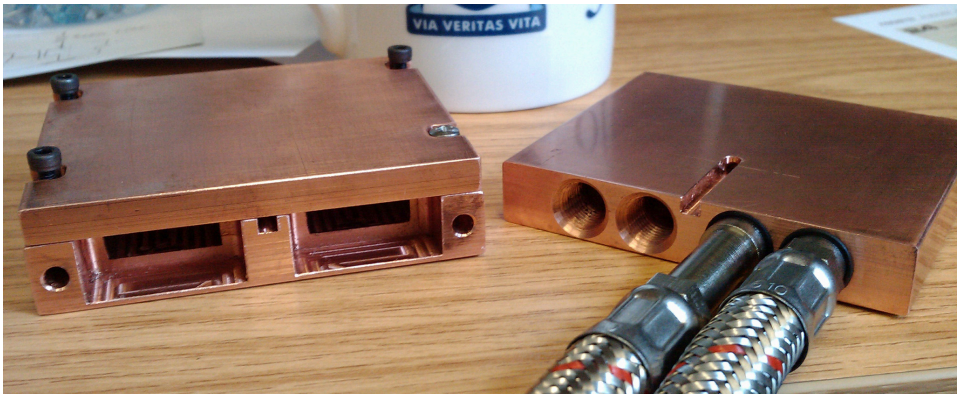

Figure 4.3: Picture of the hot (left) and cold (right) blocks developed for the third test rig.

Figure 4.4: Picture showing the temperature distribution on the copper, after testing the block up to 600°C.

4.2 Current test rig for TEGs

The contents included in this section are published in [J5].

The current fixture developed at the University of Glasgow as of February 2014 allows the hot temperature to be increased to in excess of $800°C$ with minimal thermal losses and thermal short-circuit; the clamping force can be measured and adjusted up to $5\,kN$ and the temperatures are sensed by thermocouples placed directly on the TEGs surfaces. A computer program controls all the instruments in order to minimise errors and to aid precise measurement and test repeatability.
The system can measure four TEGs simultaneously, each one individually controlled and separately heated by a maximum electrical power of $2\,kW$. This allows testing of the effects of series and

parallel connection of TEGs under mismatched conditions, *e.g.*, TEG dimensions, clamping force, temperature, etc. The apparatus can be employed both as a performance characterisation system and as a quality control unit, due to the ability to provide non-parametric testing of four TEGs concurrently. It can also be used to concurrently characterise devices of different dimensions at the same time.

The present measurement system, shown in Fig. 4.5, is included in a standard 19" equipment rack and is entirely self contained.

The schematic of Fig. 4.6 helps to understand the architecture of the system now in use. A data

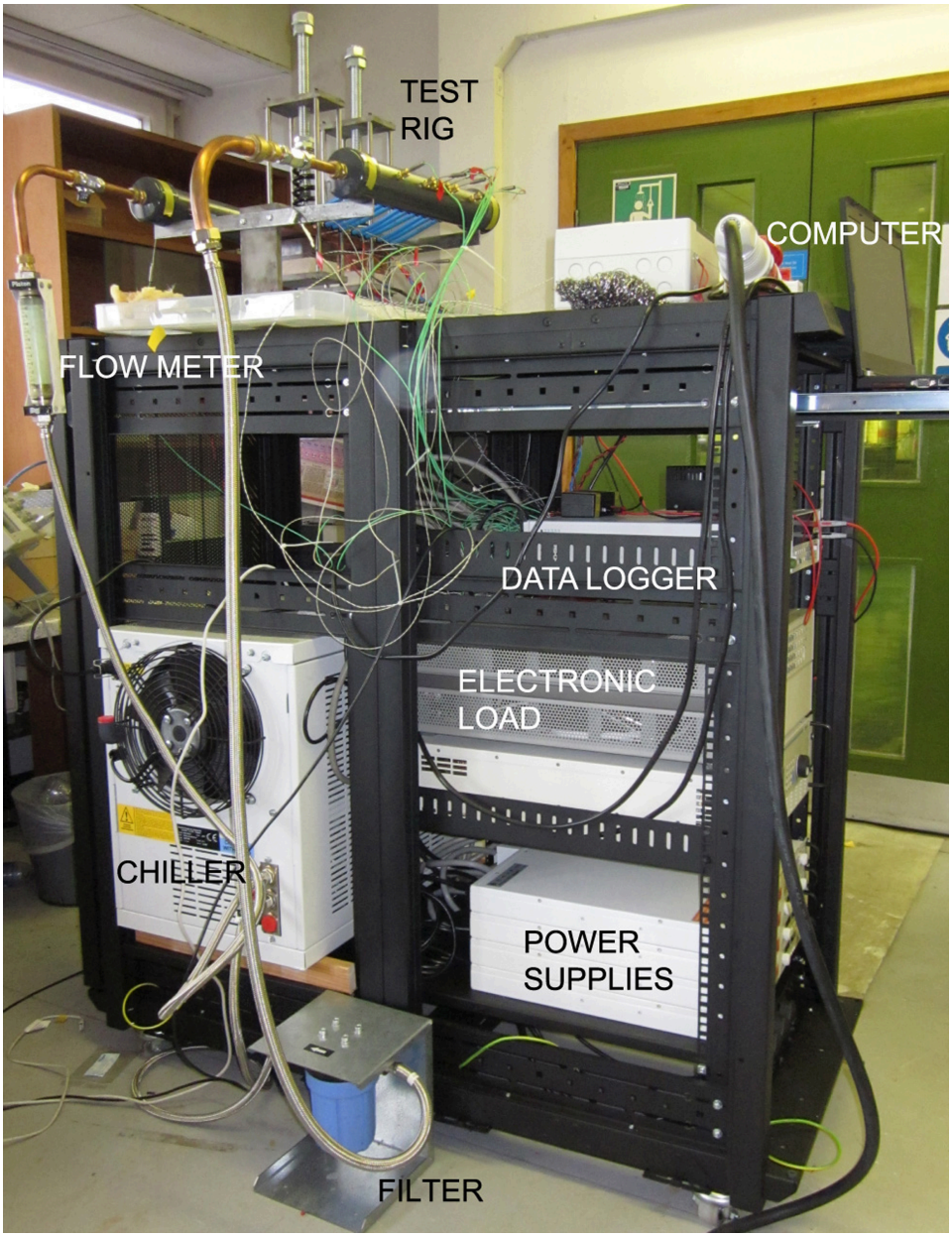

Figure 4.5: Picture of the complete measurement system used for the experiments.

logger unit is used to feed back temperature and mechanical pressure readings to the computer, where a completely automated program controls the amount of electrical power provided to the hot side,

and sets the electrical load connected to the TEG. A much improved chiller unit (*Thermal Exchange* $CS-10$) with closed loop Proportional Integral Derivative (PID) control and 0.1°C hysteresis is used to cool the cold side of the system. The main mechanical, electrical and computer features of the system are described in the next subsections.

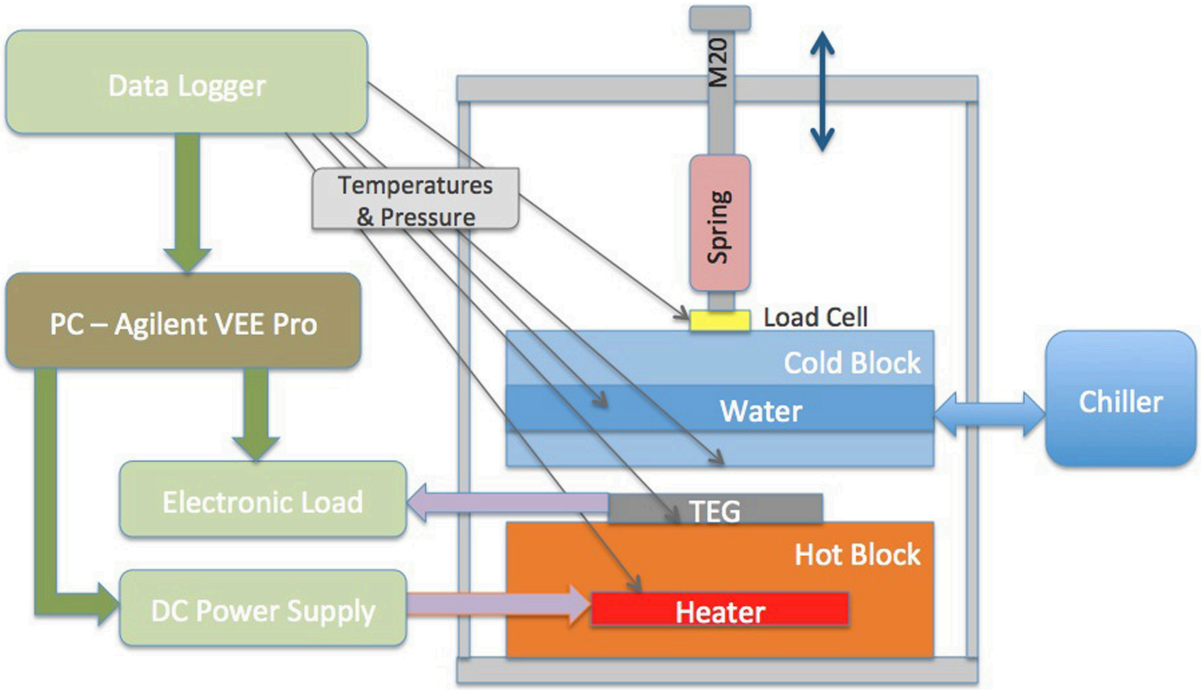

Figure 4.6: Schematic diagram of the measurement system.

4.2.1 Mechanical side

The CAD model of the mechanical side (top part of the test rig) is pictured in Fig. 4.7. The general idea behind the test rig is to have a common cold side which also serves as the mechanical support for the other components, while separate and independent mechanical fixtures can be vertically adjusted over a range of approximately 75 mm; as a consequence each thermoelectric module, placed in an individual hot block, is brought towards the cold block.

Fig. 4.8 shows a picture of the top part of the mechanical fixtures, with two TEG channels assembled. The 300 mm-long cold block is made of pure copper and is supported by steel columns at a height of 18 cm. It is water-cooled by the chiller unit. A manual valve adjusts the quantity of water delivered to the inlet manifold from the chiller and the fluid flow rate is measured by a Hall-effect flow meter; the incoming water temperature is sensed by a thermocouple. The water passes through twelve straight holes (three for each TEG) in the cold-side block and its temperature in several of the outgoing pipes is sensed by thermocouples before arriving to the outlet manifold. The chiller unit is

capable of extracting $1\,kW$ of heat power and controls the water temperature with a PID controller to an accuracy of $\pm 0.1°C$ between $5°C$ and $25°C$. Four thermocouples are placed inside the copper block, emerging from the bottom side with an aperture of just $1\,mm$ of diameter (to minimise the formation of hot spots), in order to measure the TEG cold side temperature directly on its surface.
Each of the four TEGs is placed within a separate mechanical structure of fixed height, composed of two steel plates connected together by 4 columns. An M20 bolt runs through the top plate and it is positioned over the top face of the cold block, touching a load sensor cell (type *Omega* LCMKD-5KN) at a single point of contact. For mechanical compliance a $1000\,lb/inch\,(179\,N/mm)$ spring with thrust bearings has been added; it is locked on the M20 bolt by a pair of nuts. When turning the M20 bolt, the external structure climbs the bolt and the bottom steel plate is drawn towards the bottom face of the cold block.

A large copper block serves as the hot side and it is shown in Fig. 4.9; it contains a silicon-nitride high-temperature high-power heater rated to $1200°C$ and $500\,W$. Two thermocouples are fitted inside each hot-side block, one terminating on the TEG hot side face with an aperture of just $1\,mm$ of diameter, and another one directly sensing the heater's temperature. The TEG is positioned on top of the hot-side block, hence when the bottom plate rises the device under test is sandwiched between the hot and cold copper blocks.
If the device under test requires a thermal input power in excess of $500\,W$, alternative copper heater blocks are available to host two and four heaters respectively, thus providing a rated maximum electrical power of $2\,kW$. The maximum temperature tested to date has been with an *Oxide* TEG at $800°C$. The absolute maximum temperature the test rig is capable of has not yet been measured. All the copper blocks are designed by the author and produced by a local precision engineering firm.

4.2.2 Heat isolation

The cold and hot side blocks are thermally decoupled except for conduction through the TEG. The only mechanical point of contact between the cold block and the hot block is the load cell onto which each individual structure is balanced, and the very long thermal path formed of the mechanical components of the test fixture. Between the hot copper block and the bottom steel plate there is a $2.5\,cm$-thick block of vermiculite, therefore the heat conducted through the four steel columns is minimized and it can be readily calculated by means of a thermocouple placed on the underside of the vermiculite board.
A thin mica sheet on top of the hot block, with a cut in its center of the dimension of the TEG module, is used to reduce thermal radiation losses from the hot to the cold side around the TEG module (Fig. 4.10). A thin graphite sheet (eGRAF HT-1205, not shown in Fig. 4.10) is used as a gap filler to reduce the thermal resistance between the hot block and the TEG hot face.
For studies of thermal conductivity and efficiency of the TEG module, it is important to control the

Parameter	Value	Unit
TEG Volume	$40x40x3$	mm^3
Hot block Volume	$75x70x25$	mm^3
Glass fibre Thickness	10	mm
Glass fibre Thermal Conductivity	0.035	W/mK
Vermiculite Thickness	25	mm
Vermiculite Thermal Conductivity	0.15	W/mK
Air Thermal Conductivity	0.024	W/mK

Table 4.1: Coefficients and dimensions used to calculate the heat losses from the hot block.

heat losses from the hot block and/or to quantify them. It is difficult to precisely calculate the heat dissipated to air through convection, thus the hot block was enclosed into a box (open on one side) made of a thin mica sheet and surrounded on the sides with glass fiber, as shown in Fig. 4.10).

The following data are for the system in use today. Future work will further increase the accuracy of the results and the calculation of losses. Reasonable values for the thermal conduction coefficient and the efficiency of the device under test can be obtained, and these are considered to be representative of likely practical applications which are invariably not loss-less. The thermal characterisation presented considers the heat losses to ambient through the insulation of the hot copper block, using the classic equation of thermal conduction

$$P_{loss} = \frac{kA}{x}(T_H - T_C) \tag{4.1}$$

where k is the thermal conduction coefficient, A is the surface area of thermal conduction, x is the thickness of the medium, and T_H and T_C are the temperatures of the two bodies. The values used for the material properties and dimensions are listed in Table 4.1.

The data obtained in steady state (at open-circuit, MPP, and short-circuit) are used to calculate the variation of the effective thermal conductivity and efficiency of the device under test according to the output current. The total electrical power P_{in} provided to the heater is transformed into heat energy; this energy, minus the mentioned losses P_{loss} and the energy used to change the internal heat energy of the hot copper block, flows through the TEG module. However, in steady state there is no change in the temperature of the hot block, therefore $P_{in} - P_{loss}$ flows through the TEG module. The efficiency η is calculated as the ratio between the output electrical power and the heat power flowing through the TEG:

$$\eta = \frac{P_{out}}{P_{in} - P_{loss}} \tag{4.2}$$

Fig. 4.11 illustrates how the effective thermal conductivity and MPP efficiency of a TEG vary with the temperature difference. The efficiency at the MPP increases asymptotically. It is interesting to note the great change in effective thermal conduction between the three operating points selected (open-circuit, MPP and short-circuit); this happens because a higher load current increases the Peltier effect (Eq. 3.6), which pumps more heat from the hot to the cold side, as explained in Section

3.3.2.

Future work will add a heat flux sensor on the cold side, and will use the adjustable fluid rate and the water pipe temperatures to precisely calculate the heat power being released to the water; this constitutes an invaluable way to compare the results obtained by calculating the heat losses from the hot block and determine residual systematic errors.

4.2.3 Electrical and control functions

The thermocouples and the pressure sensors are connected to a data-logging unit. The TEGs outputs are connected to an electronic load with four independent channels, while four $750\,W$ DC PSUs provide the power to the heaters. All the instruments are connected to a GPIB computer interface and controlled by the software VEE Pro. All the experimental results presented in this paper are automatically generated by a VEE Pro program interfaced to *Microsoft* Excel. The control program can independently control the temperature difference across each TEG and use any of the electronic load channels available.

The main function of the program is to obtain an electrical characterisation of the device under test, recording all the temperatures and electrical parameters at every operating point. The program also brings the system to steady state temperature at open-circuit, at the MPP and close to short-circuit, in order to calculate the efficiency and thermal conductivity of the device. User intervention is required to set the desired pressure on the module, turning the M20 bolt on top of the test rig. Future enhancements to the test fixture will include a stepper-motor driven clamping mechanism: pressure variations due to thermal expansion and contraction within the test rig will be automatically compensated.

The flow diagram of the control program is shown in Fig. 4.12. During initialisation the program asks the user to specify the temperature difference required for each TEG, the current load step size and the dimensions of each TEG. The latter parameter is needed to set the coefficients needed by the Proportional Integral (PI) control loop which applies power to the heater. The program can bring the system to the desired temperature difference starting from an arbitrary temperature. The electronic load is initially set to open-circuit and the program controls the electrical power to the heater necessary to establish the required temperature gradient across the device. When the error is less than $\pm 0.25°C$ the program takes readings from the data logger, the electronic load and the power supply, then the current load is increased by the set step size. After every load change a delay of 10 seconds is added before controlling the temperature again, in order to ensure that any thermal transient effect due to a change in Peltier effect does not lead to an erroneous measurement. The PI control loops regulates the temperature difference again and the iterative process continues until short-circuit is reached. The VEE Pro program finally computes thermal losses and electrical data and plots useful graphs directly to Excel. For the thermal characterisation the program takes

three steady-state measurements: at the beginning (open-circuit), at MPP and at the end of the test (short-circuit); the MPP is passed when the sequent power is less than that of the previous operating point, hence the previous load is set again. For steady state, data are recorded only after waiting for 2 minutes with the temperature difference continuously within $\pm 0.25°C$ of the desired temperature.

A twin version of this measurement system has been installed in European Thermodynamics Ltd to test the performance of commercial modules and for quality control.

4.3 Performance evaluation of TEGs

When designing a thermoelectric power generation system, the most important thing, from a practical point of view, is to understand how the power generated varies depending on the electrical load applied to the TEG and on the temperature difference across it. When connected to different loads, the TEG effective thermal conductivity changes; knowing how this happens is important to estimate the thermal energy that needs to be provided to and extracted from the system, and the change in temperature difference produced.
This section presents data and graphs describing the power produced at different temperature gradients, depending on the electrical load applied, for commercial TEG devices. After gathering initial experimental data it is then possible to calculate mathematical relations that allow the generation of correct electrical values at each thermal operating point. The influence of mechanical pressure is investigated, too.

4.3.1 Experimental electrical characterisation

This Section presents the electrical characterisation of three commercial TEGs (product code GM250-127-14-10 from *European Thermodynamics Ltd*) that will be used in Chapter 6 to evaluate the performance of the MPPT converter.
Each TEG was characterised separately at three different temperature gradients ΔT: $100°C, 150°C$ and $200°C$. Every test was performed imposing $1.25\,MPa$ of mechanical pressure onto each TEG, which corresponds to $209\,kg$ on a surface of $40x40\,mm^2$. This corresponds to the mechanical load suggested by *Custom Thermoelectric*[1] to obtain optimal performance, however the effect of clamping load is investigated in 4.3.3.
Fig. 4.13 plots the output voltage and power versus current for one of the TEGs (TEG#2).
Table 4.2 lists the performance data of the three TEGs. The maximum deviation in performance between the three devices stands at less than 5% for power production; this difference may be due to

[1]Application note on www.customthermoelectric.com

	$TEG\#1$			$TEG\#2$			$TEG\#3$			Deviation		
ΔT $(^{\circ}C)$	R_{int} (Ω)	V_{OC} (V)	P_{max} (W)	R_{int} (Ω)	V_{OC} (V)	P_{max} (W)	R_{int} (Ω)	V_{OC} (V)	P_{max} (W)	R_{int} $(\%)$	V_{OC} $(\%)$	P_{max} $(\%)$
100	1.73	4.84	3.43	1.73	4.87	3.44	1.80	4.87	3.33	3.8	0.7	3.2
150	1.94	7.22	6.79	1.94	7.23	6.80	2.01	7.21	6.57	3.6	0.2	3.4
200	2.11	9.25	10.26	2.10	9.25	10.30	2.17	9.20	9.84	3.3	0.5	4.5

Table 4.2: Performance parameters for the three thermoelectric modules used in the experiment.

manufacturing tolerances, contact resistance mismatch, measurement accuracy or variations in installing the devices in the test rig (*e.g.*, thickness of heat transfer compound on either face). However, this performance variation will not influence the MPPT converter evaluation, as it will be shown in the next section.

The reproducibility of results is guaranteed by the precision of the instruments used, by measuring the temperature difference directly in contact with the device and by using an automated control program. Differences of a few percents in the results obtained could occur if the device was removed and placed again in the test rig; in this case small changes in the position of the device and the thickness of heat transfer compound used could affect the measurements. However, the reproducibility of results can be noted considering the TEG device GM250-127-14-10 which was used for the results presented in this section and at a later stage for the results presented in Section 4.5 and in Chapter 6 (Section 6.6). In particular, the results of Fig. 4.20 and Fig. 4.21 agree with the results listed in Table 4.2.

4.3.2 Mathematical electrical characterisation

The data obtained from the electrical characterisation can be used to formulate a mathematical characterization using a similar technique to that explained in [102]. Voltage and power are calculated as a function of the current load and temperature difference.

In Section 3.3.1 it was explained that the TEG's terminals voltage equals the open-circuit voltage less the voltage drop on the internal resistance (Eq. 3.10). Both V_{OC} and R_{int} vary almost linearly with temperature. The open-circuit voltage is proportional to the Seebeck coefficient α ($V_{OC} = \alpha T$), which is not constant but varies depending on the Thomson coefficient (see Section 3.1.3). In order to account for the variation of V_{OC} and R_{int} with ΔT, a 2^{nd}-order polynomial curve fitting technique has been used, as shown in Fig. 4.14 for TEG# 2. Hence Eq. 3.10 can be now written as

$$V_{load} = (a\Delta T^2 + b\Delta T + c) - (d\Delta T^2 + e\Delta T + f)I_{load} \tag{4.3}$$

where a, b, c, d, e and f are constant coefficients, different for each TEG and obtained from experimental data. Table 4.3 lists the $a, ..., f$ parameters for the three TEGs used in the experiments.

	$V_{OC}\,(V)$			$R_{int}\,(\Omega)$		
	a (V/K^2)	b (V/K)	c (V)	d (Ω/K^2)	e (Ω/K)	f (Ω)
$TEG\#1$	$-7 \cdot 10^{-5}$	0.0649	-0.9553	$-9 \cdot 10^{-6}$	0.0065	1.1734
$TEG\#2$	$-7 \cdot 10^{-5}$	0.0639	-0.8536	$-9 \cdot 10^{-6}$	0.0062	1.1972
$TEG\#3$	$-7 \cdot 10^{-5}$	0.064	-0.8369	$-1 \cdot 10^{-5}$	0.0067	1.2328

Table 4.3: a, b, c, d, e, f coefficients for the three TEGs used in the experiments.

If a TEG producing half the voltage and double the amount of current was to be used, then the coefficients a, b, c would need to be halved and d, e, f divided by 4.

Using Eq. 4.3 it is possible to replicate the electrical characteristics of the TEGs used, after obtaining the necessary parameters from the experimental data. Fig. 4.15 shows the resulting 'mathematical' electrical characterisation for TEG# 2. As it can also be appreciated from a comparison with Fig. 4.13, the average deviation between the mathematically derived values and the experimental data is always less than 1.5 %. This means that it is now possible to independently predict the output from each of the three TEGs with high confidence, even when they are at different thermal operating points. This formulation will be used in Chapter 6 to estimate the performance of the MPPT algorithm used.

4.3.3 Influence of mechanical pressure

The mechanical load applied on the TEG device is an important parameter because it directly influences the amount of power produced. A higher mechanical pressure reduces the thermal contact resistance between the TEG and the heat exchangers, and if evenly applied equalisees the temperature across the ceramic surfaces and counteracts the formation of "hot spots". *Custom Thermoelectric* suggests a clamping force of $1.275\,MPa$ for optimum power generation and thermal contact[2].

The TEG device GM250-241-10-12 produced by *European Thermodynamics Ltd* was used to investigate the effect of mechanical clamping load on the power produced.

Fig. 4.16 plots the difference in power and voltage produced with $600\,kPa$ and $1200\,kPa$ for four temperature differences: $50°C, 100°C, 150°C, 200°C$. These results show that the effect of mechanical pressure is marginal, even if a higher clamping force (up to the recommended limit) ensures best performance, especially in the case of a slightly uneven surface and/or non-uniform distribution of thermal compound, because it minimises contact resistances.

The maximum difference in power produced is found at $\Delta T = 200°C$, where it corresponds to 1.5%. Sandoz-Rosado and Stevens [50] report differences always smaller than 4%. In the experiments undertaken it was noted that there was no hysteresis effect; cycling the applied pressure between

[2]Application note on www.customthermoelectric.com

tests yielded essentially identical curves for a specific pressure. It is believed that the effect is therefore due to the heat conduction interface material elastically filling voids at the microscopic scale and thereby increasing thermal conductance between the TEGs faces and the test fixture surfaces. This was demonstrated using both dry graphite sheets and the grease-based heat-sink compounds.

4.4 Fixed thermal input power

This section presents an investigation of maximum power production under fixed thermal input power. In Section 3.3.2 it was explained that the MPP is found at half of the open-circuit voltage (or half of the short-circuit current). This statement is true for a system in a thermal steady-state with constant temperature difference across the TEG device. However, the effective thermal resistance of the TEG device changes depending on the current drawn from the TEG in accordance with the parasitic Peltier effect. In order to keep the temperature difference constant, as it is done to obtain the electrical characterisation, the thermal power flowing through the TEG device must be varied accordingly. The aim of this section is to investigate where the MPP lies for the case where constant thermal input power is applied to the TEG.

4.4.1 Variation of effective thermal conductivity

First consider a TEG sandwiched between a cold side at temperature T_C and a hot side at temperature T_H, both of which can vary their temperature. As explained in Section 3.2.2 and by Min and Yatim [98], the effective thermal conductivity K_{var} of the TEG varies depending on the amount of current drawn from it, and it can be calculated as

$$K_{var} = \frac{Q_H}{T_H - T_C} \tag{4.4}$$

where Q_H is the thermal power flowing through the TEG, considered constant throughout this discussion. Moving from open-circuit to at-load, K_{var} increases and the temperature difference decreases as T_C increases and T_H decreases [103]. If T_C is maintained at a constant temperature then T_H must decrease by the deviation corrected for in T_C to keep $\Delta T = T_H - T_C$ as previously. Hence we can set T_C as a constant without significant loss of accuracy; the only small difference is represented by the fact that the κ and ρ values slightly vary with the average temperature of the device, but in this case the average temperature is almost unchanged. This assumption is realistic: in the test rig presented in Section 4.2 the cold side temperature remains almost constant with relatively small changes in thermal power flowing into the cold side.

In Eq. 3.15 both R_{int} and α vary with ΔT. We can therefore use Eq. 4.3 obtaining

$$\begin{aligned} Q_H &= K(T_H - T_C) + \frac{a(T_H - T_C)^2 + b(T_H - T_C) + c}{T_H - T_C}(T_H + 273.15)I \\ &\quad - \frac{a(T_H - T_C)^2 + b(T_H - T_C) + c}{2}I^2 \end{aligned} \tag{4.5}$$

where $K = \kappa A/L$ is the thermal conductivity of the TEG in $[W/°\mathrm{C}]$ at open-circuit and the offset of 273.15 was added for converting from Kelvin to Celsius. Also, the second term on the right side of Eq. 4.5 considers the Seebeck coefficient for the whole device as $V_{OC}/\Delta T$; even if α should be divided by the number of pellets, it needs to be multiplied again by the same number for the calculation of the Peltier power.
Eq. 4.5 in the variable T_H has three real solutions, which can be easily calculated by *Matlab* and the correct solution thus identified.
Using Eq. 4.5 it is possible to obtain the variation of the steady-state temperature difference across the TEG versus the load current, as it will be shown in Fig. 4.17. A similar graph was presented in [98] for different values of the figure of merit Z, which was, however, considered constant over the temperature range. Whilst the variation is small, it is not a constant.
It is trivial to calculate the steady-state temperature difference at open-circuit ΔT_0, at which the TEG is producing the open-circuit voltage V_{OC_0}. If there were no changes in temperature difference due to the Peltier effect and Joule heating then the MPP would be found setting $V_{load} = V_{OC_0}/2$. In reality after starting to draw current from the TEG the temperature difference will decrease to the steady-state asymptotic value with the shape of an inverse parabola. Due to the long thermal time constant of a typical thermoelectric system, it may take several minutes to complete at least 90 % of the transition.

A program was written in *Matlab* in order to find the value of I that leads to the maximum power production: starting from open-circuit and gradually increasing the load current I the corresponding steady-state temperature difference is calculated solving Eq. 4.5, and the output power then obtained by multiplying Eq. 4.3 by I. The program stops when the maximum power is reached. A single TEG device with the thermal and electrical characteristic of the device GM250-127-14-10 (used in Section 4.3) was considered for this analysis.
The $a, ..., f$ parameters used are those of $TEG\#2$ in Table 4.3. The value of thermal conductivity at open-circuit $\kappa_{OC} = 1.5W/mK$ was selected from Fig. 4.11. $T_C = 25°\mathrm{C}$ and $Q_H = 156W$. Fig. 4.17 shows the resulting electrical characterisation computed by *Matlab* for constant thermal power input, in steady-state; for each load point (blue line), the green line plots the temperature difference (on the secondary y-axis) and the red line the related power. It can be noted that the temperature difference decreases significantly with increasing current loads due to an increase in heat pumped from the hot to the cold side. The point at which maximum power is found is for $V_{MP} = 4.38V$

which is almost half of the initial open-circuit steady-state voltage $V_{OC_{init}} = 9.13V$. When going from open-circuit to maximum power the temperature difference drops 40°C from $\Delta T_{OC} = 200$°C to $\Delta T_{MP} = 160$°C.

Next, the program compares the maximum power value to the one that would be set if the load voltage was to be continuously adjusted to half of the resulting open-circuit voltage. The program starts by calculating the open-circuit voltage relative to the temperature difference established by the previously calculated point of maximum power. This does not mean that an open-circuit condition is applied to the load (in which case the temperature difference would go back to $9.13V$), but that this point, marked by a magenta circle on the primary y-axis of Fig. 4.17, would be the voltage established right after a sudden disconnection of the load. The program uses a recursive loop to adjust the operating voltage V_{load} at half of V_{OC}. The recursive operation is needed because when a new voltage is applied the current changes accordingly and so does the temperature difference. A new V_{OC} is established and V_{load} must be updated again. The program is considered to have achieved convergence when the difference between V_{load} and $V_{OC}/2$ is less than $1\,mV$.
The result of this analysis is that the current load chosen, $I_{HV} = 1.89A$, is greater than I_{MP}, leading to a $\Delta T = 153.6$°C and a power produced of $6.90W$, which is 2.82 % smaller than $P_{MP} = 7.10W$. This result highlights the importance of the parasitic Peltier effect in power generation mode.
An important result to remark is that the output voltage that leads to maximum power production in case of fixed thermal input power is greater than $V_{OC}/2$. The smaller current drawn reduces the Peltier effect, thus allowing a higher temperature difference across the device and a corresponding higher power produced.

4.4.2 Effect of pellet size on thermoelectric performance

This section examines the electrical performance and thermal behaviour exhibited by two TEG devices of the same overall size made of different number of pellets of different sizes.

First suppose two devices of area $4x4\,cm^2$ hypothetically built without clearance space in-between the pellets, so that the surface area of thermoelectric material is the same. The first device, labelled TEG1, has $n_1 = 16$ couples of n- and p- pellets, each of cross-sectional area $A_1 = 1\,mm^2$ and length $L = 1.5\,mm$. The second device, labelled TEG2, has $n_2 = 64$ couples of $A_2 = 0.25\,mm^2$ and same $L = 1.5\,mm$. Consider operation in steady-state at constant temperature difference ΔT. Each couple of both devices produces the same voltage $V_{np} = \alpha \Delta T$ where the Seebeck coefficient α is the same because the pellets are made of the same material at the same temperature. This voltage is then multiplied by the number of couples in the device: for TEG1 $V_1 = n_1 V_{np}$ and for TEG2 $V_2 = 4V_1 = nV_1$ where $n = n_2/n_1 = 4$. The electrical resistance is calculated by $R = \rho L/A$: $R_2 = n^2 R_1$ because TEG2 has n-times the number of pellets of TEG1, and their area $A_2 = A_1/n$. Supposing maximum power production, $I_1 = V_1/2R_1$ and $I_2 = V_2/2R_2 = nV_1/2n^2R_1 = I_1/n$.

The maximum electrical powers produced are $P_{elec1} = V_1^2/4R_1$ and $P_{elec2} = V_2^2/4R_2 = n^2V_1^2/4n^2R_1 = P_{elec1}$. The Peltier powers pumped (either at the hot or cold side, hence a generically labelled temperature T_j in the next equations) are $P_{Pelt1} = n_1V_{np}T_jI_1$ and $P_{Pelt2} = n_2V_{np}T_jI_2 = n_2V_{np}T_jI_1/n = P_{Pelt1}$ where the Peltier effect happening at each couple's junction is multiplied by the number of couples. The Joule effect contributes to $P_{Joule1} = 0.5I_1^2R_1 = 0.5(nI_2)^2R_2/n^2 = P_{Joule2}$. The thermal conduction coefficent of the two devices is identical, as are the total surface area and the thickness, therfore as they are at the same temperature difference the two TEGs have the same thermal power flowing through them due to thermal conduction. As a consequence, the thermal to electrical efficiency of the two devices is the same.
This analysis showed that from both the electrical and thermal point of view the two devices considered (with the same surface area and volume of thermoelectric material, arranged in pellets of different dimensions) behave in the same way.

In practice it is impossible to manufacture two thermoelectric devices like the ones previously described in this section. The necessary clearance space between pellets usually leads to different packing factors for devices of equal overall dimensions but different pellets' size. The clearance space, labelled τ, usually ranges from 0.8 to 1.2 mm; as a consequence, devices with wider pellets usually contain a greater quantity of thermoelectric material (for the same pellets' length). In a square thermoelectric device with total surface area A comprising of N pellets, the side length w of each pellet can be calculated as

$$w = \frac{\sqrt{A} - \sqrt{N+2}\,\tau}{\sqrt{N+2}} \tag{4.6}$$

where $N + 2$ is used because two locations without pellets are occupied by the two electrical wires. In Eq. 4.6 it was considered that there is the same number of pellets and clearance spaces in each side of the device (half clearance space at each corner).
The packing factor ϕ is defined as the ratio of surface area of thermoelectric material over the total surface area of the module and obtained from

$$\phi = \frac{N\left[A + (N+2)\tau^2 - 2\sqrt{A}\sqrt{N+2}\tau\right]}{A(N+2)} \tag{4.7}$$

The open-circuit thermal conductivity of the TEG varies linearly with the packing factor, therefore TEGs with wider pellets have greater values of κ.

In order to compare the thermoelectric performance of TEGs of same A and different w, the parameters used by the *Matlab* program of Section 4.4.1 are normalised to the mechanical parameters of device GM250-127-14-10 ($N_{norm} = 254, A_{norm} = 40x40\,mm^2, w_{norm} = 1.4\,mm$) and then adapted to a TEG device with different number of pellets N with different side length w, in a similar way as already done at the beginning of this section. In particular:

- the new pellet side length w is calculated from Eq. 4.6

N	τ (mm)	w (mm)	ϕ	K (W/K)	ΔT_{MP} (K)	α $(\mu V/K)$	I_{MP} (A)	V_{MP} (V)	V_{OC} (V)	P_{elec} (W)	P_{Pelt} (W)	P_{Joule} (W)
254	1.1	1.4	0.31	0.8	159.5	187	1.61	4.41	7.56	7.10	34.9	2.54
482	0.8	1	0.31	0.8	158.9	187	0.85	8.33	14.3	7.08	35.0	2.54
110	1	2.8	0.53	1.37	93.6	190	4.12	1.19	1.96	4.89	33.7	1.58

Table 4.4: Simulation results to compare the effect of pellets' dimensions and device packing factor on the thermoelectric performance when considering a system with constant thermal input power.

- a, b, c (corresponding to V_{OC}) are scaled by $N/254$
- d, e, f (corresponding to R_{int}) are scaled by $1.4^2 N/254w^2$
- the new thermal conductivity K is scaled by $\dfrac{w^2 N}{1.4^2 \cdot 254}$

The same length of pellets is used throughout.
Table 4.4 presents three sets of results: the first for the TEG analysed in Section 4.4.1 (GM250-127-14-10, characterised in Sections 4.3.1 and 4.3.2) which has $N = 254, \tau = 1.1\,mm$, the second for a TEG with $N = 482, \tau = 0.8\,mm$ (GM250-241-10-12 by *European Thermodynamics Ltd*) and the third with $N = 110, \tau = 1\,mm$ (equivalent to GM250-31-28-12 by *European Thermodynamics Ltd* scaled from $30x30\,mm^2$ to $40x40\,mm^2$ for comparison with the other two devices). All the results are obtained with $Q_H = 156\,W, T_C = 25°\mathrm{C}$.

The first two devices in Table 4.4 have the same packing factor ϕ, which results in the same value for thermal conductivity K and resulting temperature difference ΔT across the device; the maximum electrical power produced for constant thermal power through the device, Peltier power and Joule power are also equivalent. The third device, characterised by a packing factor 1.7 times greater, demonstrates worse performance in conditions of fixed thermal input power because its higher K leads to a considerably lower ΔT and consequently lower maximum electrical power (one and a half time smaller). As a comparison with the results presented in Section 4.4.1 (for the first TEG), in which the difference between maximum power and power set by the half open-circuit voltage method was 2.82 %, for the third TEG this difference rises to 4.4 %. This important result means that the Peltier effect acquires more relevance in TEGs rated for higher current output.

It is very interesting to note that the power pumped from the hot side due to the Peltier effect (P_{Pelt}) remains constant in all three cases. The differences evinced from the results of Table 4.4 are due to the fact that the packing factor has a great influence on the performance of the thermoelectric devices, because the number of pellets does not scale in the same way as the total surface area of thermoelectric material. Comparing some parameters of the first and third TEGs the following relationships are obtained: $N_1 = 2.31N_3$, $K_3 = 1.71K_1$, $R_1 = 10.49R_3$. It is very easy to note that these parameters do not scale as in the case described at the beginning of this section, for a null clearance space (τ=0).

Even if preliminary experimental tests (not reported in this thesis) confirm the results presented in

Table 4.2, this topic will be the subject of further experimental future work.

Summarising the results obtained in this study leads to the conclusion that for power generation it is more efficient to utilise TEGs with smaller current outputs, *i.e.* with smaller cross-sectional area. It is quite easy to also reach the opposite conclusion for thermoelectric devices suited for heat pumping, but this is outside the scope of this thesis. The length of the pellets reduces the thermal conductivity of the device, thus improving the efficiency, but at the same time it increases the electrical resistance, hence decreases the current output because the open-circuit voltage is the same. A balance must be found between the desired thermal to electrical efficiency and the electrical power rating.
It is very important to re-iterate that these results are calculated for the thermal steady-state under constant thermal input power, which is usually reached after several minutes. In common thermoelectric applications the thermal input power varies fairly rapidly with time, *e.g.*, exhaust gas mass flow and temperature. When varying the electrical operating point from V_{MP} to $V_{OC}/2$, the change in hot-side temperature is quite slow - dominated by the thermal time constants in the system - so that the change in power production is negligible, if not negative. Also, it is almost impossible to find a mathematical formulation to calculate the MPP for different TEGs across the whole operating temperature range without detailed prior knowledge of the specific TEG characteristics.

The results presented in this section also confirm the effects found by Gao and Chen [104] during practical measurements of thermoelectric devices for which the difference in estimation of maximum power output when switching from open-circuit to short-circuit can be as high as 10.7 %.
Similar work has been published by Gomez *et al.* [105], who reported that "the optimum condition for load resistance ratio was observed to occur at larger values than those obtained from traditional optimization work". However, it is likely that their results are negatively influenced by not measuring the temperature directly in contact with the sides of the TEG and especially because the experimental results are undertaken at a low temperature gradient ($3.5°C$), with very low output power ($3.5\,mW$); this suggests that there might be uncertainty in data measurement accuracy because the *actual* temperature difference across the device is unknown.
McCarty [106] states that "the maximum power and efficiency occur at the same electrical load resistance ratio", when $R_{load} = \sqrt{1+ZT}R_{int}$. However, it must be again stressed that this is true only for a constant thermal input power and the analysis presented in this section does not ultimately prove this result. Nonetheless, we believe that such a result is a consequence of having used the same starting equation (Eq. 3.15) for the analysis.

The results presented in this section are significant.
The finding that large TEG pellet cross-sectional areas (and the corresponding lower voltage/higher current characteristic) negatively affects at-load system temperatures has far-reaching implications for the design of limited-heat thermoelectric systems, *e.g.*, exhaust gas and stoves. In the last five years at least three major on-vehicle commercial energy recovery systems have independently been

designed and fabricated using relatively large pellets. All have failed to reach the power output level predicted from simulation models by a considerable margin. Further, for one of the systems, after disappointing initial test results the large pellet TEGs were replaced with TEGs with a smaller cross-sectional area of pellet, and a lower packing density. When re-tested under identical hot-gas conditions to previously, the new TEGs produced considerably higher output power, contrary to conventional wisdom but in keeping with the findings presented here. The consistency of poor experimentally measured performance from systems designed using extant commercial simulation tools highlights that there is evidently a need to re-visit the design tools in use, and also for the designer to gain a deeper understanding of actual TEG performance likely to be encountered in practical systems.

4.5 Effect of temperature mismatch on interconnected TEG arrays

The contents included in this section are published in [J2].

Several TEG modules can be connected in series and/or parallel (forming an array) to provide the required voltage and/or current. However, in most TEG systems the individual thermoelectric modules are subject to temperature mismatch due to variable operating conditions. Examples of situations where this mismatch occurs directly include thermal variability as found in exhaust gas systems [13, 66] or where the thermal conductivity of the mechanical system is poorly controlled [107]. Variability of the electro-thermal performance of individual TEG modules is also sufficient to cause a significant mismatch [108]. The mechanical clamping force the TEG is subjected to indirectly contributes to similar variation in electrical operating point, due to changes associated with the thermal contact resistance which is partially pressure dependent [109], as investigated in Section 4.3.3.
Consequently, when in operation each TEG in the array will have a different maximum power point. Problems of decreased thermal efficiency (due to parasitic Peltier effects) or decreased power output arise if the TEGs connected in the same array are subject to temperature mismatch because the MPPT converter sets the same sub-optimal electrical operating point for all modules in the array.
This section analyses the impact of thermal imbalance on the power produced at module and system level in a TEG array.

4.5.1 Series and parallel TEG arrays

Fig. 4.18 illustrates the series connection of three TEGs, each of them represented by a voltage source $V_{1,...,3}$ in series with an internal resistance $R_{1,...,3}$.
Under ideal operating conditions, each module within the array will experience an equal ΔT and therefore all modules will produce an equal output voltage V_{OC} and the array will be in a balanced thermal condition. In this case the MPP is at $3V_{OC}/2$ and the overall array resistance is $3R_{int}$.
However, actual thermal operating conditions in a practical system might be such that each TEG may experience a different ΔT and therefore their voltages and internal resistances will not be equal. In this case $V_{OC} = V_1 + V_2 + V_3$ and the current flowing into the load is

$$I = \frac{V_{OC} - V_S}{R_1 + R_2 + R_3} \tag{4.8}$$

where V_S is the voltage at the array's terminals.

Fig. 4.19 shows three TEGs in a parallel configuration. For ideal operating conditions, the TEG modules in the array operate at the same ΔT. Hence each TEG produces the same voltage and operates at maximum power, with $I_1 = I_2 = I_3$.
Under non-ideal thermal conditions the different temperature gradient across each TEG unit will lead to a mismatch in the currents magnitude:

$$I_1 = \frac{V_1 - V_P}{R_1} \qquad I_2 = \frac{V_2 - V_P}{R_2} \qquad I_3 = -I_1 - I_2 \tag{4.9}$$

where V_P is the voltage at the array's terminals.

4.5.2 TEG arrays under mismatched temperaure differences

This section presents the experimental electrical characterisations of arrays of three TEGs connected in series and parallel while subject to temperature mismatch. For each configuration a theoretical analysis is presented to explain the behaviour during the open-circuit condition and to predict the at-load maximum power point.

The three TEGs characterised in 4.3 were connected electrically in series into an array. The electrical characterisation was performed with TEG# 1 at $100°C$, TEG# 2 at $150°C$ and TEG# 3 at $200°C$. The results obtained from the array of TEGs are shown in Fig. 4.20.
The maximum power that can be extracted is less than the sum of powers that could be produced by the array if the TEGs were individually connected. From Table 4.2 this value can be calculated as $3.43\,W(TEG\#1) + 6.8\,W(TEG\#2) + 9.84\,W(TEG\#3) = 20.07\,W$. This means that when under the selected temperature-mismatched condition the three thermoelectric devices produced 9.22% less

power. It must be noted that the wire and connectors used for the series connection of the TEGs contribute to additional electrical resistance which in turns decreases the total output power from the TEG array.
It can be noted that the MPP is found when the array's terminals voltage is at half of the open-circuit value. This result confirms the fact that an array of TEGs in series can be simplified to a voltage source, whose value is the sum of the individual TEGs' open-circuit voltages (from Table 4.2, $4.84\,V + 7.23\,V + 9.2\,V = 21.27\,V$), and an internal resistance equal to the sum of the individual internal resistances, as already described in 4.5.1. This in turn also confirms that a MPPT converter using the fractional open-circuit voltage method is still able to obtain the MPP of a mismatched array.
It is of great interest to understand the operating point for each module relative to its V-I curve, while series-connected in the (mismatched) array. The current is the same in each TEG and, from Fig. 4.20, is found to be $1.72\,A$. Reference to Fig. 4.13 shows that TEG# 1 ($100°C$) is working on the right-hand side of its power P-I curve (orange coloured); this means that it is working on a less efficient thermal operating point with higher Peltier effect (hence higher effective thermal conductivity) which leads to a decrease in temperature difference across it, thus amplifying the mismatched condition. TEG# 2 ($150°C$) works very close to its MPP, while TEG# 3 ($200°C$) works on the left-hand side of its power curve (in purple); this corresponds to working in a more efficient operating point which leads to an increase in the temperature gradient across it (and therefore a slightly increased power output). This results in a positive feedback effect for which, in the case where the input thermal power source remains constant, the temperature mismatch becomes greater.

Next, the three TEGs were connected electrically in parallel into an array whose electrical characterisation was performed with TEG# 1 at $100°C$, TEG# 2 at $150°C$ and TEG# 3 at $200°C$. The results are shown in Fig. 4.21.
Confirming that the MPP is still at half of V_{OC}, Fig. 4.21 shows that the available maximum power is now $17.48\,W$, which is 12.90% less than what would be available if each TEG was to be controlled individually. This is also less than the electrically-in-series case (9.22%). The additional wiring and connectors used for the array connection are responsible for part of this power lost, however the comparison of performance between series and parallel case remains valid because of the same number of connections used.
Predicting the open-circuit voltage of an array with mismatched TEGs connected in parallel is not as straightforward as when the TEGs are connected in series, because the value depends on the individual TEGs' open-circuit voltages and internal resistances. Looking at the circuit in Fig. 4.19, when R_{load} is not connected the sum of currents at node V_P is null (Eq. 4.9 remains true). Each current can be written as

$$I_n = \frac{V_n - V_P}{R_n} \tag{4.10}$$

where $n = 1, \ldots, 3$. Substituting Eq. 4.10 (for each module) into Eq. 4.9 it is now possible to obtain

V_P:

$$V_P = \frac{R_2R_3V_1 + R_1R_3V_2 + R_1R_2V_3}{R_1R_2 + R_1R_3 + R_2R_3} \tag{4.11}$$

Depending on the value of V_P, the value of each TEG's current may be positive or negative. A positive value of current means that the module, while the array is in open-circuit, *i.e.* no external load is applied, is generating current; on the contrary a negative value of current means that the module is absorbing current, hence working in heat pumping mode. The values of currents in the situation chosen for the experiment are not irrelevant, as it will be now calculated and measured. Using the mathematical technique described in 4.3.2 (Eq. 4.3) the currents in each TEG were found to be:

$$I_1 = 1.19A \quad , \quad I_2 = -0.14A \quad , \quad I_3 = -1.05A \tag{4.12}$$

These values were then confirmed by a transient experiment: the three TEGs, disconnected from each other, were first brought to the selected temperature gradients ($\Delta T_{TEG\#1} = 100°C; \Delta T_{TEG\#2} = 150°C; \Delta T_{TEG\#3} = 200°C$), then instantaneously connected in parallel through two multimeters in current mode, as depicted in Fig. 4.22. The current going from TEG# 3 to TEG# 2, I_{32}, was $0.95\,A$ while the current going from TEG# 2 to TEG# 1, I_{21}, was $1.10\,A$. The difference between the experimental results and those calculated using the results of Eq. 4.12 are approximately 10 %, which can be attributed to the difficulty in reading the multimeter during the transient, to the frequency response of the multimeter itself and to the thermal effects occurring in the TEGs during the transient from open-circuit to short-circuit conditions.

As in the previous procedure for the series array, it is relevant to establish the operating point of each TEG with reference to its P-I curve. In this case of parallel electrical connection of the modules the operating voltage is the same for each TEG ($3.48\,V$). TEG# 1 ($100°C$) works on the left-hand side of its power P-I curve (orange coloured), which corresponds to a higher efficiency point which tends to increase its temperature difference. TEG# 2 ($150°C$) works very close to its MPP, and TEG# 3 ($200°C$) works on the right-hand side of its power curve (purple-coloured), where the Peltier effect is greater, leading to a decrease in temperature difference across it. The overall effect can be described as a negative feedback, for which the TEGs operating at lower and higher temperature gradients, *i.e.* TEG# 1 and TEG# 3 respectively, are pushed towards the middle temperature difference of TEG# 2. This is consistent with the results showing that parallel interconnection under mismatched conditions yields a lower array power output than for the series case.

4.5.3 Discussion of results

The presented results substantiate that connecting thermoelectric generators in series produces better electrical system efficiency, provided that the temperature differences remain constant, when compared to the parallel connection. The temperature-mismatch situation created in the experiment demonstrated a power production drop of 9.22% and 12.90%, for the series and parallel case

respectively, from the maximum power that would be available in case each TEG was controlled individually. Part of the power lost is due to the wiring and connectors used for the array interconnections.
However, from the thermal point of view the parallel connection showed that its thermal equalising influence would bring all the TEGs' temperature differences towards a value in the middle, if the thermal input powers to the TEGs remain constant. This would tend to decrease the temperature mismatch and increase the array electrical efficiency. However, reducing the temperature gradient across the TEG at highest temperature difference could prove unwanted because output power increases exponentially with temperature difference. This situation has not been studied in this work and will be researched in the future to better understand the relative advantages and disadvantages.

From the electrical connection point of view, the parallel-connected array has lower voltage and higher current, which leads to higher I^2R losses (Joule heating) in the wiring and MPPT converter, thus further decreasing the overall system electrical efficiency. This is particularly acute in automotive systems where the absolute value of current can be very high (10s or even 100s of Amps), with the converter attached via several metres of cable. System's cost and weight in parallel connection is adversely affected because of the need for high-current inductors in the Switch-Mode Power Supplys (SMPSs), and possibly more complicated SMPS topologies in case that a high-step up ratio is required. Especially in low-temperature applications a higher open-circuit voltage is preferred because it requires a simpler and more efficient power converter.
When designing a thermoelectric generating system a balance must be found between the number of MPPT converters and the number of TEGs connected into an array controlled by one of those power converters. This work ultimately suggests that the connection of thermoelectric devices in series yields a more efficient system at lower cost, compared to parallel connection. This is true considering both non-uniform temperature distributions, as researched in this paper, and the aforementioned considerations related to Joule losses and size and cost of wiring and electronic components.
Future work will investigate solutions to reduce the negative impact of thermo-mechanic mismatches on the thermal and electrical efficiency of interconnected TEG arrays.

The experimental results presented in this section show that the power lost by mismatched conditions (temperature, mechanical load, manufacturing tolerances, aging) can be significant. Using the mathematical formulation of Eq. 4.3 (obtainable from the experimental characterisation) and electrical circuit equations it is possible to predict the output electrical power in any temperature mismatch situation. The work presented in this section analysed arrays of three TEGs, however, the results and the circuit equations can easily be adapted for a higher number of TEGs.
In commercial systems that are currently under development for energy scavenging from vehicle exhaust gases there are different temperatures both between arrays and within individual arrays. Hence there is a need for multiple power converters, however, this is necessary but not sufficient to guarantee that the maximum possible power will actually be achieved. Simulation models currently in use should be updated to include the additional physical effects due to temperature imbalance,

otherwise they risk over-estimating total power production. In the practical case where thermal-mechanical imbalances may be expected, a compromise must be found between the number and cost of MPPT converters in a distributed system, and the expected power loss incurred due to mismatched conditions.

4.6 Conclusions

This chapter described the testing apparatus that was built at the University of Glasgow to measure the performance of TEG devices. The test setup is completely automated and provides accurate and repeatable experimental data. The system can individually control the temperature difference and the mechanical force applied across up to four TEG devices in order to investigate the effects of thermo-mechanical mismatches occurring in an interconnected array of TEGs. Experimental and theoretical results have demonstrated that temperature mismatch negatively affects the total power generated by the TEG array.
This chapter also proposes a mathematical characterisation of the predicted performance of the tested TEGs at any thermal state. This characterisation is then used to study the optimum at-load electrical operating point when the thermal power through the TEG is constant.

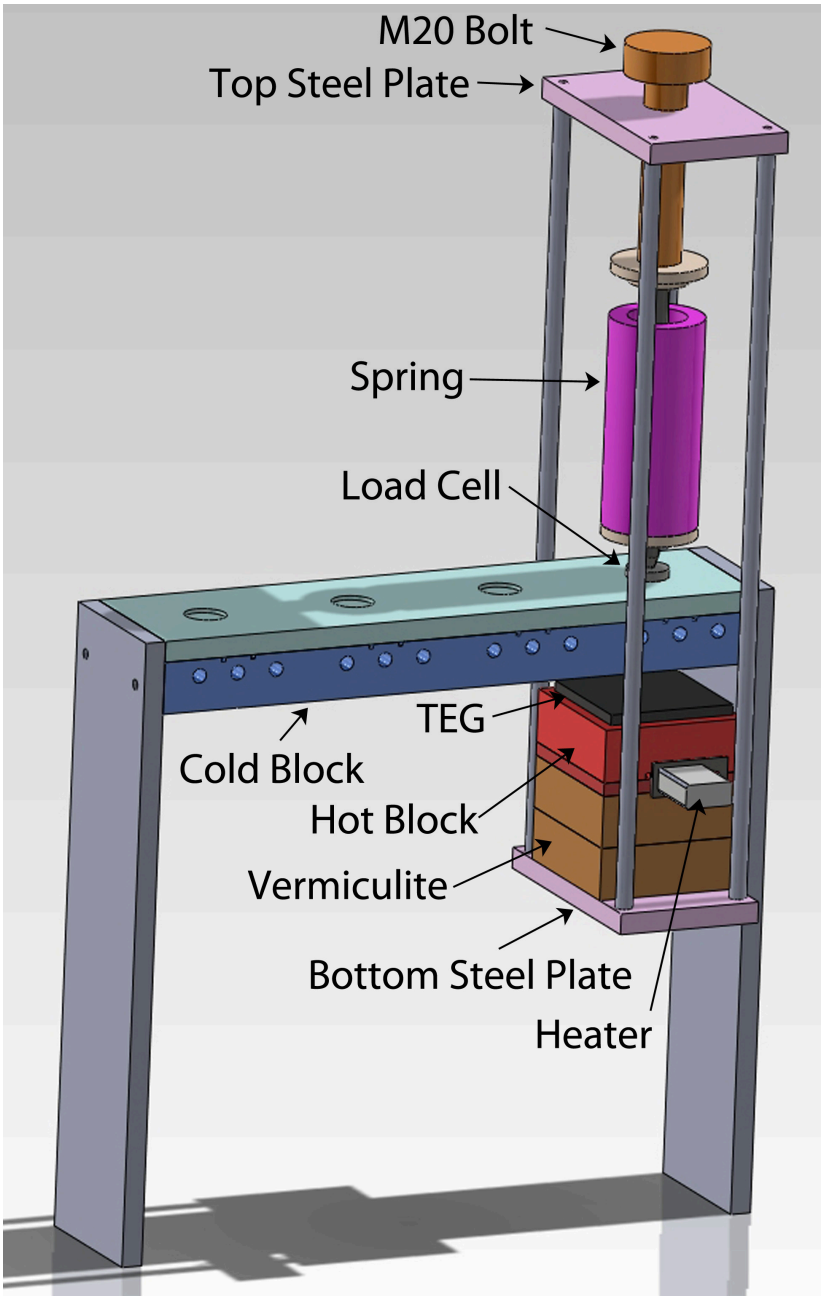

Figure 4.7: CAD model of the mechanical part of the test rig, showing just one TEG measurement fixture.

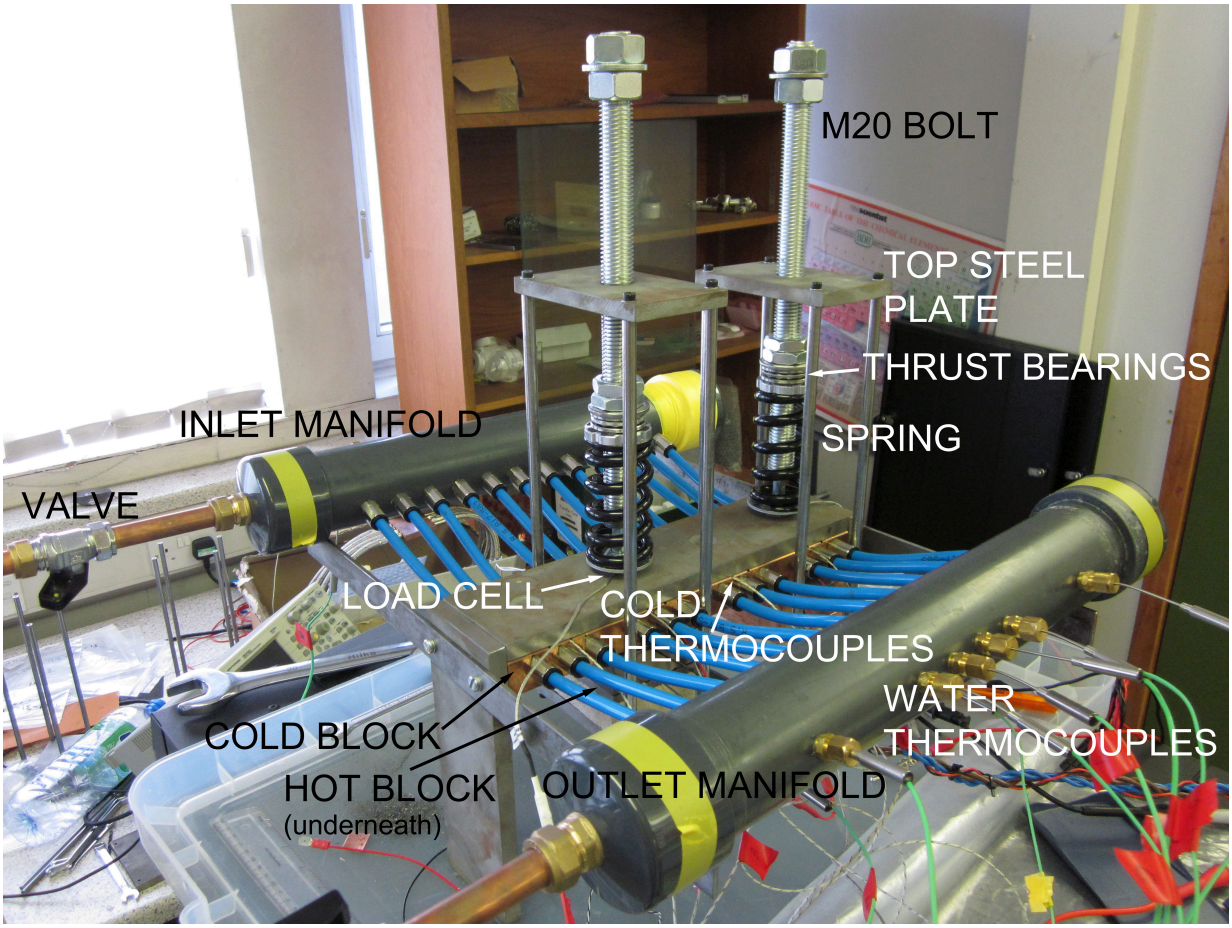

Figure 4.8: Picture of the test rig, showing just two measurements structures.

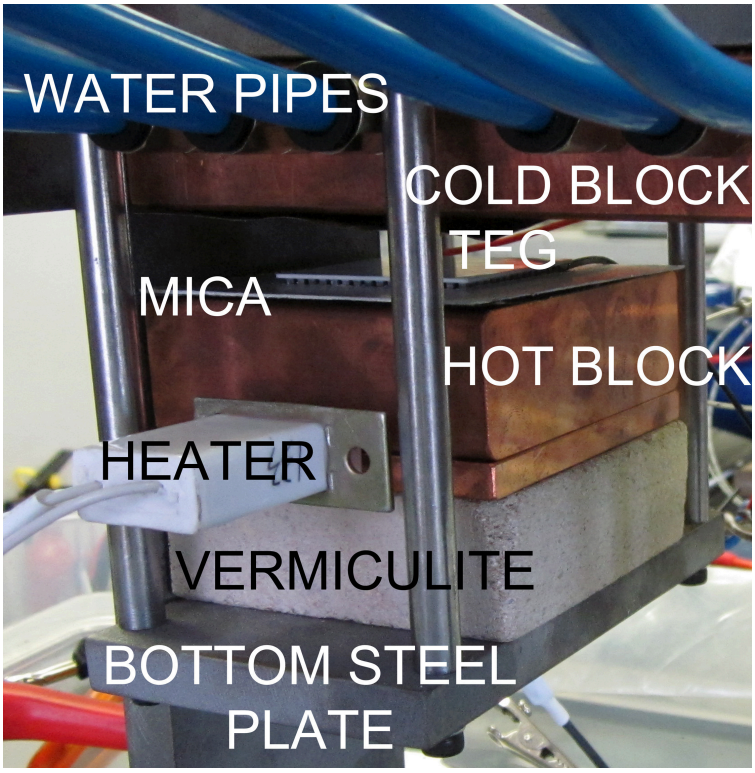

Figure 4.9: Picture of one of the four hot-side mechanical fixtures.

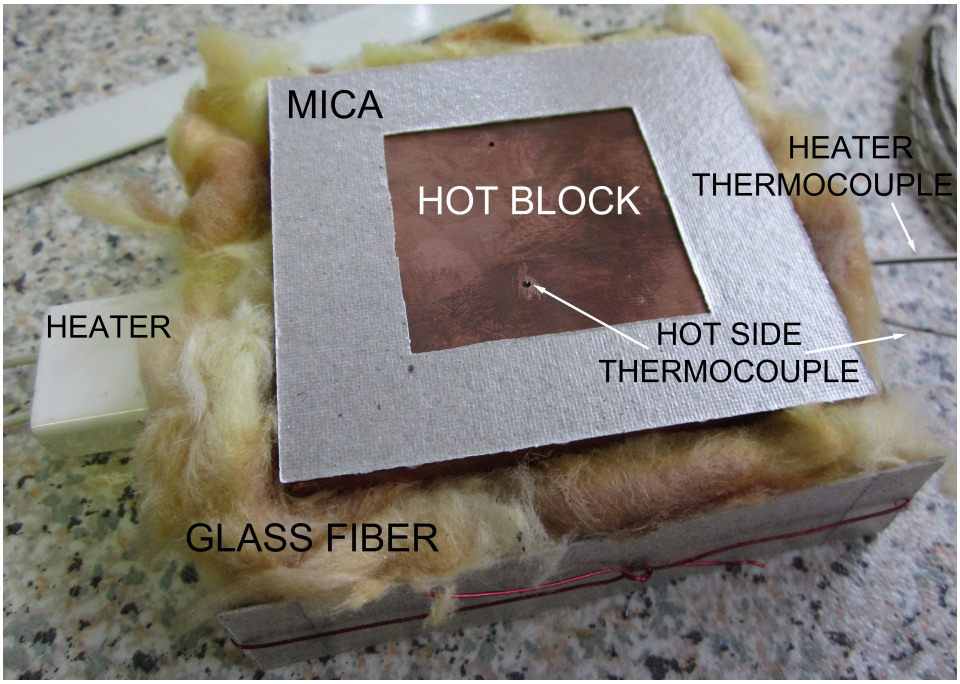

Figure 4.10: Picture of the insulating box for the hot block with mica anti-radiation screen.

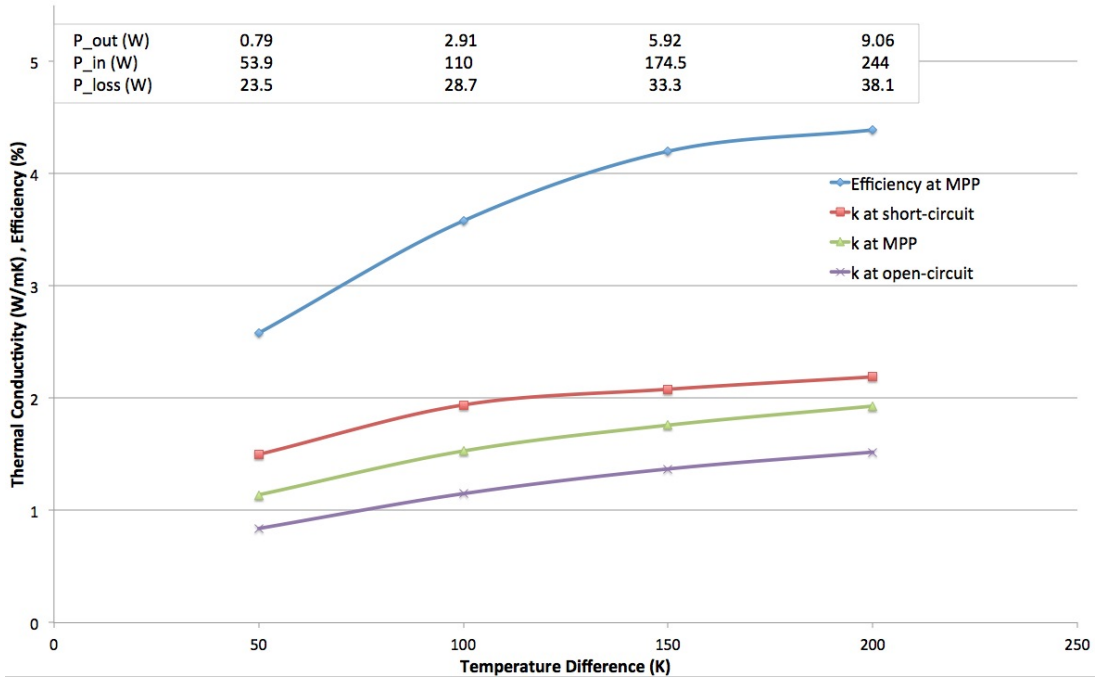

Figure 4.11: Efficiency at MPP and thermal conductivity (at open-circuit, MPP, and short-circuit) versus temperature difference. The table on the top lists the values of P_{out}, P_{in} and P_{loss} used to calculate η from Eq. 4.2.

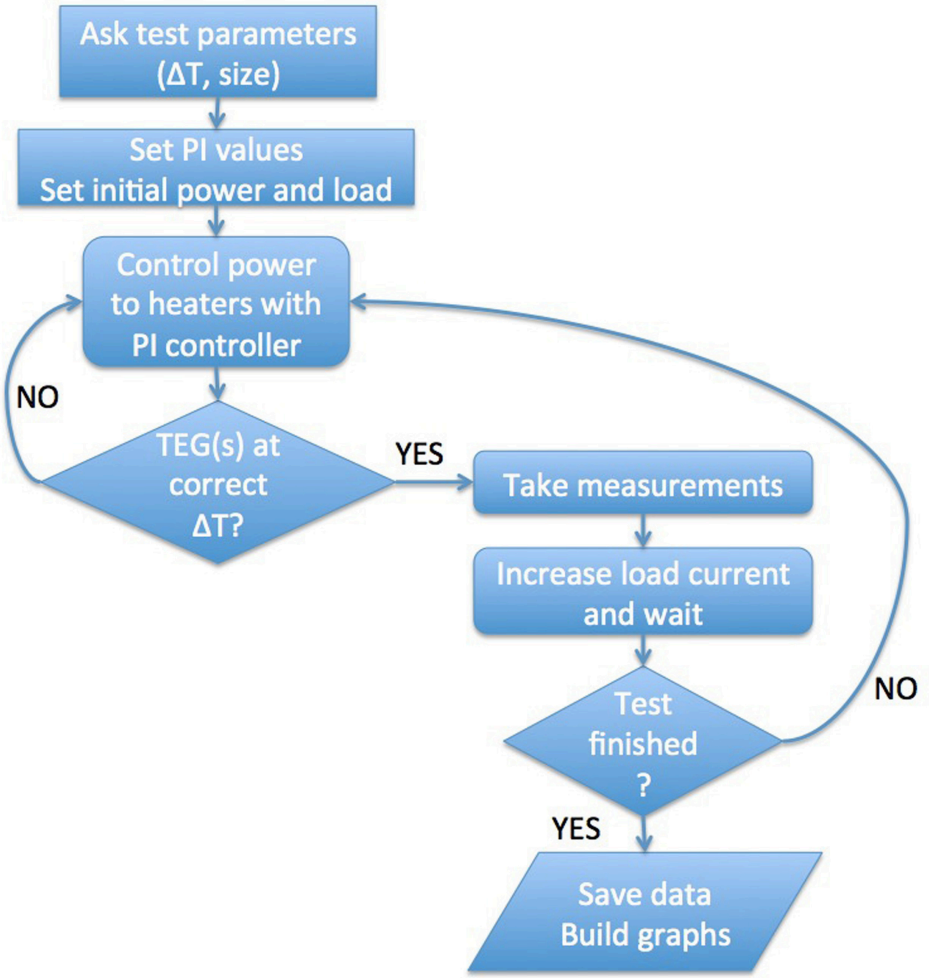

Figure 4.12: Flow diagram of the Agilent VEE Pro control program.

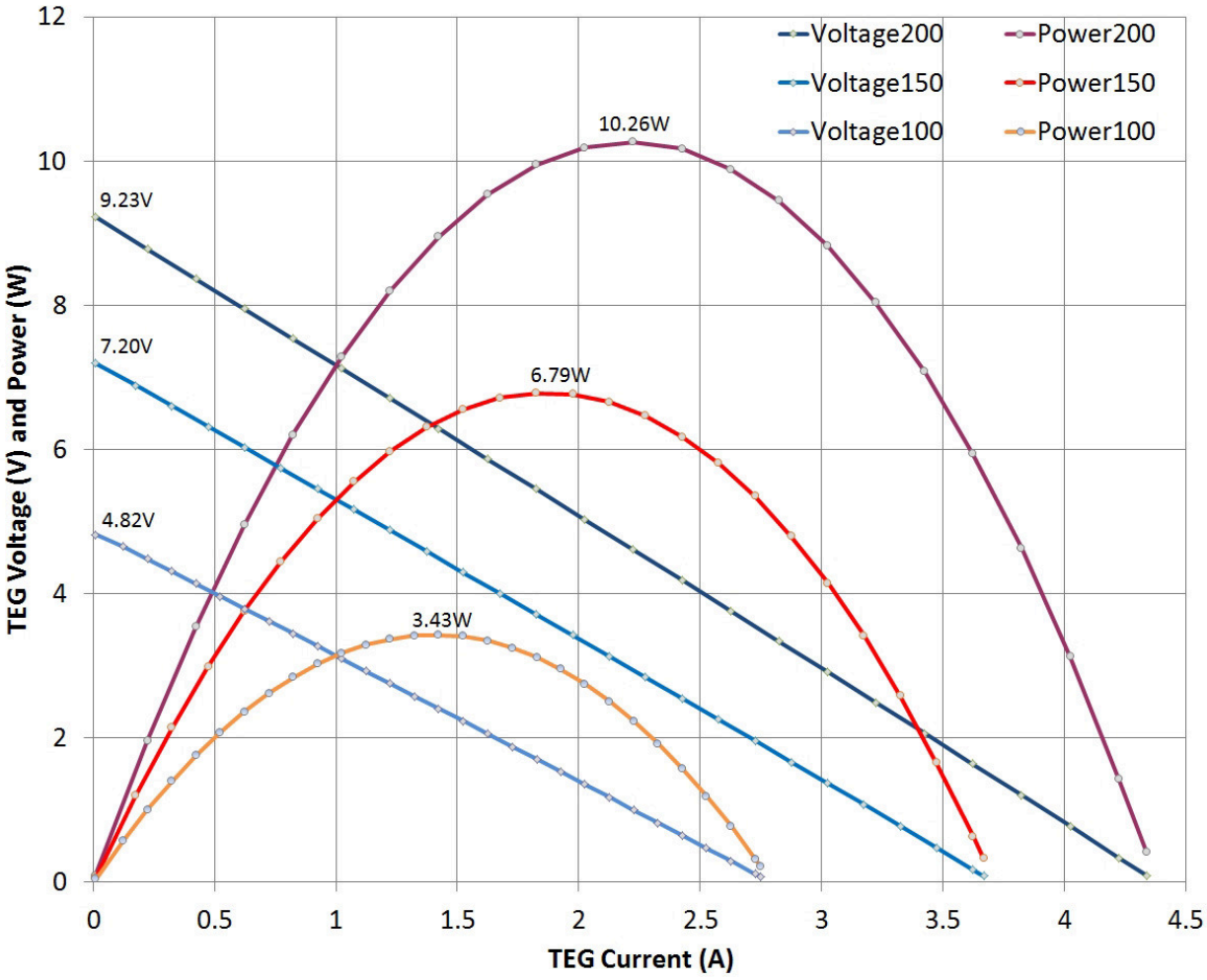

Figure 4.13: Experimental electrical characterisation for the TEG module # 2. The grey dots in the curves represent experimental data points. $\Delta T = 100°C, 150°C, 200°C$, clamped at $2kN/1.25MPa$.

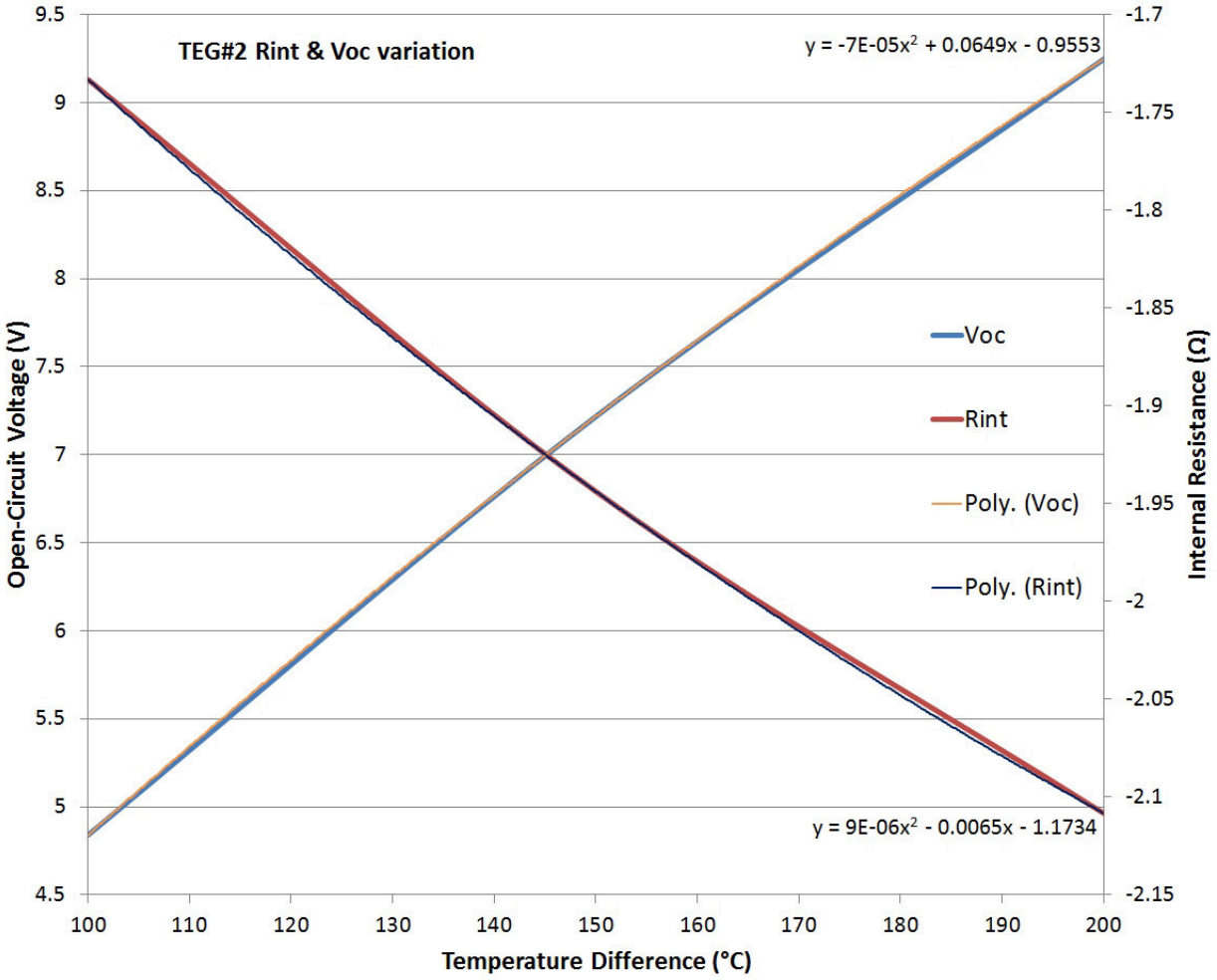

Figure 4.14: Variation of the open-circuit voltage and the internal resistance of TEG# 2 with the temperature difference. 2^{nd}-order polynomial fitting has been used to express the variation mathematically.

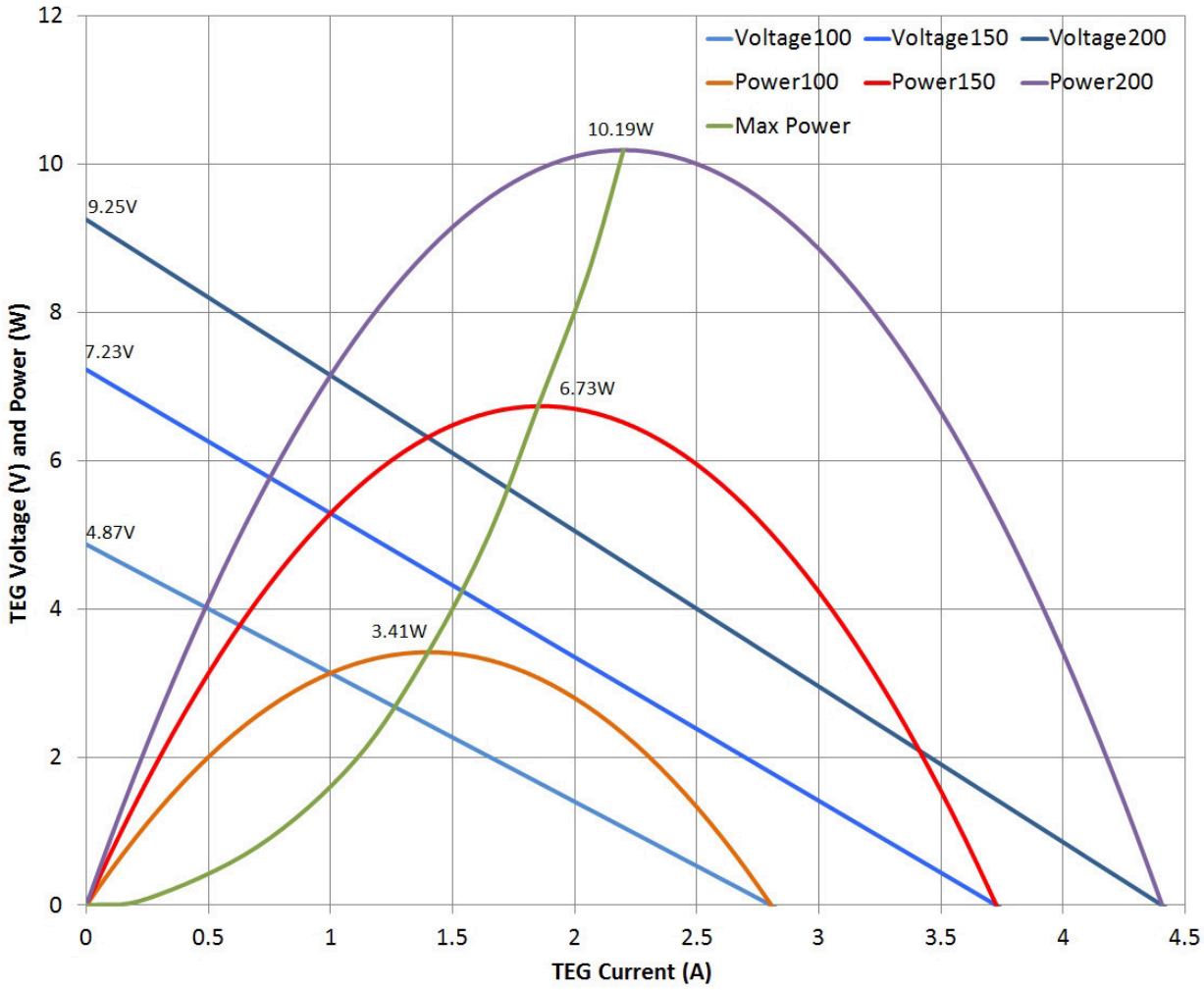

Figure 4.15: 'Mathematical' electrical characterisation for the TEG module # 2.

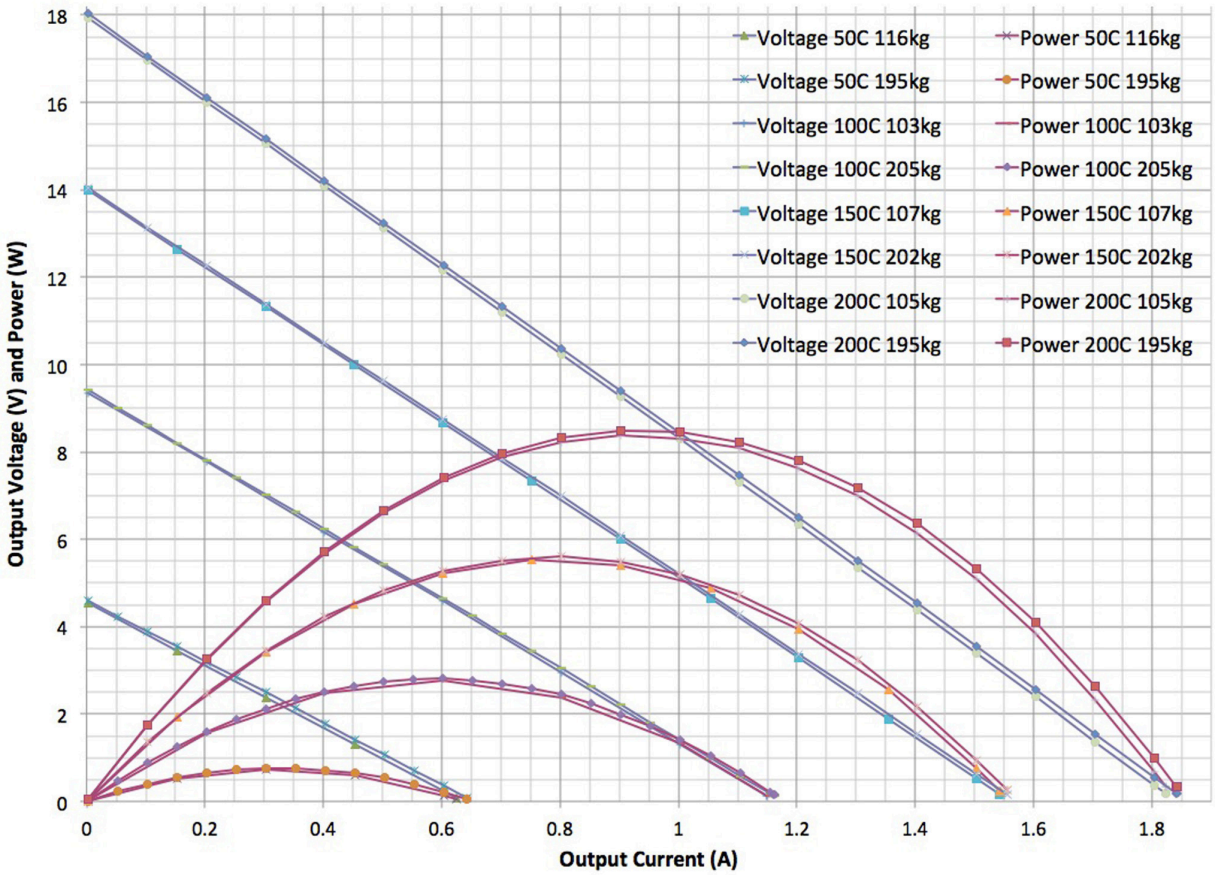

Figure 4.16: Experimental electrical characterisation for the TEG device GM250-241-10-12 at four temperature differences: $50°C, 100°C, 150°C, 200°C$, each one clamped at $1kN/600kPa$ and $2kN/1200kPa$.

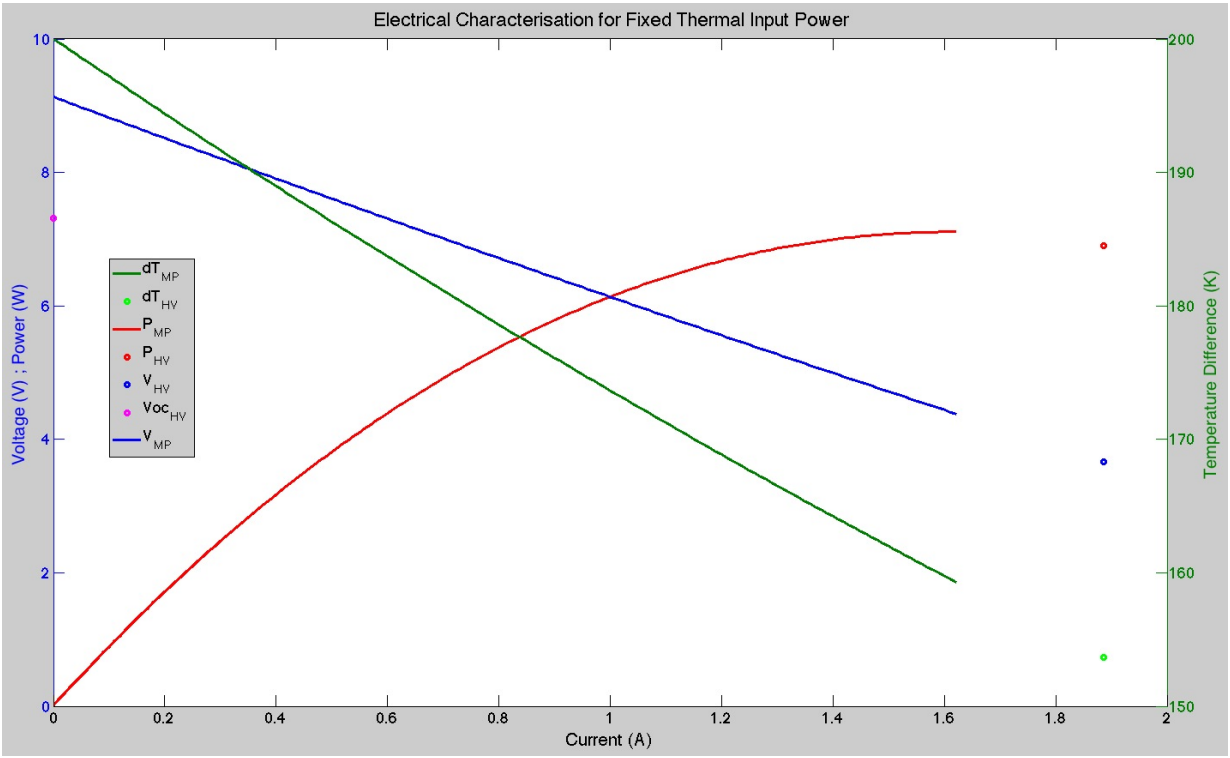

Figure 4.17: Electrical characterisation of a TEG with fixed thermal power input computed by *Matlab*. V-I line in blue, P-I curve in red, ΔT-I line in green; the point of maximum power production is found at $I_{MP} = 1.61A$. The red, blue and green circles represent the power, voltage and temperature difference, respectively, resulting by continuously adjusting the load voltage to half of the open-circuit voltage (reported in the magenta circle for reference ($7.31V$), for $\Delta T = 153.6°\text{C}$.

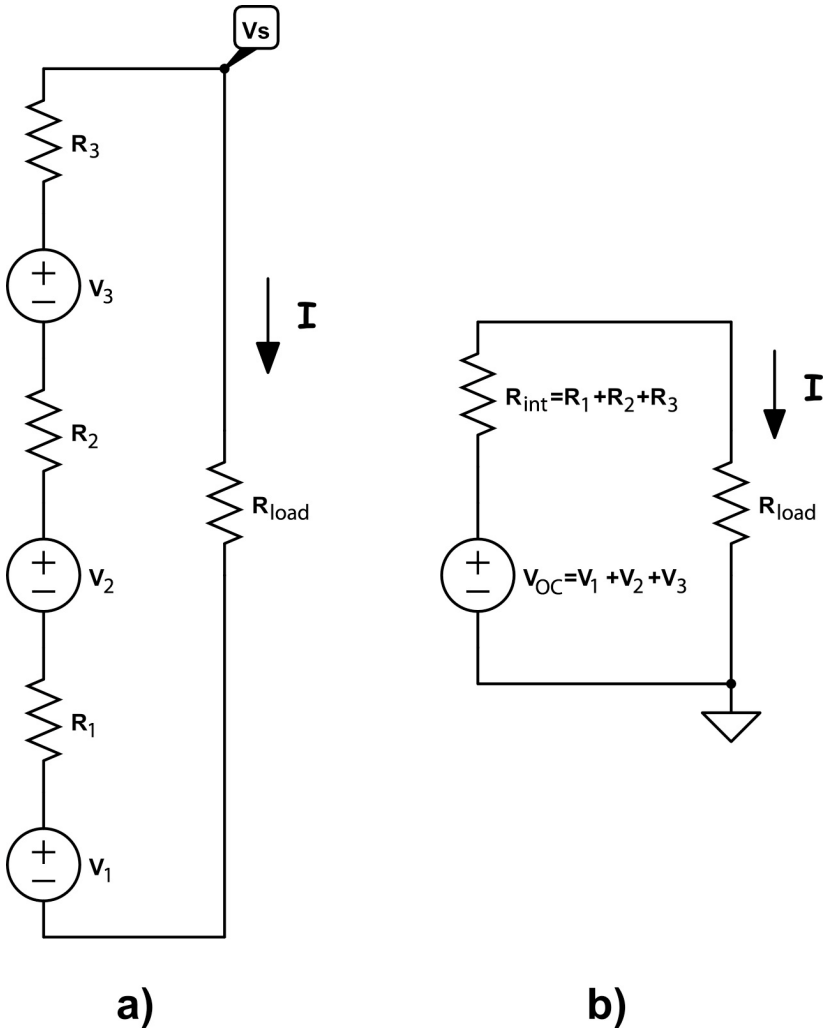

Figure 4.18: Electrical schematic of an array of three TEG modules electrically connected in series (left) and its equivalent representation (right).

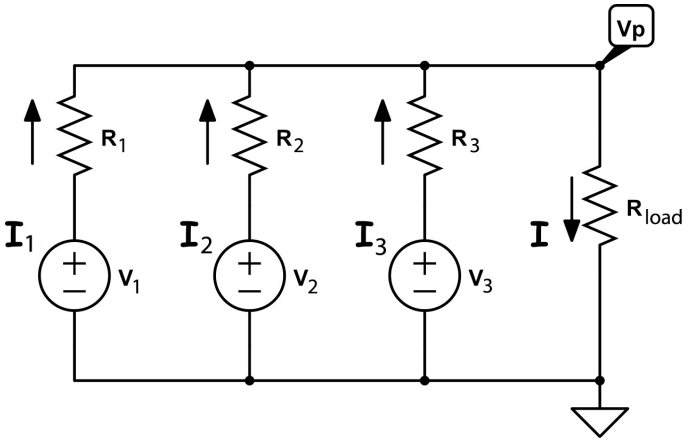

Figure 4.19: Electrical schematic of an array of three TEG modules electrically connected in parallel.

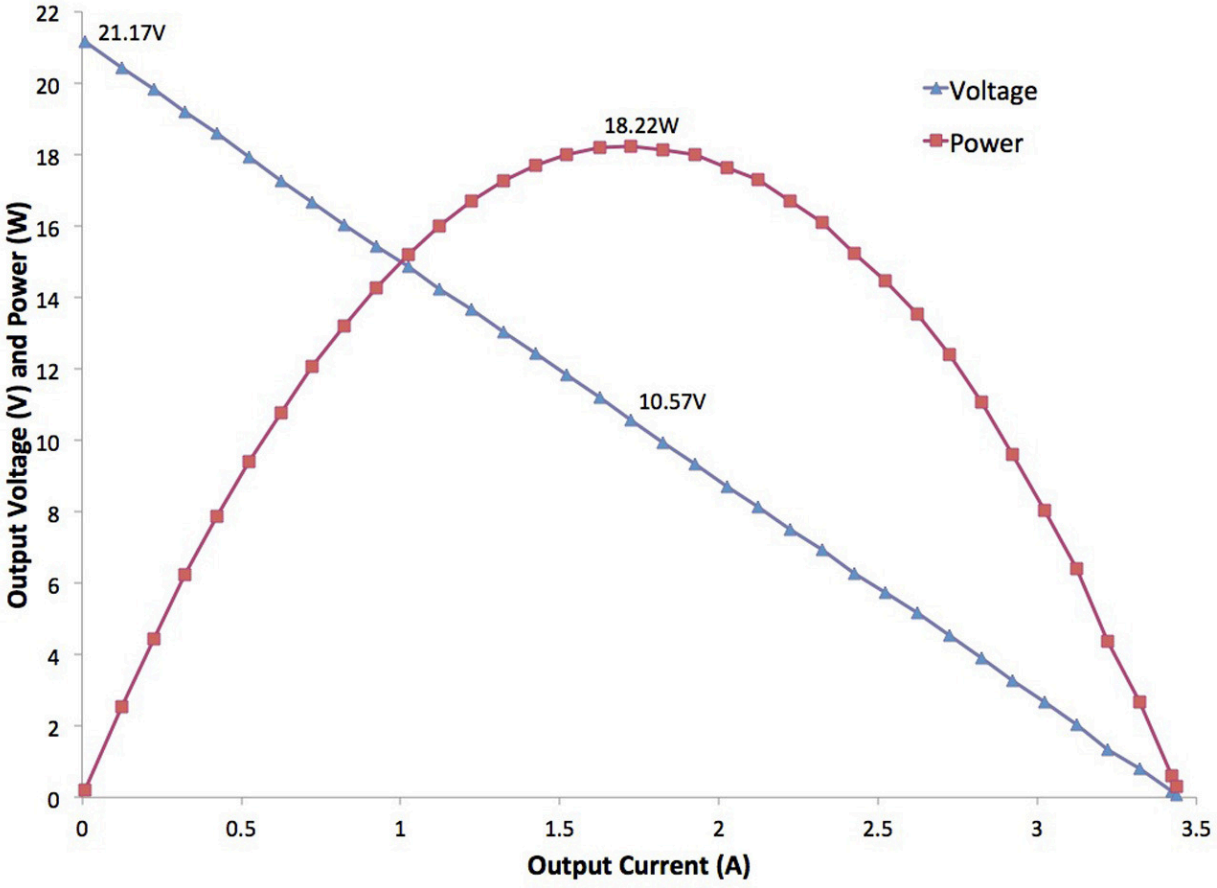

Figure 4.20: Electrical characterisation of an array with three TEGs in series under mismatched temperature difference: $\Delta T_{TEG\#1} = 100°C; \Delta T_{TEG\#2} = 150°C; \Delta T_{TEG\#3} = 200°C$.

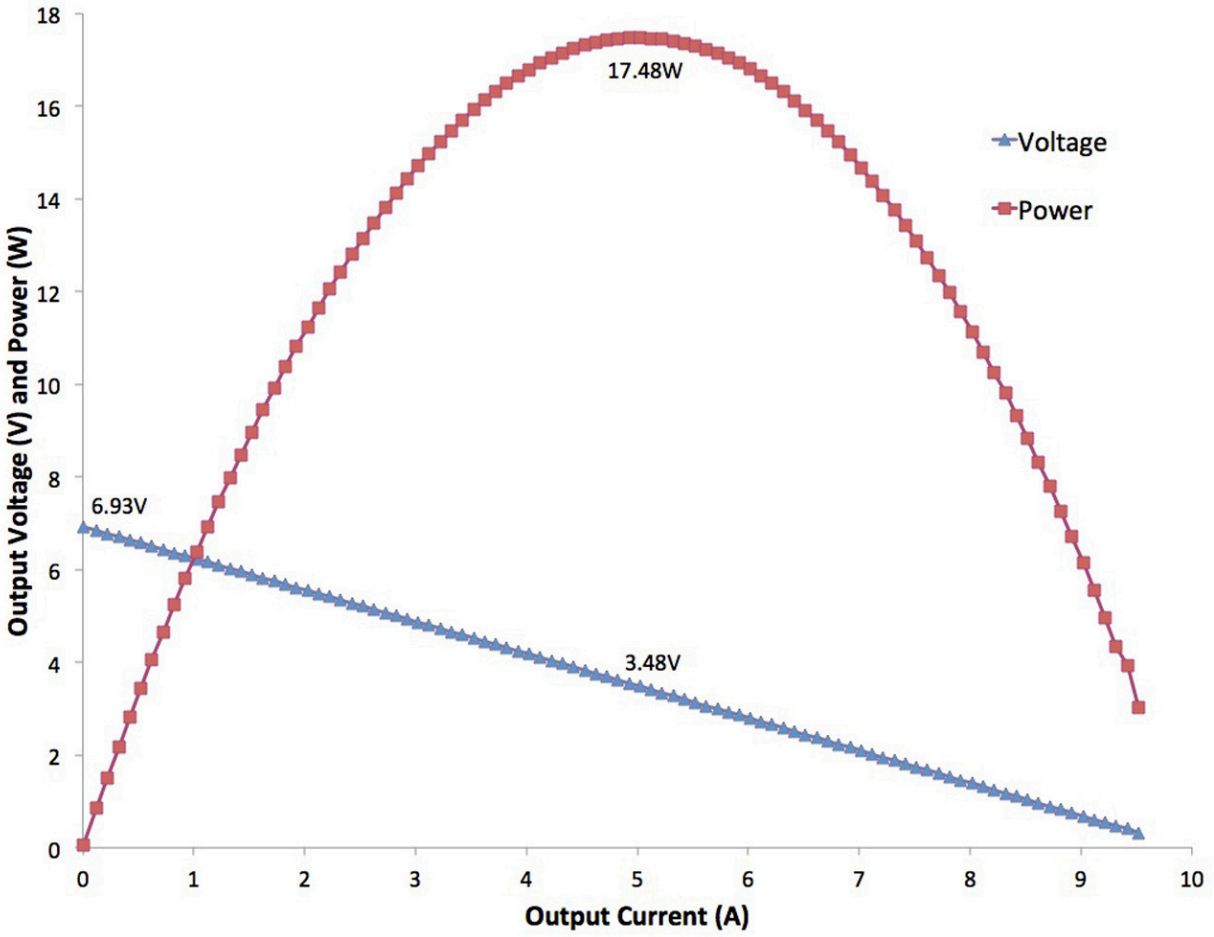

Figure 4.21: Electrical characterisation of an array with three TEGs in parallel under mismatched temperature difference: $\Delta T_{TEG\#1} = 100°C; \Delta T_{TEG\#2} = 150°C; \Delta T_{TEG\#3} = 200°C$.

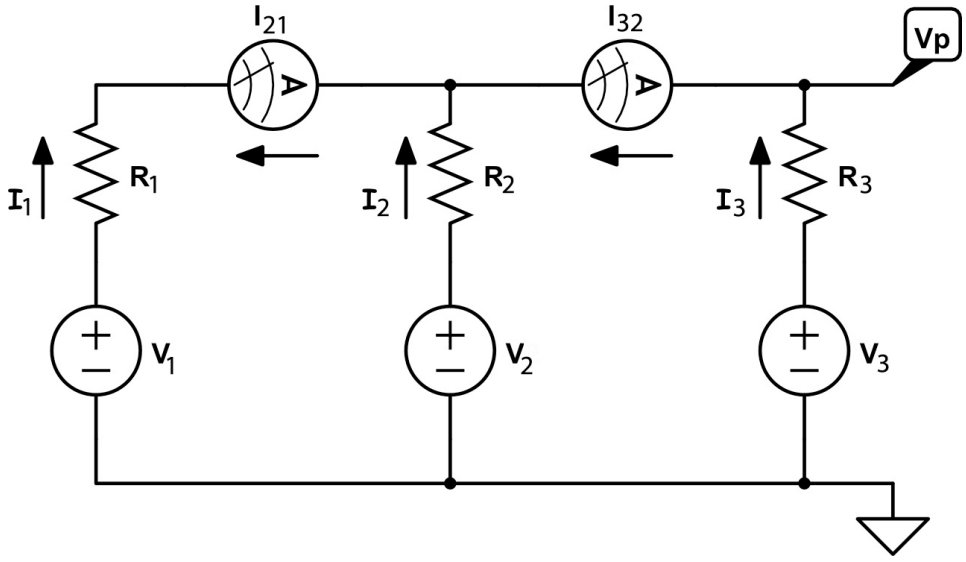

Figure 4.22: Equivalent circuit diagram of the experimental setup used to measure the instantaneous current flowing after the sudden parallel connection of mismatched thermoelectric devices.

Chapter 5

Simulation of Thermoelectric Systems

It is important to understand the behaviour of thermoelectric devices during thermal and electrical transients in order to properly simulate and design complex and dynamic thermoelectric systems, which frequently undergo thermal transients.
This chapter proposes a model for simulating dynamic thermoelectric systems. The first section provides the transient solution to the one-dimensional heat conduction equation with internal heat generation and dynamic exchanges of heat through the hot and cold sides. The analytical solution proposed is then included in a computer-aided model in which the thermal and electrical dynamics of a real thermoelectric power generating system are accurately simulated. This model takes into account the dynamic relations between the several thermal masses and the most important thermoelectric phenomena occurring in a generalised thermoelectric system. Simulation results are finally compared to experimental data obtained from a real thermoelectric system.

5.1 Heat equation with internal Joule heating

The contents included in this section are published in [J6] as a result of a joint work with Dr. Steven Roper of the School of Mathemathics and Statistics of the University of Glasgow.

Eq. 3.16 accurately describes the balance of powers in a system under steady-state. However, it is not usable in a time-varying environment because it does not take temporal variations into consideration and because the boundary conditions used to solve Eq. 3.16 assume that the temperatures at the hot and cold sides are constant.

Fig. 5.1 shows the schematic diagram of the physical system considered in this study. In thermoelectric devices the Peltier heating or cooling acts only at junctions where there is a connection with

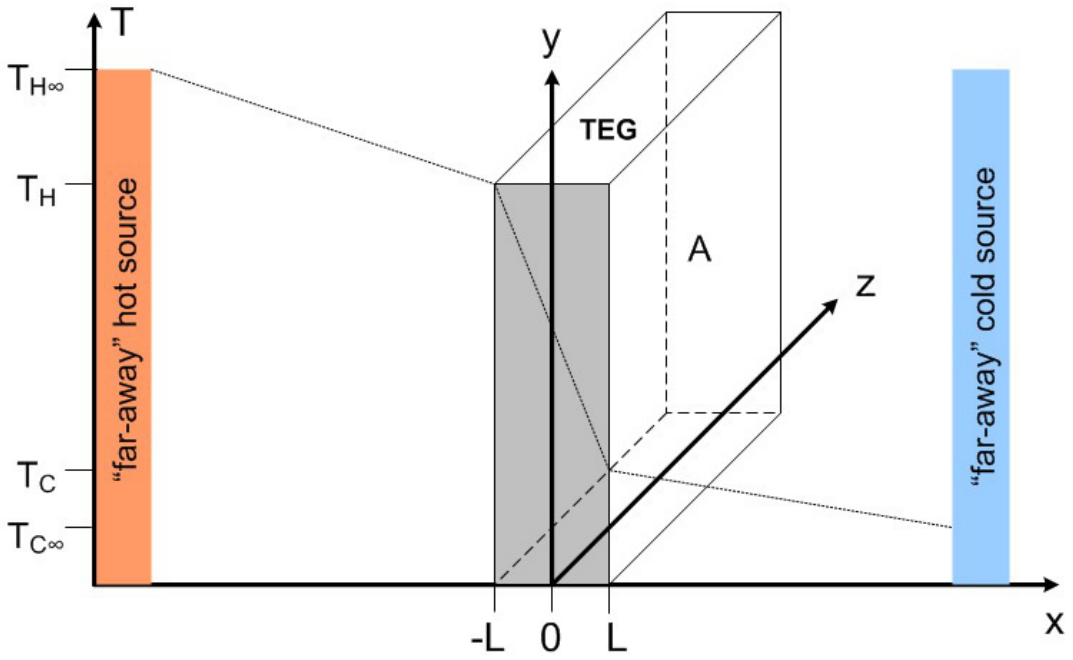

Figure 5.1: Schematic diagram of the physical system considered for the solution of the heat equation.

metal, therefore, assuming there are no temperature gradients and losses in the y and z directions, the heat propagation and generation inside the device can be modeled through the one-dimensional (1-D) unsteady heat conduction equation with constant thermal conductivity and internal heat generation, expressed as

$$\frac{\partial^2 T}{\partial x^2} + \frac{\dot{g}}{k} = \frac{1}{\epsilon}\frac{\partial T}{\partial t} \tag{5.1}$$

where T is the temperature in Kelvin degrees function of both the space x and the time t, $\dot{g}$ is the rate of heat energy generation per unit volume $[W/m^3]$, k is the thermal conductivity coefficient $[W/mK]$, and ϵ is the thermal diffusivity coefficient defined as

$$\epsilon = \frac{heat\ conducted}{heat\ stored} = \frac{k}{\rho C_m} = \left[\frac{m^2}{s}\right] \tag{5.2}$$

where ρC_m is the heat capacity per unit volume $[J/m^3K]$.

The objective is to study thermoelectric devices under conditions where both time and temperatures are varying, hence the temperatures at the hot and cold sides are not considered constant. They are on the contrary considered connected to "far-away" constant temperatures, thus allowing their temperatures to vary depending on the rate of heat flow through them and the generation of heat inside the thermoelectric device.

5.1.1 Description of the problem

To simplify the symmetry of the problem, consider a thermoelectric module of thickness $2L$ and area A, positioned on the x-axis in such a way that the hot side is at $x = -L$ and the cold side is at $x = L$. Hence, simplifying the notation, consider the following equation:

$$T_{xx} + \frac{\dot{g}}{k} = \frac{1}{\epsilon} T_t \tag{5.3}$$

on the interval [-L,L].
In order to be able to solve this partial differential equation it is necessary to have two boundary conditions and an initial state. The latter is assumed to be a linear distribution of temperature throughout the whole module, starting from the initial hot temperature T_{Hi} at $x = -L$, to the initial cold temperature T_{Ci} at $x = L$; referring to Fig. 5.1, T_{Hi} is the value of T_H and T_{Ci} the value of T_C, at $t = 0$. Hence the initial condition is

$$T(x, 0) = T_0(x) = \frac{T_{Ci} - T_{Hi}}{2L} x + \frac{T_{Ci} + T_{Hi}}{2} \tag{5.4}$$

The boundary conditions are those appropriate to the Newton's Law of Cooling, stating that the heat flux (per unit area) out of a boundary with normal $\mathbf{n}$ is $\mathbf{q} = -k\mathbf{n} \cdot \nabla T$, so that the boundary conditions for this problem are written as

$$T_x = \beta_H (T - T_{H\infty}), \quad \text{at } x = -L \tag{5.5a}$$

$$T_x = -\beta_C (T - T_{C\infty}), \quad \text{at } x = L \tag{5.5b}$$

where $T_{H\infty}$ and $T_{C\infty}$ are the temperatures "far away" from the hot and cold sides of the TEG.
Fig. 5.1 illustrates the physical system.

5.1.2 Scaling

It is convenient to appropriately scale the problem in order to identify the important parameter combinations:

$$\begin{aligned} x = L\xi \quad &; \quad t = \frac{L^2}{\epsilon}\tau \\ T = \Delta T \theta \; &+ \; \frac{T_{H\infty} + T_{C\infty}}{2} \\ \beta_{H,C} = \frac{\beta_{h,c}}{L} \quad &; \quad \gamma = \frac{\dot{g} L^2}{k \Delta T} \end{aligned} \tag{5.6}$$

where $\Delta T = \dfrac{T_{H\infty} - T_{C\infty}}{2}$. The parameter γ represents how much heat is internally generated by Joule heating compared to the heat flux through the device for conduction, and this is due to the temperature gradient across the device.
After this scaling the problem in Eq. 5.3 becomes

$$\theta_{\xi\xi} + \gamma = \theta_\tau \tag{5.7}$$

and the boundary conditions in Eq. 5.5 become

$$\theta_\xi = \beta_h(\theta - 1), \qquad \text{at} \quad \xi = -1 \tag{5.8a}$$
$$\theta_\xi = -\beta_c(\theta + 1), \qquad \text{at} \quad \xi = 1 \tag{5.8b}$$

Finally, the initial state in Eq. 5.4 becomes

$$\theta_0(\xi) = \frac{(T_{Ci} - T_{Hi})\xi - (T_{H\infty} + T_{C\infty} - T_{Hi} - T_{Ci})}{T_{H\infty} - T_{C\infty}} \tag{5.9}$$

The solution of this problem will be the sum of a steady-state solution and a transient solution, as described in the next two sub-sections. The final solution for θ can then be written as

$$\theta(\xi, \tau) = \theta_{ss}(\xi) + \hat{\theta}_t(\xi, \tau) \tag{5.10}$$

where θ_{ss} is the steady-state profile and $\hat{\theta}_t$ is the transient evolution.

5.1.3 Steady-state solution

We wish to find the steady-state part of the solution in Eq. 5.10. If $t \to \infty$ then $\partial/\partial t \to 0$, that is $\theta_\tau = 0$. Hence the Poisson's equation $\theta_{\xi\xi} + \gamma = 0$, which leads to

$$\theta_{ss}(\xi) = A + B\xi - \frac{\gamma}{2}\xi^2 \tag{5.11}$$

where A and B must be chosen to satisfy the boundary conditions, namely:

$$B + \gamma = \beta_h\left(A - B - \frac{\gamma}{2} - 1\right) \tag{5.12a}$$
$$B - \gamma = -\beta_c\left(A + B - \frac{\gamma}{2} + 1\right) \tag{5.12b}$$

leading to

$$A = \frac{\gamma\left(2 + \frac{3}{2}\beta_h + \frac{3}{2}\beta_c + \beta_c\beta_h\right) + \beta_h - \beta_c}{\beta_c + \beta_h + 2\beta_c\beta_h} \tag{5.13a}$$

$$B = \frac{\gamma\left(\beta_h - \beta_c\right) - 2\beta_c\beta_h}{\beta_c + \beta_h + 2\beta_c\beta_h} \tag{5.13b}$$

5.1.4 Transient solution

The transient part of Eq. 5.10, $\hat{\theta}_t$, is

$$\hat{\theta}_{\xi\xi} = \hat{\theta}_\tau \tag{5.14}$$

with boundary conditions

$$\hat{\theta}_\xi - \beta_h\hat{\theta} = 0 \quad at \quad \xi = -1 \tag{5.15a}$$

$$\hat{\theta}_\xi + \beta_c\hat{\theta} = 0 \quad at \quad \xi = 1 \tag{5.15b}$$

Eq. 5.14 is the heat equation with homogeneous boundary conditions (Eq. 5.15); as such we search for separable solutions and using the transform methods (Fourier transform on finite domain gives Fourier series) we arrive at the following expression for $\hat{\theta}_t$:

$$\hat{\theta}_t(\xi, \tau) = \sum_{allowable\ k} \left(A_k \cos k\xi + B_k \sin k\xi\right) e^{-k^2\tau} \tag{5.16}$$

where the coefficients A_k and B_k and the allowable wave-numbers k are determined by the boundary conditions and the initial condition. First we consider the allowable k. The boundary conditions of Eq. 5.15 give

$$kA_k \sin k + kB_k \cos k - \beta_h\left(A_k \cos k - B_k \sin k\right) = 0 \tag{5.17a}$$

$$-kA_k \sin k + kB_k \cos k + \beta_c\left(A_k \cos k + B_k \sin k\right) = 0 \tag{5.17b}$$

which can be written in matrix form as

$$\begin{bmatrix} \beta_c \cos k - k \sin k & \beta_c \sin k + k \cos k \\ -\beta_h \cos k + k \sin k & \beta_h \sin k + k \cos k \end{bmatrix} \begin{bmatrix} A_k \\ B_k \end{bmatrix} = \begin{bmatrix} 0 \\ 0 \end{bmatrix}$$

whose determinant is

$$|\det| = (\beta_c\beta_h - k^2)\sin 2k + k(\beta_c + \beta_h)\cos 2k \tag{5.18}$$

which has non-trivial solutions ($|det| = 0$) for values of k such that

$$\tan 2k = \frac{k\left(\beta_c + \beta_h\right)}{k^2 - \beta_c\beta_h} \tag{5.19}$$

To find a corresponding eigenfunction consider Eq. 5.17a in the form

$$A_k \left(k \sin k - \beta_h \cos k\right) + B_k \left(k \cos k + \beta_h \sin k\right) = 0 \tag{5.20}$$

A corresponding eigenfunction is

$$\psi_k(\xi) = -\beta_c \sin k \left(\xi - 1\right) + k \cos k \left(\xi - 1\right) \tag{5.21}$$

Enumerating the solutions of Eq. 5.19 as k_n, with $0 < k_1 < \ldots < k_n < \ldots$ for $n \in \mathbb{N}$, it can be noted that $\tan 2k_n \cong 0$ for large values of k_n. This occurs when $2k_n = m\pi$, with m integer, that is when $k_n = \dfrac{m\pi}{2}$.
The solution for $\hat{\theta}_t$ can then be written as

$$\hat{\theta}_t(\xi, \tau) = \sum_n A'_n \psi_{k_n} e^{-k_n^2 \tau} \tag{5.22}$$

where the coefficients A'_n are determined by the initial conditions $\theta_0(\xi)$ of Eq. 5.9, as described in the following section.

5.1.5 Transforming the initial condition

The operator defined by $L_k\hat{\theta} = \hat{\theta}_{\xi\xi} + k^2\hat{\theta} = 0$ with the boundary conditions of Eq. 5.15 is self-adjoint.
At this point it is convenient to define some notation, let

$$\psi_k(x) = -\beta_c \sin k(\xi - 1) + k \cos k(\xi - 1) \quad \text{for } k \neq 0$$

and

$$\psi_l^*(x) = \beta_h \sin l(\xi + 1) + l \cos l(\xi + 1)$$

then for $k \neq l$ and both k and l satisfying Eq. 5.22:

$$\int_{-L}^{L} \psi_l^*(x)\psi_k(x)dx = 0 \tag{5.23}$$

and for $k = l \neq 0$:

$$\begin{aligned} &\int_{-1}^{1} \psi_k^*(\xi)\psi_k(\xi)\, d\xi = \\ &= \cos 2k[k^2 - \beta_c\beta_h] + \sin 2k \left[\frac{k}{2} + \frac{\beta_c\beta_h}{2k} + \beta_c k + \beta_h k\right] \end{aligned} \tag{5.24}$$

Suppose the initial condition is $\theta_0(\xi)$, then at $\tau = 0$, $\hat{\theta}_t(\xi, 0) = \theta_0(\xi) - \theta_{ss}(\xi)$.
Defining

$$A'_n = \frac{\int_{-1}^{1} \psi^*_{k_n}(\xi) \left(\theta_0(\xi) - \theta_{ss}(\xi)\right) d\xi}{\int_{-1}^{1} \psi^*_{k_n}(\xi)\psi_{k_n}(\xi) d\xi} \tag{5.25}$$

Then the solution for θ is

$$\theta(\xi, \tau) = \theta_{ss}(\xi) + \sum_n A'_n \psi_{k_n}(\xi) e^{-k_n^2 \tau} \tag{5.26}$$

The final solution in Eq. 5.26 obviously needs to be scaled back to temperature using the reverse scaling of Eq. 5.6.

5.1.6 The boundary conditions

The boundary conditions used to solve the heat equation come from the Newton's Law of Cooling and they are written in the form of Eq. 5.5. It is now important to define the coefficient β $[m^{-1}]$ in physical terms.

Considering a body of volume B, with boundaries ∂B, the total energy in the body is

$$E = \int_B \rho C_m T \, dV \tag{5.27}$$

where ρC_m represents the heat storage capability of the body per unit volume $[J/m^3K]$.
From the heat flux $\mathbf{q} = -\mathbf{k} \cdot \nabla T$ and the heat conduction equation $\dfrac{\partial T}{\partial t} = \dfrac{k}{\rho C_m} \nabla^2 T$ the rate of change of energy is

$$\begin{aligned} \frac{dE}{dt} &= \int_B \rho C_m \frac{\partial T}{\partial t} \, dV = \int_B k \nabla^2 T \, dV \\ &= \int_{\partial B} k \mathbf{n} \cdot \nabla T \, dS = -\int_{\partial B} k\beta (T - T_\infty) \, dS \\ &= -k\beta A (\bar{T} - T_\infty) \end{aligned} \tag{5.28}$$

where $\bar{T}$ is the average temperature over the surface ∂B, that is

$$\bar{T} = \frac{1}{A} \int_{\partial B} T \, dS \tag{5.29}$$

Noting the similarity between Eq. 5.28 and the heat convection equation in the form

$$\dot{q}_{conv} = -\frac{dE}{dt} = -hA(T - T_\infty) \tag{5.30}$$

where h is the heat convection coefficient $[W/m^2K]$, it is clear that

$$\beta = \frac{h}{k} = \left[\frac{1}{m}\right] \tag{5.31}$$

The boundary condition needs to assure continuity of temperature at the two sides of the TEGs. Therefore, depending on if the two sides are in thermal contact with a solid or with a liquid/gas, it will be necessary to substitute in Eq. 5.31 the appropriate values, where for a solid h is

$$h_{solid} = \frac{k_{solid}}{thickness} \tag{5.32}$$

It is preferable for clarity to re-write Eq. 5.31 as

$$\beta = \frac{h_{medium}}{k_{TEG}} = \left[\frac{1}{m}\right] \tag{5.33}$$

5.2 Simulation results in Matlab

The solution presented in Section 5.1 has two main benefits: 1) it allows dynamic exchange of heat power throughout the sides of the TEG and 2) it allows the simulation of transients in thermoelectric devices. The latter feature will be used in section 5.4. It is now interesting to compare the temperature distribution inside the TEG in steady-state provided by Eq. 3.16 (with constant temperature at the sides of the TEG) and by Eq. 5.11 (with dynamic exchange of heat through the TEG's sides).
The solution calculated in the previous section is coded in Matlab, because of the need for a numerical calculator to solve the Fourier series of Eq. 5.16. Matlab's *symbolic* toolbox has been used.
First, an interval bisection algorithm is used to find the roots of Eq. 5.19, setting a limit to the maximum value of k. Then for every k the correspondent coefficient A'_n is computed using Eq. 5.25 and finally the solution for θ is computed using Eq. 5.26 and scaled back to temperature.

Fig. 5.2 illustrates the system considered for the simulations in this section. It is composed of a TEG sandwiched between a heater and a water-cooling block through two Aluminum heat-spreading plates of thickness $L_C = 1\,cm$ and $L_H = 4\,cm$, therefore the h coefficients of Eq. 5.32 are:

$$\begin{aligned} h_C = \frac{k_{Al}}{L_C} = \frac{237\,W/mk}{0.01\,m} &= 23700\,W/m^2K \\ h_H &= 5925 W/m^2K \end{aligned}$$

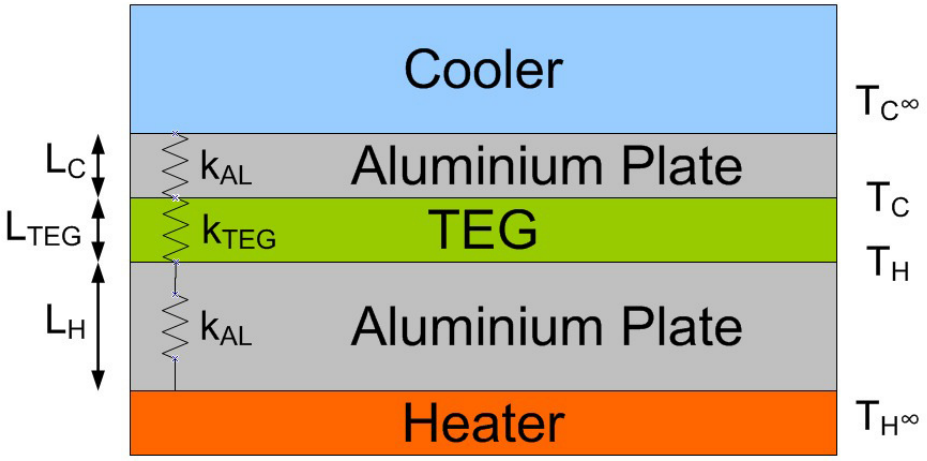

Figure 5.2: The system used for the simulations of temperature distribution and variation in a TEG (not to physical scale).

The parameters used for the TEG are:

$$\begin{aligned} \text{Area: } A &= 40x40\,mm^2 = 0.04^2\,m^2 \\ \text{Thickness: } L_{TEG} &= 0.004\,m \\ \text{Thermal Diffusivity: } \epsilon &= 10^{-7}\,m^2/s\,^1 \\ \text{thermal Conductivity: } k_{TEG} &= 1.4\,W/mK \end{aligned} \tag{5.35a}$$

R_{int} and V_{OC} are calculated as a function of ΔT:

$$\begin{aligned} R_{int} &= 0.00569\Delta T + 1.466 \\ V_{OC} &= 0.042\Delta T + 0.00263\left(1 - e^{-\frac{\Delta T - 50}{50}}\right)\Delta T \end{aligned}$$

The Peltier effect brings additional power from the hot to the cold side, thus increasing the overall thermal conductivity. During "normal" TEG use the Peltier effect is usually greater than the Joule heating effect, therefore it is important to take it into account in the Matlab model. In order to do this, the power from the heater to the TEG through the Aluminium block can be considered as the sum of the Peltier power and the power from $T_{H\infty}$ to T_H in the heat equation. In this way the solution is computed in a loop. At every iteration the heat equation is calculated and the real h

[1]The thermal diffusivity of Bi_2Te_3 is in the order of 10^{-6} [110], but the real one is difficult to estimate because of the ceramic layer included in the TEG for isolation and all the interfaces, which slow down the thermal wave, therefore a value of 10^{-7} has been used.

coefficient of Eq. 5.3 (called h_{Hreal}) is modified depending on the Peltier power and called h_{Hmod}:

$$h_{Hmod} = h_{Hreal} - \frac{\alpha T_H I}{A(T_{H\infty} - T_H)} \tag{5.37}$$

Similar considerations can be applied to the cold side:

$$h_{Cmod} = h_{Creal} - \frac{\alpha T_C I}{A(T_C - T_{C\infty})} \tag{5.38}$$

Therefore at the end of every iteration β_h and β_c are modified accordingly so that the new steady-state and transient values will account for the Peltier term. The initial condition remains the same.

If the temperatures at the sides were to be assumed constant as in Eq. 3.16, the effect of Joule heating would be visible only on the points inside the TEG. Fig. 5.3 shows such a case in a simulation in which the load current is changed. As T_H and T_C are constant, there is no difference in heat transfer through the TEG unless k_{TEG} is modified to account for the change in internal Joule heating.

Conversely, the steady state solution of Eq. 5.11 varies because when a load variation takes place T_H and T_C can change even if $T_{H\infty}$ and $T_{C\infty}$ remain constant. In this way it is possible to understand the effect that different loads have on the overall conduction coefficient, *i.e.* to understand how the temperature gradient across the TEG will change. This can be seen in Fig. 5.4, and it demonstrates that the overall thermal conductivity of the TEG changes.

The effect is more relevant at the hot side because T_H is more distant from $T_{H\infty}$ than T_C is from $T_{C\infty}$. From $0\,A$ to $4\,A$, T_H decreases because the Peltier effect is more relevant than the Joule heating, but when the current is $8\,A$ the Joule heating makes T_H increase even more than $T_{H\infty}$; this would suggest a thermal operating point of great efficiency for TEGs, but unfortunately the TEG, working close to I_{SC}, would be producing low voltage and consequently low electrical power output (in other words, to the right of the MPP of the graph shown in Figure 3.4). It can clearly be understood that the Peltier effect decreases T_H and increases T_C, while the Joule heating increases both T_H and T_C and the temperatures of the other points inside the TEG; this effect depends on the square of the load current, so it is particularly relevant when considering thermoelectric heat pumps.

The solution described by Eq. 5.26 can thus be included into a model which also takes into account the thermal masses of the system and the thermal and electrical power flow, thus enabling the possibility of simulating both transients and the final operating point of a complex thermoelectric system. The solution presented here describes the dynamic behaviour inside the thermoelectric device and it constitutes the starting point for creating a generic simulation model for TEGs which accurately predicts their physical behaviour.

5.3 Generic model of a thermoelectric system

The contents included in this section and the following sections in this chapter are published in [J4].

Generally speaking, a thermoelectric system is composed of several thermal masses which store and exchange heat through conduction and/or convection. Heat is partially converted to or from electricity inside the thermoelectric device and/or in other elements, *e.g.*, electrical heaters. It is very important to optimally design the thermal interconnection of the thermoelectric device with the rest of the system to assure optimal overall performance [107]. In order to aid thermoelectric system design, it is useful to develop a model that can be used to accurately simulate the electro-thermal coupled effects which take place during changes in the system operating conditions, *e.g.*, temperature (especially during start-up and shut-down), power or load changes. This would greatly assist in the actual engineering task: when designing a thermoelectric system it is difficult to predict the steady-state operating point due to the effects taking place internally to the thermoelectric device that cause the temperatures at the sides to change. The insertion of a TEG into a system in thermal equilibrium changes massively the initially-available hot and cold temperatures, depending on the load and on the capacity of the system to provide and remove "hot" and "cold" thermal energy, respectively.

Fig. 5.5 shows the architecture of a generic thermoelectric power generating system. The TEG is usually in contact with a thermal mass on both the hot and cold sides. Energy is provided to or removed from the thermal masses in the form of electrical or heat power, leading to changes in the thermal energy stored inside the thermal masses. Through conduction or convection part of this energy is transferred to and from the TEG module. The TEG is modelled considering the sides of the TEG separately from the inner part formed of the pellets. The Heat Equation (HE) deals with both the heat conduction and generation (Joule heating) inside the TEG. Additional heat is pumped at the sides where there is a junction of two dissimilar materials (Peltier effect).

Part of the energy flowing through the TEG is converted into electrical power and the process is closely related to the thermoelectric effects described by Eq.s 3.1 and 3.6.
Conduction and convection equations provide the rate of thermal energy flowing from one medium to the other with time. The thermal conduction equation (Fourier's law) is written in time-derivative form as:

$$\frac{dE_{cond}}{dt} = -\kappa A \frac{dT}{dx} \tag{5.39}$$

where $E_{cond}\,[J]$ is the thermal energy, $\kappa\,[W/mK]$ is the thermal conduction coefficient, $A\,[m^2]$ is the surface of heat exchange and $x\,[m]$ is the direction of heat transfer, perpendicular to A. The heat convection equation is

$$\frac{dE_{conv}}{dt} = hA\Delta T(t) \tag{5.40}$$

where $h\,[W/m^2K]$ is the heat convection coefficient and $\Delta T(t) = T(t) - T_\infty$ is time-dependent.

Any lumped thermal mass experiences a change in temperature when receiving or losing thermal energy:

$$E_{therm} = mC\Delta T(t) \tag{5.41}$$

where $mC\,[J/K]$ is the heat capacity of the thermal mass, which defines its ability to retain heat energy.

As indicated in Fig. 5.5, $T_{\infty H}$ represents the temperature of the hot thermal mass and T_H is the temperature on the hot side of the TEG, while $T_{\infty C}$ and T_C are the temperatures of the cold thermal mass and TEG cold side, respectively.

5.4 Computer model

The solution to the Heat Equation (HE) presented in 5.1 was programmed in Matlab, therefore the Mathworks suite was chosen to develop the simulation program. The model includes several blocks and performs time-step simulations. Simulink is an excellent choice of environment for this task.
Section 5.4.2 presents the heat equation block, Section 5.4.3 deals with the thermal elements and Section 5.4.4 explains the electrical element of the system.

5.4.1 System architecture

Fig. 5.6 shows the architecture of the Simulink model developed and is referred to throughout the following discussion.
The HE computes the transient solution starting from an initial condition of T_C and T_H, and with constant values for $T_{\infty H}, T_{\infty C}$ and the load current I_{load}. It can provide the temperature distribution inside the thermoelectric device at any instant in time, even if for this model, at system level, only the temperatures at the hot and cold sides of the TEG module are of interest. The HE allows the side temperatures T_H and T_C to change depending on the temperatures $T_{\infty H}$ and $T_{\infty C}$ of the thermal masses in contact with the TEG through conduction or convection media. The temperature difference across these media changes dynamically, in accordance with the Newton's Law of Cooling, as described in Section 5.1.1.
In the solution of the HE the temperatures of the thermal masses $T_{\infty H,C}$ are considered constant; however, in a real system during a transient they vary depending on the energy added or removed by P_{in} and P_{out}. Similarly, the temperatures at the sides of the TEG are influenced also by the actual load current which in turn determines the value of the Peltier effect (see Eq. 3.6). This is why in

Fig. 5.6 the 'HE Block' is connected to both to the 'Electrical Block' and to the 'Thermal Block'. The thermal block requires α and I_{load} form the electrical block to deal with the Peltier effect. The transient evolution of the temperature difference across the TEG device and the system's dynamic exchange of heat due to P_{in} and P_{out} continuously influence the temperatures in the whole system. Hence, in order to couple the continuous-time transient solution provided by the HE to the temperatures' evolution in the remaining parts of the system (thermal masses, input/output thermal energy and electrical load), the model is designed in the discrete-time domain. Within each time step of duration $t_{step}\,[s]$ the HE computes the dynamics inside the TEG for a transient of duration t_{step}. The temperatures in the remaining parts of the system change as described by Equations 5.39, 5.40 and 5.41, in which the derivative term is substituted by slope terms. This direct examination in discrete terms aids the comprehension of the underlying physical effects taking place in the system.
To understand how the model is structured, consider two successive time steps, corresponding to two discrete iterations, called i and $i+1$. It must be noted that the calculations made during each iteration are computed directly using the equations provided in this chapter, without recourse to any empirical, trial-and-error or other iterative methods. During the iteration i the heat equation uses the electrical parameters and the heat masses' temperatures $T_{\infty H(i)}$ and $T_{\infty C(i)}$, considered constant during t_{step}, and the hot and cold side temperatures $T_{H(i)}$ and $T_{C(i)}$ as initial values; it computes the values of $T_{H(i+1)}$ and $T_{C(i+1)}$ corresponding to their evolution after the transient time t_{step} and outputs them through a memory block of duration t_{step}, so that they are actually available only at the start of iteration $i+1$. The HE block is described in Section 5.4.2. At iteration i the model also updates the temperatures of the thermal masses depending on the quantity of heat energy provided by P_{in} and P_{out} during t_{step}, so that they are ready for iteration $i+1$. The equations used to update these temperatures are described in the Section 5.4.3.

5.4.2 The TEG heat equation block

The solution to the HE provided in 5.1 treats the TEG device as a whole block, *i.e.* it does not deal with the different materials (ceramic, semiconductor, solder) separately; it also does not divide the semiconductor materials into single pellets or thermocouples. This is by design because the parameters for the model are obtained only from the physical dimensions of the module and from its direct use in the system, *i.e.* by representing a real system.

The HE code is programmed into a Matlab embedded equation block. The input variables to the block are:

- TEG geometrical parameters: surface A and thickness L
- conduction and convection coefficients: open-circuit thermal conductivity k and thermal diffusivity coefficient $\epsilon = \frac{thermal\ conductivity k}{volumetric\ heat\ capacity \rho C_p}$ of the TEG; thermal transfer coefficients through

the hot and cold mediums β_H and β_C

- electrical parameters of the TEG: internal resistance R_{int} and current I_{load}
- temperatures at the beginning of the iteration: $T_{\infty H}, T_{\infty C}, T_H$ and T_C
- time step duration t_{step}

β_C and β_H may vary if the materials in contact with the cold and hot sides change properties, *e.g.*, increased convection. ϵ can vary with temperature, but in this model it is considered constant. The time step size t_{step} is constant and chosen based on the knowledge of the thermoelectric system; it is a compromise between the thermal time constant of the transient evolution inside the TEG and the temperature change in the thermal masses of the system. Values between 1 second and 3 seconds have been found to satisfactorily model the physical system. For systems with a very high energy flux, *e.g.*, large engine exhaust gas systems with high dynamic load, values of under 1 second may be more appropriate. Conversely, for high-mass low-power systems such as energy harvesters a much longer time step may be satisfactory.

$T_{\infty H}, T_{\infty H}, T_C, T_H, I_{load}, R_{int}$ are fed iteratively at the beginning of every iteration from the rest of the Simulink model.
As already explained in Section 5.4.1, the HE block produces two outputs, T_C and T_H, that are the temperatures on the cold and hot sides after that particular iteration cycle of duration t_{step}. T_C and T_H are then passed through a memory block so that they are effectively available only after t_{step}, *i.e.* at the beginning of the next iteration. The block could be set to calculate temperatures inside the TEG too, but these are not of interest to the aim of the simulation (nor, usually, to the system designer).
If there are multiple TEGs electrically connected in series or parallel some of the inputs required by the HE will be scaled accordingly depending on the total number of modules N_{tot}: $A_{tot} = N_{tot}A$, while R_{int} and I_{load} will be provided by the electrical block, as described in Section 5.4.4.

5.4.3 The thermal block

The most important tasks executed by the hot side block are the update of the temperature $T_{\infty H}$ of the hot thermal mass and the update of the TEG hot side temperature T_H, accounting for the Peltier effect.
Consider the input power transferred to the hot thermal mass. This can be provided by an electrical heater or by thermal conduction/convection. For the electrical case it is easily measured while in the thermal case it can be calculated using the well-known laws of heat conduction or convection. As shown in Fig. 5.5, a fraction of the input power changes the quantity of heat energy stored in

the hot thermal mass, while the remaining thermal energy is transferred (through the hot thermal mass) to the TEG. Heat losses can be accounted for in another term P_{lossH}. It can be written:

$$P_{in} = \frac{m_H C_H \Delta T_{\infty H}}{t_{step}} + h_H A \Delta T_H + P_{lossH} \tag{5.42}$$

where $m_H C_H$ is the hot thermal mass heat capacity J/K, $\Delta T_{\infty H}$ is the change in temperature of the hot thermal mass during t_{step}, h_H is the convection coefficient (or for conduction the conduction coefficient over the thickness) of the medium between the hot thermal mass and the TEG, A is the area of the TEG and ΔT_H is the temperature difference across the medium.
From Eq. 5.42 it would be possible to obtain the new value for $T_{\infty H}$, however, it is first necessary to account for the Peltier effect which acts on the second term on the right of Eq. 5.42. The Peltier effect pumps additional power from the hot side to the cold side, thus effectively reducing the hot side temperature T_H provided by the HE. Writing $P_{convH} = h_H A \Delta T_H = h_H A \left(T_{\infty H} - T_H\right)$, where T_H is the result of the HE, then the value of T_H can be corrected by calculating its 'real' value:

$$T_{Hreal} = T_{\infty H} - \frac{P_{convH} + P_{PeltH}}{h_H A} \tag{5.43}$$

where $P_{PeltH} = \alpha I T_H$ from Eq. 3.6. Now that the 'real' value for T_H is obtained, from Eq. 5.42 it is possible to calculate $T_{\infty H}$ for the next iteration:

$$T_{\infty H(i+1)} = T_{\infty H(i)} + \frac{\left[P_{in} - P_{lossH} - h_H A (T_{\infty H(i)} - T_{Hreal})\right] t_{step}}{m_H C_H} \tag{5.44}$$

It can be noted that, depending on the polarity of the second term on the right of Eq. 5.44, $T_{\infty H(i+1)}$ can be greater or smaller than $T_{\infty H(i)}$. T_{Hreal} and $T_{\infty H(i+1)}$ will be used in the next iteration $(i+1)$ of the HE as the initial value of the hot side temperature and as the temperature of the hot thermal mass, respectively.

For the cold part of the system similar considerations hold true. The power flowing to the cold thermal mass is the sum of the thermal power flowing through the TEG and the thermal power pumped to the cold junction by the Peltier effect. In a similar way as for the hot side T_C is updated to its 'real' value:

$$T_{Creal} = T_{\infty C} + \frac{h_C A (T_C - T_{\infty C}) + \alpha I T_C}{h_C A} \tag{5.45}$$

It is now possible to obtain $T_{\infty C(i+1)}$ as

$$T_{\infty C(i+1)} = T_{\infty C(i)} + \frac{\left[h_C A (T_{Creal} - T_{\infty C(i)}) - P_{out} - P_{lossC}\right] t_{step}}{m_C C_C} \tag{5.46}$$

where P_{out} is the power removed from the cold thermal mass and $P_{C_{out}}$ takes into account any thermal power lost to ambient on the cold side.
Both the values calculated in Eq. 5.45 and 5.46 are passed to the HE block for the next iteration

$(i+1)$.

5.4.4 The electrical block

A TEG can be modelled as a voltage source V_{OC} in series with its internal resistance R_{int}, even during transients, because their electrical dynamic response is in order of nanoseconds [60] and is many orders of magnitude less than even the shortest thermal time constant in the system (usually the pellets forming the TEG). Therefore, when the TEG is connected to a load R_{load} it can be written that the load voltage is

$$V_{load} = V_{OC} - R_{int} I_{load} \tag{5.47}$$

It can be noted that both the internal resistance and the open-circuit voltage can be approximated to linear functions of the temperature difference ΔT across the device [102], therefore Eq. 5.47 can be updated to

$$V_{load} = m_{V_{OC}} \Delta T - (m_{R_{int}} \Delta T + q_{R_{int}}) I_{load} \tag{5.48}$$

In this model the Thomson effect is neglected without significant loss of accuracy (see Section 3.1.3); therefore, $m_{V_{OC}}$ is considered constant and equal to the Seebeck coefficient $\alpha\,[V/K]$. $m_{R_{int}}\,[\Omega/K]$ and $q_{R_{int}}\,[\Omega]$ are also constant coefficients.
In order to use Eq. 5.48 in the model, the appropriate values for the coefficients $m_{V_{OC}}, m_{R_{int}}$ and $q_{R_{int}}$ should be obtained through an electrical characterisation of the TEGs used in the thermoelectric system [111] and such as can be performed using the apparatus described in Section 4.2.
The electrical block also deals with series and parallel interconnection of TEG modules. It is assumed for this purpose that all the modules are identical and all are subjected to equal thermal conditions, so that scaling can be applied (clearly unequal conditions and/or modules cannot be accurately computed by a model designed for a single device). The results presented in Section 4.5 highlighted the importance of temperature mismatch on the output power. In order to account for uneven temperature distributions, a TEG system may be divided into separate sections as it will be done in Section 7.2.1.
If there are N_S modules in series and N_P modules in parallel, for a total of N_{tot}, the total open-circuit voltage is $V_{OCtot} = N_S V_{OC}$ and the load current I_{load} is N_P times the current in a single branch. It can then be written, from Eq. 5.47, that

$$V_{load} = N_S V_{OC} - \frac{N_S R_{int} I_{load}}{N_P} \tag{5.49}$$

The dimension-less figure of merit ZT is calculated from Eq. 3.21 and the actual efficiency η (Eq. 3.19) is obtained from

$$\eta = \frac{V_{load} I_{load}}{P_{in} - P_{lossH}} \tag{5.50}$$

The electrical part of the Simulink model computes the values of R_{int} and V_{load} depending on the actual temperature gradient ΔT and on the electrical parameters I_{load}, N_S, N_P. The Peltier term is calculated as $N_{tot}\alpha T_j I_{single}$, where I_{single} is the current passing through a single TEG device. The load current (or voltage) in a real thermoelectric system is set either by a constant R_{load} connected to the TEG, or by an interfacing power electronic converter with MPPT [112]. For flexibility of simulation, the desired load is passed to the model as an input, but the model also provides the maximum theoretical power, *i.e.* when $V_{load} = V_{OC}/2$, to compare actual electrical power output with the maximum that can be extracted.

5.5 Experimental and simulation results

In order to test the ability of the proposed *Simulink-Matlab* model to simulate real thermoelectric generating systems, a transient experiment was performed in the laboratory and then simulated by computer. The results obtained for both tests and a discussion about their comparison is presented in this section.

5.5.1 Experimental test rig

The thermoelectric system described in 4.2 was used in the experiment.
The copper blocks have a thermal mass of approximately $565\,J/K$ (Copper volumetric heat capacity $C_{V_{Cu}} = 3.45\,J/cm^3K$) [2], the thermal transfer coefficient for between the TEG and the hot and cold thermal masses are respectively 9100 and $11800\,W/m^2K$ (Copper thermal conductivity $k_{Cu} = 400\,W/mK$; the heater is $2.2\,cm$ from the TEG hot side, the water pipes are $1.7\,cm$ from the TEG cold side).
The input power is provided by electrical heaters and thermal energy is removed from the cold side through forced liquid flow. The mass flow rate of the water/glycol mixture is measured as $17\,g/sec$ and the coolant mixture heat capacity is $3.89\,J/gK$. The convection coefficient was determined empirically and is $1400\,W/m^2K$.
Heat losses from the hot block (which is insulated with glass-fibre) are included in the simulation as described in Section 4.2.2. The time step size used for the simulation is $3\,sec$.
The TEG module used is manufactured by European Thermodynamics Ltd. (model code: GM250-127-14-10) and has an open-circuit thermal conductivity $k = 1.62\,W/mK$ [3], surface $A = 1600\,mm^2$,

[2] It has been assumed that only one fourth of the cold-side copper block is relevant when using only one TEG fixture.

[3] The thermal conduction coefficient of the TEG k_{TEG} has been calculated letting the system get to steady-state with constant input power to the hot side and open-circuit at the TEG terminals (taking into account the losses of the system).

thickness $L = 3\,mm$, thermal diffusivity $\epsilon = 1e^{-6}\,m^2/sec$. The electrical characterisation of the module used is provided in Section 4.3.1.

5.5.2 Comparison and discussion of results

The designed transient lasts for 55.5 minutes and is intended to produce several power and load steps. The VEE program records all the electrical data, temperatures, mechanical pressure and time. The transient parameters are as follows, where P_{in} is the DC electrical power to the heater and I_{load} is the current value set in the electronic load:

1. $P_{in} = 50\,W$; $I_{load} = 0\,A$ (open-circuit) @ time=0 s
2. $P_{in} = 50\,W$; $I_{load} = 0.2, 0.4, 0.6, 0.8, 1\,A$ @ time=1195,1210,1229,1247,1286 s
3. $P_{in} = 150\,W$; $I_{load} = 1\,A$ @ time=1286 s
4. $P_{in} = 150\,W$; $I_{load} = 1.2, 1.4, 1.6, 1.4, 1.2, 1.0, 0.8, 0.6\,A$
   @ time=2761,2780,2795,2828,2844,2877,2946,3109 s

This experiment is designed to test the simulation model under thermal and electrical transients of difference magnitude. Different temperature variation rates were applied both in open-circuit and at-load, with several electrical load steps. The Simulink program runs without interruptions, therefore testing it under different thermal and electrical conditions ensures that there are no offsets that would make the results valid for just one of those operating conditions.

Fig. 5.7 shows both the experimental and simulation results in the same graph, for comparison. In particular the temperature difference and the output electrical power are plotted versus the transient time.
During the transient the temperature difference across the TEG device varies from 5°C to almost 150°C, leading to some thermal expansion effects in the whole system. The mechanical pressure on the system could not be controlled during the test[4]. In Section 4.3.3 it was noted that different pressure loads slightly influence the contact resistances in the system, thus affecting the thermal conductivity and the power produced by the TEG. Their effect should not account for more than a 5 % change in the results.
As can be appreciated from Fig. 5.7, there is no temporal delay in the response of the simulated performance with respect to the experimental data. The simulation results show very good agreement with the experimental results, accurately tracking the electro-thermal coupled effects occurring in

[4]Active control of the clamping force will be incorporated into a future test rig to compensate for thermo-mechanical effects, as already stated in Chapter 4

the thermoelectric system. The Root Mean Square Error (RMSE) is 3.58°C for the temperature difference and $0.2\,W$ for the power output. The RMSEs normalised to the values range become 2.76 % and 4.55 % for the temperature difference and the output power, respectively. There are no works in the literature that proposed a simulation model for TEG systems demonstrating similar prediction performance under varying thermal and electrical conditions as is presented here. As a consequence it is difficult to compare the data presented here to other simulation results reported in the literature.
It is very interesting to note the close effect that the load current has on the temperature gradient across the device. Every increase in I_{load} leads to a decrease in temperature due to the greater value of the Peltier term of Eq. 5.43. Conversely, the last 500 seconds of the test show that a smaller load current increases the rate of change of temperature. This observed behaviour is consistent with the expected performance of the system when the input power rather than temperature difference is the defined variable, and supports the conclusions drawn in Section 4.4. The effective thermal conductivity of the TEG module varies markedly, depending on the current flowing through the module. MPPT converters should take this thermal variation into account when setting the optimum operating point for maximum efficiency or power generation. However, current MPPT algorithms do not have this functionality, yet.

Future work will develop a model of the system that incorporates the non-linear effects introduced by a MPPT converter due to the fast change in electrical load imposed while seeking for the optimum power point. The Simulink model will be adapted to a typical waste heat energy recovery system from exhaust gas for automotive applications in Section 7.2.1.

5.6 Conclusions

This chapter presented an innovative and powerful numerical model to accurately simulate real thermoelectric power generating systems even during transient conditions which occur during changes in the operating conditions, *e.g.*, temperature or load changes. The comparison of simulation results with experimental data from a real TEG system demonstrates the accuracy and capability of the model, showing that it can be employed to study transients and steady-state operation of real thermoelectric systems with confidence and with a maximum error of ±5 %. As such, the model is of great utility in assisting with the design of large-scale and/or complicated thermoelectric systems.

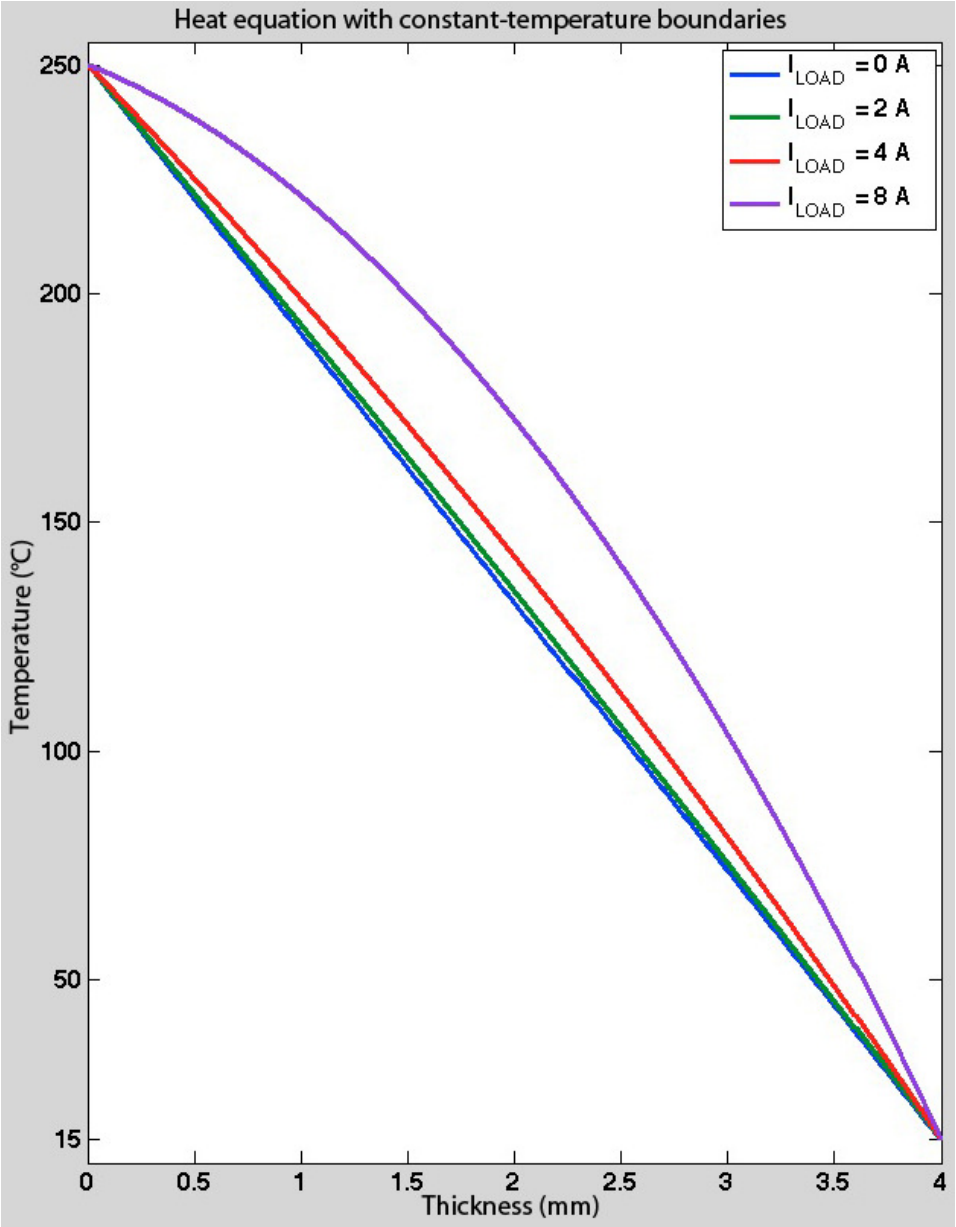

Figure 5.3: Heat Equation with constant temperature boundary conditions, for different current loads. The hot side is at $x = 0\,mm$ while the cold side is at $x = 4\,mm$. $T_C = 15°\text{C}; T_H = 250°\text{C}$. Regardless of the load current, the side temperatures are fixed.

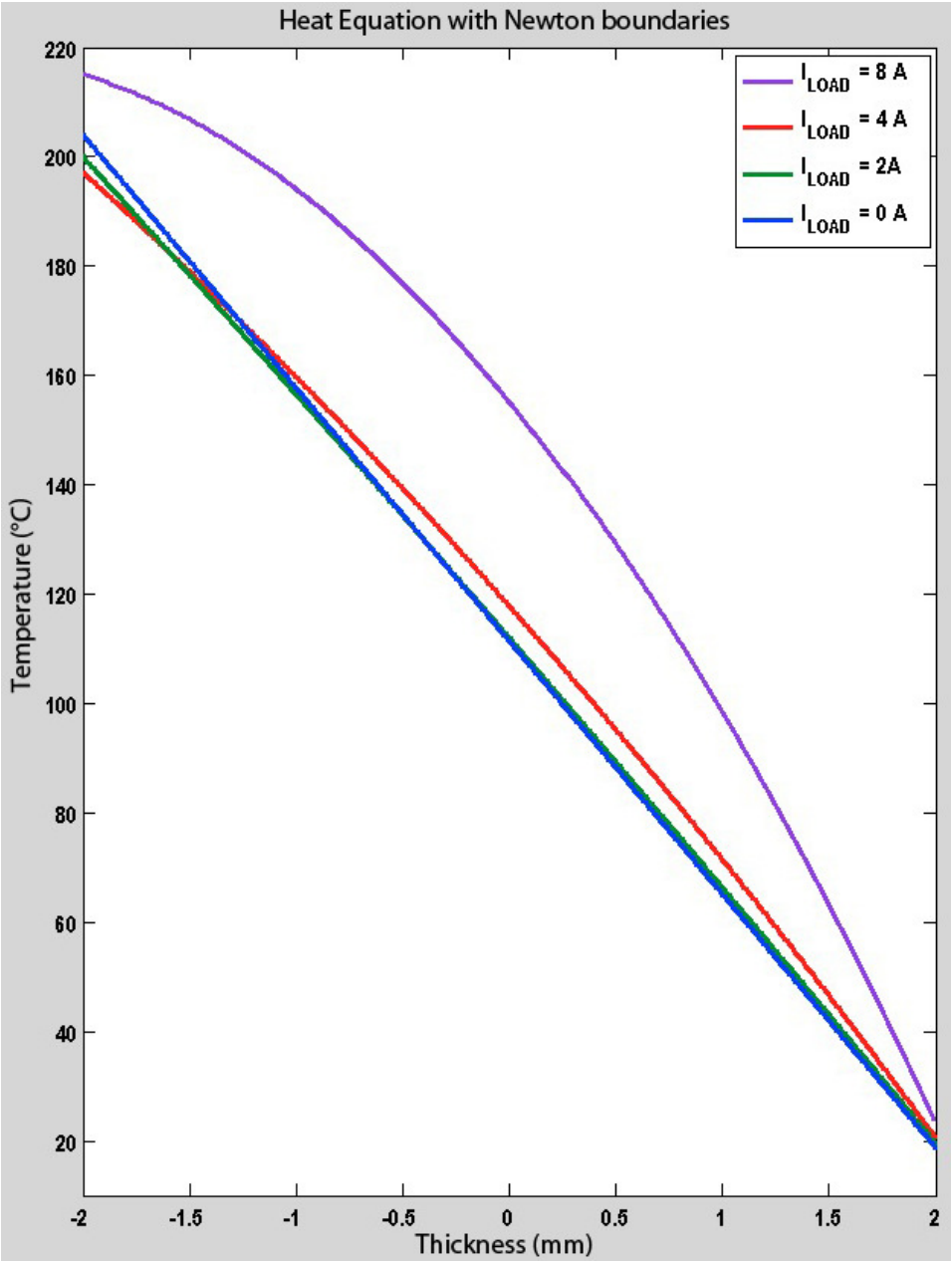

Figure 5.4: Heat equation with Newton boundary conditions and Peltier effect, for different loads. The hot side is at $x = -2\,mm$ while the cold side is at $x = 2\,mm$. $T_{C\infty} = 15°\text{C}; T_{H\infty} = 250°\text{C}$. The hot side temperatures vary with the load current (points in °C on the y-axis: 196, 200, 204.4, 215); the cold side temperatures vary as well (points in °C on the y-axis: 18, 19, 20, 24).

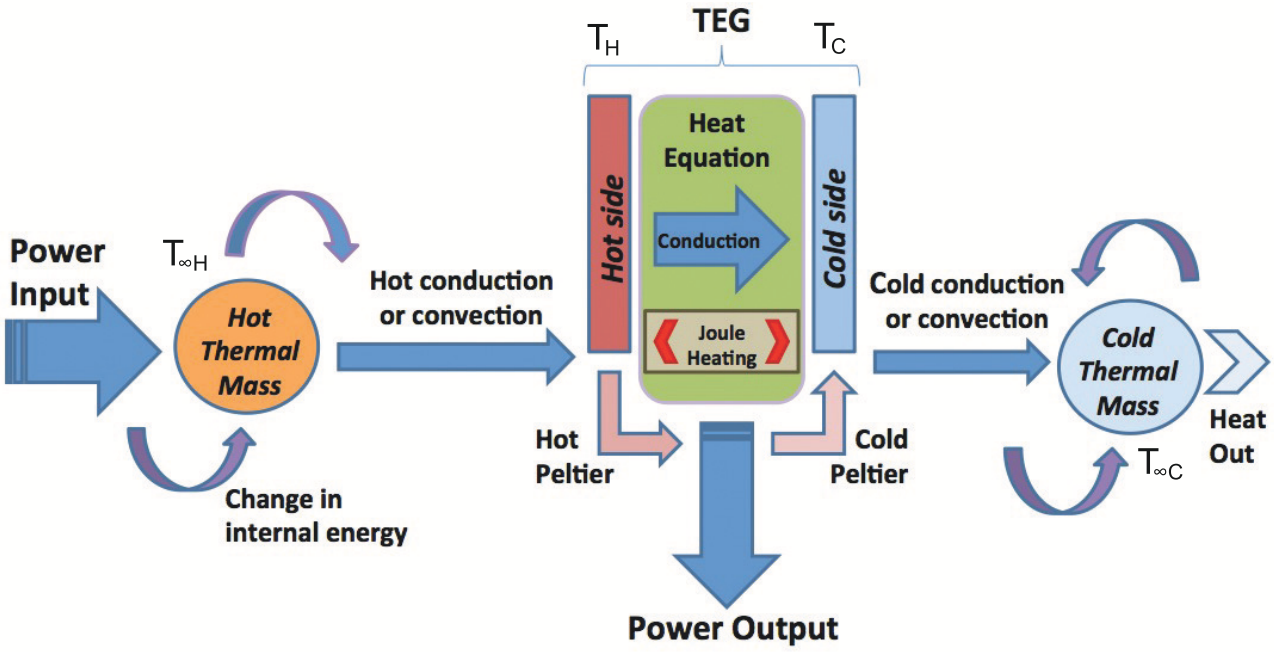

Figure 5.5: Architecture of a thermoelectric power generating system.

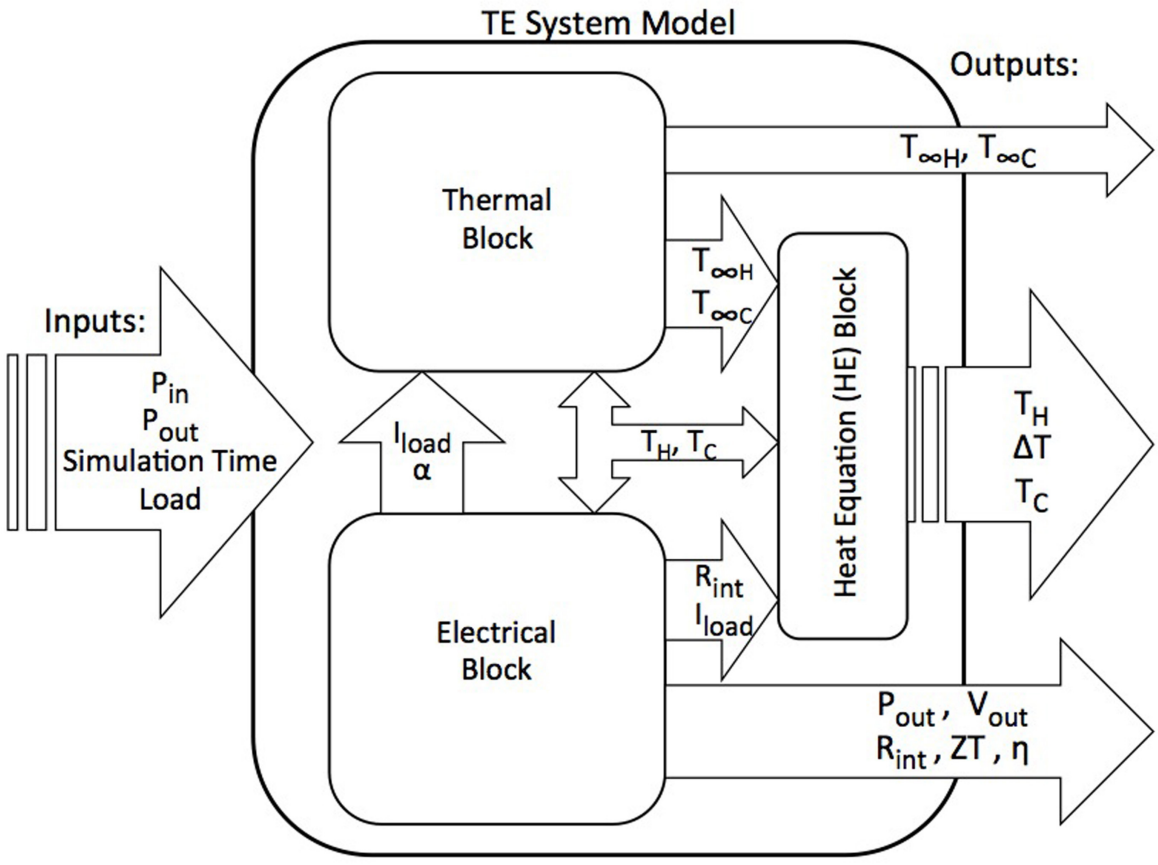

Figure 5.6: Architecture of the system model. Exchange variables are inside the arrows.

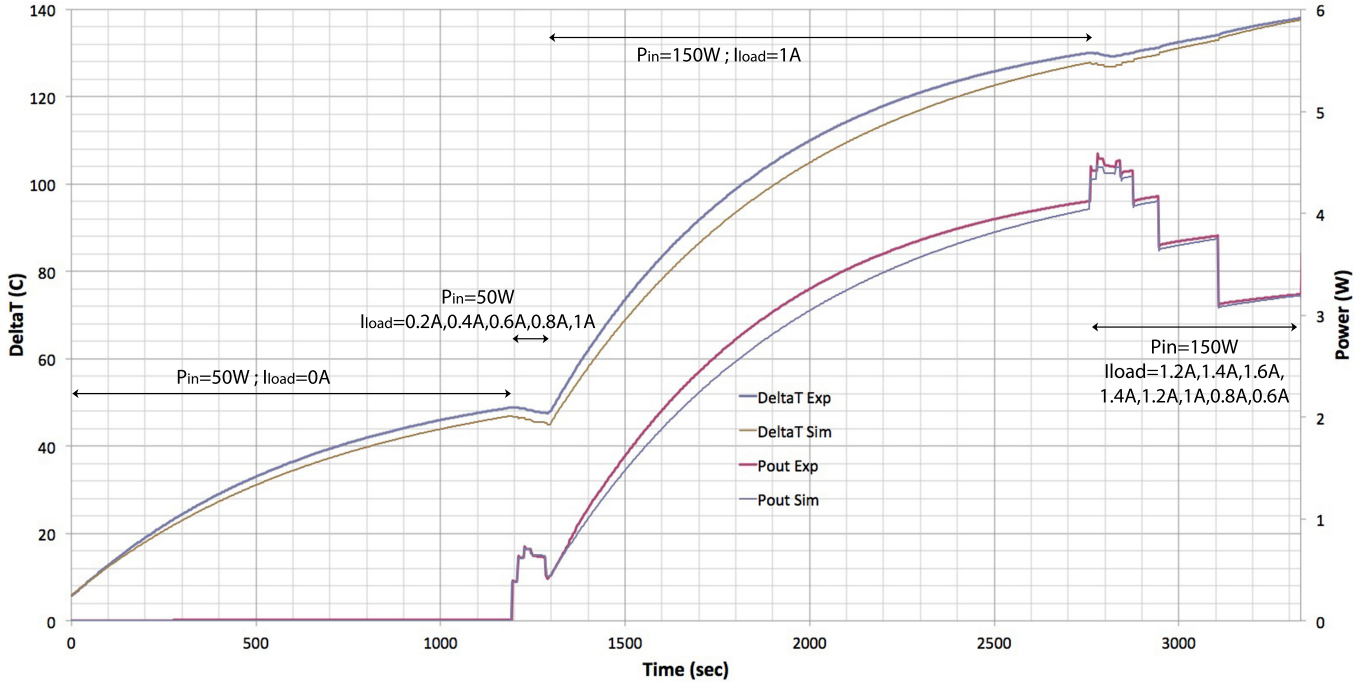

Figure 5.7: Experimental and simulated transient results showing the temperature difference and the output electrical power versus the time.

Chapter 6

MPPT Converters for TEGs

A portion of the contents included in this chapter is published in [J1].

This chapter deals with a very important part of most thermoelectric generating systems: the MPPTelectronics that interface the TEG to the load. This electronic sub-system usually comprises of a DC-DC power converter controlled in such a way to always maximise the power extracted from the TEGs, under any thermal condition. If the TEGs were to be directly connected to the load their operating point would be set by the load voltage (if connected to a battery) and/or by the load impedance, which would usually result in the TEGs not producing maximum power. The MPPT converters can on the contrary adjust the impedance "seen" by the TEGs so as to maximise power generation.
The most commonly used non-isolated converter topologies and MPPT control strategies are described. Greater focus is put on the circuitry and control techniques developed and used in the experimental work which is associated with this thesis.

TEGs are often employed in dynamic thermal environments with time-varying temperature differences (see Chapter 5), *e.g.*, cars' exhaust gas systems, therefore it is of great importance to track the best operating point quickly and effectively. It is necessary to control the power electronic converter with a MPPT algorithm to match the virtual load seen by the TEGs to their actual internal resistance. MPPT algorithms are covered in Section 6.2 while Section 6.3 presents a detailed analysis of an innovative technique to obtain the TEG's open-circuit voltage measurement. Section 6.4 analyses the transient response of TEGs to sudden load disconnection and presents a snubber circuit to reduce over-voltage spikes. The MPPT synchronous buck-boost converters developed during the period of study are described in Section 6.5. Experimental results are reported in Section 6.6 to establish the performance of the MPPT converter. Finally, Section 6.7 briefly discusses about the topic of DMPPT systems for TEGs.

6.1 Power electronic converters for TEGs

DC-DC converters are power electronic devices able to transform DC voltages from one level to another, possibly also reversing the voltage polarity. The most common 'basic' topologies are the *Buck* which steps down the input voltage, the *Boost* which steps up the input voltage and finally the *Buck-Boost* that is able to step either up or down the output voltage relative to that applied at the input. Some other converter types, derived from the aforementioned topologies, provide electrical isolation between the input and the output; however, this thesis considers only *non-isolated* converters.

Section 3.2.2 examined how the size and the number of pellets contained in a thermoelectric device greatly influences its electrical characteristic, *i.e.* the current and voltage it produces when in generating mode. Table 3.1 highlights this important feature using two commercial TEGs as examples. This means that depending on the TEG devices used the levels of output voltage and current may vary considerably. Additionally, several TEGs can be electrically connected in series and/or parallel, as presented in Section 4.5.1, thus modifying the voltage and current at the output. As a consequence the choice of converter topology depends on the prevailing output and input voltages. Using the devices listed in Table 3.1 as example inputs and a $6\,V$ battery at the output, a Buck-Boost might be a good choice when using the GM250-449-10-12, while a Boost is necessary for the TEHP1-12656-0.2. In case two or more GM250-449-10-12 were to be connected in series, a Buck converter can be used, assuming the devices are producing a useful amount of voltage.

6.1.1 The switching operation

The main components of Buck, Boost and Buck-Boost are an inductor L, a switch S and a diode D. A Pulse Width Modulation (PWM) controls how long the switch stays closed during each switching period. The *on* and *off* states of the switch divide the converter's operation into two phases: a charge phase and a discharge phase, both of which describe the energy transfer to or from the inductor. Fig. 6.1 shows the basic circuit schematics of the three converter topologies and the inductor's charging and discharging phases. During t_{on} (PWM high) the inductor L is magnetised by the voltage difference (ΔV) which is applied to its terminals, varying on the converter's topology. This ΔV imposes a slope, $di/dt\,[A/s]$, obtained from the well-known *Lenz formula* $v_L(t) = L\dfrac{di_L(t)}{dt}$. As a result, the current in the inductor is incremented by

$$\Delta I_{L_{on}} = \frac{\Delta V_L t_{on}}{L} \tag{6.1}$$

When the switch opens during t_{off}, there cannot be a discontinuity in the current of the inductor, *i.e.* a way to keep the current circulating in the same direction has to be provided in order to guarantee

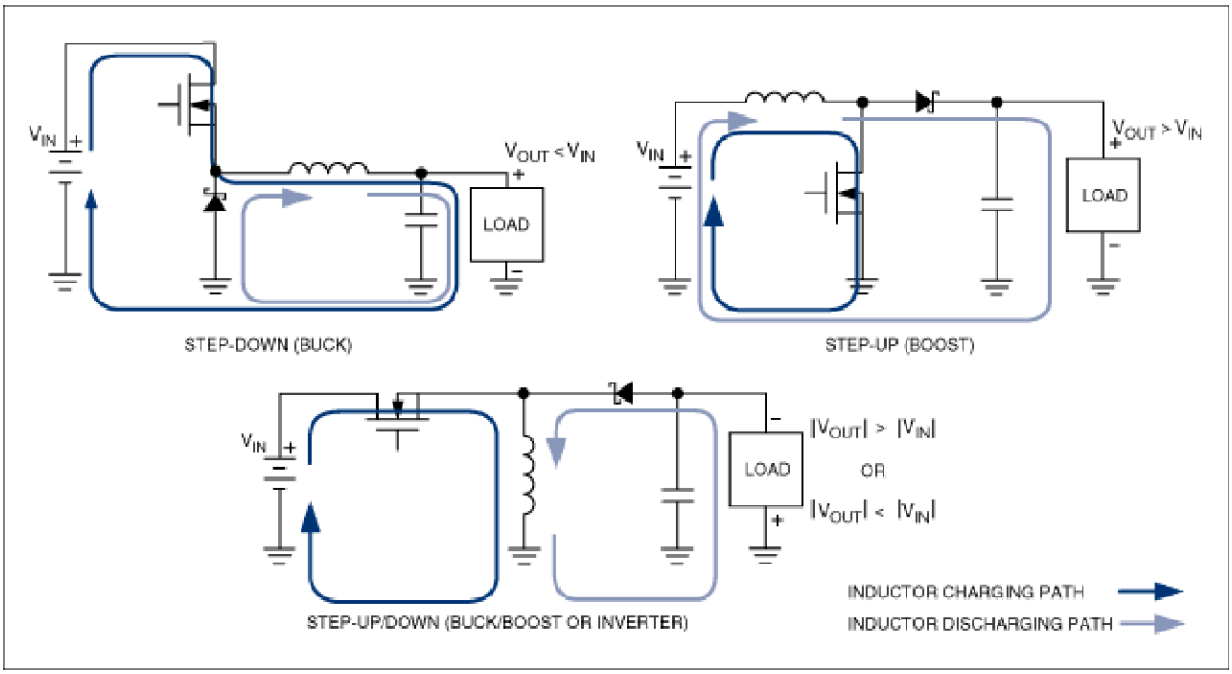

Figure 6.1: Inductor charging and discharging paths in the buck, boost and buck-boost converters.

the ampere-turns continuity in the inductor. The solution is found in the so-called freewheel diode D, which in the *synchronous* version of the converters is replaced by another switch. During t_{off} there will be another similar change in the current in the inductor.
Input and output capacitors are added as buffer elements: the former is charged by the source during t_{off} and releases power during t_{on}, while the latter provides power to the load when the diode is reverse-biased. This cyclical transfer of energy between the circuit elements maintains the output voltage at the proper value, in accordance with its topology. The value of the duty cycle, which is the ratio of the PWM's high time to its switching period ($D = t_{on}/T_{sw}$), directly affects the ratio between output and input voltage $M = V_{out}/V_{in}$

$$M_{buck} = D \qquad M_{boost} = \frac{1}{1-D} \qquad M_{buck-boost} = \frac{D}{1-D} \tag{6.2}$$

The book "*Switch-mode Power Supplies*" by C. Basso [113] provides further detailed information about the operation of DC-DC converters.

6.1.2 MOSFET gate driving

Gate driving is an important feature of switch-mode converters because it controls the switching operation of the MOSFET usually employed as switch S. It is fairly easy to drive the gate of a low-side MOSFET, *i.e.* with the source connected to ground, while it is more complicated to drive a high-side MOSFET, for which the source voltage varies during the operation of the converter. There

are numerous gate driving circuits that can be used for low- and high-side gate driving, many of them described in [114]. Low-side MOSFETs can either be driven directly from a microcontroller or using a low-side gate driver IC, like the *Microchip* TC4427A. Following are presented the high-side gate driving circuits used in the converters developed during the research described in this thesis.

The simplest and cheapest solution is using the so-called *bootstrap* half-bridge gate drivers, like the *Texas Instrument* LM5109. A detailed description of the function of this type of circuits can be found in [114].
A very reliable but more expensive option involves using a small isolated DC-DC converter, like the *muRata* MER1 Series, to provide the voltage to apply to the gate through a normal low-side gate driver IC. Additional isolation between the gate driver IC (power side) and the microcontroller or PWM controller (signal side) can be provided using an opto-coupler gate driver IC, like the *Avago* HCPL-3180.
Another alternative is to use a pulse transformer to isolate the MOSFET's source voltage to the

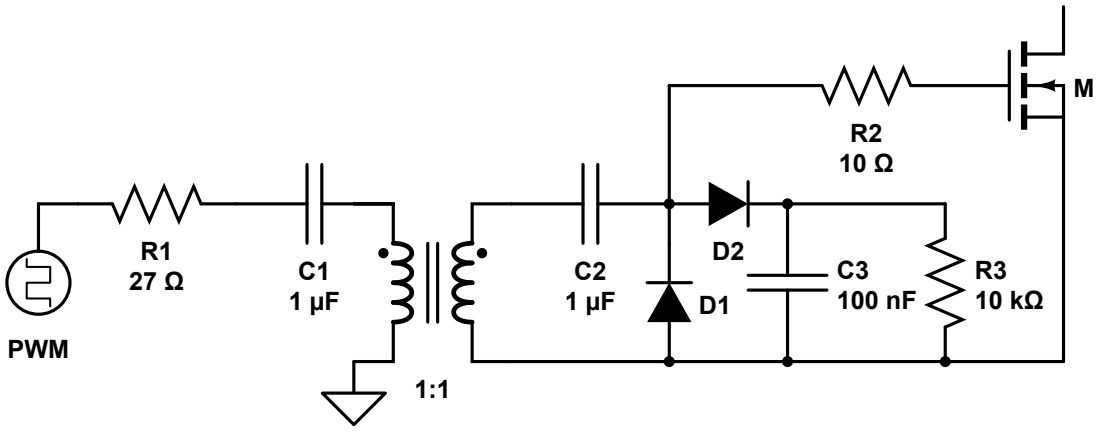

Figure 6.2: Pulse transformer gate driving circuit schematic.

negative reference (usually at ground) of the voltage source used to provide the energy to charge the MOSFET's gate terminal. The circuit required to implement this is shown in Fig. 6.2.

Problems arise if continuous conduction time is required by the high-side switch for a long period relative to the switching cycle period. Of the above methods, only the isolated gate driver guarantees proper operation with 100% duty cycle. The bootstrap technique only recharges the capacitor used to provide the required gate-source charge during the off-time of the PWM, *i.e.* when the low-side MOSFET conducts and the source of the high-side MOSFET is at ground. Similarly, the pulse transformer of Fig. 6.2 would saturate if subject to what is effectively DC, *i.e.* continuous on operation.
A solution for the bootstrap technique is provided by the use of a charge pump circuit, an example of which is shown in Fig. 6.3. The circuit uses a 555 IC in charge pump configuration to boost-up

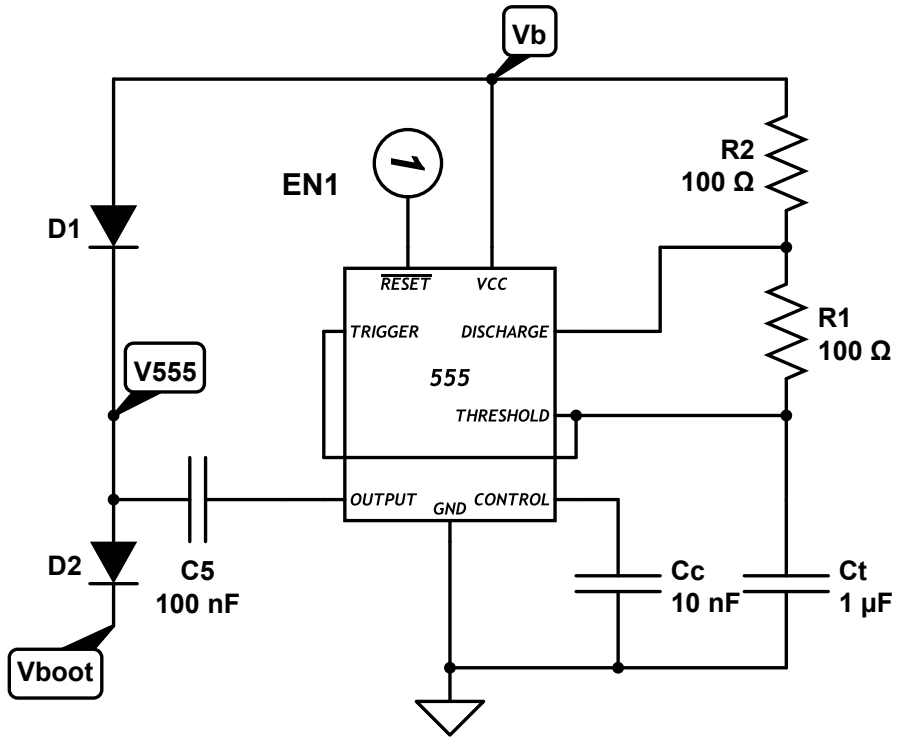

Figure 6.3: Charge pump schematic circuit to provide continuous conduction time to the bootstrap half-bridge gate driving circuit.

the output PWM, whose high value becomes:

$$V_{boot} = V_b + V_{555} - V_{D1} - V_{D2} \tag{6.3}$$

The idea is to activate (using the enable pin) the 555 IC when continuous conduction time is required on the high-side switch, so that the PWM produced by the charge pump keeps the bootstrap capacitor charged to almost double the value of the supply voltage V_b.

6.2 Maximum power point tracking algorithms

Chapters 3 and 4 explained that for any fixed thermal condition the electrical power produced by a TEG varies depending on the electrical load connected at the TEG's terminals. Under open-circuit and short-circuit the TEG is not producing any electrical power, whereas for any other electrical operating point on the V-I characteristic the TEG is producing usable output power. As explained in section 3.3, the maximum power is achieved in the centre of the V-I line, when the voltage is half of the open-circuit voltage V_{OC} or likewise when the current drawn is half of the short-circuit current I_{SC}. In case that the temperature gradient across the TEG was to be kept constant, a resistive load

of value

$$R_{load} = \frac{V_{OC}/2}{I_{SC}/2} \tag{6.4}$$

would ensure that maximum power is extracted from the TEG, and no additional electronics would be required. However, this condition is almost always impossible to satisfy for two main reasons: 1) the temperature difference is unlikely to be constant and it is not common to have a purely resistive load, especially of the precise value required, and; 2) the same conclusions could be drawn if the load was not resistive, in which case the electrical point at-load would be likely to vary in time, depending on the actual power consumption of the load.
In applications of waste heat harvesting the input thermal power to the TEG is essentially "free"; therefore the low thermal to electrical conversion efficiency of TEGs is not a serious drawback *per se*, but it is important to maximise the power produced from the TEGs in order to minimize the cost per Watt. Even if the actual power produced is not met by the current load demand, surplus electrical energy can be stored in batteries or super-capacitors.
In a practical TEG system the temperature difference available across the TEG varies during operation. This in turns means that the at-load electrical operating point needs to be frequently updated in order to always maximise power extraction, irrespective of the thermal conditions. For this reason particular electronic converters are typically employed to track the electrical point at which maximum power is extracted. Such converters are controlled by what are commonly known by MPPT algorithms, which set the optimum operating electrical point by changing the duty cycle of the converter. The optimum operating condition for a TEG is to ensure that the load impedance is greater than or equal to the internal resistance, to assure a relatively high thermal to electrical conversion efficiency of the overall system as was previously explained in 3.3.2.
MPPT converters usually interface the TEGs to storage elements such as batteries or supercapacitors. If the load requires a fixed voltage for correct operation another DC-DC converter can be used to feed the load from the battery with a constant regulated output voltage.

Following is a description of the most commonly used MPPT algorithms for TEGs published in the literature: the P&O and the INC. These MPPT algorithms were originally developed for PV systems and are referred to as *hill-climbing* techniques because of the shape of the PV power curve, which is logarithmic. Other MPPT algorithms are described in [115], but they are less common in TEG applications.
The ESC algorithm has also been used during the Ph.D. in a work in collaboration with Coventry University [86], [J3]. ESC is a non-model based real-time optimisation approach for dynamic problems where only limited knowledge of a system is available.
All the MPPT algorithms mentioned above require the measurement of both current and voltage and usually present a substantial computational load per PWM period, while the fractional open-circuit method requires only a voltage reading and has a relatively low computational overhead. This last MPPT method is described in Section 6.3.1.

6.2.1 "Perturb & Observe"

The P&O algorithm is one of the most used due to its simplicity [60, 24, 116, 83]. The basic operating principle entails continuously perturbing the electrical operating point and comparing it to the previous value. By this method the operating point moves along the parabola-shaped P-I curve and the maximum value corresponds to maximum power extracted. The P&O algorithm's flowchart is shown in Fig. 6.4

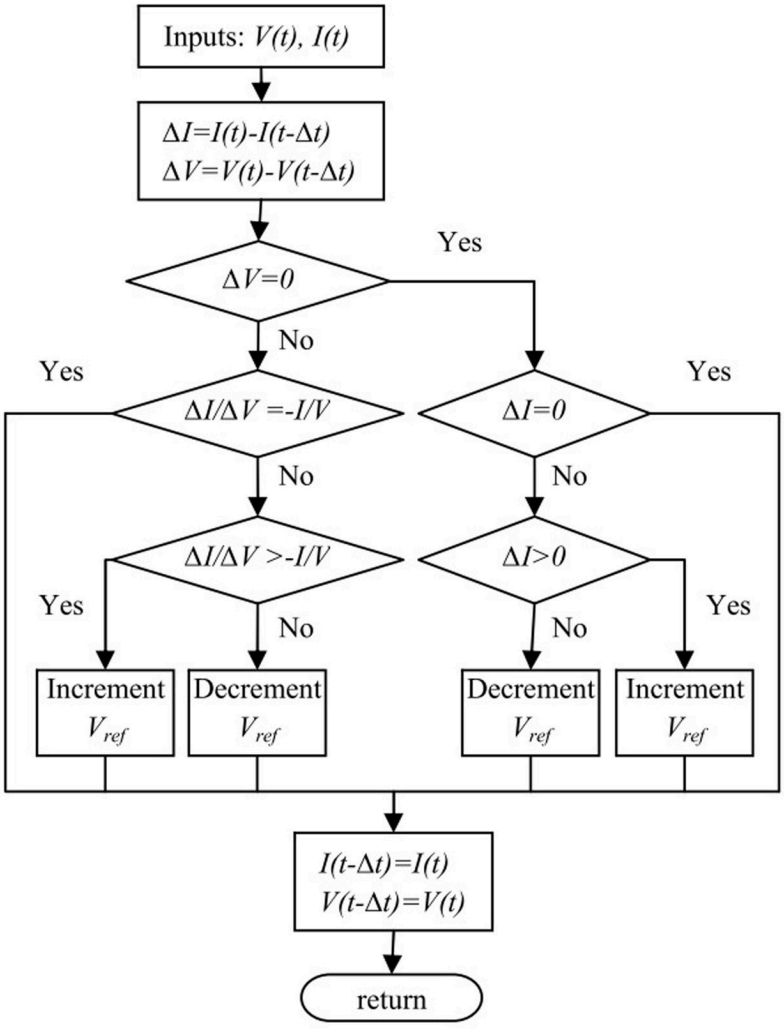

Figure 6.4: Flowchart of the P&O algorithm.

The 'classic' P&O method, which makes use of a fixed perturbation step and frequency, has two main drawbacks: when the system is in thermal equilibrium the electrical operating point oscillates around the MPP due to the continuous adjustment; this effect is known as Limit Cycle Oscillation (LCO). Moreover, during rapidly changing thermal conditions it cannot be guaranteed to find the MPP. To mitigate these problems, the *Adaptive* P&O adjusts the step-size and the perturbation frequency to reduce oscillation in steady state and achieve faster and more precise transient response

[117]. In either case, the parameters must be customized to the dynamic behavior of the specific converter adopted [118]. Also, measurement noise must be taken into account when considering reduction of perturbation size and increase of tracking speed [119].

6.2.2 "Incremental Conductance"

The INC technique is based on the fact that slope of the P-I curve, dP/dI, is zero at the MPP. Also, $dP/dI > 0$ to the left of the MPP and $dP/dI < 0$ to its right. It can be written that

$$\frac{dP}{dI} = \frac{d(VI)}{dI} = V + I\frac{dV}{dI} \approx V + I\frac{\Delta V}{\Delta I} \tag{6.5}$$

Therefore the MPP can be tracked by comparing the instantaneous conductance I/V with the incremental conductance $\Delta I/\Delta V$, as shown in the flowchart of Fig. 6.5, where V_{ref} is the desired voltage at the source [84, 120].

As for the P&O technique, the speed and accuracy of convergence to the approximate value of the MPP can be improved by introducing automatically adjustable step size to the conventional INC technique [121, 122].

6.3 The developed MPPT technique

The technique developed in this research programme to measure the TEG's open-circuit voltage requires a switch in series with the input; this is naturally found in the Buck and Buck-Boost topologies. The following sections describe this technique in detail and present a theoretical analysis to quantify the power lost due to additional components and to the sampling event associated with measuring the open-circuit voltage of the TEG.

6.3.1 Open-circuit voltage MPPT method

In Section S:maximising it was noted that the method usually called *(fractional) open-circuit voltage* consists of measuring the TEG's open-circuit voltage and then setting the *at-load* operating voltage to be half of V_{OC}. This method normally requires the converter to be disconnected for some interval to allow for the converter's input capacitors to be charged up to V_{OC} [56]; during this interval no energy is transferred from the TEG to the converter. In order to meet the Root Mean Square (RMS) input current requirements input capacitors might be of the order of tens of μF and they may need hundreds of μs to charge up to approximately V_{OC}, depending on R_{int}. Sometimes an additional series switch is needed to disconnect the TEGs from the converter [89, 37] and this

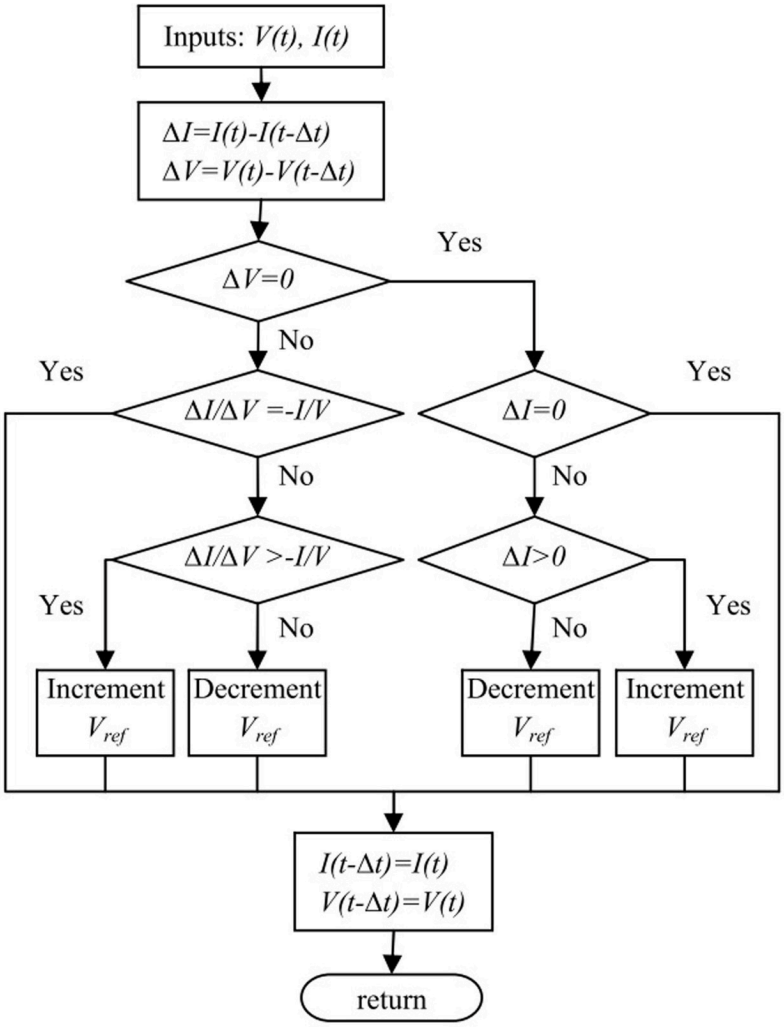

Figure 6.5: Flowchart of the INC algorithm.

switch may require a high-side gate driver with continuous conduction time for long periods. This switch introduces additional I^2R losses when closed and its use interrupts the normal operation of the converter, thus creating a transient event every time the V_{OC} measurement is taken.

This section describes an innovative technique to measure the open-circuit voltage of a TEG which can be used with any converter topology derived from the Buck or Buck-Boost having a switch at its input. This method was presented at ECCE'12 [112] and reduces the drawbacks of the fractional open-circuit MPPT method.
The basic circuit schematic highlighting the necessary components required is shown in Fig. 6.6. A TEG is connected to the input of a Buck or Buck-Boost derived converter. The converter's input capacitors C_{in} are connected to ground through the switch M_{cap}. The high-side switch M_1 represents the input switch of a Buck or Buck-Boost converter, while the remaining converter's components are generically represented by the following box connected to the output capacitors C_{out}.

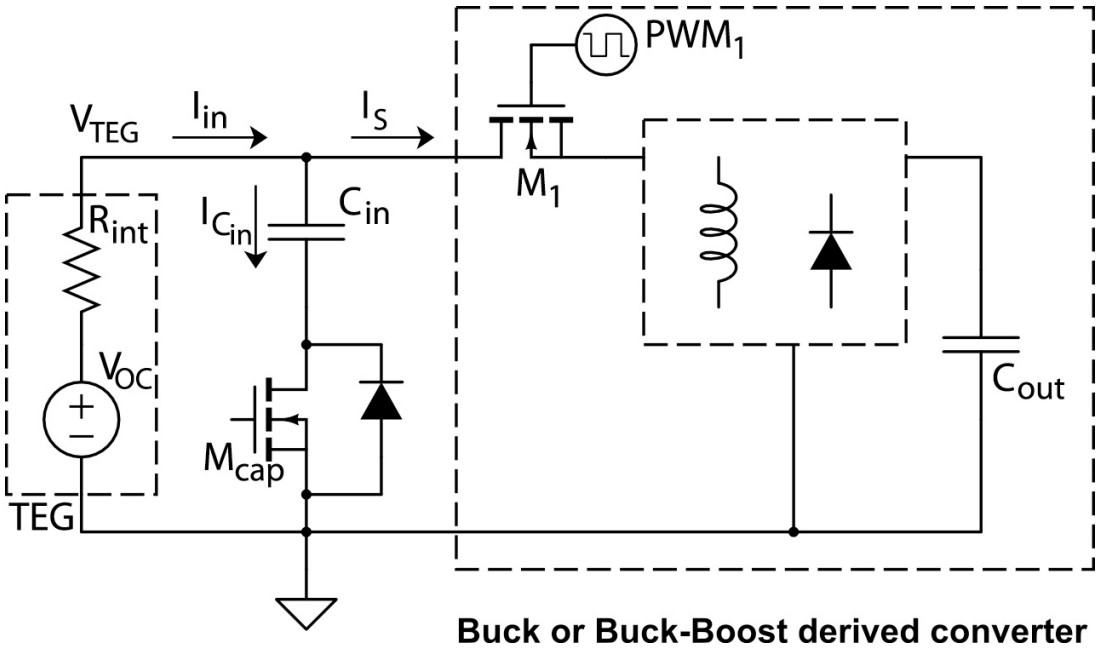

Figure 6.6: Schematic drawing of the components required for the proposed MPPT technique.

To aid explanation of how the voltage measurement is achieved, a timing diagram for the operation of the switches is provided in Fig. 6.7. In the following description t_{on} and t_{off} are the high and low states of PWM_1 respectively. Under normal operation M_{cap} is closed and C_{in} contributes to the pulsating input current required by the converter during t_{on}. When the open-circuit voltage measurement is required M_{cap} is opened. The bottom part of Fig. 6.7 provides an expanded view of what happens during the measurement event. During t_{off} M_1 is open and the TEG is momentarily disconnected from the converter. The current cannot flow into C_{in}, hence the potential at the TEG's terminals rises to the open-circuit voltage V_{OC}, typically within a few to tens of $nsec$ [60]. The microcontroller is timed to measure V_{TEG} during t_{off} while the converter is still operating in a pseudo-normal state: as will be discussed in the next section, both the TEG and C_{in} are still providing power to the converter during t_{on}. The open-circuit measurement process is repeated every T_{meas}, which is a design parameter that depends on the thermal time constant of the TEG system used. It is usually tuned based on experience and observed behaviour, and it is typically between 0.1 and 1 seconds $(1 - 10\,Hz)$.
In-between V_{OC} measurements, a digital control loop keeps on adjusting the converter's duty cycle to maintain V_{TEG} at half of V_{OC}.

By removal of the input capacitor time constant this V_{OC} measurement technique is considerably faster than disconnecting the converter (by keeping PWM_1 low) until C_{in} reaches V_{OC}. Also, it is more accurate because when the TEG is kept at open-circuit during the capacitor charging period the Peltier effect is null, therefore the temperature difference increases slightly, and with it V_{OC}, leading to a marginally higher V_{OC} value [104]; this means that the converter would choose a slightly higher operating voltage. Such a problem does not occur using the preferred MPPT method because

the TEG is left at open-circuit for less than a switching period (12.8 μs for the converter of Section 6.5), during which the thermal operation point is almost unchanged.
Finally, it must be noted that changes in the load applied to the converter's output have no effect on the value of V_{OC}, thus they can be tracked without re-determination of the operation set point.

6.3.2 Theoretical analysis of MPPT efficiency

This section presents a theoretical analysis to quantify the losses introduced by the additional switch M_{cap} in series with C_{in}, and by the V_{OC} measurement technique used. In order to do so, it is necessary to calculate the RMS current $I_{C_{in_{RMS}}}$ flowing into the input capacitors and to understand the converter's behaviour in response to the measurement technique.
Without loss of accuracy we can consider either a Buck or Buck-Boost converter for the input capacitors' RMS current calculations.

The input capacitors are important because they store additional energy from the input source when the switch M_1 is open during the off-time t_{off} of the switching period T_{sw}, and provide it to the load when M_1 closes. The input current is pulsating, and the amount of current that the input source can provide is limited by its series resistance, which is usually fairly high (one-half to several Ohms) in the case of TEGs.
Referring to the plots in Fig. 6.8, the current I_S (in red) flows in the converter's switch only during the on-time t_{on} of the switching period T_{sw}, while it remains at zero for the rest of T_{sw}. During t_{off} the input source charges C_{in}, which effectively filters an AC current. The input current I_{in} (in light blue) can be written as $I_S + I_{C_{in}}$ or as the average of I_S over T_{sw}.

Assume that the MPPT converter is setting the correct MPP at the TEG's output, so that the average input capacitor's voltage is $V_{MP} = V_{OC}/2$. During t_{off} C_{in} is charged by the current

$$i_{C_{in,off}}(t) = \frac{V_{OC}}{2R}\epsilon^{-\frac{t}{RC_{in}}} \tag{6.6}$$

where $R = R_{int} + ESR$, sum of the TEG's internal resistance and the Equivalent Series Resistance of the input capacitors. We can calculate the RMS of Eq. 6.6 as

$$I^2_{C_{in,off_{RMS}}} = \frac{1}{T_{sw}}\int_0^{t_{off}} \left(\frac{V_{OC}}{2R}\right)^2 \epsilon^{-\frac{2t}{RC_{in}}}\, dt = \frac{V^2_{OC}C_{in}}{8RT_{sw}}\left(1 - \epsilon^{-\frac{2t_{off}}{RC_{in}}}\right) \tag{6.7}$$

However, considering a small voltage ripple on C_{in} Eq. 6.6 and Eq. 6.7 can be approximated to

$$I_{C_{in,off}} = \frac{V_{OC}}{2R} \tag{6.8}$$

$$I^2_{C_{in,off_{RMS}}} = D' I^2_{in} = \frac{D' V^2_{OC}}{4R^2} \tag{6.9}$$

where D is the duty cycle of the converter and $D' = (1 - D)$.
For the trapezoidal segment of $i_{C_{in}}(t)$ during t_{on} the RMS current into C_{in} is

$$I^2_{C_{in,on_{RMS}}} = \frac{D}{3}\Big[(I_{in} - I_{L_{min}})^2 + (I_{in} - I_{L_{max}})^2 + (I_{in} - I_{L_{min}})(I_{in} - I_{L_{max}}) \Big] \tag{6.10}$$

For both buck and buck-boost converters $I_L = I_{in}/D$, therefore we can write

$$I_{in} - I_L = I_{in}\left(1 - \frac{1}{D}\right) = -I_{in}\frac{D'}{D} \tag{6.11}$$

Knowing that $I_{L_{min}} = I_L - \Delta I_L/2$ and $I_{L_{max}} = I_L + \Delta I_L/2$ we can re-write Eq. 6.10 as

$$I^2_{C_{in,on_{RMS}}} = \frac{D}{3}\left[\left(\frac{\Delta I_L}{2} - I_{in}\frac{D'}{D}\right)^2 + \left(\frac{\Delta I_L}{2} + I_{in}\frac{D'}{D}\right)^2 + I^2_{in}\frac{D'^2}{D^2} - \frac{\Delta I^2_L}{4} \right] \tag{6.12}$$

For both buck and buck-boost converters $\Delta I_L = \dfrac{V_{out} D'}{f_{sw} L}$, so that we can re-write Eq. 6.12 as

$$I^2_{C_{in,on_{RMS}}} = D'^2 \left[\frac{I^2_{in}}{D} + \frac{D V^2_{out}}{12 f^2_{sw} L^2} \right] \tag{6.13}$$

$i_{C_{in}}(t)$ is a periodic waveform composed of two orthogonal piecewise segments [123], therefore its RMS value can be obtained from Eq. 6.9 and 6.13:

$$I_{C_{in_{RMS}}} = \sqrt{D' \left[\frac{I^2_{in}}{D} + \frac{D D' V^2_{out}}{12 f^2_{sw} L^2} \right]} \tag{6.14}$$

The power dissipated on the low-side switch M_{cap} in series with the input capacitors is

$$P_{M_{cap}} = r_{on} I^2_{C_{in_{RMS}}} \tag{6.15}$$

where r_{on} is the on-resistance of the switch used. Section 7.2.2 provides the losses value for the converter used. The switching and body diode losses of M_{cap} are almost irrelevant because they occur for a few μs every T_{meas}.

Referring to Fig. 6.6 and 6.8 now consider what happens when M_{cap} is switched open. In this case the TEGs can supply power to the converter only during t_{on}, because during t_{off} M_1 is open and

current cannot flow into C_{in}, hence the TEGs go to open-circuit. During t_{on} the internal resistance R_{int} limits the quantity of current that can flow from the TEGs, and the body diode of M_{cap} is forced into conduction so that C_{in} supplements the additional current required by the converter and slightly discharges.

After each PWM period T_{sw} the voltage across C_{in} decreases because when M_{cap} is off the input capacitor cannot be charged as it would normally happen during t_{off}. Provided that M_{cap} is left open for just a few PWM cycles, the capacitance of C_{in} is sufficient to prevent $v_{in}(t)$ from decreasing significantly; the following calculations are useful to estimate how much the voltage on the capacitor sags during the V_{OC} measurement.
At the beginning of the V_{OC} measurement procedure the initial energy stored in C_{in} is

$$E_{C_{in}0} = \frac{1}{2} C_{in} V_{C_{in}0}^2 \tag{6.16}$$

To derive the worst case scenario, consider that $I_{L_{min}} - I_{in} \geq 0$ and calculate the energy removed from C_{in} during the t_{on} of one switching cycle:

$$E_{1_{PWM}} = \int_0^{t_{on}} v_{C_{in}(t)} i_{C_{in}(t)}\, dt = \int_0^{t_{on}} \left(I_{L_{min}} - I_{in} + \Delta I_L \frac{t}{t_{on}} \right) V_{in}\, dt = P_{in} D' T_{sw} \tag{6.17}$$

where $v_{in}(t)$ is considered constant at V_{in}. This slightly over-estimates the calculation of the voltage drop because after every T_{sw} $v_{in}(t)$ decreases.
The final energy stored in C_{in} is

$$E_{C_{in}f} = E_{C_{in}0} - n_{PWM} E_{1_{PWM}} = \frac{1}{2} C_{in} V_{C_{in}f}^2 \tag{6.18}$$

where n_{PWM} is the number of PWM cycles elapsed with M_{cap} open. From Eq. 6.18 it is possible to obtain $V_{C_{in}f}$, which is the voltage on C_{in} at the end of the V_{OC} measurement procedure.

6.4 DCD over-voltage snubber

When a TEG is suddenly disconnected from its load it goes to open-circuit after a very fast under-damped oscillation with frequency usually in the order of MHz [60]. This is due to the fact that a parasitic inductance L_P is built up in the many solder connections between pellets in the TEG, in the cables from the thermoelectric device to its load and in the Printed Circuit Board (PCB)'s tracks. Such parasitic inductance forms a resonating tank with the parasitic capacitances of the circuit and it is damped by the TEG's internal resistance R_{int}.
In the circuit of Fig. 6.6, when M_{cap} is closed and M_1 opens at the beginning of t_{off}, I_{in} finds an alternative path into C_{in}, which is a fairly big capacitance. This cannot happen when M_{cap} is open

hence the TEG is suddenly open-circuited. The current in L_p cannot stop flowing instantaneously and its energy is dissipated in the ringing with the parasitic capacitances of the circuit, damped by R_{int}, *i.e.* an RLC circuit. The decrease of I_{in} reverses the voltage across the parasitic inductance, so that a voltage considerably greater than V_{OC} appears at the converter's input.

Fig. 6.9 shows an experimental switching transient test undertaken on one of the TEG modules used. At the beginning of the transient, t_0, the voltage sharply rises from the operating voltage V_{load} to V_{max}; this increases the switching transition losses on M_1 and it also requires M_1 to have a higher maximum drain-source voltage rating. Due to the RLC oscillatory nature, when V_{TEG} reaches V_{max} the inductor current (in blue in Fig. 6.9) reverses and flows into the TEG; the Peltier effect is reversed and the Joule heating is of similar magnitude, therefore it is not a problem for the TEG. The maximum voltage that can be applied to a thermoelectric device in Peltier cooling mode is higher than V_{OC} and a TEG can stand high levels of Joule heating; also, thermoelectric devices do not contain voltage insulating layers or other materials susceptible to voltage stress. However, the additional heat pumped due to the Peltier effect, and the loss of energy harvested from the TEG clearly are undesired consequences of the switching event.

L_P can be approximately calculated from Fig. 6.9. At the end of t_{on} the current $I_{in}(t_{on})$ flows through L_P. In order to avoid ambiguity in the equations, $I_{in}(t_{on})$ will be written $I_{in,t_{on}}$. The energy contained into L_P is

$$E_{L_P} = \frac{1}{2} L_P I_{in,t_{on}}^2 \tag{6.19}$$

This energy is completely transferred to the parasitic capacitance when $V_{TEG} = V_{max}$ and $I_{in} = 0$. The basic inductor relationship $v_L(t) = L\frac{di(t)}{dt}$ can be approximated for L_P to

$$V_{max} - V_{load} = L_P \frac{I_{in,t_{on}}}{t_{max} - t_0} \tag{6.20}$$

where t_{max} is the time at which $V_{TEG} = V_{max}$. L_P can be calculated from Eq. 6.20 using the values obtained from the waveforms of Fig. 6.9. However, it should be noted that the rise of V_{TEG} to V_{OC} is not linear. The linear region is approximately between 20% and 80% of the increase. Dividing $\Delta T = t_{max} - t_0$ in three intervals where the middle interval ΔT_2 corresponds to the linear region, $\Delta T_2 \approx (\Delta T_1 + \Delta T_3)/4$. As a consequence a 'correction factor' can be applied to the calculated value for L_P, which now becomes

$$L_P = \frac{\Delta T(V_{max} - V_{load})}{4 I_{in,t_{on}}} \tag{6.21}$$

In order to damp the over-voltage, while still achieving a fast transient of the TEG's voltage to open-circuit, a capacitor C_S is added across the TEG's terminals. C_S needs to be sufficiently large so that the energy transferred from L_P does not charge it to much more than V_{OC}, but small enough to let V_{TEG} quickly settle to V_{OC}. The value of such capacitor can be chosen using the energy calculated in Eq. 6.19. Before the transient C_S is already charged at V_{load}, with a stored energy $1/2 C_S V_{load}^2$. If all the energy in L_P is to be transferred to C_S when it reaches V_{OC}, then the energy balance states

that

$$\frac{1}{2}L_P I_{in,t_{on}}^2 = \frac{1}{2}C_S \left(V_{OC}^2 - V_{load}^2\right) \tag{6.22}$$

When working at MPP $V_{OC} = 2V_{load}$, therefore Eq. 6.22 leads to $C_S = L_P/3R_{int}^2$. However, given the wide range of V_{load} (depending on the temperature difference), the choice of C_S is by necessity a compromise. Experiments have shown the following solution to yield the most satisfactory value for a wide operating temperature range:

$$C_S = \frac{L_P}{R_{int}^2} \tag{6.23}$$

which corresponds to removing the DC offset V_{load} in C_S from Eq. 6.22, which becomes $L_P I_{in,t_{on}}^2 = C_S V_{load}^2$. It is convenient to design the snubber capacitor C_S for I_{MP} at ΔT_{max}.

These results are now applied to the experimental case of Fig. 6.9, in which $\Delta T = 0.37\,\mu s$, $V_{max} - V_{load} = 18\,V$ and $I_{in}(t_{on}) = 2.17\,A$. Using Eq. 6.19 L_P is estimated at $767\,nH$, hence using Eq. 6.23 the required snubber capacitor is $174\,nF$.

Fig. 6.10 shows the improvements to the TEG's transient response when adding a $220\,nF$ ceramic capacitor (commercial value closest to $174\,nF$), during the same operating conditions. Also, two diodes, D_{S1} and D_{S2}, are used to add some damping due to their conduction resistances, and to provide a Schmitt-trigger function because of their voltage drops. Its use is shown in Fig. 6.13. The resulting circuit is effectively a *DCD snubber* (diode - capacitor - diode), which suppresses over-voltages storing energy during t_{off} and releasing it back during t_{on}. Fig. 6.10 also includes results using the proposed DCD snubber circuit. The peak over-voltage transient is reduced from $18\,V$ to $1\,V$ in both cases. Experimental and simulation results have consistently demonstrated that the settling time is shorter when the two diodes are used. By way of comparison, the settling time is reduced from $2.5\,\mu s$ to $2.09\,\mu s$ with the capacitor only, and to $1.48\,\mu s$ with the DCD snubber circuit. It is a design choice to use smaller values for the snubber capacitor in order to reach a compromise between speed of transient response and magnitude of over-voltage. Emphasis on the choice due to the higher energy and higher output voltage produced at the top end of the temperature range should be considered.

As an alternative it would not be possible to use a Transient Voltage Suppression (TVS), because the TEG's open-circuit voltage varies in virtually all TEG applications (the exception being the radio-nuclide generators used on satellite power supplies), therefore a constant breakdown voltage cannot be selected.

6.5 Synchronous Buck-Boost

During this work, several converters were developed with power ratings from $10\,W$ to $100\,W$. A Buck converter was presented in [112], while this thesis focuses on a four-switch version of the

Operating Mode	G_1	G_2	G_3	G_4
Boost	high (1)	low (0)	PWM_1	PWM_2
Buck-Boost	PWM_1	PWM_2	PWM_1	PWM_2
Buck	PWM_1	PWM_2	low (0)	high (1)

Table 6.1: State of the converter's switches needed for operation in Boost, Buck-Boost or Buck mode.

buck-boost, which is commonly referred to as the *synchronous* Buck-Boost. This converter accepts a wide input voltage range, smaller or greater than the output voltage (which is fixed by the battery voltage), and consequently is able to harvest power from the TEGs over a wide range of temperature differences. Also, it is able to work in 'buck-only' or 'boost-only' mode, with high efficiency (reduced switching losses and larger step-down and step-up ratios). This converter can be used without knowledge of the electrical characteristic of the TEGs used, provided that the maximum and minimum ratings for current, voltage and power are respected.
The converter supplies power to a lead-acid battery and to an auxiliary electronic load. A microcontroller, measuring the input and output voltages, computes the MPPT algorithm and controls the gate drivers of the converter's MOSFETs. Fig. 6.11 shows the block diagram of the resulting TEG system.
This section presents the non-inverting synchronous Buck-Boost DC-DC converter in three slightly different configurations.

The most commonly known version of the non-inverting synchronous Buck-Boost converter [124, 125, 78, 79, 126] uses four switches to select between the boost, buck-boost or buck operating modes. The basic circuit is shown in Fig. 6.12 and the operating mode is selected as listed in Table 6.1. More details on this type of converter are presented in Section 6.5.3.

6.5.1 Three-switch synchronous Buck-Boost

In case the converter runs in Discontinuous Conduction Mode (DCM) when the TEG's current is low [113], the battery would discharge through M_2 and M_4. To prevent this occurrence, the output switch M_4 can be replaced by a Schottky diode to block reverse current flow. The schematic of the resulting topology of the synchronous Buck-Boost with three switches and an output diode is shown in Fig. 6.13. A generic TEG is represented by a voltage source V_{OC}, an internal resistance R_{int} and a parasitic inductance L_p. The DCD snubber circuit described in the Section 6.4 is connected across the input of the converter to suppress over-voltage transients. In order to maintain the high-side MOSFETs continuously "on" in Boost-only mode the charge pump technique of Fig. 6.3 is used together with the *Texas Instrument* LM5109 gate drivers powered by the battery.
A *Microchip* PIC16F microcontroller activates the gate drivers with two 180° anti-phase PWMs, running at $78\,kHz$. The microcontroller measures the TEG voltage at the converter's input and

the battery's voltage at the output. After measuring the open-circuit voltage V_{OC} the algorithm calculates the initial PWM duty cycle using the ideal relation: $2V_b/V_{OC} = D/(1-D)$. At every successive microcontroller's program iteration the input voltage V_{in} is measured and a digital control loop keeps on adjusting the duty cycle to maintain $V_{in} = V_{OC}/2$. In this way the converter minimises parasitic effects and deals with changes in the battery voltage, *e.g.*, load transients.
Several converter PCBs were created using different component models for the power MOSFETs, depending on the voltage and current ratings. The maximum TEG's voltage mainly influences the drain-source breakdown voltage rating; high current values call for low *on-resistance*. Commonly used packages are DPAK and SOIC. The electrolytic capacitors used are *Rubycon* ZL, ZLJ, ZLH or ZLK Series, which can handle high RMS current ripple. The inductors are *Coilcraft* SER2000 or SER2900 Series, which offer a good compromise between cost, dimensions, weight and can handle relatively high currents with low series resistance. An example PCB is shown in Fig. 6.14

6.5.2 The open-circuit measurement

The V_{OC} measurement is performed every $500\,ms$ and it lasts for 8 switching cycles T_{sw}, which corresponds to less than $110\,\mu s$ for the $78\,kHz$ switching frequency used. Considering a PWM duty cycle of 50 % the converter is disconnected from the TEGs for just 0.011 % of the time and this has a tiny impact on the overall system efficiency.
Fig. 6.15 shows the converters input voltage and current during the V_{OC} measurement. The converter is initially running at $13.35\,V, 2.07\,A$ at the input. After $45\,\mu s$ M_{cap} is switched off therefore the input voltage goes to V_{OC}, during t_{off}, after an overshoot of less than $6\,V$ when using a DCD snubber with $100\,nF$ ceramic capacitor. The Analogue-to-Digital Conversion (ADC) measurement starts $2\,\mu s$ after the PWM goes low. It can be noted that during t_{on} current is drawn from the TEGs and that during the V_{OC} measurement the voltage across the input capacitors decreases from $12.86\,V$ to $12.46\,V$ as described by Eq. 6.18. The initial drop from $13.35\,V$ to $12.86\,V$ is due to the voltage drop across the body diode of M_{cap}.

6.5.3 Reverse current protection at light-load

The switch M_4 of Fig. 6.12 was replaced in 6.5.1 with a diode to protect against reverse current flow. The four-switch synchronous Buck-Boost introduced in Fig. 6.17 requires protection against reverse current flow in DCM, which occurs if the current in the inductor falls to zero before the end of t_{off} of PWM_1. This situation is problematic in buck-boost or buck only mode, when reverse current can flow to ground because M_2 and M_4 are closed. This situation can occur not only when the power source is constituted by TEGs, but also with other energy sources, *e.g.*, solar cells. A possible solution is to sense when the output current becomes null (the voltage across the inductor

is zero) and to open M_2.

The circuit of Fig. 6.16 has been developed for this task. It uses a current transformer to convert current into a measurable voltage. A comparator detects when the voltage across R_s falls to zero with a temporal offset prediction that can be tuned by means of the two resistors R_u and R_d. The RC filter provided by R_a and C_a can be used to measure the average output current. R_p and D are necessary to provide a reset path for the transformer to prevent core saturation.

A similar result could be achieved sensing the voltage across a shunt resistor placed in series with the inductor, but this solution would introduce additional I^2R losses since the entire inductor current would flow through this resistance which would have to be of relative high value to enable accurate detection of the onset of DCM.

6.5.4 Four-switch synchronous Buck-Boost

The schematic diagram of the complete TEG system with the four-switch synchronous Buck-Boost is shown in Fig. 6.17.

The DCM detection circuit of Fig. 6.16 is introduced in Fig. 6.17 instead of the ammeter I_{out}.

The microcontroller uses two pins EN_1 and EN_2 to select the operating mode and five external logic ports (*Diodes Incorporated* 74LVC1G Series) as shown in Fig. 6.18. The ouput of the comparator of Fig. 6.16 is used to open M_2 when the output current goes to zero during t_{off} of PWM_1. Boost-only mode is selected when $EN_1 = 1, EN_2 = 0$; buck-only when $EN_1 = 0, EN_2 = 1$; buck-boost when $EN_1 = 0, EN_2 = 0$.

The converter PCB which makes use of the circuits presented in this section is shown in Fig. 6.19

6.6 Experimental results

Three experiments were designed to test the steady-state and transient performance of the MPPT converter with the output diode of Fig. 6.13. However, similar results could be obtained for any converter utilising the MPPT technique presented in Section 6.3.1, because these tests aim at characterising the MPPT ability of converter, not its electrical efficiency.

The three TEG devices GM250-127-14-10 described in Section 4.3 were electrically connected in series. The maximum open-circuit voltage is approximately $27\,V$ and the maximum power is approximately $30.4\,W$ at $V_{MP} = 13.5\,V$ and $I_{MP} = 2.25\,A$. The choice of using three TEGs is dictated by the need of testing the MPPT converter around its power rating and with a relatively high maximum TEG voltage. As explained in Section 4.3 not only are the performances of the three devices almost identical, but the mathematical characterisation guarantees the estimation of performance relative

to each independent TEG device.

As a first step, the steady-state converter performance is measured using TEGs. To test the converter's response to a sudden V_{OC} transient, the TEGs are substituted with a programmable PSU in series with a power resistor. This allows the generation of voltage steps that could not be obtained from a physical TEG system with high thermal mass, at least with the energy levels available in the laboratory. Finally, a long thermal transient was created using the test rig, to analyse the tracking performance of the MPPT converter during continuously-changing thermal operating conditions.
The PCB used is not equipped with a current sensor, therefore it cannot be used for experimental comparison with other MPPT techniques. However, where possible the obtained performance are compared to results found in the literature. In all the experiments a $12\,V, 7\,Ah$ lead-acid battery is used to accumulate the power transferred through the converter. An electronic load was also connected to prevent the battery from over-charging.

6.6.1 Steady-state performance

The aim of this experiment is to compare the power extracted by the MPPT converter to the maximum power available from the three TEGs, each maintained at the same temperature difference. Three separate tests have been undertaken, each one selecting a different thermal operating point, *i.e.* temperature gradient across the devices. The temperature gradients used are $\Delta T = 100°C, 150°C, 200°C$, which are the same used for the electrical characterization of the devices in Section 4.3.
When the three modules are electrically connected in series their open-circuit voltages and internal resistances sum so that the resulting array can still be represented by a voltage source in series with an internal resistance and the MPP remains at half V_{OC}, as confirmed in Section 4.5.2. The procedure to compare the electrical operating point set by the converter to the MPP is the following:

1. Confirm that the actual series open-circuit voltage $V_{OC,S} = V_{OC,1} + V_{OC,2} + V_{OC,3}$ from Table 4.2.

2. Calculate the theoretical current for maximum power: $I_{MP} = \dfrac{V_{OC,S}}{2(R_1 + R_2 + R_3)}$

3. Calculate the theoretical MP: $P_{max} = V_{MP} I_{MP} = \dfrac{V_{OC,S}^2}{4(R_1 + R_2 + R_3)}$

4. Read the current I_{op} set by the MPPT converter

5. Use I_{op} to calculate the actual power produced by each of the three TEGs, using the individual 'mathematical' formulation from Eq. 4.3 ($\pm 1.5\,\%$ accuracy).

	Exp Max Power		MPPT Converter		
ΔT ($^\circ C$)	I_{MP} (A)	P_{max} (W)	I_{MPPT} (A)	P_{MPPT} (W)	P_{var} (%)
100	1.38	10.09	1.33	10.07	0.15
150	1.84	19.88	1.84	19.89	0.00
200	2.17	30.06	2.09	30.02	0.14

Table 6.2: Comparison of the steady-state tracking performance of the MPPT converter with the maximum available power from the series-connected array.

It is important to note that it is not possible to sum the individual values of maximum power from Table 4.2 (and thus replace points 1. to 3.) because those MPPs are relative to slightly different values of current, which are not possible to have in a series array.
As an alternative, it would also be possible to use the voltage reading from the multimeter or the oscilloscope, however this procedure is less precise due to the switching noise; the current reading is measured with both a multimeter and an oscilloscope probe. The results of the steady-state test are summarised in Table 6.2. The last column shows that the MPPT converter has an accuracy, sometimes called *tracking efficiency*, of 99.85 % (calculated with a maximum error of 1.5 %).
The fractional open-circuit voltage MPPT converter presented in [89] maintains the input voltage within 5 % of $V_{OC}/2$ except for small values of V_{OC}. In [73] fractional short-circuit and P&O are compared but the MPPT efficiency is not calculated. The INC MPPT control proposed in [84] shows a 95 % tracking efficiency. The P&O MPPT converter of [83] is calculated to have around 99 % tracking efficiency, but this is not accurately proved experimentally, as done in this work.

6.6.2 Sudden-transient performance

This test allows characterising the settling response of the converter after a step change in open-circuit voltage. Such a test cannot be performed with real TEGs: it is impossible to instantaneously change their open-circuit voltage, therefore the TEGs have been replaced by a power supply in series with a power resistor of 4.7 Ω. Fig. 6.20 shows the response of the MPPT converter after a V_{OC} step from $10V$ to $20\,V$. After measuring the open-circuit voltage for $141\,\mu s$ (DCD snubber with $100\,nF$ ceramic capacitor), the MPPT converter regulates the input voltage to half of V_{OC} in $8\,ms$. It can be noted that the input voltage starts at $5\,V$ and ends at $10\,V$ which correspond to half of $10\,V$ and $20\,V$ respectively, as expected.
A similar test was undertaken in [84], demonstrating a $300\,ms$ settling time.

6.6.3 TEG transient performance

The third experiment assesses the ability of the MPPT converter to respond to changes of the thermal input power to the TEGs, *i.e.* changes of the temperature gradient. In the test rig the fastest thermal transient occurs during the cool down of the TEGs. The TEGs are initially maintained at $200°C$, then the power to the heaters is disconnected and the temperature difference diminishes at a rate of $0.25°C/s$ due to the heat absorbtion capacity of the water cooling system and the thermal conductivity of the TEGs. A datalogger records all the temperatures, while two multimeters measure the converter's input voltage and current. Both instruments are controlled by an *Agilent* VEE program that records all the data in spreadsheet format.
The temperature differences across the three devices are not always exactly the same at any given instant, therefore the actual power extracted by the MPPT converter is compared to the theoretical maximum power available, as calculated for the steady-state experiment. This experiment is effectively a continuous series of steady-state experiments because the thermal time constant of the TEG system is much slower than the transient response of the converter, which samples and then adjusts the operating point every $0.5\,s$. The results (in blue) are shown in Fig. 6.21, where a $\pm 2\,\%$ margin has been added over the maximum available power (in red), to take into account the accuracy of the mathematical characterization and measurement errors. Considering each point, the average tracking efficiency of the MPPT converter is $98.7\,\%$.

None of the MPPT converters for TEGs presented in literature is tested with a TEG thermal transient in a similar way as done in this work. The test rig used cannot provide faster temperature transients, however it must be noted that due to how this MPPT algorithm is computed, without any integral term, the converter can track the MPP every $500\,ms$, even if this period could be simply reduced in the microcontroller's code. It has been selected based on practical experience about the thermal time constant of the thermoelectric system.

6.7 Distributed MPPT for TEG systems

As the use of TEGs extends into progressively lower cost applications, or higher power unbalanced systems, the overall system economics dictate that a compromise must be found between the number of MPPT converters and the number of TEG modules connected to each converter. Problems of decreased thermal efficiency (due to the parasitic Peltier effect) or decreased power output arise if the TEGs connected in the same array are subject to temperature mismatch because the MPPT converter sets the same suboptimal electrical operating point for each module in the array.

This leads to the formation of what is called a distributed MPPT subsystem (DMPPT) in which each TEG array's electrical operating point is controlled independently [68], in a similar way as for

photovoltaic systems [67]. The primary motivation for this approach is that if the TEGs in the same system are likely to be subject to different temperatures their optimum operating point may vary considerably.

The analysis in Chapter 4 showed that in most TEG systems the individual thermoelectric modules are subject to temperature mismatch. Consequently, when in operation each TEG will have a different maximum power point. Ideally each TEG should be independently electronically controlled but this would greatly increase the number and complexity of the MPPT power electronic converters needed and adversely affect the cost of implementing the system. Also, it is often convenient to electrically connect several thermoelectric modules in series or parallel to increase the voltage and current levels such that the converter can efficiently transform the resultant output to the system voltage required in a single step-up or step-down stage.

6.8 Conclusions

This chapter presented an effective technique to obtain the open-circuit voltage measurement of a TEG, with minimal disconnection of the load. The MPPT algorithm is programmed to a low-cost microcontroller and does not require expensive sensors; it checks the open-circuit voltage every $500\,ms$ and accurately adjusts the optimum operating point in less than $10\,ms$.
The power converter used is a DC-DC non-inverting synchronous Buck-Boost with high conversion efficiency which can work in boost-only, buck-boost or buck-only mode, thus enabling the extraction of power over a wide range of temperature differences across the TEG.
The presented MPPT system was tested under steady-state and transient conditions with real TEGs, demonstrating its ability to set the optimum electrical operating point quickly and very accurately. It is able to extract close to $100\,\%$ of the maximum power that can be produced by the TEG in steady-state and $98.7\,\%$ during thermal transients.
Future work will focus on comparing the proposed MPPT technique to other MPPT algorithms, and on integrating several MPPT converters together to form a DMPPT system.

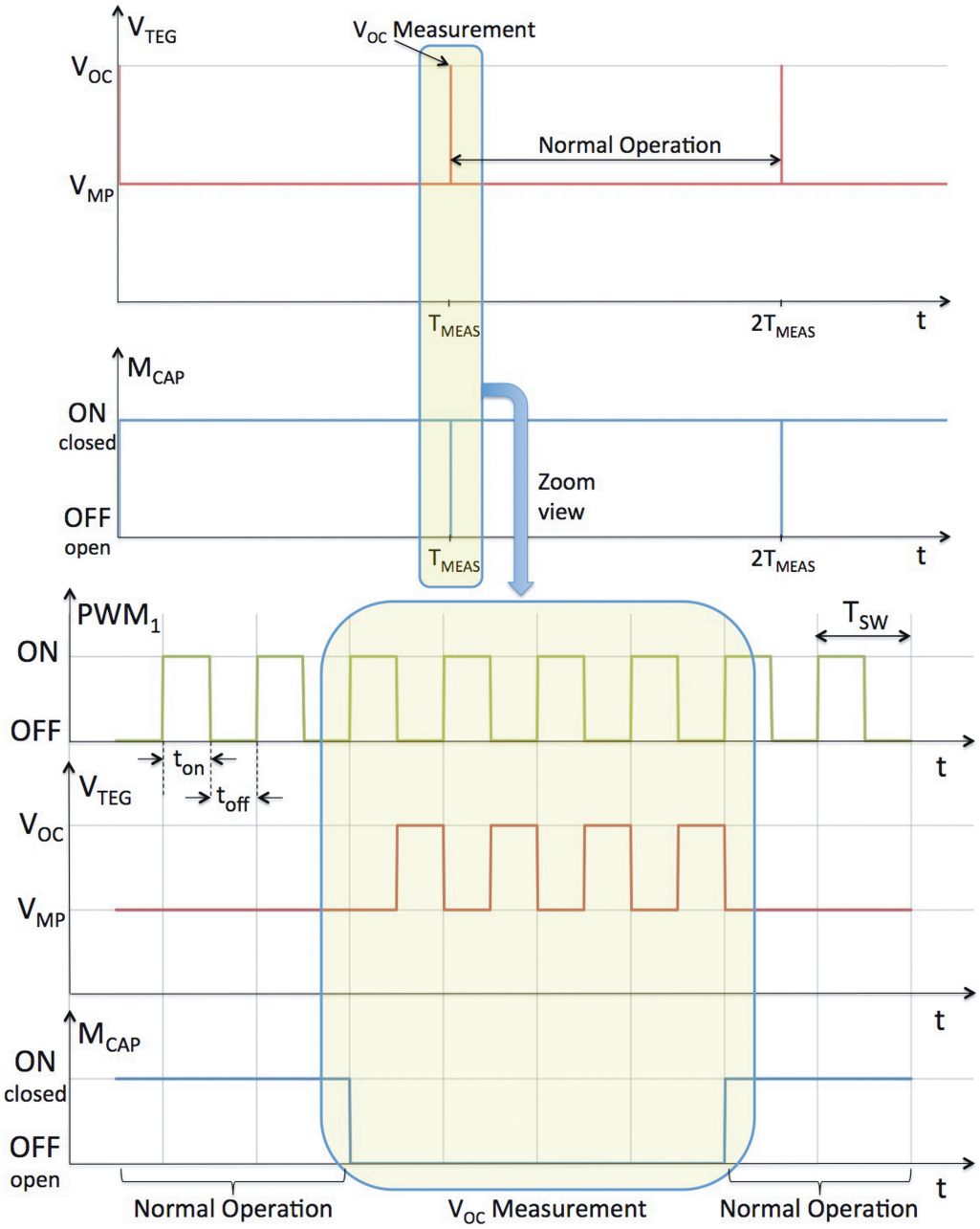

Figure 6.7: Timing diagram explaining how the open-circuit voltage measurement is achieved. The bottom part of the image provides an expanded view of the measurement operation, which takes place every T_{meas}.

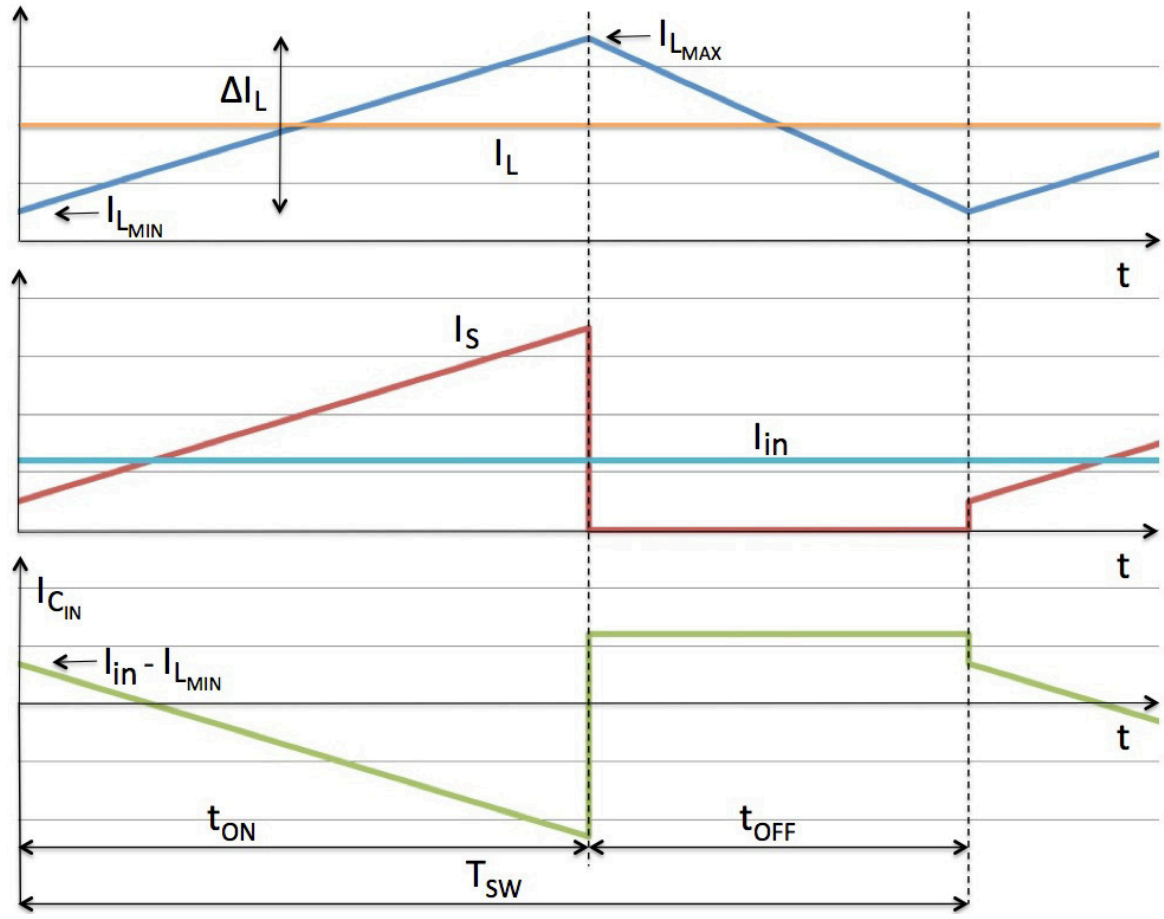

Figure 6.8: Plots of the currents in a Buck or Buck-Boost derived converter (values are generic): in the inductor (I_L blue, and $I_{L_{AVG}}$ orange); in the the switch (I_S red) and average input current (I_{in} light blue); in the input capacitor ($I_{C_{in}}$ green).

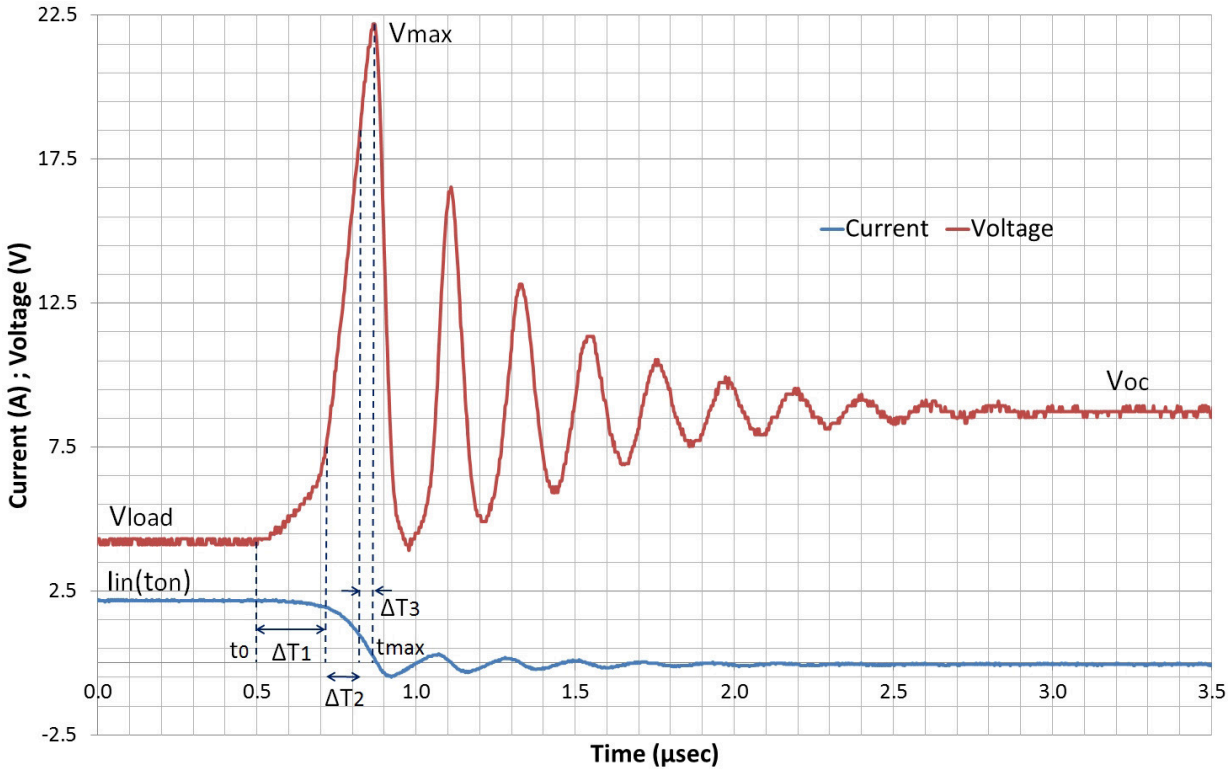

Figure 6.9: TEG's voltage and current during a switching transient from at-load operation to open-circuit.

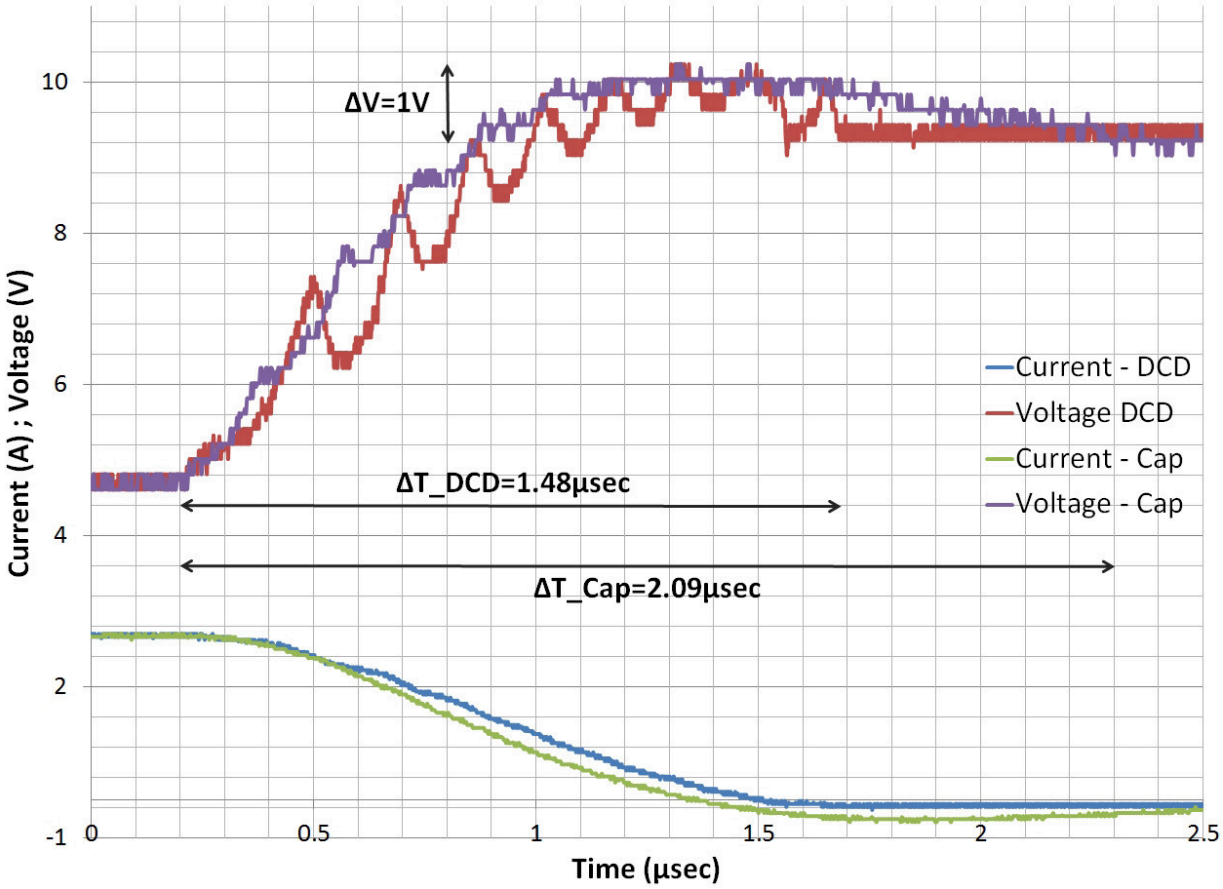

Figure 6.10: Experimental comparison of TEG's voltage and current during a switching transient from at-load operation to open-circuit, when using a damping capacitor only or with the proposed DCD snubber.

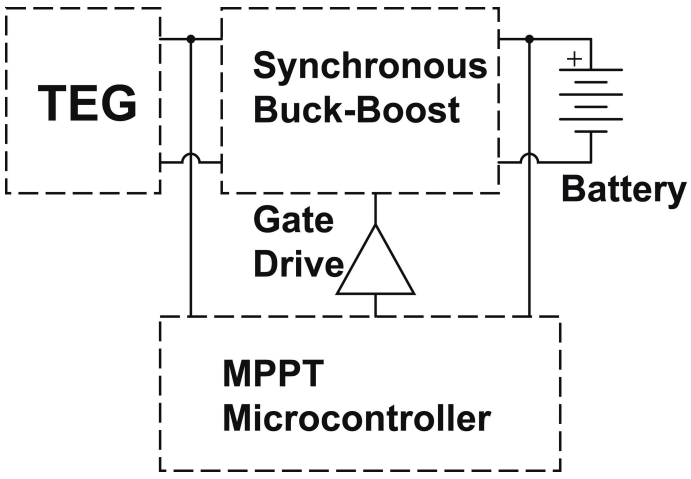

Figure 6.11: Block diagram illustrating the fundamental structure of the proposed system.

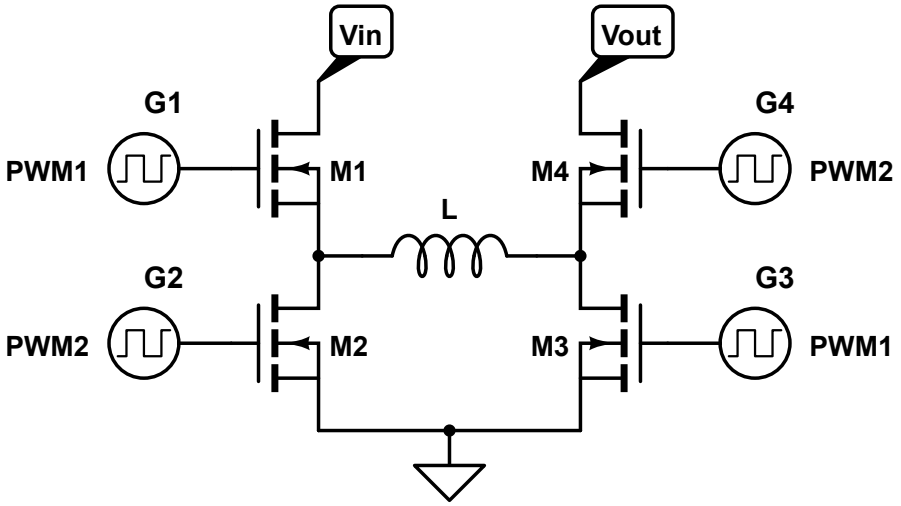

Figure 6.12: Basic circuit of the four-switch synchronous Buck-Boost.

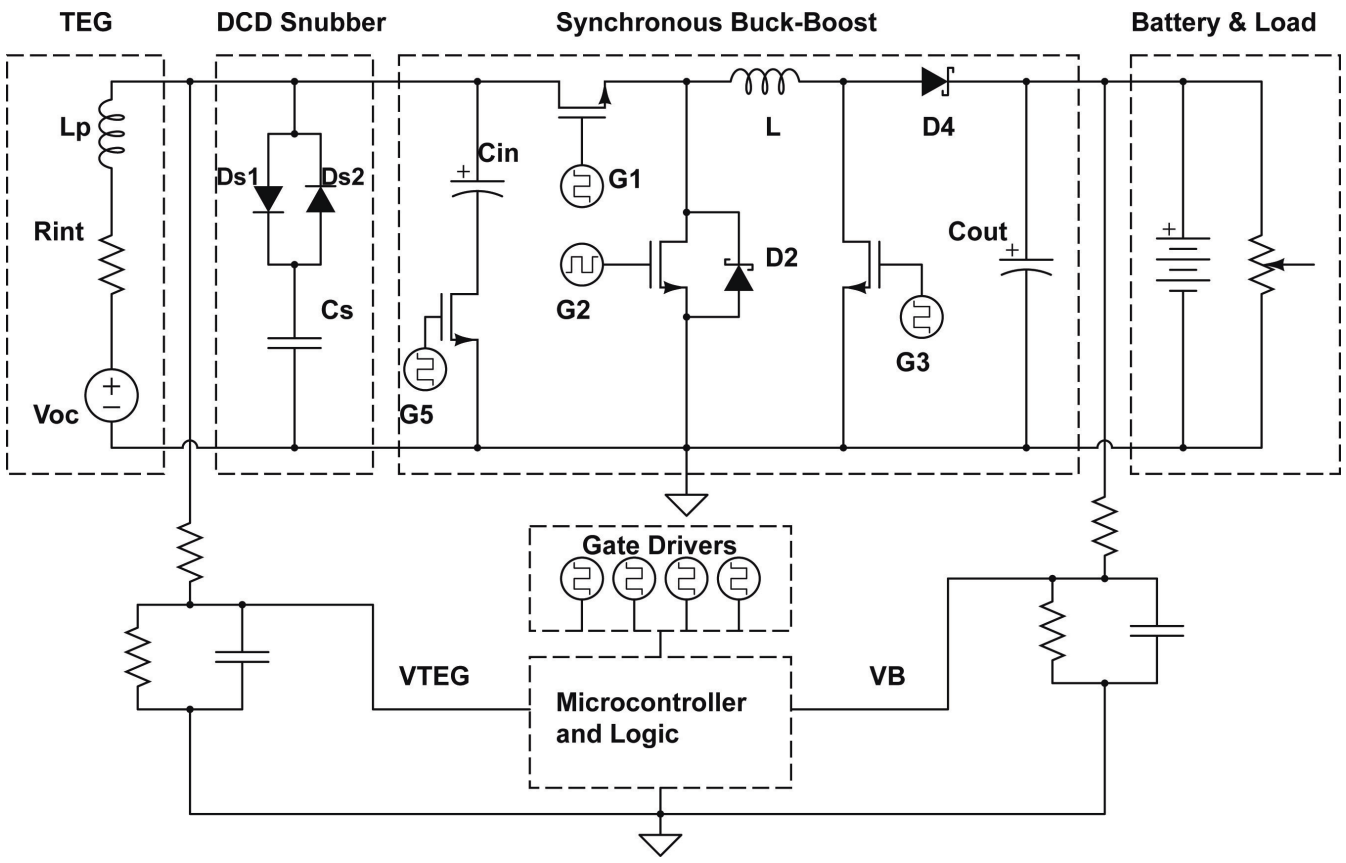

Figure 6.13: Schematic of the complete TEG system using the synchronous Buck-Boost with output diode.

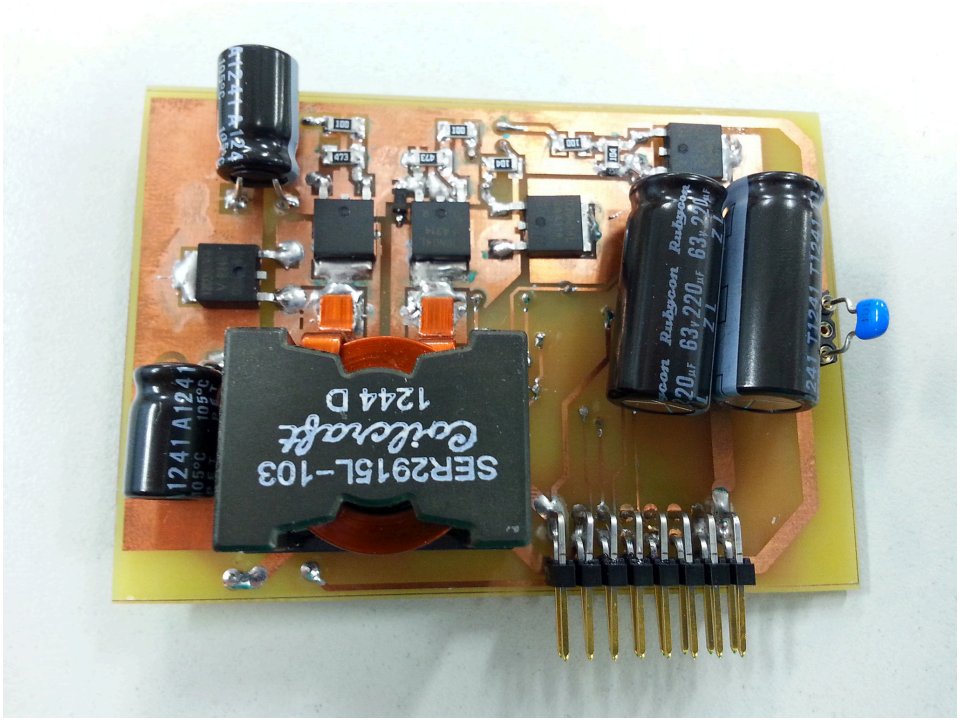

Figure 6.14: Top layer of a prototype PCB with a synchronous Buck-Boost with output diode.

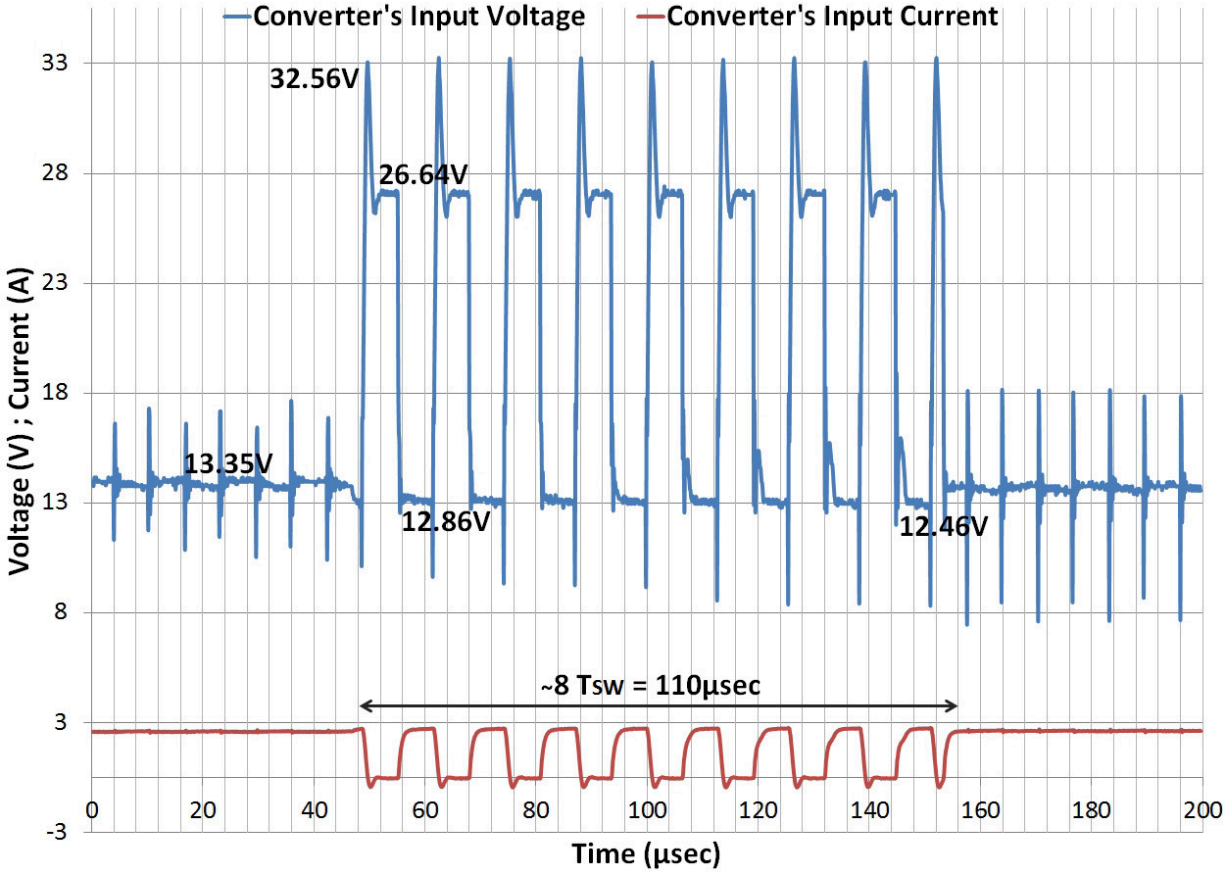

Figure 6.15: Converter's input voltage and current during the measurement of the open-circuit voltage.

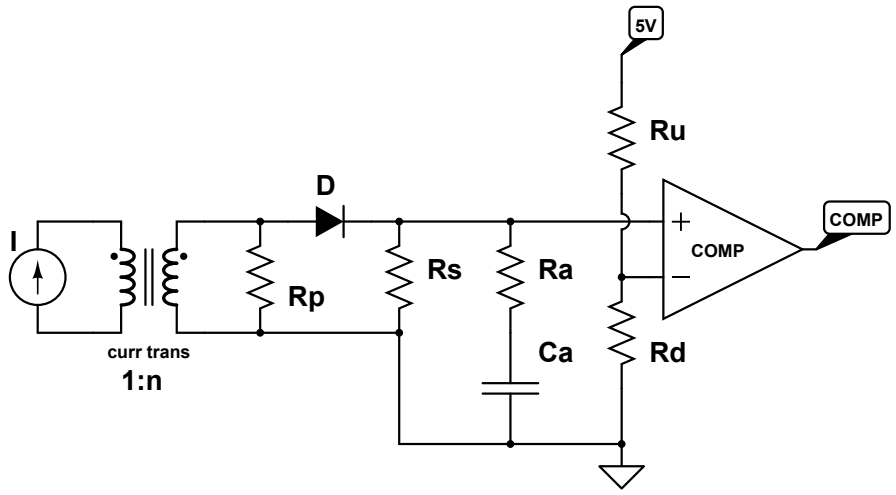

Figure 6.16: Circuit to detect DCM operation of the converter, using a current transformer.

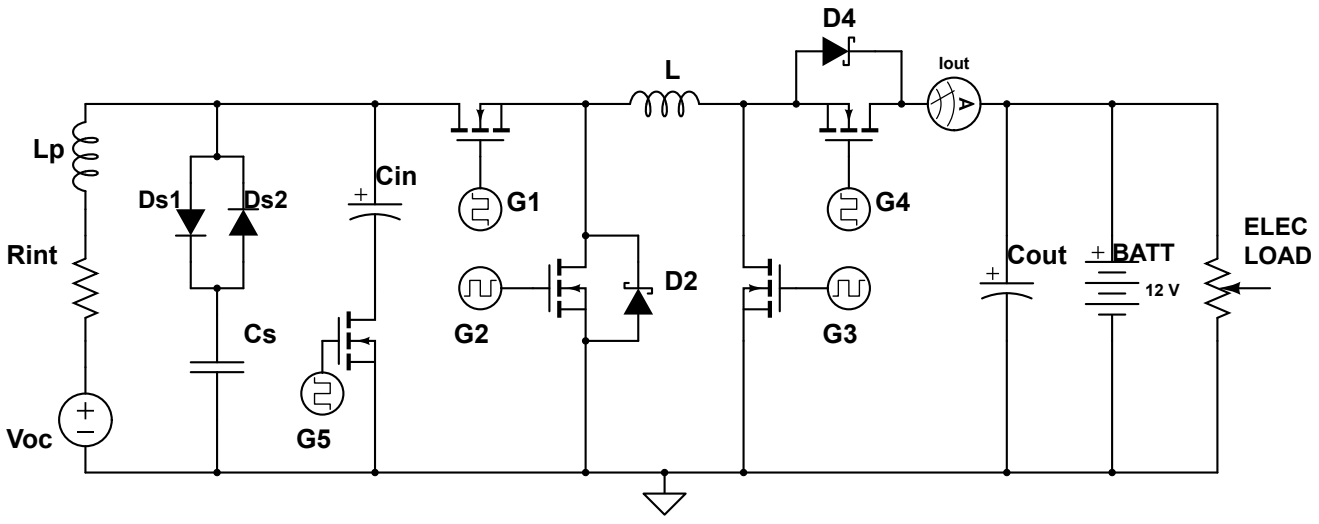

Figure 6.17: Circuit schematic of the complete TEG system using the four-switch synchronous Buck-Boost.

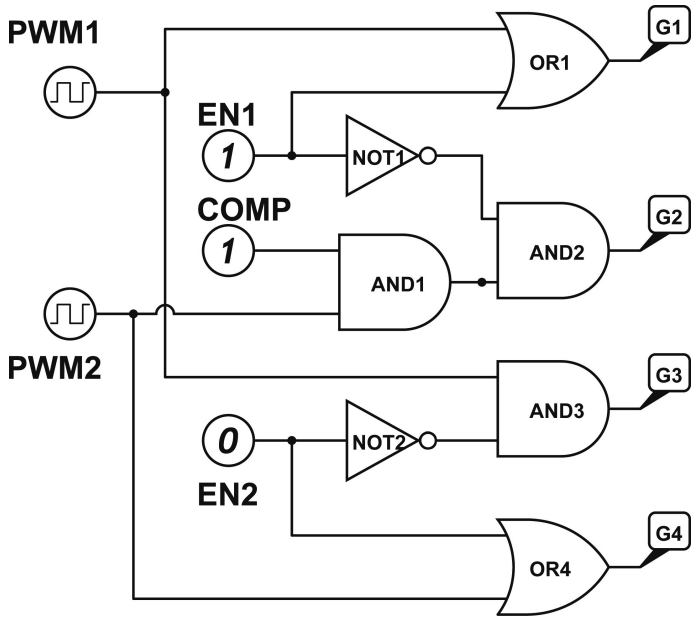

Figure 6.18: Schematic of the logic gates used to select the converter's operating modes.

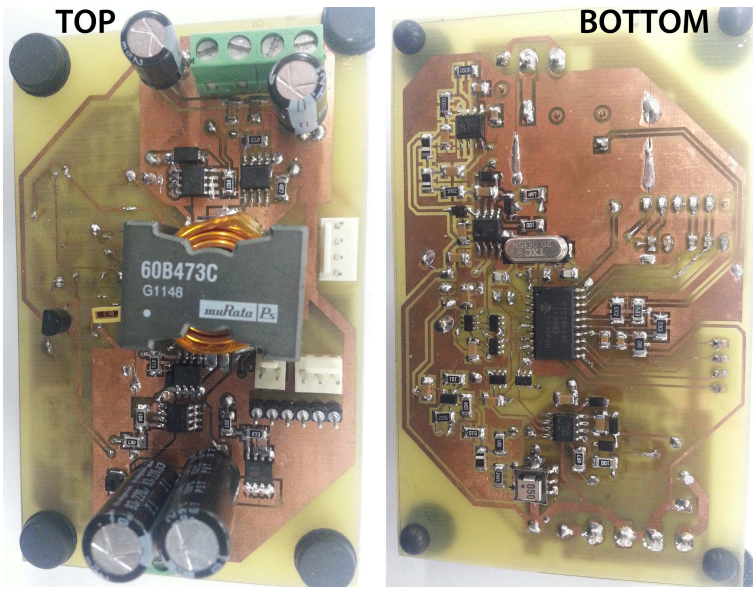

Figure 6.19: Image of the PCB of the MPPT synchronous Buck-Boost converter with four switches.

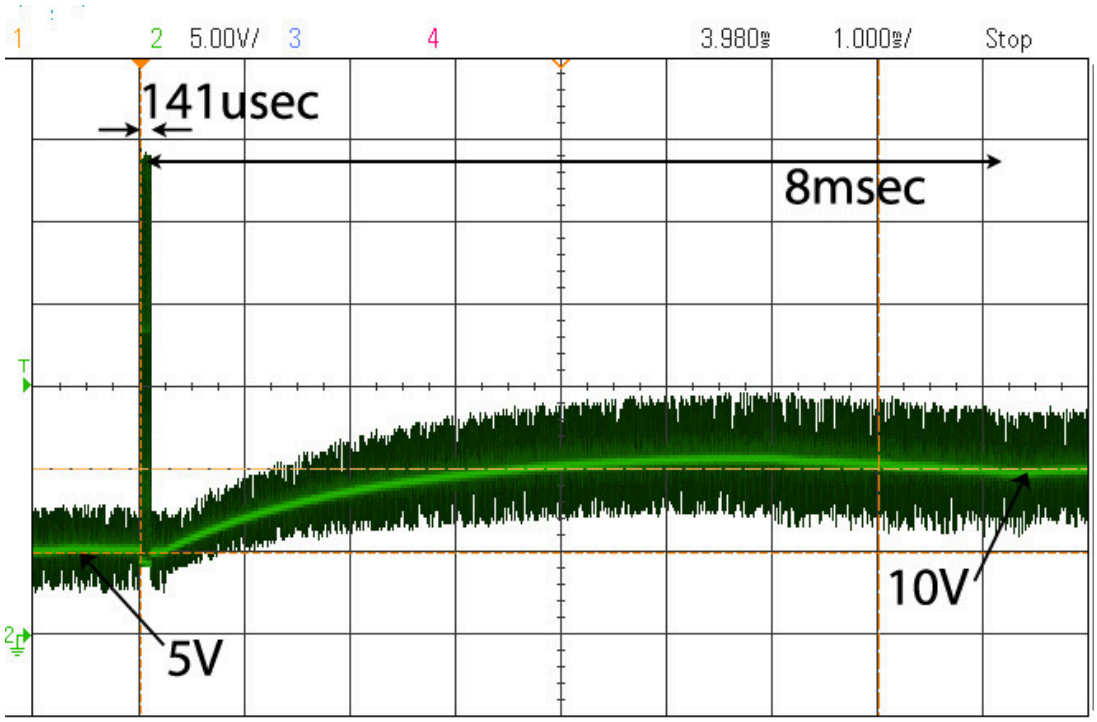

Figure 6.20: Converters input voltage after a V_{OC} step-up from $10\,V$ to $20\,V$. Time: $1\,ms/div$ (x-axis); Voltage: $5\,V/div$ (y-axis).

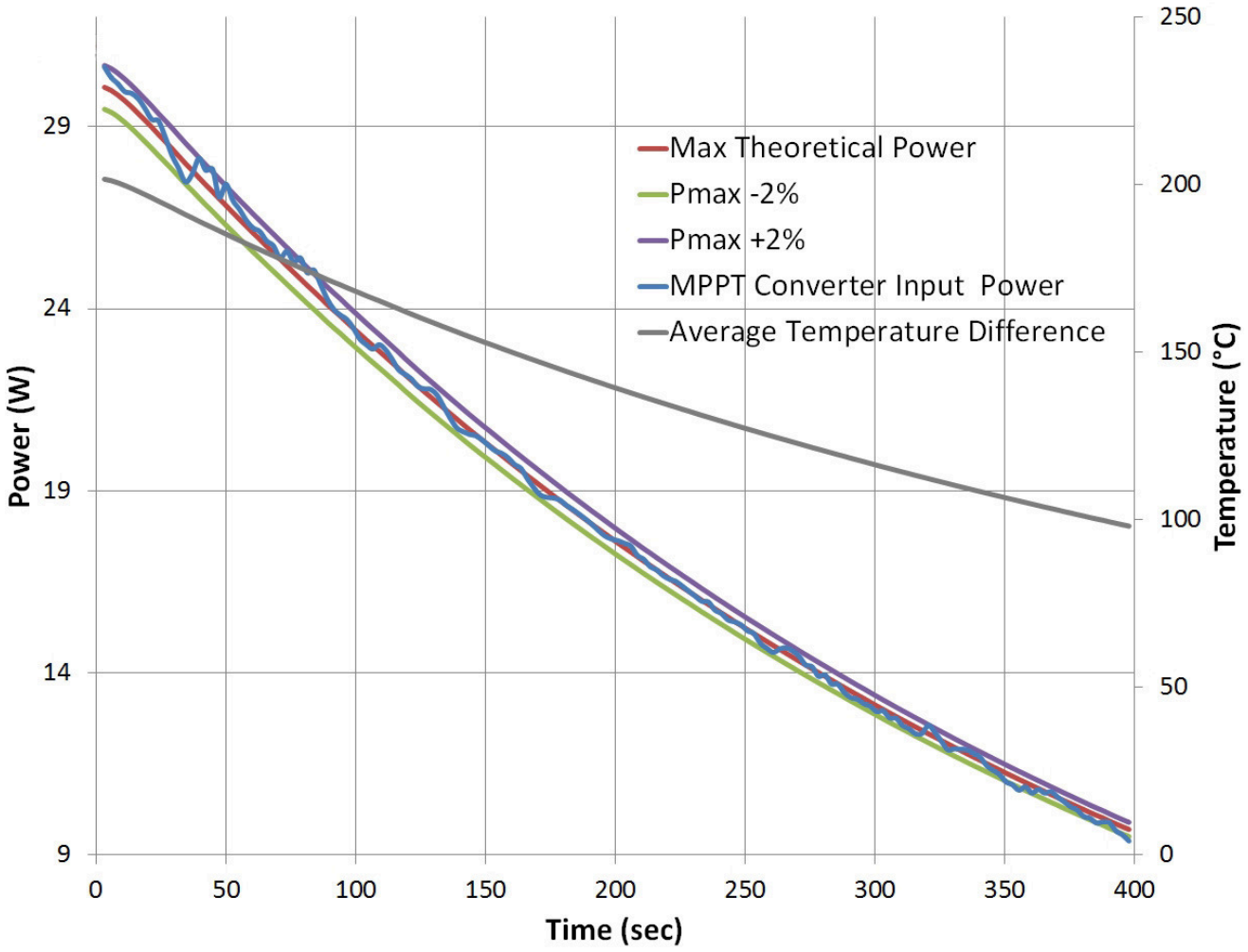

Figure 6.21: Thermal transient from $\Delta T = 200°C$ to $\Delta T = 100°C$ across the three TEGs. Available and extracted output power on the left y-axis and temperature difference on the right y-axis.

Chapter 7

Applications of Thermoelectric Generators

This chapter examines two applications of thermoelectric generators: a symbiotic system to produce electricity from the heat produced by a stove, while pre-heating the cold water; and the recovery of heat from the exhaust gas system of internal combustion engines. For each application, two slightly different systems are proposed. For the stove application, first four Bi_2Te_3 TEGs are used, then a cascade arrangement of two TEGs is described. For the application of TEGs to the automotive system the work undertaken for two industry-led research projects is presented.

7.1 Stove CHP systems

The concept behind this application was first suggested by Min and Rowe [23]. Part of the heat produced by a common stove, burning coal, wood or charcoal is directed through a TEG to circulating cold water in such a way that the cold water is heated up and the TEG produces electrical energy. This is effectively a CHP system. The following two sections present the experimental systems and results when using four TEG devices thermally in paralell or two cascaded TEGs thermally in series.

The block diagram for the two applications of TEGs to the stove is shown in Fig. 7.1. The TEG is positioned between two Aluminum blocks: the hot block is partially inserted into the top opening of the stove and the cold block is water-cooled by a chiller. A clamping mechanism, not shown in Fig. 7.1, ensures good mechanical pressure on the TEG system and provides mechanical compliance during thermal expansions or contractions.
The Bi_2Te_3 TEGs used in the stove experiments are the GM250-241-10-12 produced by *European Thermodynamics Ltd.* Their electrical characterisation is shown in Fig. 4.16.

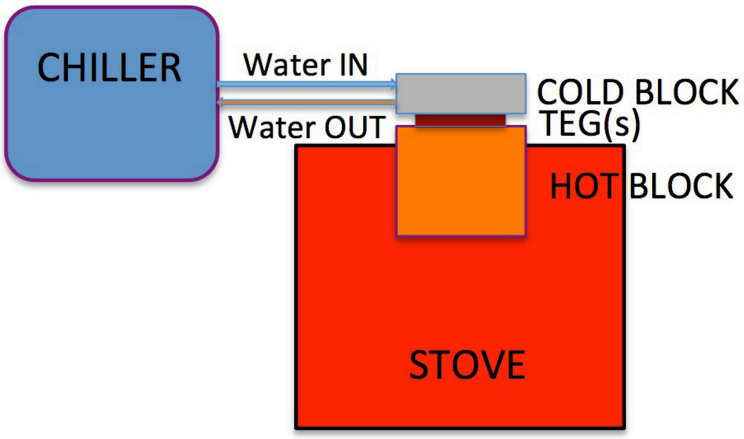

Figure 7.1: Generic schematic diagram of the system used for the application of TEGs to the stove.

7.1.1 Stove with four TEGs

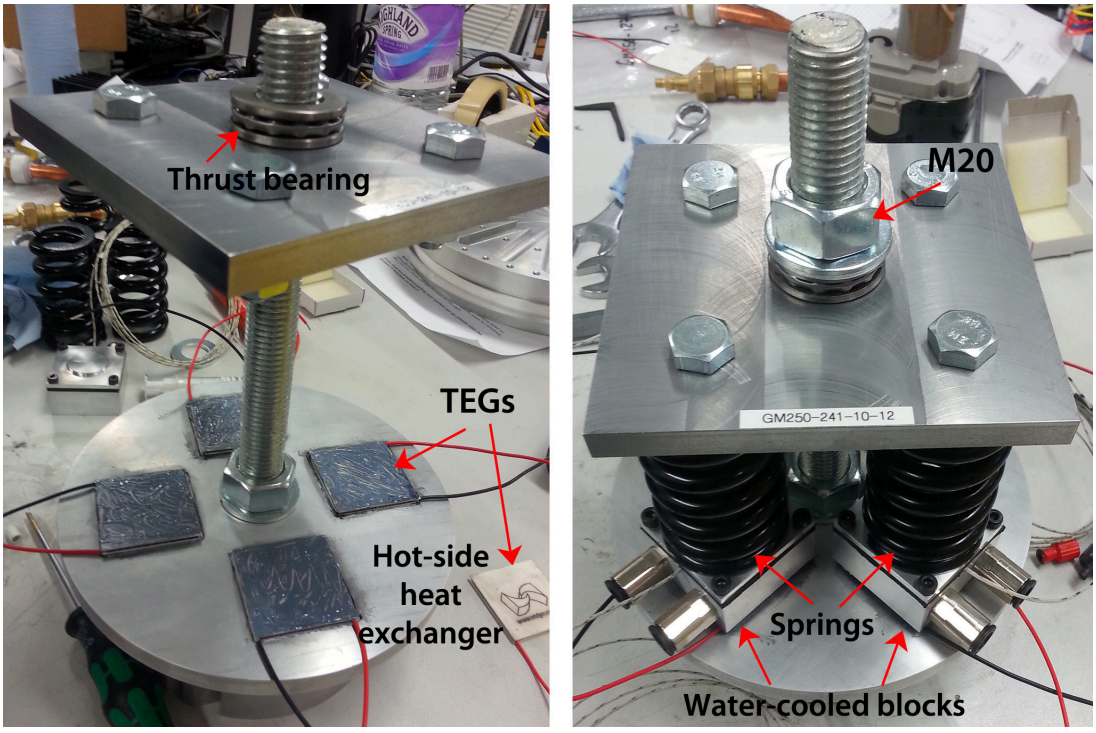

Figure 7.2: Pictures of the mechanical fixtures to use four $40x40\,mm^2$ TEG devices with the stove.

The first system comprises of a common hot-side heat exchanger on which are placed four Bi_2Te_3 TEGs, each with its individual cold block. All the Aluminium blocks are custom designed and are shown in Fig. 7.2. The bottom part of the hot-side heat exchanger (shown in Fig. 7.6) has fins to improve the capture of heat from inside the stove. This heat exchanger is milled from a single large block and there are no interfaces between the fins and the plate the TEGs are mounted on. On the top-side flat surface of the plate four slots are milled ($1\,mm$) to retain the TEG devices during assembly. Graphite-based thermal grease was used on both sides of the TEGs to minimise

thermal contact resistance. On top of each TEG there is a water block with an internal labyrinth to exchange heat with cooling water flow. A thermocouple is fitted directly in contact with the cold side of the TEG, passing through the cold block. The whole system is mechanically clamped by a single M20 nut and bolt acting via a thrust bearing, and one 1000 $lb/inch$ spring per TEG ensures even distribution of the force onto each fixture. A thermocouple is placed underneath the flat surface of the hot-side heat exchanger. The thickness of this layer and its high thermal conductivity ensures that its temperature is fairly uniform and similar to that seen on the hot side of the TEG devices.

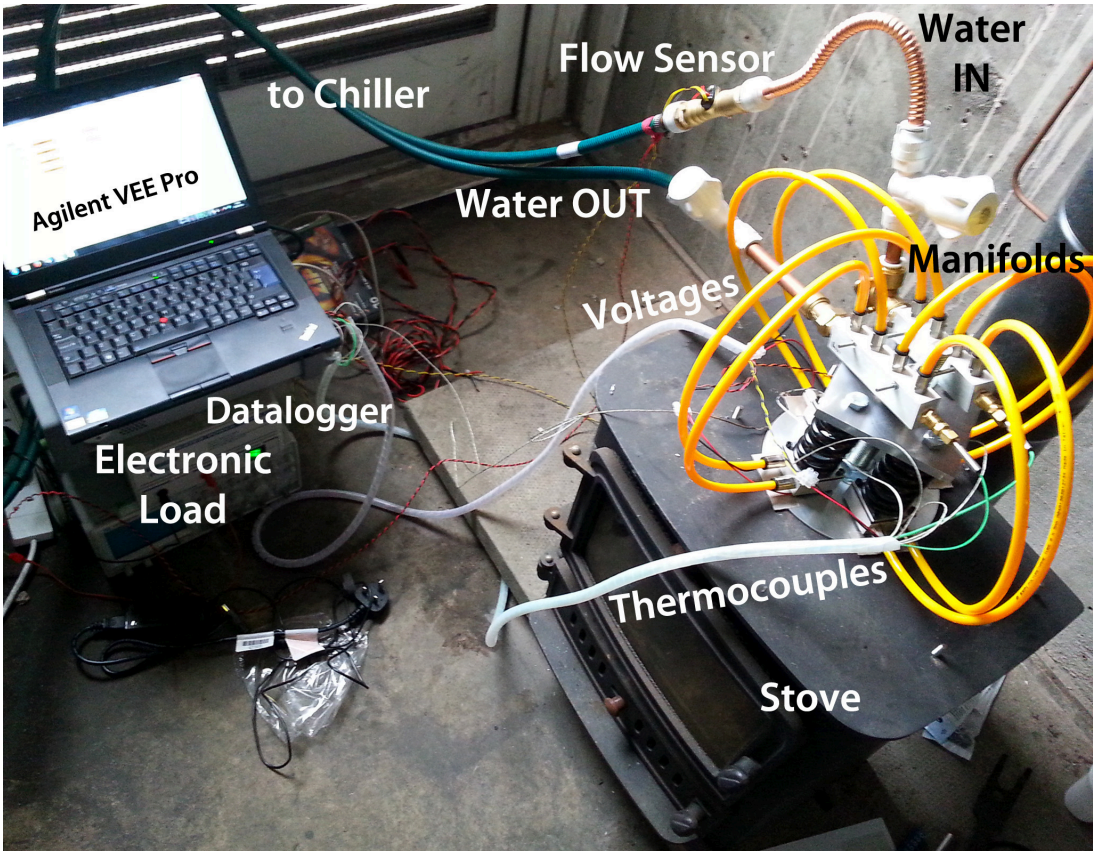

Figure 7.3: Picture of the stove, CHP TEG system and electronic instruments.

The assembled mechanical fixture was mounted in the top opening of the stove, as shown in Fig. 7.3 with a glass fibre gasket used to ensure no combustion gases escaped. Flow and return manifolds are used for the distribution of the water to and from the chiller unit (not shown in the picture) between each of the four labyrinth blocks. Thermocouples sense the water temperature inside each manifold. A Hall effect in-line flow sensor is fitted to measure the total rate of water flow through the system. All the heat exchangers are of the same design and the pipework to each was of the same length to ensure each cold end receives one quarter of the total flow, thereby ensuring temperature uniformity for each device. All the sensors were connected to an *Agilent* datalogger to record the data through a program in *Agilent* VEE Pro. An electronic load was used to manually measure the actual power production, but it was not connected to the computer for automatic control or data recording. An indication of the maximum power produced was manually obtained by measuring

the open-circuit voltage from the set of TEGs and then adjusting the load resistance such that the output voltage was approximately half of the value obtained.

Figure 7.4: Close-up of the stove and the mechanical fixture for the experiment with four TEGs.

After firing the stove burning coal the temperature on the hot-side heat exchanger quickly rose up to more than 250°C, therefore the stove's door was partially opened to decrease the temperature inside the stove by regulating the gas flow through the system. Fig. 7.4 shows a close-up picture of the stove and mechanical fixture. With an average measured temperature difference between the bottom side of the flat part of the heat exchanger and the cold side of the TEGs of 223°C, the voltage produced was $17.3\,V$. Using the value of this voltage, Fig. 4.16 suggests that the actual temperature difference across the TEGs was slightly less than 200°C with the difference being due to the temperature drop across the thermal resistances between the hot face of the TEGs and the heat exchanger.

The TEGs were electrically connected in a 2 x 2 series-parallel array and connected to the electronic load in constant current mode without automatic maximisation of power production.

Fig. 7.5 shows a portion of the experiment under this configuration. The temperature difference (red) corresponds to the average value across the four TEGs; the four individual values never differed by more than 1°C. The same was done for the single TEG's output voltage (green in Fig. 7.5). After around $1200\,s$ the open-circuit voltage was measured and the electronic load set around the MPP.

Next, the temperature difference was increased up to almost 260°C. At this point the MPP was set again: each TEG produced around $10\,W(10\,V, 1\,A)$, for a total of $40\,W(20\,V, 2\,A)$. Comparing the V_{OC} and V_{MPP} values at this point with the data of Fig. 4.16 and using the mathematical formulation of Eq. 4.3 it can be estimated that the "real" temperature difference across the TEGs is around 215°C. The hot side temperature is then around 240°C, but the stove could have easily reached higher temperatures [1].

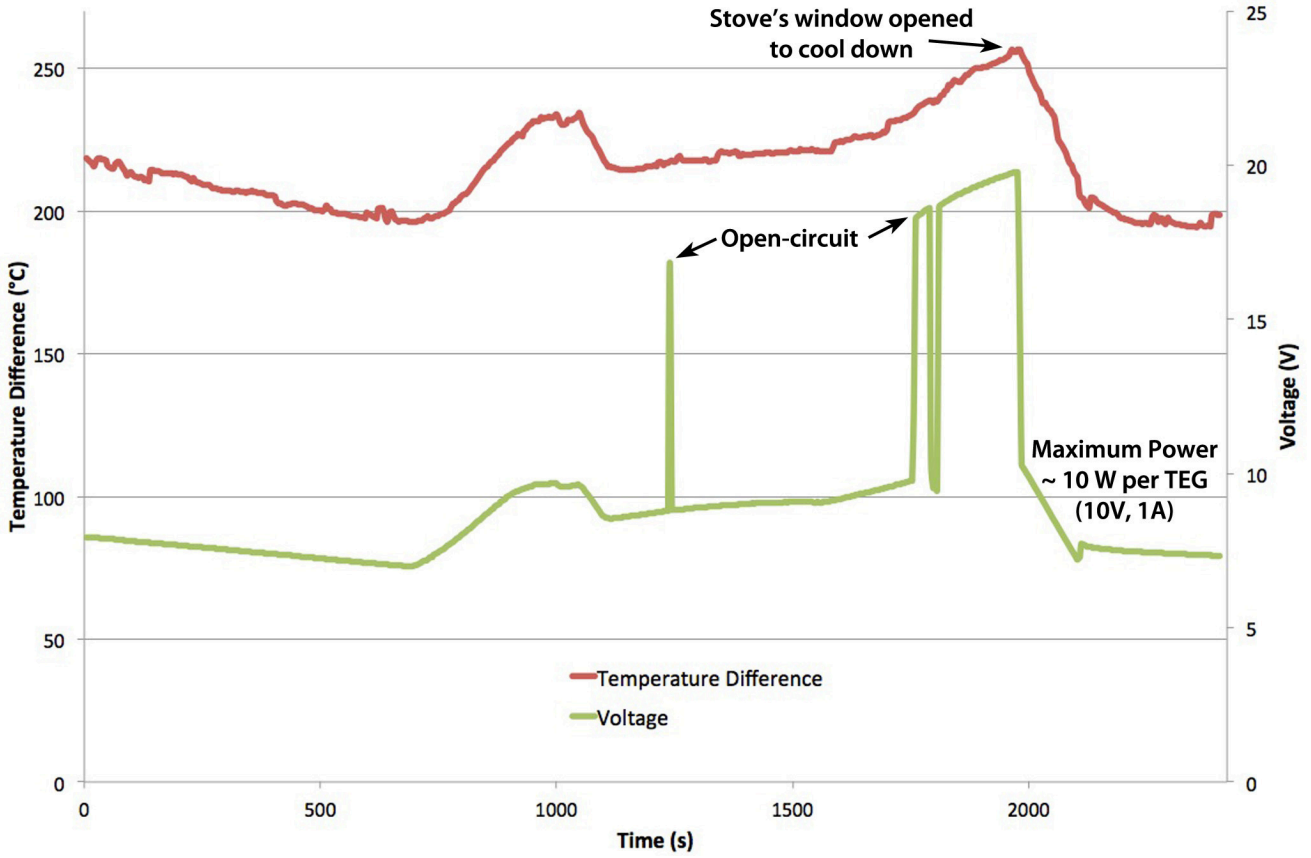

Figure 7.5: Part of the thermal transient occurring on the stove with the four TEGs.

The results obtained from this experiment are quite encouraging: the four TEGs are producing a significant amount of electricity each, enough to charge a laptop or run a pump to circulate the water around. The main concern is the potentially excessive temperatures on the hot side of the TEGs.

The recorded inlet and outlet water temperatures have not yet been used to estimate the thermal power transferred to the chiller, which would be useful to estimate the quantity of power transferred from the stove through the heat exchanger. This will be done in the future, together with a complete investigation of the system's power flow. Such information will also be included into the simulation model presented in 5.4. Future work also includes testing the whole system with MPPT converters to calculate the total quantity of energy obtained during the whole run of the stove on a single charge

[1] In a subsequent experiment, described in the next section, the hot side reached 600°C

of fuel.

7.1.2 Stove with two cascaded TEGs

The experiment presented in 7.1.1 demonstrated that the quantity of heat produced inside the stove is sufficient to rise the temperature on the hot-side heat sink to above 300°C. This is the maximum temperature that can be withstood by commercial Bi_2Te_3 TEGs, therefore using the configuration of 7.1.1 may damage the TEG devices if no protection is introduced.
A solution proposed in this section is to cascade two TEGs thermally in series. The TEG directly in contact with the hot-side heat exchanger is made of materials that can withstand high temperatures, *e.g.*, Oxides, while the second is made of Bi_2Te_3 and is in contact with the cold surface of the water-cooled block; they are in contact in the middle of the cascaded arrangement with a thermal coupling block. Using this method, not only is the temperature in-between the two TEGs lower than that present on the hot side, but also it is possible to exercise limited control of the middle point temperature without modifying the thermal power produced by the stove. As explained in detail in Chapter 3 the amount of current taken from a TEG influences its effective thermal conductivity. Hence by acting on the current drawn from the TEG placed on the hot side it is possible to vary the temperature of the middle point, which corresponds to the hot-side temperature of the TEG at lower temperature. Two cascaded TEGs can be seen as two thermal resistances in series. As an example, open-circuiting the TEG on the hot side increases its thermal resistance, thus decreasing the temperature in the middle and effectively protecting the Bi_2Te_3 TEGs. The higher the current, the higher the Peltier effect and the greater the swing of middle temperature that can be obtained. Additionally, operating the Bi_2Te_3 TEG to the right of the MPP will decrease its thermal resistance, thereby further lowering its hot-side temperature and providing further thermal protection. The concept of a variable thermal resistance implemented with a thermoelectric device was originally introduced in literature by Min [98].

This experiment utilises a prototype high-temperature TEG, whose material composition and architecture cannot be disclosed, for the hot device, and a commercial Bi_2Te_3 TEG (GM250-449-10-12 by *European Thermodynamics Ltd*) for the cold device. The former was made by Dr. Ryoji Funahashi [2] and is placed directly in contact with the hot-side heat exchanger, and the latter is seated underneath the water-cooled block. This would basically correspond to substituting the TEG block of Fig. 7.1 with two TEGs one on top of each other. A heat coupling thin Aluminium block separates the two TEGs, and its temperature, corresponding to the middle point, is sensed by a thermocouple. The temperatures on the Bi_2Te_3 TEG's cold side and on the hot-side heat exchanger are also sensed by thermocouples. Graphite-based thermal grease is used for the Bi_2Te_3 TEG, while a thermal-conducting, electrical-insulating pad (*Laird* Tgard K52) is used for the cold side of the

[2] http://www.aist.go.jp

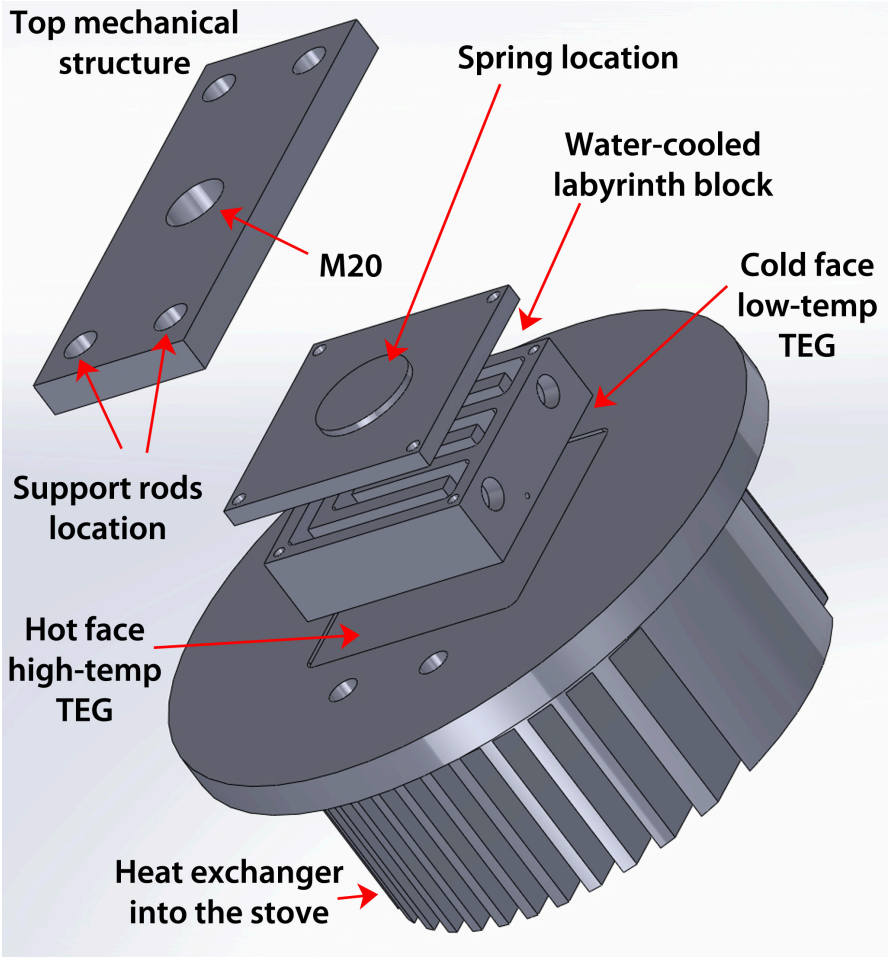

Figure 7.6: Mechanical drawing of the heat exchangers designed to use two TEGs in cascade arrangement on the stove.

high-temperature TEG. The mechanical drawing of the heat exchangers is shown in Fig. 7.6. The fins of the hot-side heat exchanger extend into the top of the stove near the flue gas exit. On top of the exchanger is seated the high-temperature TEG, then a thin block (not shown) separates it from the other TEG. The water-cooled labyrinth block completes the thermal stack; its lid has a protrusion to fix the position of the spring, which ensures mechanical compliance during thermal expansions.

The assembled mechanical fixture to test the cascade TEG arrangement was installed on the stove and connected to the chiller. The stove was fired and the temperatures and voltages of the two TEGs were recorded by the datalogger. The results of this experiment are plotted in Fig. 7.7 versus time.

It can be seen that even when the hot-side temperature peaks around 600°C the temperature on the middle point does not exceed 250°C, keeping the Bi_2Te_3 TEG within its safe operating range, but still producing close to $10\,W$. Note that during this experiment the stove was run at very high temperature and hence the fuel load was consumed quickly, resulting in the decrease of all the temperatures shown in Fig. 7.7 as the experiment progressed.

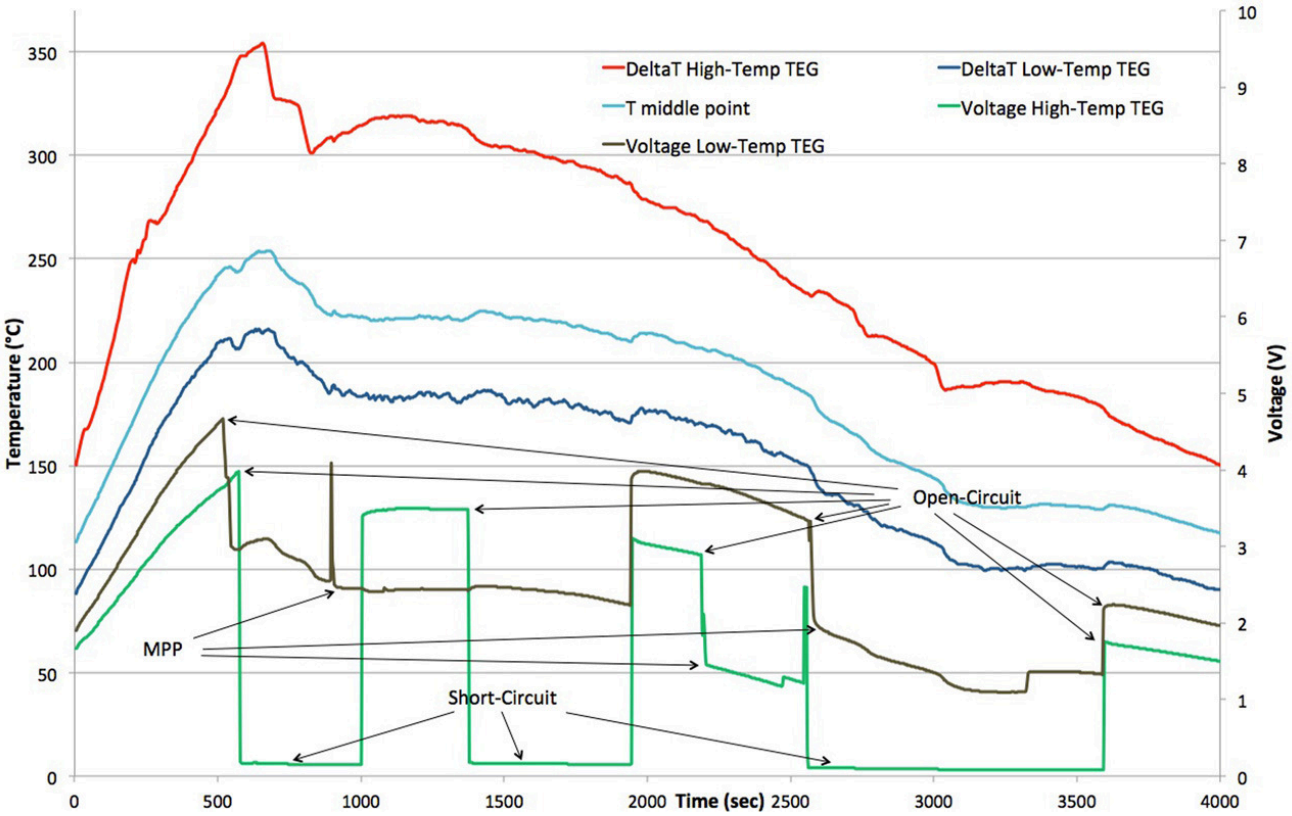

Figure 7.7: Experimental results using two cascaded TEGs on the stove. Temperature (left axis) and voltage (right axis) are plotted versus time.

This experiment validated the use of a TEG made of materials for high temperatures able to both protect the Bi_2Te_3 TEG and to produce some usable electrical power.

The preliminary results obtained during this experiment are adversely influenced by the poor electrical performance of the experimental high-temperature TEG, but they do not undermine the principles of operation outlined before. This particular characterisation experiment is being re-visited with a view to the use of a pair of MPPT converters, one for each TEG, sharing a common microprocessor controller that will establish the greatest MPP for the cascade by varying the mid-plane temperature. This concept is also the subject of a patent application filed in 2012 and due to issue later in 2014 [P1].

7.1.3 Economics of a stove CHP system

The purpose of this section is to study the economics of a TEG CHP system for stoves, similar to that described in Section 7.1.1. The system uses part of the heat generated burning coal, wood or charcoal in the stove, captured using a heat exchanger, and transferred to recirculating water from a water tank through four TEGs that convert part of the thermal energy into electricity. If the

water tank was to be placed at a higher location compared to the TEG system no circulating pump would be needed due to gravity circulation; in any case, such a system could be integrated in an already-present water and/or heating system at minimal extra cost. In Section 7.1.1 it was shown that the four TEGs could easily produce up to $40\,W_{el}$ during the normal use of the stove, and this does not represent the total thermal power available from the stove. Assuming a reasonable TEG efficiency of 4%, the thermal power transport through the system is

$$P_{stove} = \frac{P_{el}}{\eta} = \frac{40}{0.04} = 1\,kW \tag{7.1}$$

Cernunnus[3] suggests that the average consumption of hot water per person per day is around $40\,l$. UK mains water is provided at 4°C and the water ought to be heated up to at least 60°C (this is a requirement by UK Health and Safety to kill off any *Legionella* bacteria). Thus the water temperature needs to be raised by at least 56°C in the tank. It must be noted that rarely is water needed at 60°C, therefore hot water is mixed with cold water, hence the volume of hot water required is less. However, for the sake of this analysis and to take into account possible losses in the pipes and tank, $40\,l$ remains a reasonable requirement.
The thermal power (in Wh) required to increase the temperature of one litre of water by 1°C is $1.16\,Wh$. Therefore the total quantity of power needed is

$$P_{water} = 40l \cdot 1.16Wh/°\mathrm{C}l \cdot 56°\mathrm{C} = 2.6\,kWh \tag{7.2}$$

This corresponds to leaving the stove heated up for $2.6\,h$, which is a reasonable expectation during the normal use of the stove for heating or cooking, and easily achievable during an evenings use.
The cost of $1\,kWh$ of electricity in the UK is around £0.13, therefore the daily saving would be £0.338; assuming one stove use per day for every day of the year, this equates to £123 per year. However, the cost of coal, which stands at around $£0.036/kWh$ must be taken into consideration, so that the yearly saving decreases to £89. This figure does not take into consideration the production of electricity which could be stored in a battery for use with low-power electronics (smart-phones, computers) and energy-saving lighting; such features would be of great benefit in rural households not connected to, or interrupted from, mains power.

7.2 Automotive heat recovery TEG systems

This research programme was partially funded by the Energy Technology Partnership (ETP) and by European Thermodynamics Ltd. The agreement included participation in two multi-million industry-led projects related to the development of TEG systems to recover part of the heat energy rejected to ambient vehicle exhaust systems. Consortium confidentiality agreements prevent a com-

[3]http://www.cernunnos-homes.co.uk/technology/boilers-explained/sizing-a-hot-water-tank/

plete disclosure of all the system design details but do not inhibit the presentation of the important research findings here.

The two UK or EU funded projects (VIPER and PowerDriver, respectively) aim to design and validate a TEG system to be fitted to a 2013 2.0 l car. The target is to produce a peak electrical power of 300 W at 14 V of electrical power during the New European Driving Cycle (NEDC). The final product is expected to last for at least 20 years and to operate without failure for a period of 5000 hours of continuous operation. The system, with a mass of less than 10 kg, should increase the overall vehicle fuel efficiency by at least 2 %. The thermal input power to the system is provided by the exhaust gas and thermal power is absorbed by the vehicle's cooling system.

The required project tasks included support on the choice of TEG devices [99], testing of TEGs, simulation of TEG systems for automotive applications and design and production of the MPPT electronics to maximise the power extracted from the TEGs and to interface to the car's control system for diagnostics and communication.

The next section describes an adaptation of the model described in Section 5.3 to simulate automotive TEG systems and the chapter concludes with a description of the electronic system delivered to maximise power production from the TEG systems built by the other project members.

7.2.1 Simulation of automotive TEG systems

The simulation model described in Section 5.4 can be easily modified to simulate a common TEG automotive system.

Without loss of generality we can consider the tubular design showed in Fig. 7.8 in which the

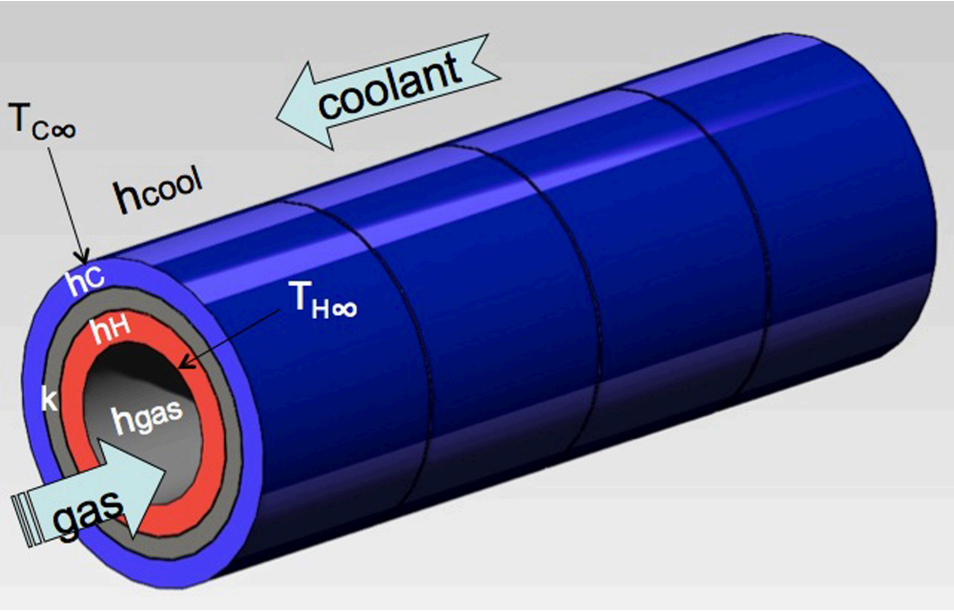

Figure 7.8: Model representation for an automotive tubular TEG system, divided in four sectors.

exhaust gas flows inside the system from the left, while the coolant comes from the opposite side in a counterflow arrangement [127]. In this way it is possible to achieve a more uniform temperature difference distribution across the length of the system. However, to account for different temperatures along the gas and coolant direction of flow, in the simulation the system is divided in n sectors (four shown in Fig. 7.8) cut in the plane perpendicular to the gas flow.
Using the same notation of Chapter 5, the TEGs (thermal conductivity k) are in the middle of two heat exchangers (thermal transfer coefficients h_H and h_C) directly in contact with the flows of gas and coolant, where the temperatures are $T_{H\infty}$ and $T_{C\infty}$, respectively. A number from 1 to n is added to identify each sector.
Thermal input power is provided by the gas. If $T_{gas_{IN}}$ is the temperature of the exhaust gas entering the heat exchanger and $T_{gas_{OUT}}$ is the temperature of the gas after it has provided thermal power to the TEG system, the total power provided to the system is

$$P_{in} = \dot{m} C_H \left(T_{gas_{IN}} - T_{gas_{OUT}}\right) \tag{7.3}$$

where $\dot{m}$ is the mass flow rate $[g/s]$ and C_H is the heat capacity of the exhaust gas $[J/gK]$. $T_{gas_{OUT}}$ changes depending on the quantity of power transferred to the heat exchanger.
Consider now only the first sector. There is forced convection from the gas to the heat exchanger surface, therefore the power transferred to the first sector can be calculated as

$$P_{gas1} = h_{gas} A_{HX} \left(T_{gas1} - T_{H\infty 1}\right) \tag{7.4}$$

where h_{gas} is the convection coefficient and A_{HX} is the surface of exchange of heat between the gas and the hot-side heat exchanger. P_{gas1} changes $T_{H\infty 1}$ for the next iteration and decreases the gas temperature arriving to the second sector, which can be obtained by

$$T_{gas2} = T_{gas1} - \frac{P_{gas1}}{\dot{m} C_H} \tag{7.5}$$

Eq. 7.4 can be repeated for the second sector and so on for the whole TEG system. The same technique is valid for the heat removed by the coolant on the cold side. In Simulink, a memory block is used on the cold side, to deal with the counterflow arrangement.

In the Simulink model each sector is represented by a block which contains an adapted version of the model described in Section 5.4. Fig 7.9 shows the general view of the resulting model to simulate the system of Fig. 7.8 with four sectors.
The parameters considered constant in Matlab are the following:

- geometrical: surface, thickness
- thermal: heat capacity, thermal conduction and convection coefficient
- electrical: TEGs characteristic, number of TEGs in series/parallel

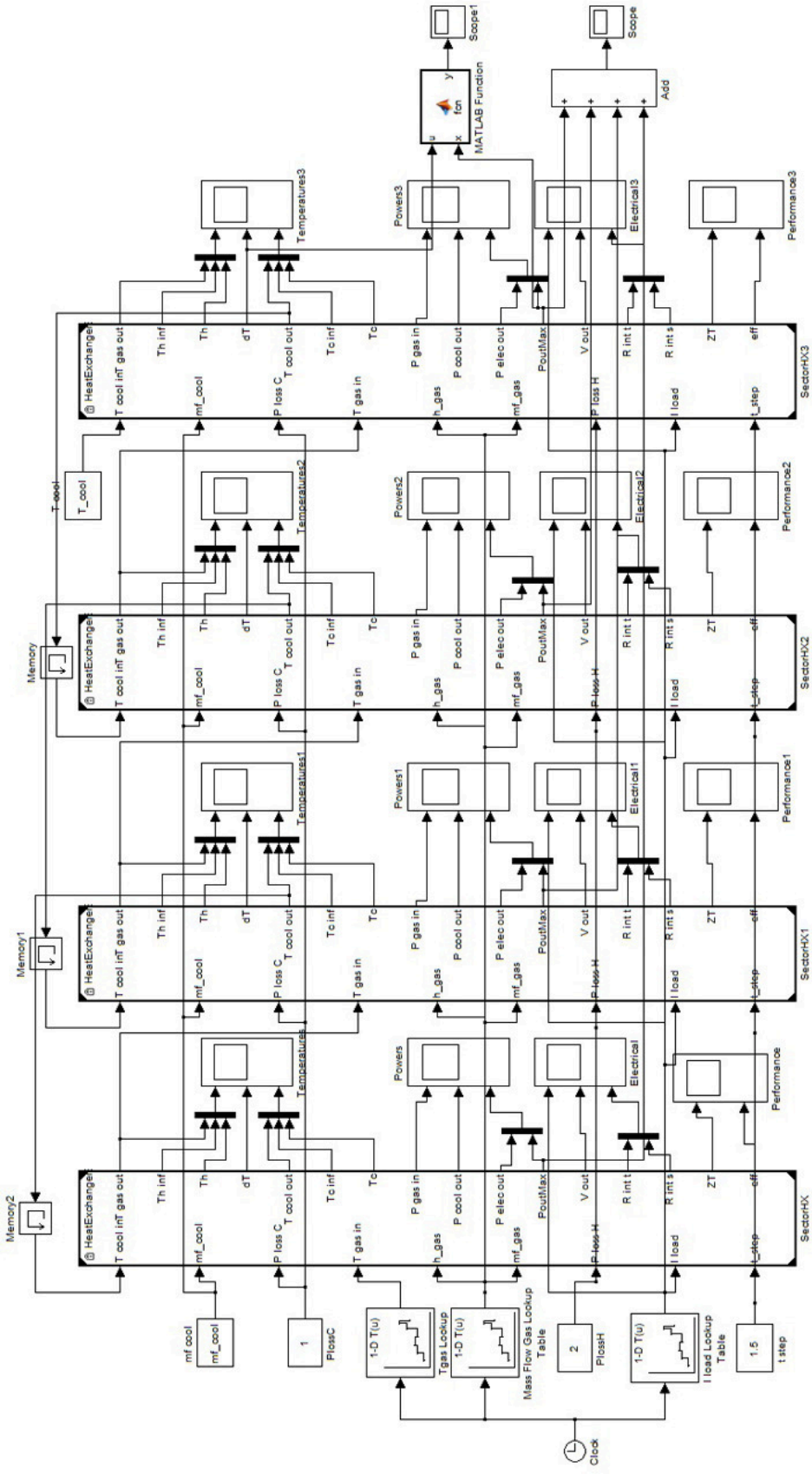

Figure 7.9: General view of the Simulink model to simulate an automotive tubular TEG system divided in four sectors.

The gas and coolant temperatures and mass flows are inputs to the model, so that they can be dynamically updated depending on the driving cycle or type of simulation. The electrical load can also be dynamically updated to investigate load matching techniques. In Fig. 7.8 look-up tables were used to feed the parameters for the NEDC and for a common current load to all the sectors. The sectors interact with each other, exchanging input and output gas and coolant temperatures. The simulation system provides the following output values from each sector:

- temperatures: $T_{gas_{OUT}}, T_{H_\infty}, T_H, \Delta T, T_C, T_{C_\infty}, T_{cool_{OUT}}$
- powers: $P_{gas_{IN}}, P_{cool_{OUT}}, P_{el_{MAX}}, P_{el_{load}}$
- electrical: $I_{load}, V_{load}, R_{int,tot}, R_{int,s}$
- performance: estimated ZT and η

where $P_{el_{MAX}}$ is the theoretical maximum power (under matched load), while $P_{el_{load}}$ is the actual power produced when the I_{load} is used. $R_{int,tot}$ is the total internal resistance for the TEG array connected to the sector (see Eq. 5.49), while $R_{int,s}$ is the internal resistance of a single TEG.

Fig. 7.10 shows some results from a simulation with 32 TEGs, 8 in each sector (4 TEGs electrically connected in series and 2 such strings connected electrically in parallel), and data from a NEDC. The first three windows present the outputs from the second sector: in the first window the temperature distribution (from top to bottom, hot side, temperature difference, cold side); in the second window the powers (from top to bottom, power frm gas, power to coolant and electrical power outputs); in the third window the electrical parameters (current, voltage and internal resistances). The last window on the right shows the temperature differences across the four sectors in the top plot and the electrical power outputs in the bottom plot.

7.2.2 MPPT electronics for automotive TEG systems

The design philosophy behind the sets of electronics designed for both projects consists of a main motherboard onto which several MPPT converters can be installed vertically through the use of a single connector and two plastic supports. The motherboard hosts a microcontroller which manages the communication to the car's system through Controller Area Network (CAN) or Local Interconnected Network (LIN), and to the MPPT converters through Inter Integrated Circuit (I^2C). The connection between the motherboard and the $12\,V$ car's battery is split into four connections, each one equipped with fuse and TVS. Output current is measured by a current transducer and the temperature reading is provided by a thermistor. A Universal Serial Bus (USB) connector is added for future interface to a Personal Computer (PC) for effective monitoring of live performance of the

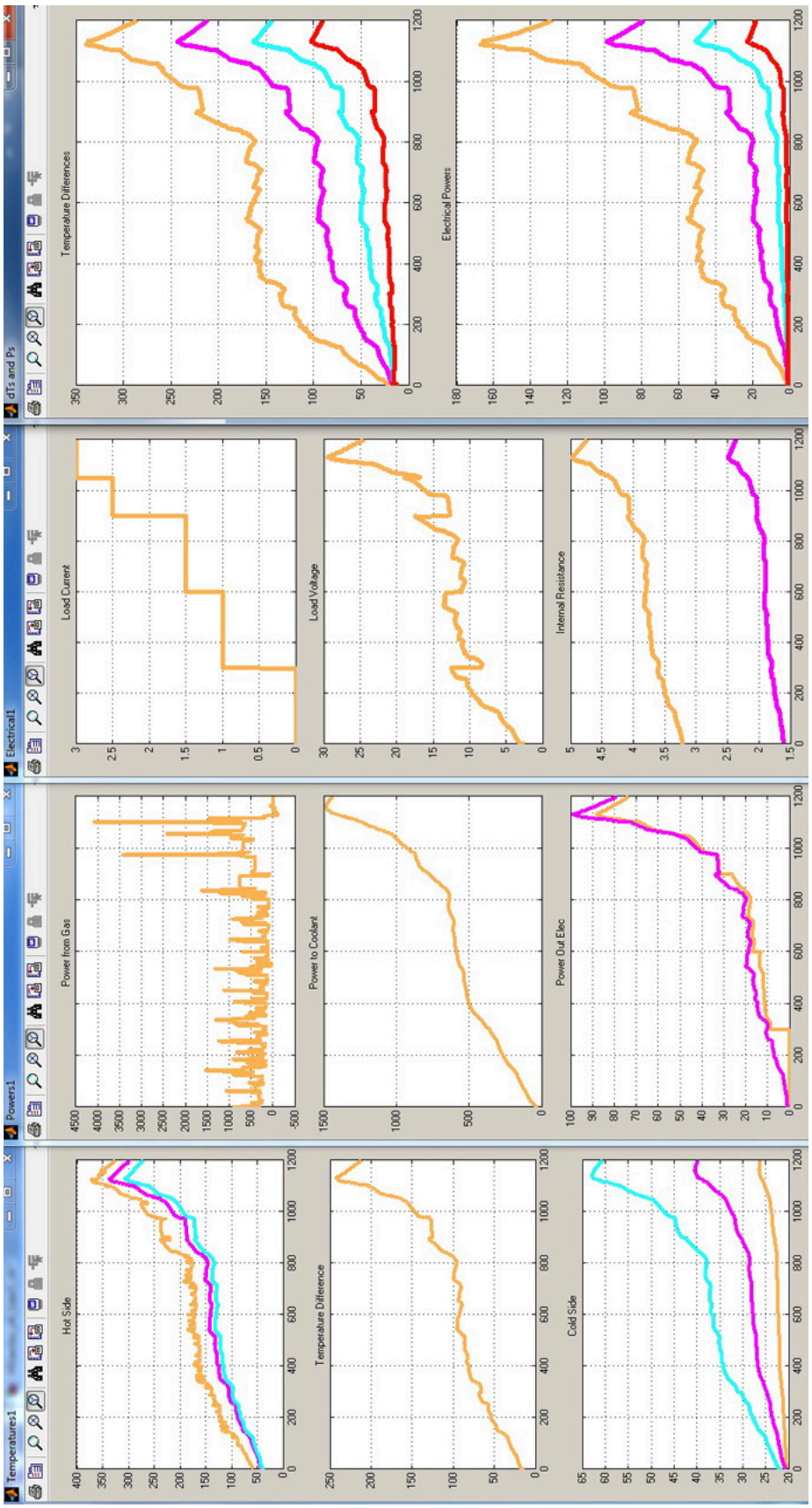

Figure 7.10: Results of the simulation of a tubular TEG system divided into four sectors. Outputs relative to the second sector are shown in the first three windows from the left and temperature differences (top plot) and electrical power outputs (bottom plot) in the window on the right.

MPPT converters and TEG system during vehicle testing. Fig. 7.11 shows the complete electronic system comprising of the motherboard and 16 MPPT converters. The fuses, current transformer, communications microprocessor, individual converter sockets, and various other components are clearly shown.

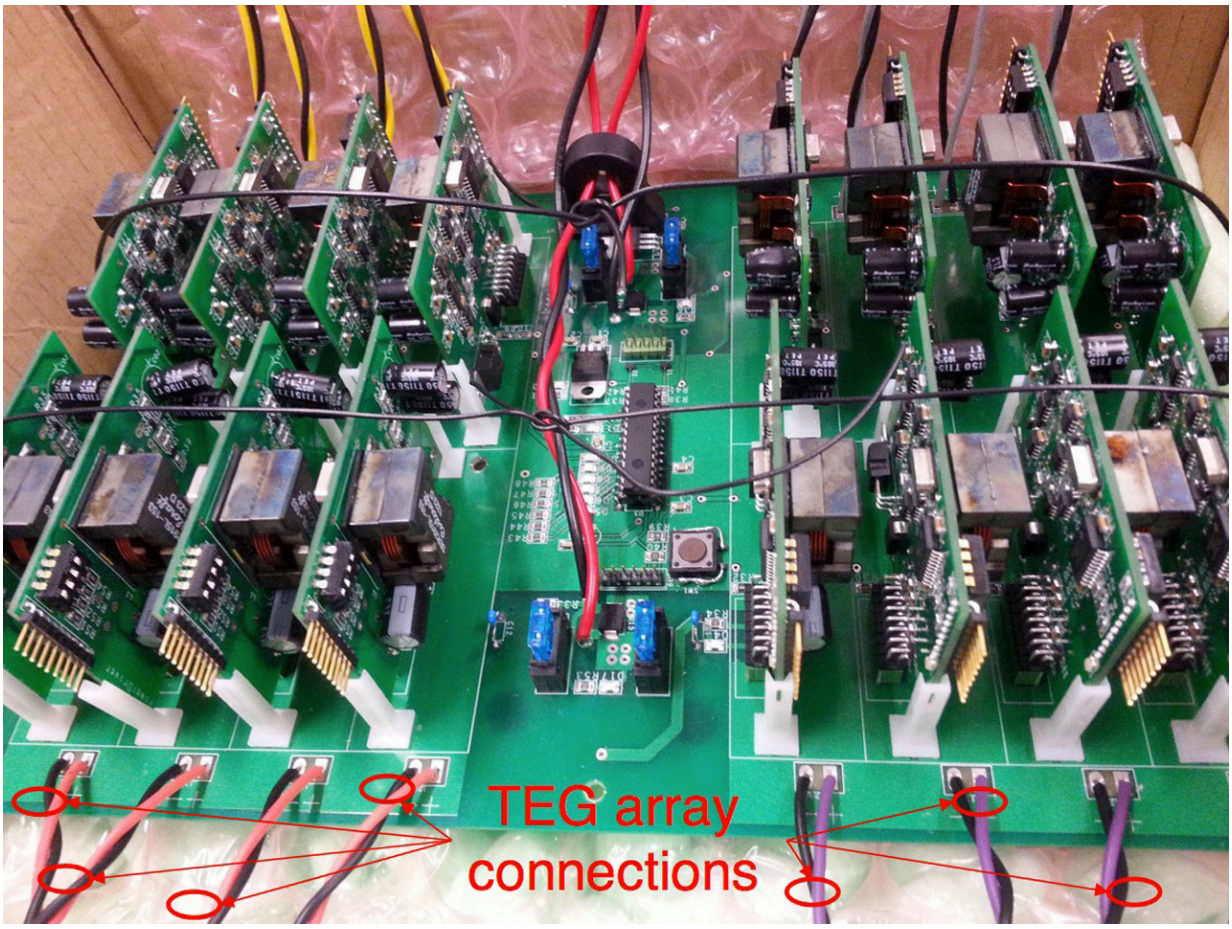

Figure 7.11: Picture of the complete electronic system for one of the two projects related to the development of a TEG system for the recovery of waste heat from a car's exhaust gas system.

Fig. 7.12 shows the top and bottom faces of the PCB, which measures $75x55\,mm^2$, for one of the two MPPT converter designs. The circuit is similar to that described in Section 6.5.1 and the MPPT performance is identical to that measured in Section 6.6. The power rating is $40\,W$, with maximum open-circuit TEG voltage of $30\,V$ and maximum input current of $5\,A$.

The n-MOSFETs used are IPD036N04L, the power Schottky is VS-12CWQ03FN and the inductor is $15\,\mu H$ ($I_{sat} = 14\,A$), the input capacitors total $440\,\mu F(50\,V)$ and the output capacitors total $660\,\mu F(25\,V)$. Both input and output capacitors were chosen based on their RMS current capabilities. Using the electrical values at maximum available TEG power and with a battery voltage of $12V$, the maximum RMS current in the input capacitors is calculated from Eq. 6.13 to be $2.75\,A$. The maximum power loss on M_{cap} is $25\,mW$ (from Eq. 6.15, assuming an on-resistance of $3.6\,m\Omega$). This

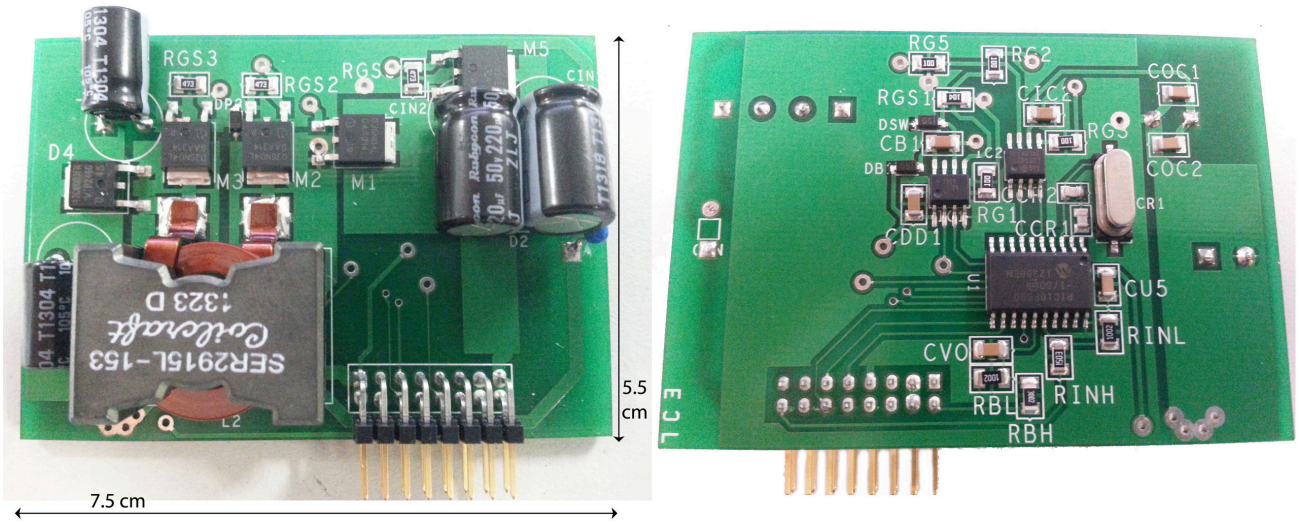

Figure 7.12: Picture of the first of the two MPPT converter PCBs.

$V_{in}(V)$	$I_{in}(A)$	$P_{in}(W)$	$P_{out}(W)$	$\eta_{el}(\%)$
3	0.5	1.5	1.17	78.1
5	0.83	4.17	3.69	88.5
7.5	1.25	9.38	8.40	89.6
10.5	1.75	18.38	16.70	90.9
13.5	2.25	30.38	28.13	92.6

Table 7.1: Electrical performance of the synchronous Buck-Boost with output diode, tested with a power supply in series with a $6\,\Omega$ power resistor.

corresponds to $10.5\,mJ$ lost every $500\,ms$. As a comparison, with the 'common' fractional open-circuit technique that waits for the input capacitors to charge up to open-circuit through the TEG's internal resistance ($\sim 6\,\Omega$), the RC time constant is $\tau_{RC} = 2.64\,ms$. Waiting for $3\tau_{RC}$ not harvesting $30\,W$ equates to losing $237\,mJ$.
The converter's electrical efficiency was tested with a power supply in series with a fixed $6\,\Omega$ power resistor and the results are listed in Table 7.1. The electrical efficiency is 92.6 % when tested at $30.4\,W(13.5\,V, 2.25\,A)$ input.

The second MPPT converter designed utilises the same MPPT technique described in Section 6.3. The DC-DC converter is based on the four-switch synchronous Buck-Boost presented in Fig. 6.12, however, the actual implementation differs somewhat from the circuit of Section 6.5.4.

This converter makes use of the gate driver IC MCP14628 produced by *Microchip*. This gate driver can be set to be working in either Continuous Conduction Mode (CCM) forced operation or in diode emulation mode which turns off the low-side MOSFET when the current reaches zero. This latter feature is used for the gate driver controlling M_1 and M_2 of Fig. 6.12, so that $M2$ is opened at light loads preventing the battery from discharging through M_4 and M_2. The MOSFETs used are the IRF8734PBF by *International Rectifier*, chosen because of their low gate threshold voltage,

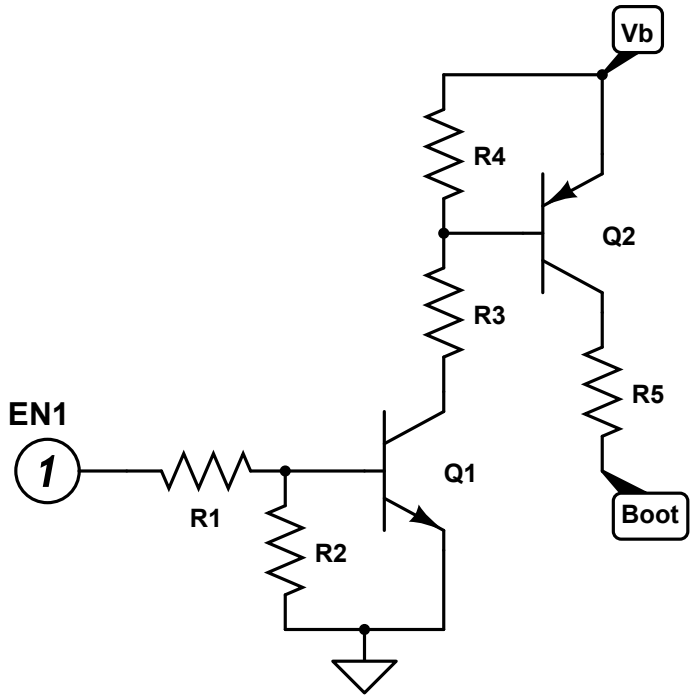

Figure 7.13: Circuit to keep the high-side MOSFET continuously closed using the *Microchip* MCP14628 gate driver.

drain-source resistance and gate capacitance. The two gate driving ICs are powered by a $5\,V$ voltage regulator during buck-boost mode, but make use of the circuit shown in Fig. 7.13 to allow for continuous high-side conduction, without the need of the charge pump circuit of Fig. 6.3. When boost-only operation is required the microcontroller sets EN1 which, activating Q_1 and Q_2, connects the battery voltage V_b to the *boot* pin of the MCP14628, so that it can keep M_1 closed.

The same capacitors and inductor of the previous converter are used for this second version, as the power rating and voltage/current specifications are identical. The produced PCB is shown in Fig. 7.14. The dimensions are $75x58\,mm^2$. This converter includes a TVS, a $5\,V$ voltage regulator and a 4-bit switch is added to the PCB to allow manual selection of the I^2C address. The maximum efficiency measured at the rated power of $40\,W$ is 94.7 %.

7.3 Conclusions

This chapter initially demonstrated the potential of generating electrical energy from the thermal energy produced by a stove, while using the rejected heat to heat water. The proposed system generated $40\,W_{el}$. In order to protect commercial Bi_2Te_3 TEG devices from over-temperatures (> 300°C) a cascade arrangement comprising of two TEGs thermally is series, one of which able to withstand high temperatures, was described. More work is required to experimentally demonstrate the benefit of this configuration and for the development of the necessary power and control electronics.

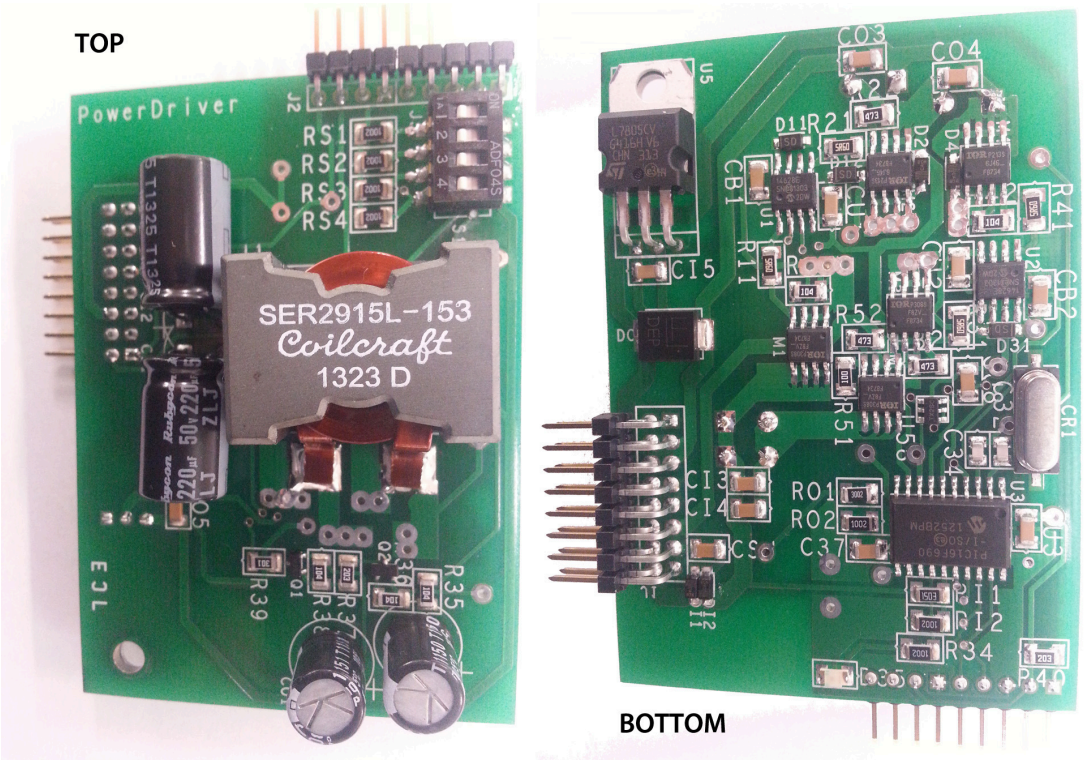

Figure 7.14: Picture of the second version of the MPPT converter designed for an automotive TEG system.

This chapter also described the adaptation of the computer-aided simulation tool of Chapter 5 to simulate the fast dynamics and uneven temperature distributions of a TEG system recovering waste heat from a vehicle's exhaust gas system.
Finally, the MPPT electronic converters and control boards designed for automotive TEG systems were presented.

Chapter 8

Conclusions

This thesis contributes to the existing body of knowledge about thermoelectric generating systems with original work, novel ideas and results spacing from testing and characterising the performance of thermoelectric generators (TEGs), to simulation of the dynamics of thermoelectric generating systems, and to maximum power point tracking (MPPT) converters for physical TEG applications.

Chapter 4 described an automated test apparatus that generates accurate and repeatable characterisations of TEG devices for a wide range of temperatures and mechanical clamping forces. A mathematical formulation was then provided to predict the performance at any thermal and electrical operating point, using the experimental data obtained from a minimum of two electrical characterisations.
This mathematical characterisation was then used to study the impact of the Peltier effect on the temperature difference and consequently on the maximum power generated by a TEG with constant thermal input power. Under this condition simulation results and preliminary experimental data suggest that working on the left side (in the V-I curve) of what is generally considered the maximum power point (MPP) leads to greater power production due to reduction of the parasitic Peltier effect and consequent increase of temperature difference. These results are subject to the relatively long thermal constants of the system, therefore it is not yet clear if and how future MPPT converters will be able to exploit this phenomenon due to the close dependence of temperatures to the input and output thermal powers, which usually vary considerably and quickly in TEG systems for waste heat recovery applications, *e.g.*, car's exhaust gas system, stoves. Future work will address this topic, to maximise the overall power production and efficiency of TEG systems for waste heat applications in which the available thermal power is usually limited.
Due to its ability to concurrently test up to four TEG devices with independent control on temperature difference and clamping force, the test rig was also used to investigate the effects of temperature imbalance on the power produced by TEG arrays. The electrical characterisations obtained for mismatched TEG arrays electrically connected in series and parallel showed that the power "lost" due to

different thermal conditions across the TEGs connected in the same array can be relevant. The issue of temperature imbalance was clearly described and a theoretical model was presented to quantify and predict the impact. However, the experimental results were obtained with constant temperature differences, *i.e.* varying the thermal input power to maintain the desired temperature gradients. As a consequence the variation of the temperatures due to a change in Peltier effect was not investigated and will be subject of future work.

Chapter 5 presented an analytical analysis of the transient behaviour of thermoelectric devices, which was then included into a computer simulation program modelling the whole TEG system. Comparison of simulated results with experimental data from a physical TEG system confirmed the ability of the program to accurately predict temperatures and powers during transients and steady-state conditions. This model can therefore be used to design both the mechanical and the electrical subsystems. This program was successively adapted to investigate temperature distributions and power production in a TEG system for automotive exhaust gas systems, and it was used to aid in the design of industry-led TEG projects.

Chapter 6 introduced a novel technique to measure the TEG's open-circuit voltage with minimal disconnection of the MPPT converter. This MPPT technique was theoretically analysed in detail and it was calculated that the period of time required for the measurement and the additional components contribute to almost irrelevant cost and losses. A snubber circuit was also added to reduce over-voltages that could occur due to the parasitic inductance in the TEG and connection to it, and experimental results were provided to support the efficacy of this circuit.
Two versions of the synchronous Buck-Boost DC-DC converter employing this fractional open-circuit MPPT technique were used to interface the TEG system to a battery load. These converters do not need expensive sensors or controllers and allow the extraction of power from the TEGs over a wide range of temperature differences. A technique to prevent current to reverse-flow from the battery when the energy source does not provide high quantities of power was also presented. These converters can be used without knowledge of the electrical characteristic of the TEGs used, provided that the maximum and minimum ratings for current, voltage and power are respected.
Rigorous experimental results with real TEGs under steady-state and transient conditions demonstrated that this MPPT system is capable of quickly setting the optimum electrical operating point with a tracking efficiency close to 100 %.
The speed of tracking of common MPPT algorithms is orders of magnitude faster than the thermal time constant of the TEG system, which results in the controller quickly settling towards the MPP for the instantaneous value of temperature difference, corresponding to half of the actual open-circuit voltage. However, the variation in electrical load influences the temperature difference due to the Peltier effect. As a consequence, following the rate of change of the thermal variation the MPPT controller might modify the operating point again. At the same time, however, a change in electrical output power could be due to a variation in thermal input power, thus resulting in an erroneous modification of the electrical operating point by the MPPT controller. This combined electro-thermal

effect has not yet been investigated in practise and will be studied in the future to design a new breed of MPPT controllers able to predict not only the instantaneous point of maximum power, but also the thermal evolution of the system in relation to the electrical operating point established at the TEG's terminals. This could potentially further enhance the overall efficiency of the TEG system in the case of limited thermal power and consequently varying temperature differences; this condition is actually found in most waste heat recovery applications, in which thermal energy is essentially free, but not unlimited.
Future work will also focus on comparing the proposed MPPT technique to other MPPT algorithms, and on integrating several MPPT converters together to form a DMPPT system, which could partially mitigate the effect of thermal mismatch on the TEG devices of the same array.

Chapter 7 presented the mechanical fixtures developed to convert into electricity part of the thermal energy generated in a stove, and concurrently transfer thermal energy to water in a CHP system. Experimental results proved the technical feasibility of this system and an economic analysis demonstrated the benefits that such technology could generate. Future work will further develop the system, also connecting MPPT converters, and gather more precise experimental results. Moreover, two separate DC-DC converters controlled by the same microcontroller will be used to practically demonstrate the presented technique to protect Bi_2Te_3 TEGs from excessive temperatures. This original technique utilises another TEG device, made of materials rated for high temperatures, as a variable thermal resistor thermally in series with the Bi_2Te_3 TEG: the controller can vary the temperature between the two TEGs controlling the amount of current drawn from each of them. This solution could be used not only in stoves but also in other waste heat recovery applications where high-temperature energy sources are available, *e.g.*, car's exhaust, heavy-industry.
Chapter 7 also presented the MPPT electronic systems designed and produced for automotive TEG systems. Their modular structure allows a flexible adaptation to several power ratings. These systems will be further developed and controlled with a DMPPT approach. Moreover, the effect of the alternator operation on this electronic system will be studied using a test rig currently under development and with several TEG power sources.

Bibliography

[1] R. Decher, *Direct Energy Conversion: fundamentals of electric power production.* Oxford University Press, 1997.

[2] D. M. Rowe, *Thermoelectrics Handbook: Macro to Nano.* CRC Press, 2005.

[3] R. E. Simons and R. C. Chu, "Application of Thermoelectric Cooling to Electronic Equipment: A Review and Analysis," in *16th SEMI-THERM Symposium*, pp. 1–9, IEEE, 2000.

[4] G. Min and D. Rowe, "Experimental evaluation of prototype thermoelectric domestic-refrigerators," *Applied Energy*, vol. 83, no. 2, pp. 133–152, 2006.

[5] D. Astrain, A. Martínez, and A. Rodríguez, "Improvement of a thermoelectric and vapour compression hybrid refrigerator," *Applied Thermal Engineering*, vol. 39, pp. 140–150, 2012.

[6] Q. Luo, G. Tang, Z. Liu, and J. Wang, "A novel water heater integrating thermoelectric heat pump with separating thermosiphon," *Applied Thermal Engineering*, vol. 25, pp. 2193–2203, Oct. 2005.

[7] J. Siviter, A. Knox, J. Buckle, A. Montecucco, and E. McCulloch, "Megawatt scale energy recovery in the Rannkine cycle," in *Energy Conversion Congress and Exposition (ECCE), IEEE*, pp. 1374–1379, 2012.

[8] A. R. Knox, J. Buckle, J. Siviter, A. Montecucco, and E. McCulloch, "Megawatt-Scale Application of Thermoelectric Devices in Thermal Power Plants," *Journal of Electronic Materials*, 2013.

[9] D. Rowe, "Thermoelectrics, an environmentally-friendly source of electrical power," *Renewable Energy*, vol. 16, pp. 1251–1256, 1999.

[10] D. Rowe, "Thermoelectric waste heat recovery as a renewable energy source," *International Journal of Innovations in Energy Systems and Power*, vol. 1, no. 1, pp. 13–23, 2006.

[11] J. Haidar and J. Ghojel, "Waste heat recovery from the exhaust of low-power diesel engine using thermoelectric generators," in *20th International Conference on Thermoelectrics (ICT)*, pp. 413–418, 2001.

[12] L. I. Anatychuk, R. V. Kuz, and Y. Y. Rozver, "Efficiency of thermoelectric recuperators of the exhaust gas energy of internal combustion engines," in *9th European Conference on Thermoelectrics (ECT)*, pp. 516–519, 2011.

[13] D. Crane, J. LaGrandeur, V. Jovovic, M. Ranalli, M. Adldinger, E. Poliquin, J. Dean, D. Kossakovski, B. Mazar, and C. Maranville, "TEG On-Vehicle Performance and Model Validation and What It Means for Further TEG Development," *Journal of Electronic Materials*, Nov. 2012.

[14] S. Risse and H. Zellbeck, "Close-Coupled Exhaust Gas Energy Recovery in a Gasoline Engine," *Research Thermal Management*, vol. 74, pp. 54–61, 2013.

[15] M. Brignone and A. Ziggiotti, "Impact of novel thermoelectric materials on automotive applications," in *9th European Conference on Thermoelectrics (ECT)*, pp. 493–496, 2011.

[16] J. W. Fergus, "Oxide materials for high temperature thermoelectric energy conversion," *Journal of the European Ceramic Society*, vol. 32, pp. 525–540, Mar. 2012.

[17] J. C. Bass and A. Killander, "A Stove-Top Generator for Cold Areas," in *14th International Conference on Thermoelectrics*, pp. 390–393, 1996.

[18] R. Nuwayhid, A. Shihadeh, and N. Ghaddar, "Development and testing of a domestic woodstove thermoelectric generator with natural convection cooling," *Energy Conversion and Management*, vol. 46, pp. 1631–1643, June 2004.

[19] G. Rinalde, L. Juanicó, E. Taglialavore, S. Gortari, and M. Molina, "Development of thermoelectric generators for electrification of isolated rural homes," *International Journal of Hydrogen Energy*, vol. 35, no. 11, pp. 5818–5822, 2010.

[20] D. Champier, J. P. Bedecarrats, T. Kousksou, M. Rivaletto, F. Strub, and P. Pignolet, "Study of a TE (thermoelectric) generator incorporated in a multifunction wood stove," *Energy*, vol. 36, pp. 1518–1526, Mar. 2011.

[21] S. O'Shaughnessy, M. Deasy, C. Kinsella, J. Doyle, and A. Robinson, "Small scale electricity generation from a portable biomass cookstove: Prototype design and preliminary results," *Applied Energy*, vol. 102, pp. 374–385, Feb. 2013.

[22] C. Kinsella, S. O'Shaughnessy, M. Deasy, M. Duffy, and a.J. Robinson, "Battery charging considerations in small scale electricity generation from a thermoelectric module," *Applied Energy*, vol. 114, pp. 80–90, Feb. 2014.

[23] G. Min and D. Rowe, "Symbiotic application of thermoelectric conversion for fluid preheating/power generation," *Energy Conversion and Management*, vol. 43, pp. 221–228, Jan. 2002.

[24] J. A. B. Vieira and A. M. Mota, "Thermoelectric generator using water gas heater energy for battery charging," *International Conference on Control Applications*, pp. 1477–1482, July 2009.

[25] M. Chen, H. Lund, L. a. Rosendahl, and T. J. Condra, "Energy efficiency analysis and impact evaluation of the application of thermoelectric power cycle to todays CHP systems," *Applied Energy*, vol. 87, pp. 1231–1238, Apr. 2010.

[26] T. Furue, T. Hayashida, Y. Imaizumi, T. Inoue, K. Nagao, A. Nagai, I. Fujii, and T. Sakurai, "Case study on thermoelectric generation system utilizing the exhaust gas of interal-combustion power plant," *17th International Conference on Thermoelectrics (ICT)*, no. 1, pp. 473–478, 1998.

[27] T. Kyono, R. Suzuki, and K. Ono, "Conversion of unused heat energy to electricity by means of thermoelectric generation in condenser," *IEEE Transactions on Energy Conversion*, vol. 18, pp. 330–334, June 2003.

[28] H. Kaibe, K. Makino, T. Kajihara, S. Fujimoto, and H. Hachiuma, "Thermoelectric generating system attached to a carburizing furnace at Komatsu Ltd., Awazu Plant," in *9th European Conference on Thermoelectrics (ECT)*, pp. 524–527, 2011.

[29] C. Suter, Z. Jovanovic, and A. Steinfeld, "A 1kWe thermoelectric stack for geothermal power generation Modeling and geometrical optimization," *Applied Energy*, vol. 99, pp. 379–385, Nov. 2012.

[30] W. V. Sark, "Feasibility of photovoltaic Thermoelectric hybrid modules," *Applied Energy*, vol. 88, pp. 2785–2790, Aug. 2011.

[31] D. Yang and H. Yin, "Energy Conversion Efficiency of a Novel Hybrid Solar System for Photovoltaic, Thermoelectric, and Heat Utilization," *IEEE Transactions on Energy Conversion*, vol. 26, pp. 662–670, June 2011.

[32] J. Xiao, T. Yang, P. Li, P. Zhai, and Q. Zhang, "Thermal design and management for performance optimization of solar thermoelectric generator," *Applied Energy*, vol. 93, pp. 33–38, May 2012.

[33] K. Qiu and A. C. S. Hayden, "Development of a novel cascading TPV and TE power generation system," *Applied Energy*, vol. 91, pp. 304–308, Mar. 2012.

[34] M. Ferrari, V. Ferrari, M. Guizzetti, D. Marioli, and A. Taroni, "Characterization of Thermoelectric Modules for Powering Autonomous Sensors," in *Instrumentation and Measurement Technology Conference (IMTC)*, pp. 1–6, 2007.

[35] H. Yu, Y. Li, Y. Shang, and B. Su, "Design and Investigation of Photovoltaic and Thermoelectric Hybrid Power Source for Wireless Sensor Networks," in *3rd IEEE Int. Conf. on Nano/Micro Engineered and Molecular Systems*, pp. 196–201, 2008.

[36] Y. K. Ramadass and A. P. Chandrakasan, "A Battery-Less Thermoelectric Energy Harvesting Interface Circuit With 35 mV Startup Voltage," *IEEE Journal of Solid-State Circuits*, vol. 46, pp. 333–341, Jan. 2011.

[37] J. Kim and C. Kim, "A DC-DC Boost Converter With Variation-Tolerant MPPT Technique and Efficient ZCS Circuit for Thermoelectric Energy Harvesting Applications," *IEEE Transactions on Power Electronics*, vol. 28, no. 8, pp. 3827–3833, 2013.

[38] W. Wang, V. Cionca, N. Wang, M. Hayes, B. O'Flynn, and C. O'Mathuna, "Thermoelectric Energy Harvesting for Building Energy Management Wireless Sensor Networks," *International Journal of Distributed Sensor Networks*, vol. 2013, 2013.

[39] A. Elefsiniotis, N. Kokorakis, T. Becker, and U. Schmid, "A thermoelectric-based energy harvesting module with extended operational temperature range for powering autonomous wireless sensor nodes in aircraft," *Sensors and Actuators A: Physical*, vol. 206, pp. 159–164, 2014.

[40] A. Elefsiniotis, M. Weiss, T. Becker, and U. Schmid, "Efficient Power Management for Energy-Autonomous Wireless Sensor Nodes for Aeronautical Applications," *Journal of Electronic Materials*, Feb. 2013.

[41] J. R. Buckle, A. Knox, J. Siviter, and A. Montecucco, "Autonomous Underwater Vehicle Thermoelectric Power Generation," *Journal of Electronic Materials*, vol. 42, pp. 2214–2220, Apr. 2013.

[42] A. Patyk, "Thermoelectrics: Impacts on the Environment and Sustainability," *Journal of Electronic Materials*, vol. 39, pp. 2023–2028, Dec. 2009.

[43] A. Patyk, "Thermoelectric generators for efficiency improvement of power generation by motor generators Environmental and economic perspectives," *Applied Energy*, vol. 102, pp. 1448–1457, Feb. 2013.

[44] B. I. Ismail and W. H. Ahmed, "Thermoelectric Power Generation Using Waste-Heat Energy as an Alternative Green Technology," *Recent Patents on Electrical Engineering*, vol. 2, no. 807, pp. 27–39, 2009.

[45] M. Zebarjadi, K. Esfarjani, M. S. Dresselhaus, Z. F. Ren, and G. Chen, "Perspectives on thermoelectrics: from fundamentals to device applications," *Energy & Environmental Science*, vol. 5, no. 1, p. 5147, 2012.

[46] K. Biswas, J. He, I. D. Blum, C.-I. Wu, T. P. Hogan, D. N. Seidman, V. P. Dravid, and M. G. Kanatzidis, "High-performance bulk thermoelectrics with all-scale hierarchical architectures," *Nature*, vol. 489, pp. 414–418, Sept. 2012.

[47] R. J. Mehta, Y. Zhang, C. Karthik, B. Singh, R. W. Siegel, T. Borca-Tasciuc, and G. Ramanath, "A new class of doped nanobulk high-figure-of-merit thermoelectrics by scalable bottom-up assembly.," *Nature materials*, vol. 11, pp. 233–40, Mar. 2012.

[48] L. Rauscher, S. Fujimoto, H. T. Kaibe, and S. Sano, "Efficiency determination and general characterization of thermoelectric generators using an absolute measurement of the heat flow," *Measurement Science and Technology*, vol. 16, pp. 1054–1060, May 2005.

[49] H. Takazawa, H. Obara, Y. Okada, K. Kobayashi, T. Onishi, and T. Kajikawa, "Efficiency measurement of thermoelectric modules operating in the temperature difference of up to 550K," in *25th International Conference on Thermoelectrics (ICT)*, pp. 189–192, IEEE, 2006.

[50] E. Sandoz-Rosado and R. J. Stevens, "Experimental Characterization of Thermoelectric Modules and Comparison with Theoretical Models for Power Generation," *Journal of Electronic Materials*, vol. 38, pp. 1239–1244, Mar. 2009.

[51] H. S. Han, Y. H. Kim, S. Y. Kim, S. Um, and J. M. Hyun, "Performance Measurement and Analysis of a Thermoelectric Power Generator," in *12th Intersociety Conference on Thermal and Thermomechanical Phenomena in Electronic Systems (ITherm)*, pp. 1–7, IEEE, 2010.

[52] L. Anatychuk and M. Havrylyuk, "Procedure and Equipment for Measuring Parameters of Thermoelectric Generator Modules," *Journal of Electronic Materials*, vol. 40, pp. 1292–1297, Mar. 2011.

[53] D. Rowe and G. Min, "Evaluation of thermoelectric modules for power generation," *Journal of Power Sources*, vol. 73, pp. 193–198, June 1998.

[54] S. Lineykin and S. Ben-Yaakov, "Modeling and Analysis of Thermoelectric Modules," *IEEE Transactions on Industry Applications*, vol. 43, no. 2, pp. 505–512, 2007.

[55] J. Bird, *Electrical and Electronic Principles and Technology*. Routledge, 2010.

[56] I. Laird, H. Lovatt, N. Savvides, D. Lu, and V. G. Agelidis, "Comparative Study of Maximum Power Point Tracking Algorithms for Thermoelectric Generators," in *Australasian Universities Power Engineering Conference (AUPEC'08)*, 2008.

[57] G. Liang, J. Zhou, and X. Huang, "Analytical model of parallel thermoelectric generator," *Applied Energy*, vol. 88, pp. 5193–5199, Dec. 2011.

[58] M. Alata, M. A. Al-Nimr, and M. Naji, "Transient Behavior of a Thermoelectric Device under the Hyperbolic Heat Conduction Model," *International Journal of Thermophysics*, vol. 24, no. 6, pp. 1753–1768, 2003.

[59] M. Naji, M. Alata, and M. A. Al-Nimr, "Transient behaviour of a thermoelectric device," *Proceedings of the Institution of Mechanical Engineers, Part A: Journal of Power and Energy*, vol. 217, pp. 615–621, 2003.

[60] L. Chen, D. Cao, H. Yi, and F. Z. Peng, "Modeling and power conditioning for thermoelectric generation," in *Power Electronics Specialists Conference*, pp. 1098 – 1103, IEEE, June 2008.

[61] M. Chen, L. A. Rosendahl, T. J. Condra, and J. K. Pedersen, "Numerical Modeling of Thermoelectric Generators With Varing Material Properties in a Circuit Simulator," *IEEE Transactions on Energy Conversion*, vol. 24, pp. 112–124, Mar. 2009.

[62] C.-H. Cheng and S.-Y. Huang, "Development of a non-uniform-current model for predicting transient thermal behavior of thermoelectric coolers," *Applied Energy*, vol. 100, pp. 326–335, Dec. 2012.

[63] J.-H. Meng, X.-D. Wang, and X.-X. Zhang, "Transient modeling and dynamic characteristics of thermoelectric cooler," *Applied Energy*, vol. 108, pp. 340–348, Aug. 2013.

[64] J.-Y. Jang, Y.-C. Tsai, and C.-W. Wu, "A study of 3-D numerical simulation and comparison with experimental results on turbulent flow of venting flue gas using thermoelectric generator modules and plate fin heat sink," *Energy*, vol. 53, pp. 270–281, May 2013.

[65] M. Brignone, A. Ziggiotti, P. Repetto, V. G. Lambertini, and P. Perlo, "Generator of electric energy based on the thermoelectric effect," 2008.

[66] Y. Wang, C. Dai, and S. Wang, "Theoretical analysis of a thermoelectric generator using exhaust gas of vehicles as heat source," *Applied Energy*, vol. 112, pp. 1171–1180, Dec. 2013.

[67] R. C. N. Pilawa-Podgurski and D. J. Perreault, "Submodule Integrated Distributed Maximum Power Point Tracking for Solar Photovoltaic Applications," *IEEE Transactions on Power Electronics*, vol. 28, no. 6, pp. 2957–2967, 2013.

[68] H. Wu, K. Sun, M. Chen, Z. Chen, and Y. Xing, "Hybrid Centralized-Distributed Power Conditioning System for Thermoelectric Generator with High Energy Efficiency," in *Energy Conversion Congress and Exposition (ECCE)*, pp. 4659–4664, IEEE, 2013.

[69] H. Wu, K. Sun, M. Chen, and Y. Xing, "Evaluation of Power Conditioning Architectures for Energy Production Enhancement in Thermoelectric Generator Systems," *Journal of Electronic Materials*, Oct. 2013.

[70] S. Poshtkouhi, V. Palaniappan, M. Fard, and O. Trescases, "A General Approach for Quantifying the Benefit of Distributed Power Electronics for Fine Grained MPPT in Photovoltaic Applications Using 3-D Modeling," *IEEE Transactions on Power Electronics*, vol. 27, no. 11, pp. 4656–4666, 2012.

[71] M. Vitelli, "On the necessity of joint adoption of both Distributed Maximum Power Point Tracking and Central Maximum Power Point Tracking in PV systems," *Progress in Photovoltaics: Research and Applications*, July 2012.

[72] M. Molina, L. Juanicó, G. Rinalde, E. Taglialavore, and S. Gortari, "Design of improved controller for thermoelectric generator used in distributed generation," *International Journal of Hydrogen Energy*, vol. 35, no. 11, pp. 5968–5973, 2010.

[73] I. Laird and D. D.-C. Lu, "High Step-Up DC/DC Topology and MPPT Algorithm for Use With a Thermoelectric Generator," *IEEE Transactions on Power Electronics*, vol. 28, no. 7, pp. 3147–3157, 2013.

[74] K. Sun, L. Ni, M. Chen, H. Wu, Y. Xing, and L. Rosendahl, "Evaluation of High Step-Up Power Electronics Stages in Thermoelectric Generator Systems," *Journal of Electronic Materials*, vol. 42, pp. 2157–2164, Apr. 2013.

[75] C. Yu and K. Chau, "Thermoelectric automotive waste heat energy recovery using maximum power point tracking," *Energy Conversion and Management*, vol. 50, pp. 1506–1512, June 2009.

[76] J. Damaschke, "Design of a low-input-voltage converter for thermoelectric generator," *IEEE Transactions on Industry Applications*, vol. 33, no. 5, pp. 1203–1207, 1997.

[77] E. J. Carlson, K. Strunz, and B. P. Otis, "A 20 mV Input Boost Converter With Efficient Digital Control for Thermoelectric Energy Harvesting," *IEEE Journal of Solid-State Circuits*, vol. 45, pp. 741–750, Apr. 2010.

[78] M. Orellana, S. Petibon, B. Estibals, and C. Alonso, "Four Switch Buck-Boost Converter for Photovoltaic DC-DC power applications," in *36th Annual Conference on IEEE Industrial Electronics Society (IECON)*, no. 1, pp. 469–474, IEEE, Nov. 2010.

[79] R. K. Hester, C. Thornton, S. Dhople, Z. Zhao, N. Sridhar, and D. Freeman, "High efficiency wide load range buck/boost/bridge photovoltaic microconverter," in *26th Applied Power Electronics Conference and Exposition (APEC)*, pp. 309–313, IEEE, Mar. 2011.

[80] H. Nagayoshi and T. Kajikawa, "Mismatch Power Loss Reduction on Thermoelectric Generator Systems Using Maximum Power Point Trackers," *25th International Conference on Thermoelectrics (ICT)*, pp. 210–213, 2006.

[81] H. Nagayoshi, K. Tokumisu, and T. Kajikawa, "Evaluation of multi MPPT thermoelectric generator system," *26th International Conference on Thermoelectrics (ICT)*, pp. 318–321, June 2007.

[82] R.-Y. Kim and J.-S. Lai, "A Seamless Mode Transfer Maximum Power Point Tracking Controller For Thermoelectric Generator Applications," *IEEE Transactions on Power Electronics*, vol. 23, no. 5, pp. 2310–2318, 2008.

[83] D. Champier, C. Favarel, J. P. Bédécarrats, T. Kousksou, and J. F. Rozis, "Prototype Combined Heater/Thermoelectric Power Generator for Remote Applications," *Journal of Electronic Materials*, Jan. 2013.

[84] R.-Y. Kim, J.-S. Lai, B. York, and A. Koran, "Analysis and Design of Maximum Power Point Tracking Scheme for Thermoelectric Battery Energy Storage System," *IEEE Transactions on Industrial Electronics*, vol. 56, pp. 3709–3716, Sept. 2009.

[85] N. Phillip, O. Maganga, K. J. Burnham, M. a. Ellis, S. Robinson, J. Dunn, and C. Rouaud, "Investigation of Maximum Power Point Tracking for Thermoelectric Generators," *Journal of Electronic Materials*, vol. 42, pp. 1900–1906, Jan. 2013.

[86] O. Maganga, N. Phillip, K. J. Burnham, A. Montecucco, J. Siviter, A. Knox, and K. Simpson, "Hardware Implementation of Maximum Power Point Tracking for Thermoelectric Generators," *Journal of Electronic Materials*, Feb. 2014.

[87] S. Cho, N. Kim, S. Park, and S. Kim, "A Coreless Maximum Power Point Tracking Circuit of Thermoelectric Generators for Battery Charging Systems," in *Asian Solid-State Circuits Conference*, no. 2, pp. 9–6, IEEE, 2010.

[88] S. Kim, S. Cho, N. Kim, N. Baatar, and J. Kwon, "A Digital Coreless Maximum Power Point Tracking Circuit for Thermoelectric Generators.pdf," *Journal of Electronic Materials*, vol. 40, no. 5, pp. 867–872, 2011.

[89] D. E. Schwartz, "A maximum-power-point-tracking control system for thermoelectric generators," *3rd International Symposium on Power Electronics for Distributed Generation Systems (PEDG)*, pp. 78–81, June 2012.

[90] R. S. Muller, T. I. Kamins, and M. Chan, *Device Electronics for Integrated Circuits*. Wiley, 2002.

[91] L. Anatychuk, "On the discovery of thermoelectricity by Volta," *Journal of Thermoelectricity*, vol. 2, pp. 5–11, 2004.

[92] M. Lazard, "Heat Transfer in Thermoelectricity: Modelling, Optimization and Design," in *7th IASME/WSEAS International International Conference on Heat Transfer, Thermal Engineering and Environment*, pp. 129–134, 2009.

[93] C.-Y. Du and C.-D. Wen, "Experimental investigation and numerical analysis for one-stage thermoelectric cooler considering Thomson effect," *International Journal of Heat and Mass Transfer*, vol. 54, pp. 4875–4884, Nov. 2011.

[94] J. Chen, Z. Yan, and L. Wu, "The influence of Thomson effect on the maximum power output and maximum efficiency of a thermoelectric generator," *Journal of Applied Physics*, vol. 79, no. 11, p. 8823, 1996.

[95] G. Min, D. M. Rowe, and K. Kontostavlakis, "Thermoelectric figure-of-merit under large temperature differences," *Journal of Physics D: Applied Physics*, vol. 37, pp. 1301–1304, Apr. 2004.

[96] L. Ferre Llin, A. Samarelli, S. Cecchi, T. Etzelstorfer, E. Muller Gubler, D. Chrastina, G. Isella, J. Stangl, J. M. R. Weaver, P. S. Dobson, and D. J. Paul, "The cross-plane thermoelectric properties of p-Ge/Si0.5Ge0.5 superlattices," *Applied Physics Letters*, vol. 103, no. 14, p. 143507, 2013.

[97] M. Brignone and A. Ziggiotti, "Impact of novel thermoelectric materials on automotive applications," in *9th European Conference on Thermoelectrics (ECT)*, pp. 493–496, 2011.

[98] G. Min and N. M. Yatim, "Variable thermal resistor based on self-powered Peltier effect," *Journal of Physics D: Applied Physics*, vol. 41, p. 222001, Nov. 2008.

[99] S. Chiwanga, K. Simpson, R. Gilchrist, and A. Montecucco, "Characterisation of Commercial ThermoElectric Module using Experimental and Numerical Techniques to Compile Performance Data," in *3rd Conference on Thermoelectrics*, 2012.

[100] G. Min, "Thermoelectric Energy Harvesting," in *Energy Harvesting for Autonomous Systems*, vol. 413-414, ch. Chapter 5, pp. 135–157, Artech House, June 2010.

[101] A. Samarelli, L. Ferre Llin, S. Cecchi, J. Frigerio, T. Etzelstorfer, E. Muller, Y. Zhang, J. R. Watling, D. Chrastina, G. Isella, J. Stangl, J. P. Hague, J. M. R. Weaver, P. Dobson, and D. J. Paul, "The thermoelectric properties of Ge/SiGe modulation doped superlattices," *Journal of Applied Physics*, vol. 113, no. 23, p. 233704, 2013.

[102] B. C. Woo, D. Y. Lee, H. W. Lee, and K. I. J., "Characteristic of Maximum Power with Temperature Difference for Thermoelectric Generator," *20th International Conference on Thermoelectrics (ICT)*, pp. 431–434, 2001.

[103] A. Montecucco, J. R. Buckle, and A. R. Knox, "Solution to the 1-D unsteady heat conduction equation with internal Joule heat generation for thermoelectric devices," *Applied Thermal Engineering*, vol. 35, pp. 177–184, Mar. 2012.

[104] J. Gao and M. Chen, "Beat the Deviations in Estimating Maximum Power of Thermoelectric Modules," *IEEE Transactions on Instrumentation and Measurement*, vol. 62, pp. 2725–2729, Oct. 2013.

[105] M. Gomez, R. Reid, B. Ohara, and H. Lee, "Influence of electrical current variance and thermal resistances on optimum working conditions and geometry for thermoelectric energy harvesting," *Journal of Applied Physics*, no. 113, pp. 0–8, 2013.

[106] R. McCarty, "Thermoelectric Power Generator Design for Maximum Power: Its All About ZT," *Journal of Electronic Materials*, vol. 42, pp. 1504–1508, Oct. 2012.

[107] H. Lee, "Optimal design of thermoelectric devices with dimensional analysis," *Applied Energy*, vol. 106, pp. 79–88, June 2013.

[108] E. Hatzikraniotis, K. T. Zorbas, I. Samaras, T. Kyratsi, and K. M. Paraskevopoulos, "Efficiency Study of a Commercial Thermoelectric Power Generator (TEG) Under Thermal Cycling," *Journal of Electronic Materials*, vol. 39, pp. 2112–2116, Nov. 2009.

[109] A. Montecucco, J. Buckle, J. Siviter, and A. R. Knox, "A New Test Rig for Accurate Nonparametric Measurement and Characterization of Thermoelectric Generators," *Journal of Electronic Materials*, Mar. 2013.

[110] D.-A. Borca-Tasciuc, G. Chen, A. Prieto, M. S. Martin-Gonzalez, A. Stacy, T. Sands, M. A. Ryan, and J. P. Fleurial, "Thermal properties of electrodeposited bismuth telluride nanowires embedded in amorphous alumina," *Applied Physics Letters*, vol. 85, no. 24, p. 6001, 2004.

[111] A. Montecucco, J. Buckle, J. Siviter, and A. R. Knox, "A New Test Rig for Accurate Nonparametric Measurement and Characterization of Thermoelectric Generators," *Journal of Electronic Materials*, Mar. 2013.

[112] A. Montecucco, J. Siviter, and A. Knox, "Simple, fast and accurate maximum power point tracking converter for thermoelectric generators," in *Energy Conversion Congress and Exposition (ECCE), IEEE*, pp. 2777–2783, 2012.

[113] C. Basso, *Switch-Mode Power Supplies: Spice Simulations and Practical Designs*. McGraw-Hill Professional, 2008.

[114] L. Balogh, "Design And Application Guide For High Speed MOSFET Gate Drive Circuits," tech. rep.

[115] T. Esram and P. L. Chapman, "Comparison of Photovoltaic Array Maximum Power Point Tracking Techniques," *IEEE Transactions on Energy Conversion*, vol. 22, pp. 439–449, June 2007.

[116] C. Favarel, D. Champier, J. P. Bedecarrats, T. Kousksou, and F. Strub, "Study of a thermoelectric system equipped with a maximum power point tracker for stand-alone electric generation," in *9th European Conference on Thermoelectrics (ECT)*, pp. 520–523, 2011.

[117] Y. Jiang, S. Member, J. A. A. Qahouq, S. Member, and T. A. Haskew, "Adaptive Step Size With Adaptive-Perturbation- Frequency Digital MPPT Controller for a Single-Sensor Photovoltaic Solar System," *IEEE Transactions on Power Electronics*, vol. 28, no. 7, pp. 3195–3205, 2013.

[118] N. Femia, G. Petrone, G. Spagnuolo, and M. Vitelli, "Optimization of Perturb and Observe Maximum Power Point Tracking Method," *IEEE Transactions on Power Electronics*, vol. 20, no. 4, pp. 963–973, 2005.

[119] A. M. Latham, R. Pilawa-Podgurski, K. M. Odame, and C. R. Sullivan, "Analysis and Optimization of Maximum Power Point Tracking Algorithms in the Presence of Noise," *IEEE Transactions on Power Electronics*, vol. 28, no. 7, pp. 3479–3494, 2013.

[120] A. Safari and S. Mekhilef, "Simulation and Hardware Implementation of Incremental Conductance MPPT With Direct Control Method Using Cuk Converter," *IEEE Transactions on Industrial Electronics*, vol. 58, pp. 1154–1161, Apr. 2011.

[121] F. Liu, S. Duan, F. Liu, B. Liu, and Y. Kang, "A Variable Step Size INC MPPT Method for PV Systems," *IEEE Transactions on Industrial Electronics*, vol. 55, no. 7, pp. 2622–2628, 2008.

[122] Q. Mei, M. Shan, L. Liu, and J. M. Guerrero, "A Novel Improved Variable Step-Size Method for PV Systems," *IEEE Transactions on Industrial Electronics*, vol. 58, no. 6, pp. 2427–2434, 2011.

[123] R. W. Erickson and D. Maksimović, *Fundamentals of Power Electronics*. Springer, 2001.

[124] B. Sahu and G. Rincon-Mora, "A Low Voltage, Dynamic, Noninverting, Synchronous Buck-Boost Converter for Portable Applications," *IEEE Transactions on Power Electronics*, vol. 19, pp. 443–452, Mar. 2004.

[125] J.-K. Shiau, C.-J. Cheng, and C.-E. Tseng, "Stability analysis of a non-inverting synchronous buck-boost power converter for a solar power management system," in *International Conference on Sustainable Energy Technologies*, pp. 263–268, IEEE, Nov. 2008.

[126] J.-J. Chen, P.-N. Shen, and Y.-S. Hwang, "A High-Efficiency Positive BuckBoost Converter With Mode-Select Circuit and Feed-Forward Techniques," *IEEE Transactions on Power Electronics*, vol. 28, no. 9, pp. 4240–4247, 2013.

[127] D. T. Crane and G. S. Jackson, "Optimization of cross flow heat exchangers for thermoelectric waste heat recovery," *Energy Conversion and Management*, vol. 45, pp. 1565–1582, June 2004.